Mechanical regulation of cardiac fibroblasts

Dissertation

for the award of the degree

“Doctor rerum naturalium” (Dr. rer. nat.)

of the Georg-August-Universität Göttingen,

Faculty of Medicine

within the doctoral program Molecular Medicine of the

Georg-August University School of Science (GAUSS)

submitted by

Gabriela de Jesus Leão Pereira dos Santos

born in Paços de Ferreira, Portugal

Göttingen, 2020

Thesis Committee Members and Examination Board

First reviewer: Prof. Dr. rer. nat, Susanne Lutz (supervisor),
Institute of Pharmacology and Toxicology, University Medical Center Göttingen.

Second reviewer: Prof. Dr. Peter Schu,
Institute for Cellular Biochemistry, University Medical Center Göttingen.

Third Reviewer: Prof. Dr. med. Ralf Dressel,
Institute of Cellular and Molecular Immunology, University Medical Center Göttingen.

Further Members of the Examination Board

Prof. Dr. mult. Thomas Meyer,
Institute of Psychosomatic Medicine and Psychotherapy, University Medical Center Göttingen.

Prof. Dr. med. Dörthe M. Katschinski,
Institute for Cardiovascular Physiology, University Medical Center Göttingen.

Univ.-Prof. Dr. med. M. Zeisberg,
Clinic for Nephrology and Rheumatology, University Medical Center Göttingen.

Guests

Prof. Dr. Anne Ridley (co-supervisor)
Randall Division of Cell & Molecular Biophysics, King's College London.

Date of the oral examination: 26th of October 2020

Affidavit

This dissertation entitled “Mechanical regulation of cardiac fibroblasts” is the result of my own work and with no other sources and aids other than specifically quoted in the text. It has not been previously submitted, in part or whole, to any university or institution for any academic degree, or other qualification.

_____

(Gabriela L. Santos)

Göttingen, July 31st, 2020

Acknowledgments

This work was carried out in the lab of Prof. Susanne Lutz (Institute of Pharmacology and Toxicology) who mentored me through the past four years. I am very grateful for the unwavering support and opportunity you provided me throughout my PhD studies. You always wanted me to succeed and did everything possible to ensure this. You never hesitated to provide me with the needed counselling, help and resources for my work during these years and I am very grateful for that.

I also want to express my gratitude to my co-supervisor Prof. Dr. Anne Ridley from King's College London, who has contributed to an enriching international experience, and shared her expertise in Rho-kinases.

My sincere gratitude also goes to Prof. Dr. Wolfram-Hubertus Zimmermann, director of the Institute of Pharmacology and Toxicology, at the University of Göttingen, for the opportunity to join an excellent international team and for making available all the technical and intellectual resources to develop my work and grow as a scientist.

The International Research Training Group (IRTG) 1816, funded by the German Research Council (DFG) and the King's College London and British Heart Foundation Centre of Research Excellence supported the entire education strategy, and for this I have to thank all members involved, including Prof. Dr. Dörthe M. Katschinski, Dr. Christina M. Würtz and Mrs. Fulya M. Ören.

I am thankful for the support and helpful discussions with Prof. Ralf Dressel and Prof. Peter Schu, who were part of my thesis committee. You both stimulated my interest in science, and guided me along the right path in the last years.

My sincere appreciation to the AG-Lutz's laboratory members, including Sebastian Pasch, Laura Sommerfeld, Abdul Rehman, Alisa DeGrave, Sara Al Disi and Helen Schröder. I would like to specially acknowledge the assistance of diligent colleagues and friends I worked and discussed with over the years on several projects, including Dr. Norman Liaw, Dr. Maria-Patapia Zafieriou, Dr. Laura Zelarayan, Dr. Cheila Rocha, Eric Schoger, Sebastian Nagel, Dr. Tim Meyer, Dr. Malte Tiburcy. My appreciation extends to all other respected members of the Institute of Pharmacology and Toxicology.

My parents, brother, Nick and all other members of my family, thank you for the continuous support, guidance and love.

Table of Contents

List of Tables

List of Figures

List of Abbreviations

(IL)-6	Interleukin-6
2D	Two-dimensional
3D	Three-dimensional
ACEI	Angiotensin-converting enzyme inhibitors
ACTA2	Actin alpha 2 (alias SMA)
Ang II	Angiotensin II
APS	Ammonium persulfate
ARNI	Angiotensin receptor neprilysin inhibitors
AT1R	Angiotensin II receptor-type 1
ATP	Adenosine triphosphate
BAPN	β-aminopropionitrile
BFA	Brefeldin A
BNP	Brain natriuretic peptide
BSA	Bovine serum albumin
cAMP	Cyclic adenosine monophosphate
CBFHH	Calcium and bicarbonate free Hanks with HEPES
CCDC80	Coiled-coil domain containing 80
CCN2	Cellular Communication Network Factor 2 (alias CTGF)
CD90	Cluster of Differentiation 90 (alias THY1)
cDNA	Complementary deoxyribonucleic acid
CF	Cardiac fibroblasts
COL1A1	Alpha-1 type I collagen
COL3A1	Alpha-1 type III collagen
COL6A1	Alpha-1 type VI collagen
CRT	Cardiac resynchronization therapy
CSA	Cross-sectional area
CTGF	Connective tissue growth factor (alias CCN2)
CVD	Cardiovascular diseases

CYR61	Cysteine-rich angiogenic inducer 61
d	Day
DAPI	4′,6-diamidino-2-phenylindole
DCM	Dilated cardiomyopathies
$_{dd}H_2O$	Double distilled water
DEGs	Differential expressed genes
DMEM	Dulbecco's modified eagle’s medium
DMSO	Dimethyl sulfoxide
DNA	Deoxyribonucleic acid
dNTP	Deoxynucleoside triphosphate
DPBS	Dulbecco's phosphate-buffered saline
ECL	Enhanced chemiluminescence
ECM	Extracellular matrix
ECT	Engineered connective tissue
EDTA	Ethylenediaminetetraacetic acid
EF	Ejection fraction
EMT	Epithelial-mesenchymal transition
EndMT	Endothelial-mesenchymal transition
eNOS	Endothelial nitric oxide synthase
EPDC	Epicardial-derived cells
ER	Endoplasmic reticulum
ESC	European Society of Cardiology
F-actin	Filamentous actin
F1	Flexible hECT day 1
F5	Flexible hECT day 5
FA	Focal adhesions
FACS	Fluorescence-activated cell sorting
FBS	Fetal bovine serum
FCS	Fetal calf serum
FGF2	Fibroblast growth factor 2
FGM3	Fibroblast growth media with 3 components
FITC	Fluorescein isothiocyanate

FN1	Fibronectin 1
FSP1	Fibroblast specific protein 1 (alias S100A4)
FW	Forward
GAPDH	Glyceraldehyde 3-phosphate dehydrogenase
GPCR	G-protein coupled receptors
GTPases	Nucleotide guanosine triphosphate hydrolases
GUSB	β-glucuronidase
h	Hour
H1152P	[(S)-(+)-2-methyl-1-[(4-methyl-5-isoquinolinyl) sulfonyl]-hexahydro-1H-1,4-diazepine]
HAS2	Hyaluronan synthase 2
hCF	Normal human cardiac fibroblasts from the ventricle
HCl	Hydrogen chloride
HCM	Hypertrophic cardiomyopathy
hECT	Human Engineered Connective Tissue
HEPA	High-efficiency particulate air
HEPES	4-(2-hydroxyethyl)-1-piperazineethanesulfonic acid
HF	Heart failure
HFpEF	Heart failure with a preserved ejection fraction
HFrEF	Heart failure with a reduced ejection fraction
HK	Housekeeping
HPRT	Hypoxanthine-guanine phosphoribosyltransferase
HRP	Horseradish peroxidase
HSF1	Heat shock factor 1
IB	Immunoblot
ICM	Ischemic cardiomyopathy
IFP	Idiopathic pulmonary fibrosis
IgG	Immunoglobulin G
kPa	Kilo Pascal
Lat-A	Latrunculin A
LGALS3	Galectin 3
LIMK	LIM kinases
LOX	Lysyl oxidase

LV	Left ventricular
MAPK	Mitogen-activated protein kinase 1
$MgCl_2$	Magnesium chloride
MI	Myocardial infarction
min	Minutes
MLC	Myosin light chain
MMP12	Matrix metalloproteinase-12
MMP2	Matrix metalloproteinase-2
MMPs	Matrix metalloproteinases
MRA	Mineralocorticoid/aldosterone receptor antagonists
MRTF	Myocardin-related transcription factor A
MYPT1	Myosin phosphatase-targeting subunit 1
NaCl	Sodium chloride
NCM	Non-cardiomyocytes medium
NRCF	Neonatal rat cardiac fibroblasts
NT-proBNP	N-terminal pro-B-type natriuretic peptide
NYHA	New York Heart Association
P	Passage
P4HA1	Prolyl 4-Hydroxylase Subunit Alpha 1
PAGE	Polyacrylamide gel electrophoresis
PBGD	Porphobilinogen deaminase
PBS	Phosphate buffered saline
PC	Principal component
PDE2	phosphodiesterase 2
PDGFRα	Platelet-derived growth factor receptor alpha
PDMS	Polydimethylsiloxane
PES	Polyethersulfone
PFA	Paraformaldehyde
PFD	Pirfenidone
PI	Propidium iodide
PKA	Protein kinases A
PKC	Protein kinases C

POSTN	Periostin
PPI	Protein-protein interaction
PTFE	Polytetra-fluoroethylene
qPCR	Quantitative polimerase chain reaction
RAAS	Renin-Angiotensin II-aldosterone system
RCF	Relative centrifugal force
rECT	Rat engineered connective tissue
RNA	Ribonucleic acid
ROCK	Rho-associated kinases
ROX	5-Carboxyrhodamine 6G
RPKM	Reads Per Kilobase of transcript, per Million mapped reads
RPM	Revolutions per minute
RV	Reverse
s	Seconds
S1	Stiff hECT day 1
S100A4	S100 calcium-binding protein A4 (alias FSP1)
S5	Stiff hECT day 5
SDS	Sodium dodecyl sulfate
SEM	Standard error of the mean
SMA	Alpha smooth muscle actin (alias ACTA2)
SMAD3	Mothers against decapentaplegic homolog 3
SRF	Serum response factor
TAE	Tris-acetate-EDTA
TAZ	Tafazzin, PDZ-binding motif
TBS	Tris-buffered saline
TBST	Tris-buffered saline with Tween 20
TCF21	Transcription factor 21
TEMED	Tetramethylethylenediamine
TGF-β	Transforming growth factor beta
THY1	Thy-1 Cell Surface Antigen (alias CD90)
TIMPs	Tissue inhibitors of metalloproteinases
TNF-α	Tumor necrosis factor alpha

Tris	Trisamine
UPR	Unfolded protein response
UVA	Ultraviolet A
VEGF	Vascular endothelial growth factor
VIM	Vimentin
WT1	Wilms tumor protein
YAP	Yes-associated protein
β-blockers	β-adrenergic receptor blockers
β-ME	2-sulfanylethanol or β-mercaptoethanol
⌀	Diameter

Nomenclature:

Gene and protein names are written according to the international guidelines for gene and protein nomenclature [1, 2].

Example:

- Murine gene: *Rock1*,
- Human gene: *ROCK1*,
- Summary of human and mouse transcripts: ROCK1,
- Murine/human protein: ROCK1.

Exceptionally, α-Tubulin, β-Actin and TGF-β proteins were not written according to the nomenclature, but as hereby indicated.

Abstract

Cardiac fibrosis progressively contributes to heart failure (HF). Yet, its complex nature still lacks a more comprehensive understanding. One main hurdle is the lack of representative human models providing insights into the behaviour of cardiac fibroblasts (CF) and their pathological derivatives. Therefore, our group developed a human engineered connective tissue (hECT) model based on primary human CF and collagen type 1, which allows studying the pathological CF conversion. In this model, the environmental stiffness provided by the mould's architecture was used as the single trigger for the CF conversion. The moulds contained either two flexible poles (flexible model) or a single central stiff rod (stiff model). Destructive tensile strength measurements showed that flexible hECT model achieved a stiffness similar to that of the healthy myocardium, while stiff hECT model achieved a stiffness comparable to the diseased myocardium. In addition, stiff hECT showed lower elasticity and extensibility compared to flexible hECT, but could withstand higher stress. A gradual increase in the stiffness of the flexible poles further demonstrated to result in an incremental increase in tissue stiffness and a decrease in tissue contraction. Furthermore, the modulation of the internal cell stiffness by interfering with the actin-myosin cytoskeleton was investigated. To that purpose, ROCK inhibitors and Latrunculin A were applied to both hECT and rat engineered connective tissue (rECT) generated with neonatal rat cardiac fibroblasts. The data indicates that the integrity of the actin-myosin network is relevant for compaction, contraction and stiffening of ECT. The underlying pathway involved the MRTF/SRF-dependent regulation of gene expression, e.g., of the collagen cross-linker enzyme lysyl oxidase (LOX).

To obtain a more profound insight into the stiffness-dependent cellular remodelling, a comparison was conducted between 2D-cultured myofibroblasts and cells from flexible and stiff hECT. It was shown that a partial reversion of the myofibroblasts phenotype of 2D-cultured cells is achievable in hECT, as demonstrated by cell cycle activity and expression of myofibroblast markers. Importantly, the direct comparison of cells in flexible and stiff hECT showed a clear time-dependent segregation in two different cellular phenotypes. By RNA sequencing it was possible to demonstrate that the gene program differs between cells embedded in flexible and in stiff hECT, especially in gene clusters assigned to extracellular matrix organization and protein folding. In comparison with published data from human samples, hECT exposed to high environmental stiffness shows a transcriptome profile similar to that of a failing human heart.

In summary, this novel engineered connective tissue model recapitulates the mechanical changes that occur during fibrogenesis and assisted phenotypic switching of cardiac myo- and fibroblasts mediated by environmental stiffness. Thus, the hECT model opens new perspectives and offers a versatile alternative to study mechanisms underlying scarring of the human heart and for screening for anti-fibrotic drugs.

1. Introduction

1.1. Cardiovascular diseases

The values reported by the World Health Organization evidence that despite the progress in understanding cardiovascular diseases (CVD) and heart failure (HF), they remain the leading cause of death. Every year there are about 17.9 million deaths recorded due to CVD, an estimated 31% of all deaths worldwide [3]. The population growth and increase in life expectancy during the first half of the 20th century was concomitant with increases in age-specific CVD mortality rates. The second half of the century was instead marked by a decline in cardiovascular mortality. Pronounced pharmacological and technological advances, and integrated health systems strategies were attributed to the improvement of CVD prevention and management, especially in regions with very high sociodemographic index [4-8]. The main contributors reported were the declining mortality rates due to cerebrovascular disease and the decline in age-standardised mortality rates for ischemic cardiomyopathy (ICM) [9]. However, additional life expectancy and socioeconomic changes, more atherogenic diet, sedentary lifestyle and the increasing prevalence of tobacco use mitigated that improvement [5, 10].

The CVD are a group of disorders affecting blood vessels and the heart. For example, abnormal heart valves and congenital heart disease typically create an unbalanced heart function in order to compensate for structural defects. More often, CVD are associated with blood flow obstruction. In acute cases, inadequate blood supply to the heart due to blockage of the blood vessels supplying the area results in infarction of the myocardium (ischemic cardiomyopathy, ICM) [7, 11]. There are also non-ischemic cardio-myopathies which are commonly associated with mechanical or electrical dysfunction

exhibiting inappropriate ventricular hypertrophy (hypertrophic cardiomyopathy, HCM) or dilatation (dilated cardiomyopathies, DCM) [12, 13]. Besides causes such as haemodynamic pathology, hypertension, infection, toxic injury and myocardial infarction (MI), in many cases HCM and DCM are inherited [14-18]. In combination of risk factors including diabetes, obesity and tobacco use, CVD result in cardiac remodelling and may lead to the development of myocardial insufficiency.

1.2. The failing heart

Heart failure (HF) is defined as a clinical syndrome resulting from any structural or functional cardiac disorder that impairs adequate blood supply to the body at a rate commensurate with the organ metabolic requirements and oxygenation needs [19, 20]. Two forms of insufficient function can be discriminated: either when the heart fills adequately but there is a reduced blood ejection by a dilated left ventricle (hyposystolic failure), or when there is an inadequate diastolic filling of the heart where thick-walled left ventricle with a normal-sized or smaller cavity is observed (hypodiastolic failure). Subsequently these forms of HF can be distinguished based on the ejection fraction (EF): the first with a reduced EF (HFrEF) and the second with a preserved EF (HFpEF) [21]. HF can also be defined as acute or chronic, and compensated or uncompensated. Left-sided HF is the predominant form of HF syndrome, but the right heart can develop isolated failure as well. Biventricular insufficiency can also occur, being mainly a terminal clinical situation of HF [19, 20, 22].

1.2.1. Remodelling of the myocardium – overview

In HF, independent of the cause, the myocardium undergoes a remodelling process, which is driven by neuro-humoral and mechanical signals. As atherosclerosis and

subsequent MI injury are one of the most common causes of HF, representing the most lethal subset of disease [23-25], it is not surprising that most of the generated knowledge regarding cardiac remodelling is derived from patients and animal models of MI [26]. However, remodelling is an adaptive process that can also occur progressively in response to prolonged wall stress associated with conditions such as sustained pressure overload (hypertension), myocarditis, DCM, and volume overload [12, 27]. On the other hand, when the heart faces an increased workload as it occurs in athletes and pregnant women, it can develop a physiological remodelling response (hypertrophy) which may be reversible [28-32]. Cardiac hypertrophy (concentric or eccentric) is the primary mechanism of cardiac remodelling by which the hypertrophic growth of the cardiomyocytes and of the heart help to maintain or increase the cardiac output [27, 33]. Increased cardiac fibrosis is a feature of hypertrophic cardiomyopathy as well as an intrinsic part of long-standing pathophysiological remodelling in other cardiomyopathies [34-37]. Cardiac fibrosis is characterised by interstitial or/and adventitial (perivascular) deposition of extracellular matrix (ECM) proteins. The accumulated ECM in a fibrotic heart can account for up to 30% of the tissue volume [38, 39], and occurs more frequently subendocardially and in the midwall, with greatest extension in the basal septum of the left ventricle [40-43]. Cardiac fibrosis is associated with increased myocardial stiffness, it is incremental with symptom intensity, contributes to reduced ventricular compliance, and deteriorates physical capacity [27, 40, 42, 43].

Clinically, it has been identified as a determinant of the prognosis of cardiomyopathy progression [44, 45]. Regardless of the origin, cardiac fibrosis is associated with unfavourable prognosis as it contributes to arrhythmias, increased risk of sudden cardiac death, coronary heart disease, more frequent attacks of atrial fibrillation,

ultimately leading to HF [44, 46-52]. Moreover, cardiac fibrosis is implicated in the effectiveness of some therapeutic actions. The assessment of its extension can be used to assist decision-making as it helps predicting response and outcomes after therapeutic interventions. For example, in patients with atrial fibrillation, extensive left atrial tissue fibrosis has shown to predict increased risk of atrial fibrillation recurrence following catheter ablation [51, 53-56]. Also in patients undergoing cardiac resynchronization therapy (CRT) higher concentration levels of the fibrosis biomarkers procollagen type I C-terminal propeptide and procollagen type III N-terminal propeptide relates to negative response after CRT [57-60].

Cardiac fibrosis is indicated as an independent and incremental predictor of mortality and higher incidence of hospitalizations in the context of HF patients [44, 61-67], pointing to cardiac fibroblasts (CF) as major determinants in these pathological processes.

1.2.2. Initiation and development of the fibrotic process – general context

The myocardium comprises a series of cell types, each with unique transcriptional, signalling, remodelling, proliferative, and death responses. After injury or stress stimulation, molecular, cellular, and interstitial events are triggered by stimuli involving extrinsic signals as neuroendocrine agonists and growth factors, and intrinsic biomechanical stress sensing. Collectively, they induce intracellular signal transduction cascades altering cardiac gene expression, ECM homeostasis and turnover, metabolism, and cardiomyocytes contractile function [12, 27, 28, 68, 69]. As these alterations drive cardiac remodelling, they are intrinsically associated with the fibrotic responses. There are two type of fibrotic responses – replacement/reparative and reactive fibrosis – which usually coexist during cardiac remodelling [39, 70, 71].

After an injury such as MI, induced structural and functional alterations within the cardiomyocytes may culminate into cell death by necrosis, apoptosis and/or phagocytosis [72-74]. Cell death triggers a gradual chain of reparative and remodelling events which is generally divided into three phases: inflammation/necrosis, fibrosis/proliferation, and long-term remodelling/maturation [28, 75-77]. Inflammation takes place from the first hours to a few days, whereby inflammatory cells including neutrophils, macrophages, and lymphocytes invade the injured area [78-80]. These cells produce metalloproteinases which degrade matrix components aiding phagocytic macrophages in the resorption of necrotic tissue. Besides, they produce a variety of cytokines and growth factors favouring CF proliferation, activation and transdifferentiation into myofibroblasts [77, 81-83]. Thus, during the following days and weeks after inflammation, replacement fibrosis is ensued in the myocardium to replace necrotic cardiomyocytes. An acute wound healing response is initiated. In this process myofibroblasts facilitate the generation and remodelling of a collagenous scar at the site of injury as a means to prevent cardiac rupture [75-77, 84, 85]. However, while fibrosis may initially provide structural integrity to the heart, also surrounding and remote areas of the injured site undergo reactive fibrosis and hypertrophy [39, 86-90], contributing to adverse remodelling and worsening the outcome after MI injury [44, 46-51]. The exact mechanisms and regulation of reactive fibrosis propagation are still not fully understood. It has been suggested that the diminished ventricular performance resulting in myocardial load changes in surrounding and remote areas of the MI site, in association with inflammation and the release of cytokines and other paracrine mediators, trigger compensatory hypertrophy and interstitial and adventitial reactive fibrosis (diffuse fibrosis) in those areas [39, 91-96].

A reactive fibrotic response can also occur in the absence of cell loss, being directly

initiated particularly in adventitial tissue from areas surrounding the intramyocardial coronary arteries and arterioles due to mechanical stress signals or inflammation [97, 98]. This type of remodelling is observed in various forms of chronic pressure overload as in hypertensive and aortic stenosis patients [99-103]. In remodelling associated to hypertension and aortic stenosis, diffuse fibrosis around vessels and in interstitium may generate microischemic regions with consequent cell loss and replacement fibrosis, which presents a patchy pattern with multiple foci [71, 91, 102]. In chronic hypertensive patients, for example, fibrosis correlates positively with hypertrophied regions and inversely with ejection fraction [91]. Moreover, in hypertrophic cardiomyopathy and systemic hypertension, a gradient of fibrosis is observed in the ventricular free wall from the endocardial to epicardial surface, reflecting transmural gradients of wall stress seen in the chamber as a result of the imposed pressure load on the heart [103].

In consequence of these reactive responses, cellular and molecular changes are enhanced, entering into a vicious cycle which contributes for progressive maladaptive (chronic) fibrosis [104]. In both post-MI and hypertension settings, long-term maladaptive remodelling generates excessive fibrotic tissue which functions as a perfusion barrier resulting in enhanced cardiomyocyte death. This will continuously trigger inflammation and contribute to the perpetuation of ECM remodelling [27, 28, 32, 68, 105]. The propagation of the fibrotic process also causes conduction deficits, contributing to arrhythmias [50-52, 106, 107] and a continuous deterioration of both systolic and diastolic function towards decompensated HF [108, 109].

Several pro-fibrotic mediators and signalling pathways have been implicated in the early stages of fibrosis and were also indicated as drivers of a sustained progressive fibrotic response (partially summarised in *section 1.3.4.*). If the resulting passive mechanical stiffness increase of the tissue over-time is the trigger for a sustained non-

physiological (reactive) fibrotic response is rather unclear. Thus, in order to more efficiently diagnose and develop targeted therapies it is fundamental to understand the underlying mechanisms by which fibrosis is triggered and progressively sustained, including the activation of fibroblasts and transdifferentiation into myofibroblasts, the major drivers of fibrosis.

1.3. Fibroblasts in the heart

In the heart, although cardiomyocytes constitute ~75% of the total tissue volume, non-myocyte cells, such as endothelial cells, fibroblasts, vascular smooth muscle cells, and hematopoietic-derived cells, compose near 70% of the total cell content of the heart [110, 111]. Up to now there had not been any human study regarding the single proportions of non-myocytes in the heart, but in a recent study using mice, Pinto and colleagues combined histology-based and flow cytometry methods, refining the approaches for cellular composition quantification used in earlier studies. They revealed that in the healthy mouse heart fibroblasts constitute under 20% of the non-myocytes, equivalent to ~11% of the total cells of the heart on the assumption that ~30% of cells are cardiomyocytes, which contradicted earlier ideas of CF being the most abundant cell type in the heart [112].

1.3.1. Origin and function of cardiac fibroblasts

Embryonic origin of cardiac fibroblasts

The origin of fibroblasts still lacks more comprehensive elucidation, but the built knowledge until now supports that fibroblasts have multiple spatiotemporal sources. Developmental studies have shown that CF in the developing heart arise from

epicardial-derived cells (EPDC) (**Figure 1**) expressing platelet-derived growth factor receptor alpha (*Pdgfrα*) or periostin (*Postn*) [113, 114]. Furthermore, Pinto and colleagues have demonstrated that 95% of the fibroblasts identified in the healthy murine adult heart, which express alpha-1 type I collagen (*Col1a1*) and *Pdgfrα* are from a *Tcf21*-lineage [112]. Transcription factor 21 (*Tcf21*, also known as epicardin) has been shown to be instrumental for cardiac fibroblast development from multipotent epicardial progenitors, prior to the process of epithelial-mesenchymal transition (EMT) [115]. The differentiation process EMT occurs mainly from around embryonic day 13.5 on, as it was shown in mice [116-118]. Studies using lineage-tracing showed that EMT involves PDGFRα, Wilms tumor protein (WT1), T-box transcription factor 18 (TBX18) and TCF21 signalling [115, 117, 119-121] and is stimulated by the transforming growth factor beta (TGF-β) [122]. Besides, it has been proposed that POSTN might promote and sustain differentiation of the fibroblast phenotype [123-128].

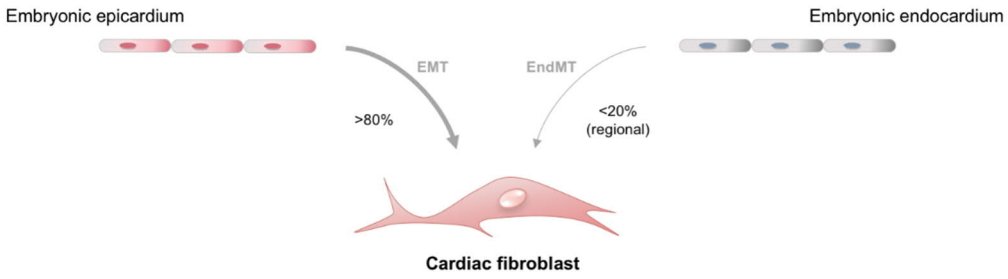

Figure 1. Developmental origin of fibroblasts in the heart.
The two documented sources of tissue resident cardiac fibroblasts in the developing embryo are the epithelial cells of the epicardium and the endothelial cells of the endocardium. The epicardial-derived fibroblasts emerge through a process termed epithelial-mesenchymal transition (EMT), initiated at embryonic day E13.5 in the mouse, originating the majority of the ventricular and atrial CF. Tissue-resident fibroblasts in the ventricular septum and valves (~10-20%) are endothelial-derived potentially through endothelial-mesenchymal transition (EndMT). (Original illustration, Gabriela L. Santos)

Moreover, resident fibroblasts have also been shown to arise from endothelial cells of the embryonic endocardium (**Figure 1**) through a process called endothelial-mesenchymal transition (EndMT) [129-132]. This occurs under the influence of

signalling molecules such as TGF-β and Wnt [133]. Yet, during embryonic development EndMT is responsible for the origin of a minority portion of the resident interstitial fibroblasts (~10-20% of total CF), occurring in particular regions like the ventricular septum and atrioventricular canal (cardiac valves) [129-132, 134].

Functions of the cardiac fibroblasts

Morphologically, fibroblasts are flat, elongated spindle shaped cells presenting dendritic-like processes extending from the cell body [135, 136]. One of the defining features that distinguish CF from other cell types of the heart is that they lack a basement membrane[137]. CF are geometrically interspersed between cardiomyocytes and its structural organisation differs regionally within the myocardium [138].

Defining baseline functions of resident CF can be equivocal, because during the past years, studies have been happening more often in a disease context or relying on markers that were only partially specific to this presumed cell type [118]. Nonetheless, it has been systematically shown that CF have crucial structural and mechanical functions necessary for proper functioning of the myocardium. That concerns in particular their function as the main regulators of ECM homeostasis. In one hand, CF are considered the main contributors for synthesis and secretion of matrix molecules, predominantly the fibrillar alpha-1 type I and III collagens (COL1A1 and COL3A1) but also the less abundant fibronectin 1 (FN1), laminins, and elastin [139-142]. Along with the cardiomyocytes, CF also participate in the regulation of ECM turnover by producing matrix metalloproteinases (MMPs) and tissue inhibitors of metallo-proteinases (TIMPs) [143-145].

Not only CF underpin mechanical tensile compliance of the collagen network by regulating ECM homeostasis [146-148], but also through their bond with ECM fibrils

via integrins interconnecting and organizing cellular network and the matrix around it. Integrins are transmembrane receptors that mediate focal adhesions (FA) integrating contractile properties of the cytoskeleton and mechanical information from the surrounding collagen network (mechanotransduction) [97, 149, 150]. Through FA, CF can exert traction forces on the ECM promoting its compaction which subsequently distributes mechanical forces throughout the myocardium [151-154]. By regulating ECM homeostasis and its mechanical compliance, CF contribute to form an organizational ECM network that interconnects and scaffolds myocyte and non-myocyte populations of cells contributing to the structural integrity of the heart [97]. This may also contribute to correct conductivity and rhythmicity throughout the myocardium [138, 155]. Although CF-cardiomyocyte coupling through connexin gap junctions *in vivo* remains a subject of debate [156], there is growing evidence indicating that CF may also participate directly in mechano-electrical feedback contributing to cardiac electrophysiology [156-158]. In general, CF have the appropriate molecular programme to respond to a wide range of different stimuli, including hypoxia, as well as changes in biochemical and mechanical signals [137, 139, 159]. Combined with their strategic positioning interspacing cardiomyocytes, CF are endowed with rapid responsiveness after injury [118].

1.3.2. Origins, functions and identification of activated cardiac fibroblasts and myofibroblasts

Tissue-resident fibroblasts as a source of activated cardiac fibroblasts and myofibroblasts

A traditional view has suggested in the past that activated fibroblasts and myo-fibroblasts in the fibrotic heart derive from resident fibroblasts. However, that has

initially not been directly and systematically investigated, while secondary cell sources have otherwise been investigated in more detail (**Figure 2**). The proportions of activated fibroblasts and myofibroblasts contributed by secondary sources, like endothelial cells [131, 132, 160, 161], pericytes [162, 163], blood born cells [164-166], have however varied considerably according to the cell source and the experimental model. This led to considerable controversies about the importance of these cells as origins of activated CF and myofibroblasts [159].

More recent studies using in-depth lineage tracing in mice, have finally confirmed that the majority of activated fibroblasts and myofibroblasts in the injured adult heart derive from the proliferation and activation of resident fibroblasts with embryonic epicardial and endocardial origin (**Figure 2**) [131, 132, 167, 168]. One of the strongest arguments for resident CF serving as origin of activated fibroblasts and myofibroblasts was delivered by a recent study published by Kanisicak and colleagues [167]. The authors used a *Postn* gene-targeted strategy combined with *Tcf21* lineage-tracing, designed to identify resident CF [112, 115], to show that, after MI injury, the *Tcf21*-positive fibroblast population increases 10-fold in the region with ongoing fibrosis. Moreover, this approach showed that the majority of myofibroblasts (around 70%) expressing *Postn* found after MI injury *in vivo* originated from *Tcf21*-positive resident fibroblasts. Importantly, similar results were described in experimental pressure overload. The same study showed that *Postn* is uniquely expressed by myofibroblasts in adult stressed cardiac ventricles and that *Postn*-traced myofibroblasts could also revert back to a less-activated state upon injury resolution [167]. Although, this study, together with other less specific studies, has proven that resident CF are of quantitative importance as source of activated fibroblasts and myofibroblasts, the role of secondary cell sources (**Figure 2**) as qualitative modulators should not be ruled out [131, 132, 167].

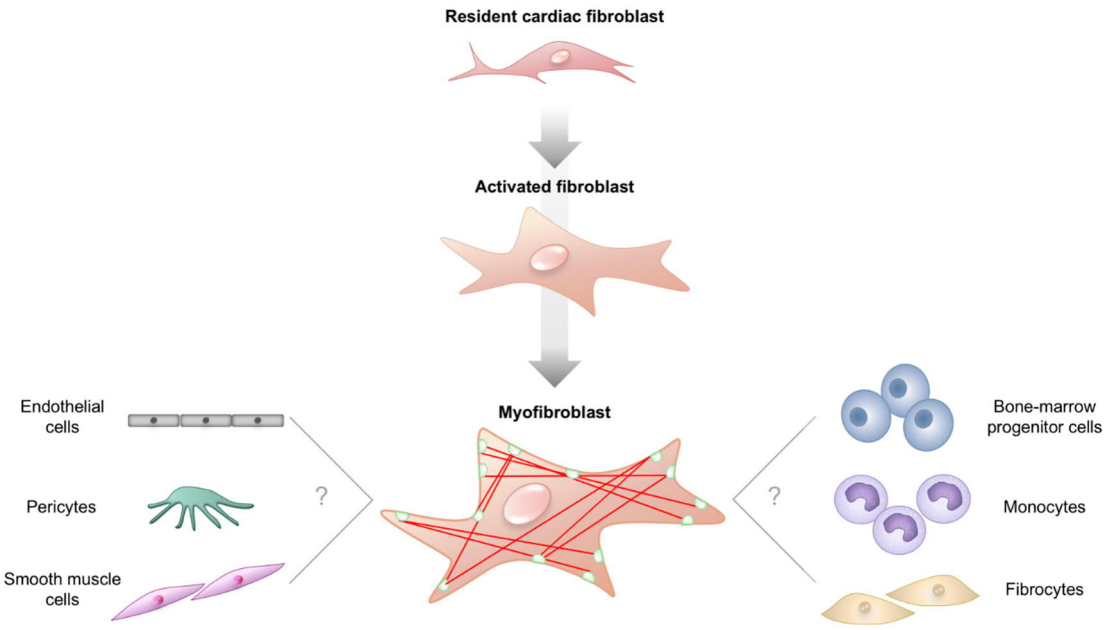

Figure 2. Origins of activated fibroblasts and myofibroblasts in the heart.
During hypertension and cardiomyopathies, the primary origin of newly generated activated fibroblasts and myofibroblasts are tissue-resident cardiac fibroblasts of developmental origin [131, 132, 167, 168]. There are also a number of non-fibroblast cellular sources such as endothelial cells, bone marrow-derived progenitor cells, monocytes, circulating fibrocytes, perivascular cells (pericytes), and smooth muscle cells discussed as potential origin [131, 132, 160-166, 168-170]. Those are designated with question marks as further work is needed to better understand their recruitment and differentiation into myofibroblasts. (Original illustration, Gabriela L. Santos)

Functions of the activated cardiac fibroblasts and myofibroblasts

Morphologically, activated fibroblasts and/or myofibroblasts transition from dendritic to a more stellate/bipolar shape, exhibiting prominent thickened and simplified extensions, consistent with the tension-dependent adhesion strengthening observed when cultured in matrices of higher density [135]. These cells also display a prominent Golgi apparatus and extensive rough endoplasmic reticulum, reflecting their high secretory activity [159, 171].

The activation of CF and transdifferentiation into myofibroblasts is a time-dependent, two phase process and occurs gradually. Each intermediate phenotype expresses different sets of characteristic genes and shows different cellular behaviour [172, 173]. During the first hours after injury, also called the inflammatory phase, activated

fibroblasts (also named proto-myofibroblasts) appear [172-174], and can last in the tissue for few days [172]. These cells show a higher cell cycle activity and are capable of rapid adhesion and migration to the injured area [172, 175-177]. Activated fibroblasts secrete biochemical mediators with autocrine and paracrine effects, thereby directing amongst others cell proliferation, migration, hypertrophy, and apoptosis of other cardiac cells and themselves [137, 139, 159] (**Figure 3**). Mouton and colleagues described that at earlier time points after MI, activated fibroblasts display a pro-inflammatory, leukocyte-recruiting, pro-survival, proliferative, pro-fibrotic, and pro-angiogenic profile [174] (**Figure 3**). For example, they secrete fibroblast growth factor (FGF) and vascular endothelial growth factor (VEGF) which are potent inducers of angiogenesis [137, 139, 159, 174].

The second phase of transdifferentiation emerges with a delay. It can start from 30 hours to 3 days later with the high levels of cytokines and mechanical stress that have accumulated within the wounded area [172, 173, 176, 177]. Activated fibroblasts become mature with the expression of alpha smooth muscle actin (SMA) – the so-called myofibroblasts emerge. These cells pursue with the auto- and paracrine signalling after the first inflammatory phase. They regulate the expression of cytokines and growth factors, such as tumour necrosis factor alpha (TNF-α), interleukin (IL)-6, TGF-β, as well as molecules with antiangiogenic effects, such as connective tissue growth factor (CTGF, coded by *CCN2*) and platelet-derived growth factor (PDGF) [137, 139, 159]. Thus, activated fibroblasts and myofibroblasts undertake regulatory functions of inflammation and propagation of pro-fibrotic and transforming signals (**Figure 3**).

The secretory function of activated CF and myofibroblasts is certainly not restricted to auto- and paracrine molecules, but also include building blocks of the ECM. Initially, activated fibroblasts secrete FN1 and collagens, predominantly COL1A1 and COL3A1,

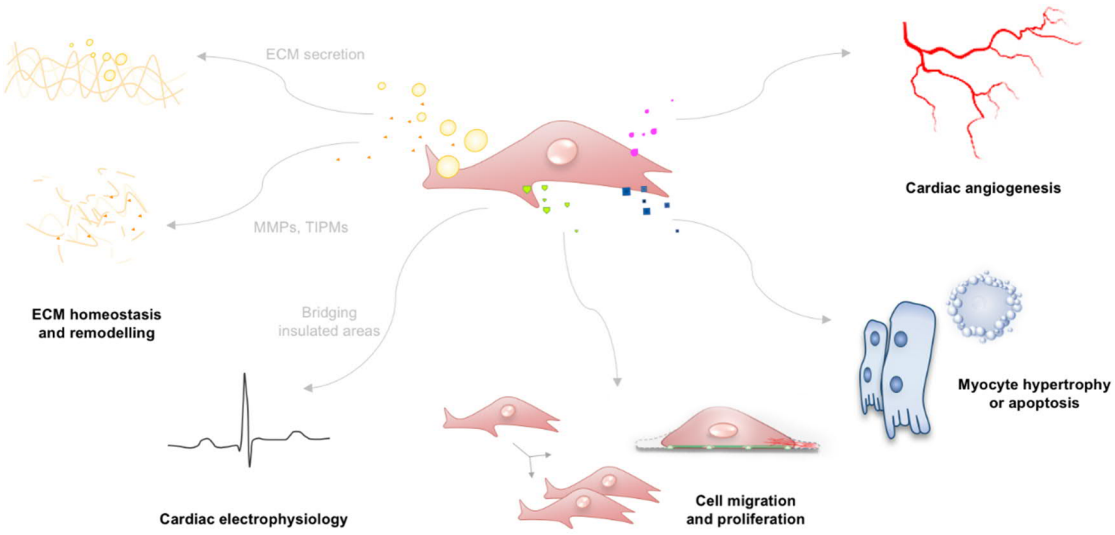

Figure 3. Functional consequences of fibroblast activation and transformation to the myofibroblast phenotype.
Cardiac fibroblasts are the main regulators of extracellular matrix (ECM) homeostasis, sustaining its assembly through the secretion of ECM component including collagens, elastin and fibronectin, and regulating its degradation through matrix metalloproteinases (MMPs) and tissue inhibitors of matrix metalloproteinases (TIMPs). In disease, activated fibroblasts and myofibroblasts present enhanced secretion of those components, collagens in particular, contributing to the ECM remodelling. It is suggested that in the fibrotic heart, myofibroblasts may bridge insulated myocyte bundles, sustaining a continuous electrical propagation. Cardiac activated fibroblasts and myofibroblasts can produce in addition a number of active mediators (e.g., TGF-β, PDGF, TNF-α, IL-1β, IL-6, FGF, VEGF, CTGF) which influence cardiac cells transformation, migration, proliferation, hypertrophy, apoptosis and angiogenesis. (Original illustration, Gabriela L. Santos)

which is further enhanced in myofibroblasts [131, 132, 167, 173, 178]. This is in line with the key function of myofibroblasts in the context of maintaining tissue integrity after a MI or other insults [75-77, 84, 85, 88] (**Figure 3**). Besides, myofibroblasts are endowed with a prominent contractile apparatus. The initially activated fibroblasts-formed actin stress fibres integrate SMA. The formation of a prominent SMA-stress fibre network is noticed after 3 to 4 days after the fibrotic process is initiated and consecutively contributes to develop the strong contractile myofibroblast phenotype [172, 173]. Along with their ability to remodel the ECM, myofibroblasts provide an endorsement of the mechanical strength of the scar tissue by increasing the number of FA with the newly deposited collagen network. Thus, given the ongoing stress and

strain environment of the scar, they help to maintain scar tension and stability over time [145, 151-154, 179] (**Figure 3**). In association with increasing mechanical tension/stiffness, myofibroblasts function as mechanic transducers, regulating several signalling pathways involved in the fibrotic process progression [136].

Markers of the differentiated phenotypes

Experimental research has recognised the importance of having specific biomarkers to differentiate between CF, activated fibroblasts and myofibroblasts, in particular when understanding disease progression and developing targeted therapeutic strategies. The challenge of identifying specific markers is partly related to the continuous phenotype flux, which allows more than one phenotype to be present at the same time [172, 173]. One of the first suggested markers for myofibroblasts was SMA, as quiescent fibroblasts and activated fibroblasts do not express this actin isoform [136, 172, 175, 180]. However, SMA expression can be found in many different cells in the heart, e.g., in smooth muscle cells [181, 182]. It is therefore not suitable as a stand-alone marker. Interestingly, SMA expression in myofibroblasts seems to be a transient event, as Fu and colleagues have demonstrated that in the infarct region of scar tissue, myofibroblasts from *Tcf21*-lineage progress loose the expression of SMA after around day 10 after injury, which prompted the authors to classify these newly appearing cells into a third category, titled as the matrifibrocytes [173]. This phenotype occurs at last in response to progressive cardiac remodelling (chronic cardiac fibrosis) and scar maturation (or hypertrophic scarring) due to ongoing neuroendocrine dysregulation or aberrantly high wall stress [173]. According to this study, matrifibrocytes can be characterised by the expression of ossification markers which are usually associated to chondroblasts and osteoclasts, including cartilage oligomeric matrix protein (*Comp*,

alias thrombospondin 5), chondroadherin (*Chad*) and cartilage intermediate layer protein 2 (*Cilp2*).

Other early markers for activated fibroblasts/myofibroblasts included ECM components, like COL1A1, COL3A1 and FN1 [167, 172, 176-178, 183-186]. However, as for SMA, there are several non-fibroblast cells in the heart expressing these ECM proteins [132, 179, 187]. Also a combination of SMA and COL1A1 was found to be not appropriate for cell identification, as it was shown that not all COL1A1-expressing cells are positive for SMA in the fibrotic heart [172, 180]. Furthermore, the number of SMA^+ and $COL1A1^+$ cells may differ between fibrotic processes with different origin and between time-points along the process [132, 179, 187]. The aetiology of cardiac fibrosis may also play a role when considering collagens as markers. In cardiac fibrosis an altered ratio between COL1A1 and COL3A1 is observed, which seems to be dependent on the condition. In MI models, it has been found that the ratio between COL1A1 and COL3A1 is increased, whereas COL3A1 expression was significantly increased in patients suffering from dilated and ischemic cardiomyopathy, resulting in a decrease of the COL1A1 to COL3A1 ratio [188-192].

In addition to the enhanced expression of collagens in fibrosis progression, the cross-linking of the collagen fibres is also enhanced. As collagen cross-linking is promoted by lysyl oxidase (LOX) and its isoforms, these genes have be also considered as potential myofibroblast markers [193]. In line, single cell analyses of fibroblasts revealed that LOX was highly up-regulated after injury in SMA-positive myofibroblasts [88, 167, 178]. However, LOX transcription takes as well place in other cells, like the numerous more abundant endothelial cells [194-197]. The same holds true for CTGF, which was widely associated with fibroblast-to-myofibroblast trans-differentiation [198, 199], but it is e.g. likewise strongly induced in injured cardio-

myocytes [200]. Other suggested markers, which clearly lack cell type specificity are vimentin (VIM), fibroblast specific protein 1 (FSP1, alias S100A4), the cell surface antigen THY1 (alias CD90), and discoidin domain-containing receptor 2 (DDR2) [118, 142, 201-203].

Recent lineage tracing studies with cardiac fibroblast populations have successfully used some specific markers to better stratify different cell populations. The genes *Tcf21*, *Wt1*, *Tbx18* and *Pdgfrα* are specific markers of early embryonic fibroblasts of epicardial origin. However, only TCF21 and PDGFRα are expressed by resident fibroblasts of the adult heart [115, 119, 167, 204]. One interesting example for specificity is POSTN, because it is not exclusive to proliferative and secretory embryonic fibroblasts during development [116, 126, 205], but as well expressed in myofibroblasts after injury in the ventricles of adult heart [167]. This expression in myofibroblasts is rather specific, as POSTN can otherwise only be found in some structural unrelated areas of the heart, such as the cardiac valves [206]. Therefore POSTN together with TCF21 is nowadays the best available approach to differentiate between myofibroblasts and resident fibroblast [167].

1.3.3. Signalling pathways involved in cardiac fibroblasts activation and regulation of myofibroblasts activity during fibrosis

Understanding the molecular events underlying fibrosis is essential to identify new therapeutic anti-fibrotic strategies to assist the treatment of HF. In response to cardiac injury, CF activation and myofibroblasts gradual transdifferentiation is initiated by the integration of released neurohumoral signals, cytokines, growth factors and mechanical signals of the extracellular environment. The signalling pathways involved contribute

simultaneously to a continuous input eliciting and maintaining the 'supraphysiological' activity of activated fibroblasts and myofibroblasts [172, 207-209].

TGF-β signalling

Whereas many fibrogenic cytokines and growth factors were found to be involved in this process, TGF-β appears to be one of the primary and most potent factors in the transdifferentiation of CF into myofibroblasts, inducing SMA expression, cell proliferation, migration, and ECM production [183, 184, 186, 210-214]. In the early stages of infarct healing, platelets may be the main source of TGF-β in the ECM, whereas macrophages and fibroblasts may be responsible for the sustained upregulation of TGF-β during the proliferative phase of healing [104, 215]. While it seems to play a protective role during the initial phase, the subsequent sustained high secretion of TGF-β enhances the deposition of ECM, contributing to cardiac muscle stiffening and impaired contractile performance [214, 216, 217]. Myofibroblast genes associated with ECM, such as alpha-1 type I and VI collagens (COL1A1 and COL6A1), MMPs, and TIMPs, were shown to be SMAD2/3-dependent upregulated through the canonical TGF-β-induced signalling [218]. Besides, SMAD3 is directly associated with TGF-β-induced expression of SMA and stress fibre formation. Its disruption showed to impair myofibroblast transdifferentiation and fibrotic remodelling after MI injury [219]. One of the non-canonical TGF-β pathway is through p38 mitogen-activated protein kinase and it has been shown to regulate myofibroblast transdifferentiation through TGF-β-induced markers like COL1A1, FN1 and SMA [208].

In addition, when acute cardiac remodelling is activated, myofibroblasts also produce TGF-β which acts as a self-pro-survival stimulus [104, 208]. It has been suggested that some of the pro-fibrotic effects of circulating TGF-β may also involve the upregulation

of CTGF and PDGFRα [210, 220], the renin-angiotensin system [214], and the activation of Rho-MRTF (myocardin-related transcription factor A) as a non-canonical signalling pathway [221, 222]. Moreover, it was shown that myofibroblasts are not only responsible for TGF-β expression, but also for the activation of this cytokine, as the contraction of these cells mechanically activates latent TGF-β residing within the ECM after being synthesized and secreted [104, 223].

Renin-angiotensin system and angiotensin II signalling

Angiotensin II (Ang II) is the effector molecule of the renin-angiotensin system (RAS) and is induced during disease in response to hemodynamic overload. When the heart is injured, macrophages can express angiotensinogen, renin and angiotensin-converting enzyme (ACE), which in turn generate Ang II [224]. Besides, mechanical stretch induces cardiomyocytes to release Ang II. This peptide hormone induces cellular responses in cardiomyocytes but dominantly acts as paracrine factor on CF [225, 226] influencing myofibroblast transdifferentiation and their activity [227, 228]. In the cardiovascular system, the effect of Ang II on the fibrotic response is thought to occur, in part, by serving as an upstream inducer of TGF-β signalling [208, 229]. In this regard, studies on CF have widely demonstrated that Ang II induces TGF-β canonical and non-canonical signalling pathways [208, 229] and can in induce secretion of collagen by interacting with the Ang II receptor-type 1 (AT1R) [230, 231]. Only one study has clearly demonstrated that Ang II-treated CF could develop SMA stress fiber and contractile function independent of TGF-β [208, 232]. That same study further suggested that Ang II signalling directly induced myofibroblast transdifferentiation through activation of MAPK/SRF (mitogen-activated protein kinase 1/ serum response factor) signalling [208, 232].

Mechanoactivation of cardiac fibroblasts involving RhoA/ROCK

CF and myofibroblasts are intrinsically mechanosensitive cells, perceiving and adapting to changes in the mechanical environment [233-242]. Stiffness has been shown numerous times to promote myofibroblast transdifferentiation. Such observation occurred during increasing tension in wounds as well as in *in vitro* studies using two-dimensional (2D) substrates or three-dimensional (3D) matrixes with high tensile strengths [104, 184, 223, 236-239, 243-248]. The mechanisms whereby cells adjust to strain stress involve mechano-transduction pathways.

Transforming protein RhoA, a member belonging to the family of small Rho GTPases, is one of the most extensively studied effectors downstream of integrins and cell adhesion by which mechanical signals can be transduced into a molecular signal [150]. Besides mechanical tension, RhoA signalling pathway (**Figure 4**) can be activated by many extracellular ligands including TGF-β or others which bind to G-protein coupled receptors (GPCR) [136, 229, 249].

Downstream RhoA, the effectors Rho-associated coiled-coil containing protein kinases (ROCK) and mDia (protein diaphanous homolog) are activated, interfering with actin dynamics and cytoskeletal reorganization [249, 250] (**Figure 4**). While mDia promotes actin filament polymerization (F-actin fibres), ROCK are critical regulators of actin-myosin contraction. ROCK (ROCK1 and ROCK2 isoforms) are serine/threonine kinases belonging to the family of AGC-kinases, which phosphorylate amongst others the regulatory myosin light chain (MLC) and LIM kinases (LIMK). LIMK phosphorylation by ROCK leads to phosphorylation of cofilin and therefore actin--depolymerisation is inhibited [251, 252]. In turn, the ROCK-dependent MLC phosphorylation enhances the induction of actomyosin bundles and increases the fibres' contractility [251, 253-255]. This mechanism is further supported by the inhibitory

phosphorylation of the myosin phosphatase-targeting subunit 1 (MYPT1), a regulatory subunit of the MLC phosphatase [256-258]. Recent data suggested that ROCK activation might in addition occur as a direct consequence of the mechanical situation and independent of RhoA. Truebestein and colleagues described ROCK as a molecular ruler which activity is regulated by the length of its coiled-coil and the spatial positioning of both kinase and substrate, possibly controlled by the cytoskeletal tension [259]. If this mechanism plays a role in myofibroblasts or if the canonical RhoA-induced ROCK activation is of more importance, is, however, completely unclear. Independent of how ROCK is activated, it seems likely that the mechanical condition and ROCK are closely interlinked and influence each other. It can be proposed that after injury ROCK may participate in the process by which transdifferentiated myofibroblasts remodel their actin cytoskeleton and form contractile SMA-containing stress fibers, enabling them to exert traction forces on the remodelled ECM through FA [151-154, 260], potentially promoting its compaction. In turn, cytoskeleton tension and increased environmental stiffness, due to cross-linking of the newly secreted ECM and increased compaction [88, 167, 178, 261, 262], may regulate ROCK activity and consequently activate and sustain mechanosignalling pathways.

That the dynamics of the actomyosin cytoskeleton play a highly critical role in processes involved in transdifferentiation of resident fibroblasts into active myofibroblasts, such as cell migration, adhesion and contraction is without doubt [249, 250], but it is also involved in the mechanical regulation of gene transcription. One of the important pathways in the regulation of gene transcription involves the co-transcriptional factor MRTF. By formation of F-actin fibres, the pool of G-actin monomers decreases, which releases MRTF out of the G-actin binding, and enhances its nuclear translocation [249, 250]. In the nucleus, MRTF binds SRF and thereby

augments its transcriptional efficacy [263]. As the promoter regions of critical genes such as *ACTA2* (coding gene for SMA), *CCN2* (coding gene for CTGF), and alpha-2 type I collagen (*COL1A2*) are highly enriched for SRF binding sites, the RhoA/ROCK/MRTF/SRF pathway contributes to the myofibroblast phenotype and functionality, and may sustain transdifferentiation of adjacent cells by integrating the cytoskeleton responsiveness to extra- and intracellular stiffness [208, 264, 265].

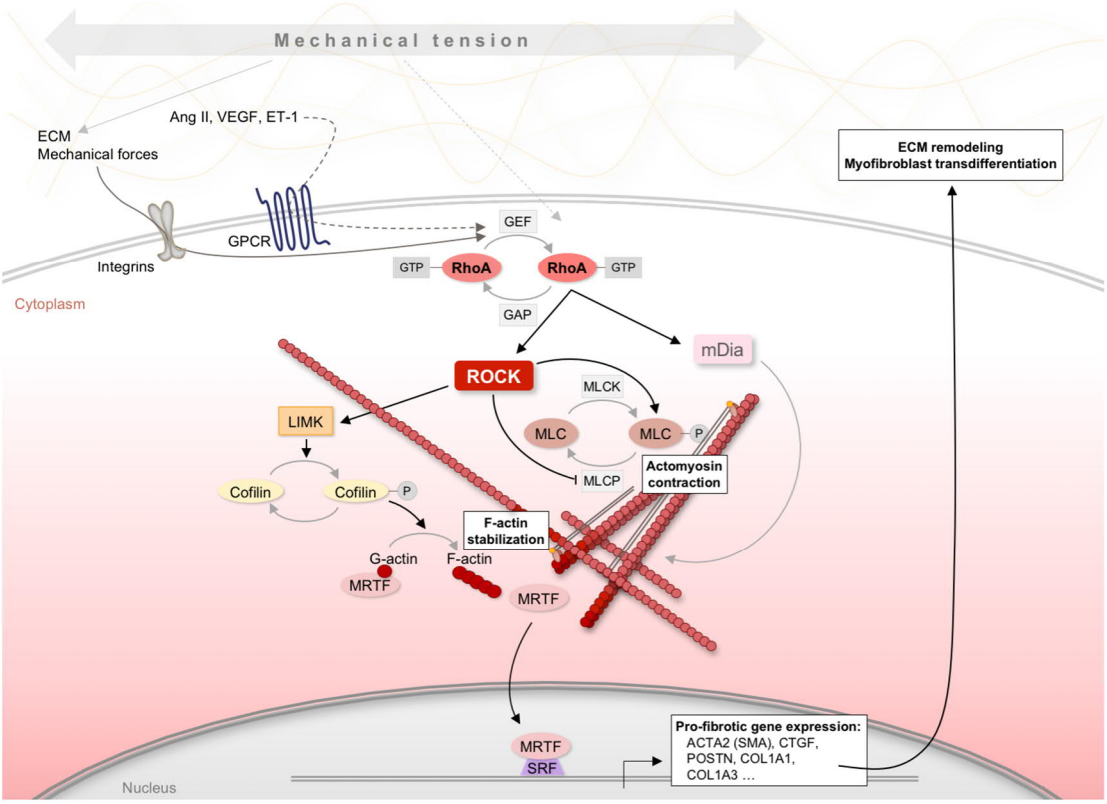

Figure 4. Mechanotransduction involving RhoA/ROCK signalling pathways associated to myofibroblast transdifferentiation and function.
Mechanical tension activates myofibroblast transdifferentiation through RhoA-MRTF/SRF pathway responsive to signals from the cytoskeleton and ECM. The RhoA-MRTF/SRF signaling pathaway regulates myosin cytoskeleton and SMA fibers dynamics. These control MRTF translocation to the nucleus where acts as cofactor for SRF, synergistically regulating transcription of pro-fibrotic genes. RhoA-MRTF/SRF can also be activated through signals such as AngII or ET-1 binding to its membrane localized G-protein-coupled receptor (GPCR), which possibly induces pro-fibrotic gene transcription (dashed line). This mechanical tension- and actin-controlled pathway amplify and sustain myofibroblast transdifferentiation and function. (Original illustration, Gabriela L. Santos)

It is likely that the mechano- and growth factor signalling pathways can work in conjunction with each other. There is data demonstrating that mechanosignalling is

sufficient to drive fibrotic processes [236, 266-268], but there are also cases in which the response of CF to mechanical stimulation in tissue culture is dependent on growth factors stimulation such as TGF-β [104, 223, 268]. Also the effect of pharmacologic inhibition of ROCK on transcriptional decrease of ECM genes and *ACTA2* (SMA) preventing tension-induced myofibroblast transdifferentiation, has been shown to be either dependent [208, 221, 269] or not [236, 266, 268] on TGF-β. An example where these mutually reinforcing and complimentary mechanisms may cooperate is in the border zone of an infarcted area. With TGF-β expression being highly regulated in the infarct border zone one week after MI [215] and with the mechanic alterations ensued by the scar formation, is very likely that the initial mechanism of fibroblasts activation in the border zone is dependent on both the mechanical environment and TGF-β signalling [92, 219, 270-274].

The role of ROCK in cardiac remodelling

Both isoforms, ROCK1 and ROCK2, have been suggested to play a role in cardiac disease and in remodelling of the myocardium. In particular, *in vivo* studies using ROCK1 and ROCK2-deficient mice suggested that cardiomyocyte apoptosis and cardiac fibrosis are regulated by ROCK [257, 275-280]. In part, the pro-fibrotic effects could be associated with the direct influence of ROCK on the fibroblast-to-myofibroblasts transdifferentiation. Studies *in vitro* showed that ROCK are not only implicated in cardiac fibroblast migration and proliferation [281-285], but also in the regulation of fibrosis-associated genes, including *CCN2* (CTGF), basic fibroblast growth factor 2 (*FGF2*), *ACTA2* (SMA) and *COL1A1* [277, 285-289]. In humans, genetic studies showed that ROCK2 polymorphisms are associated with changes in blood pressure providing evidence that Rho/ROCK pathway is important in

hypertension [290, 291]. Furthermore, it has been shown in patients that ROCK activity is increased during several CVD (see *section 1.4.1.*) [292-298].

1.4. Therapy of fibrosis – state of the art

Fibrotic remodelling is a major contributor to HF progression as it causes contractile dysfunction and arrhythmia in heart disease of various aetiologies [44, 61-64]. In the treatment of HF, fibrosis can potentially be targeted indirectly or directly by drug therapies to ameliorate cardiac function [299, 300]. Despite the mechanistic understanding of heart diseases generated over the years, the therapeutics can only slow down fibrosis [301]. According to the European Society of Cardiology (ESC) guidelines for the diagnosis and treatment of acute and chronic HF [302], neuro-hormonal antagonists are the currently used drugs to treat patients with HFrEF or after a MI. The recommended pharmacological treatments [302] for all patients with symptomatic HFrEF Class II-IV (graded according to the New York Heart Association – NYHA – functional classification), or after MI, are angiotensin-converting enzyme inhibitors (ACEI) for blockade of the renin-Ang II-aldosterone system (RAAS) and β-adrenergic receptor blockers (β-blockers). This treatment aims to ameliorate the symptoms of HF, improve functional capacity and reduce mortality, and is also recommended for patients with asymptomatic left ventricular (LV) systolic dysfunction [302]. Treatment with ACEI (e.g. Captopril, Lisinopril) and β-blockers (e.g. Bisoprolol, Carvedilol) are recommended to be coupled with diuretics, if it is necessary to reduce symptoms of circulatory congestion and peripheral edema [302]. ACEI have been shown to help recovering LV systolic function and reduce fibrosis [303, 304]. In patients with coronary artery disease, who do not present LV systolic dysfunction,

ACEI prevent or delay the onset of HF [302, 305]. In case ACEI are not well tolerated, patients can be alternatively treated with AT1R blockers, such as Candesartan and Valsartan. AT1R blockers suppress the RAAS via selective inhibition through AT1R and are indicated to reduce vasoconstriction, sodium and water retention, myocardial hypertrophy and fibrosis [302, 306-308]. When HFrEF patients are resilient to treatment with an ACEI and a β-blocker, they can subsequently be treated with mineralocorticoid/aldosterone receptor antagonists (MRA), such as Spironolactone and Eplerenone. The MRA block receptors of aldosterone and other steroid hormone receptors (e.g. corticosteroids, androgens) [302]. LCZ696 (Sacubitril/Valsartan), a new dual-acting compound in the class of angiotensin receptor neprilysin inhibitors (ARNI) [309], showed to be more effective than the ACEI Enalapril alone [310, 311], but it is being only used in patients intolerant to ACEI and MRA [302].

Besides ACEI and AT1R blockers which are considered to slow down fibrosis, no therapeutic strategy is yet available that is specifically designed to target CF and is able to fully halt or reverse the effects of pathological cardiac remodelling [299, 300].

1.4.1. Emerging anti-fibrotic strategies and pharmacological targets

Despite the critical impact of cardiac fibrosis in the progress of HF, only very few new therapeutic approaches are currently in clinical trials. One promising drug is Pirfenidone (PFD), which is already approved for the treatment of idiopathic pulmonary fibrosis (IPF) [312]. PFD has been reported to attenuate fibrotic and inflammatory processes in IFP patients, decreasing fibroblast proliferation and the expression of various fibrosis-associated mediators and ECM components, including TGF-β, tumor necrosis factor alpha (TNF-α), platelet-derived growth factor (PDGF) and collagens

[313, 314]. Preclinical studies suggest that PFD exerts its anti-fibrotic effect by interfering with the TGF-β signalling pathways [315]. PFD has also shown potential therapeutic utility in preclinical models of pressure overload, hypertension and MI [316-318], reducing ventricular hypertrophy without lowering systolic blood pressure [318], mitigating total and non-scar myocardial fibrosis with improved LV function and also preventing arrhythmias [319]. Just recently there were two phase II clinical trials being performed, wherefore the results have not yet been published. The studies aimed to examine the effectiveness of PFD in improving heart function and reducing of myocardial fibrosis in patients with hypertrophic cardiomyopathy associated with LV diastolic dysfunction (NCT00011076) and in patients with chronic HFpEF and cardiac fibrosis (NCT02932566) [320].

Additionally, mechanosignaling has been considered as an interesting target for anti-fibrotic therapy [321]. The involvement of ROCK in many cellular processes and its up-regulated activity in various CVD pathologies shows its potential clinical importance, and thus representing good targets for inhibition [295, 322, 323]. For example, ROCK activity was noticed to be increased in patients with CVDs, including hypertension [292], pulmonary hypertension [293, 294], MI [295], and acute/chronic and congestive HF [296-298]. Although the values seem to decrease over time after an acute injury [294, 297], the systemic ROCK activity measured through circulating leukocytes remains high in patients with chronic HF [296-298], and it is associated with pathologic left ventricle remodelling and systolic dysfunction [297, 298]. While no correlation could be found between enhanced ROCK activity and the established HF marker cardiac troponin I [297], increased ROCK activity was shown to correlate positively with brain natriuretic peptide (BNP) and high N-terminal pro-B-type natriuretic peptide (NT-proBNP) levels (used as a marker for HF diagnose and

stratification [302]) in patients with acute coronary syndrome [297, 324], particularly in those with MI [324].

So far, few medications in the drug class of ROCK inhibitors have been approved for human use, including Fasudil, Netarsudil, and Ripasudil [325]. Fasudil was firstly introduced in Japan in 1995 for prevention and treatment of cerebral vasospasm following subarachnoid haemorrhage [326], and is the only ROCK inhibitor so far approved that has been used in clinical trials in the context of CVD. In patients, ROCK inhibition by Fasudil has been showing to have beneficial effects treating acute and congestive HFrEF (ICM and DCM) [327], pulmonary hypertension (PH) associated with left ventricular HFpEF [328], PH with right heart failure (RHF) [329], PH associated to congenital heart disease [330], coronary artery disease (including MI) [331], PH [332-334], hypertension [292], coronary artery spasm [335], aortic stiffness [336], stable angina pectoris [337-340], vasospastic angina [341], and ischemic stroke [342]. In acute and congestive HFrEF patients, intra-arterial infusion of Fasudil increased forearm blood flow and reduced the increased forearm vascular resistance through a mechanism suggested to be Rho/ROCK dependent [327]. In reactive PH associated with HFpEF, besides decreasing pulmonary arterial systolic pressure, Fasudil ameliorated cardiac diastolic function as it was verified by an increase of early (E-wave, left ventricular relaxation) to late (A-wave, atrial contraction) diastolic transmitral flow velocity (E/A), according to Doppler echocardiography guidelines. Fasudil also lowered LV filling pressure as shown by a reduction of E to early diastolic mitral annular tissue velocity (E/e') [328]. In passive PH-HFpEF patients, those parameters were not altered by Fasudil. In both groups, Fasudil improved the levels of BNP and NT-proBNP [328]. A smaller study reported that Fasudil improved in-hospital mortality and 30-day re-hospitalization outcome for cardiovascular symptoms in PH-

RHF patients [329]. However, these studies did not systematically investigate molecular markers and potential mechanisms involved in the Rho/Rho-kinase pathway activation in the HF patients.

The underlying mechanisms of the beneficial effects of Fasudil observed in the clinical trials undertaken so far in the general CVDs context have been often attributed to the inhibition of ROCK in the vascular system resulting in the attenuation of muscular hypercontraction [322]. However, it is until now unclear if ROCK inhibition can also have a direct effect on cardiomyocyte contraction and cardiac fibroblast activation in CVD. Alternative discussed beneficial therapeutic effects of Fasudil in patients are the upregulation of endothelial nitric oxide synthase (eNOS) expression and activity, and reduction of inflammatory responses [322, 343]. The findings in patients are supported by several animal models. Pharmacological inhibition of the ROCK pathway by Fasudil [344] or other drugs [345-347] contributed to the stabilization of LV function, with reduced cardiomyocytes hypertrophy, interstitial fibrosis, and expression of fibrotic and inflammatory cytokines [344]. Nonetheless, the mechanisms of ROCK activation in patients with HF, its role in the progression of the disease, the direct effect of ROCK inhibition, and efficacy of ROCK inhibitors demand further investigation [298].

Despite promising benefits of the use of ROCK inhibitors, the effects of the drugs may also result from inhibition of other kinases given the possible non-selective effects. Drugs like Fasudil are ATP-competitive kinase inhibitors and the ATP-binding pocket is well conserved across kinases of the same family [348]. When used at higher concentrations, these inhibitors can also affect the activity of other kinases. For example, Fasudil can also inhibit protein kinases A and C (PKA and PKC) which share cellular processes with ROCK [349, 350]. In fact, some effects of Fasudil in pre-clinical models have been reproduced by structurally distinct inhibitors and there is the

possibility that the clinical effects of Fasudil result in part from the inhibition of other kinases in addition to ROCK [350]. Therefore, significant efforts to develop more potent and isoform-selective inhibitors for ROCK1 and ROCK2 have been made. One example is H1152P ([(S)-(+)-2-methyl-1-[(4-methyl-5-isoquinolinyl) sulfonyl]-hexahydro-1H-1,4-diazepine]), a derivative of Fasudil. It presents a higher potency and specificity for ROCK than Fasudil, with a K(i) value of 1.6 nM for ROCK, 0.63 µM for protein kinase A, and 9.27 µM for PKC. This compound have been tested in preclinical *in vitro* and *in vivo* studies [351].

1.5 Approaches for studying behaviour of fibroblasts and fibrotic processes

Fibroblasts react, like all cells, sensitive to their extracellular biomechanical environment, and in an interactive way, cellular shape, mechanical properties, and cellular functions adapt to imposed changes and feed back to the external environment. When fibroblasts are isolated from tissues and cultivated in non-compliant 2D substrata, they undergo major alterations, not at least due to high environmental stiffness [242, 352, 353]. The standard 2D culture system substrate stiffness range in the GPa magnitude, while the stiffness of a healthy human myocardium is estimated to be of 8-10 kPa and the stiffness of a diseased myocardium ranges between 25 to 100 kPa [354-357]. Thus, isolated CF transdifferentiate relatively fast into SMA-expressing myofibroblasts when cultured on stiff cell culture surfaces. Furthermore, the phenotype of myofibroblasts cultivated in 2D formats appears not to reflect the phenotype of their tissue-embedded counterparts [183, 184, 186, 213], showing that the stiffness of the substrate is correlated with the ‘degree’ of the myofibroblast phenotype [184, 239, 352, 358, 359] (**Figure 5**). Therefore, engineered tissue constructs may support a more

"physiological" 3D growth environment as found in the natural tissue, aiding the study of cellular processes, mechanics, structure and function under *in vitro* conditions [353].

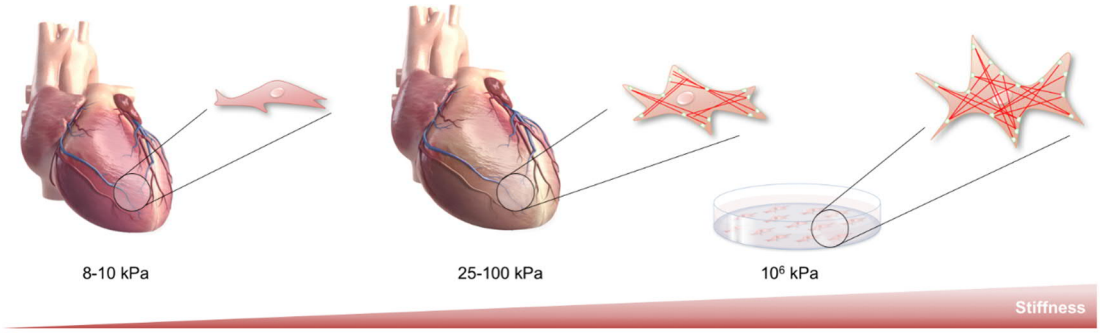

Figure 5. Artificial and non-compliant stiffness of 2D culture surfaces determine abnormal myofibroblast-like phenotype.
Mechanical environment is a key instructor of cardiac fibroblasts fate and function. Commonly used 2D cultivation methods have artificially high non-compliant stiffness [354-357] and neglect third dimensionality of a surrounding extracellular matrix. The exacerbated phenotype of myofibroblasts cultivated in 2D formats does not resemble the phenotype of their tissue-embedded counterparts, constituting a limitation for studying fibrotic processes. (Original illustration, Gabriela L. Santos with image of hearts edited from iStock.)

1.5.1. 3D culture in vitro models – new perspectives

At present, there are several 3D and quasi-3D *in vitro* systems available for cultivating cells within or on 3D matrices. These type of systems have been supporting the development of engineered tissue models, where chemical testing can be integrated with matrix components and mechanical properties manipulation to interfere with cell behaviour. That includes cell survival, migration, invasion, differentiation, mechanical properties, and mechanical sensing. The two last are particularly important in generating forces and signal transduction in response to their surrounding environment [360-362].

Quasi-3D systems consist of compliant lattices, either film-coated or gel-like surfaces, produced with synthetic polymers or ECM proteins with cells seeded atop. Studies using CF showed that increasing stiffness led to an increase in cell spreading area [358, 359] and an increased elastic modulus of the cell, as revealed by atomic force microscopy [352]. The elasticity change observed in the CF in response to external

stiffness was found to be regulated by actin filaments [352]. Moreover, isotonic cell contraction was observed by wrinkle formation on collagen lattices. Increased SMA expression in response to high lattice stiffness up-regulated fibroblast contractility [363], and increased traction forces were measured by traction force microscopy [247]. These events were linked to the activation of mechanoresponsive signalling pathways, including YAP/TAZ (Yes-associated protein and its transcriptional coactivator PDZ-binding motif) [247] and RhoA/ROCK [236], associated with the transdifferentiation into myofibroblasts. Hinz summarized a series of observations from studies using this sort of systems regarding phenotypic characteristics of cells based on substrate stiffness. At 1 kPa, fibroblasts do not present stress fibres; activated fibroblasts present actin stress fibres at 3-5 kPa; TGF-β receptors are activated at 5-9 kPa; and myo-fibroblasts present SMA-containing stress fibres from 16-20 kPa [364]. In particular, compliant matrices mimicking healthy tissue stiffness (~7 kPa) were clearly shown to preserve native phenotypes of porcine valvular fibroblasts or partially revert the myofibroblast phenotype observed in stiffer matrices (~32 kPa), based on proliferation rates and expression of markers such as SMA, CTGF and COL1A1 [237, 238]. Cyclic stretching experiments in compliant lattices with cells seeded atop showed that fibroblasts responded not only to stiffness but also to continuous mechanical stretch and collagen fibrils alignment. Expression and secretion of COL1A1 increased in response to stretch [234, 239] independently of collagen fibrils alignment [239]. An increased cell spreading area was also observed. On the other hand, cell proliferation was decreased on lattices with randomly organised collagen [239]. Other study further demonstrated that on stiffer matrices, cells and their actin-stress fibres oriented perpendicular to the direction of cyclic stretch, while on softer matrices actin-stress fibres oriented parallel to stretch direction. This orientation was independent of

collagen fibrils alignment but dependent of MLC activation [241]. However, it is necessary to consider that stiffness thresholds may be different between quasi-3D and 3D tissues, as the cell behaviour is expectably different in 3D environments in which cells are fully embedded in the matrix. By using quasi-3D and cell aggregation systems, Yu and colleagues clearly showed with genomic transcription analysis that CF phenotypic profile was highly changed not only by the stiffness of lattices but also according to topological arrangement of the cells [240].

Engineered tissue constructs, composed of cells fully embedded in a 3D matrix, have therefore brought advantages over previous models. Not only allowing for adjustable matrix stiffness and a 3D tissue-like environment, they also allow for measuring of their mechanical properties dependent on the geometry. Without disregarding heterogeneous cardiac tissues consisting of matrix components, cardiomyocytes and non-cardiomyocytes [365-367], homogeneous CF tissues have the advantage to allow addressing specifically cardiac fibrosis mechanisms. Some of the 3D models comprising only CF include floating discs and microspheres, sheet-like tissues, and ring-shaped models. [230, 235, 240, 281, 286, 368-379].

Attached and free floating discs or microspheres constitute a simple way to address the function of fibroblasts and myofibroblasts in wound contraction. In line with the studies referred above [236, 247, 363], as the collagen matrix is remodelled and the fibroblasts exert traction forces on the collagen fibrils, the matrix compacts reducing microsphere's diameter and volume, as it was shown by Barocas and Tranquillo and colleagues [380, 381]. Their mathematical model allowed to estimate the contractile force of the cells based on the variation of the tissue diameter over time [380, 381]. Similar results were obtained with CF. Several groups have demonstrated that CF cause tissue compaction/isotonic contraction in a time-dependent manner and that the effect

is enhanced by serum, Ang II and TGF-β [230, 235, 368, 369, 371, 382]. Cell-dependant collagen matrix compaction was shown to be mediated by integrins [369, 371]. Moreover, by using floating disks it was reinforced the potential involvement of ROCK signalling in gel contractility. Treatment with ROCK inhibitors hindered gel compaction as well as SMA expression, even in the presence of pro-fibrotic molecules including TGF-β [383], which is line with the studies in quasi-3D systems [236, 247, 363].

Sheet-like engineered tissues, clamped to anchorage points and/or force transducers, allow uni-, bi- or multi-axial stretch testing by inducing strain variation. Thus, this kind of 3D models opened the possibility to study homeostatic regulation of viscoelastic properties of tissues, namely through cyclic strain tests. These tensile measurements have demonstrated that tissue stiffness increases with the number of cells [384]. Besides, researchers were able to provide evidence of a direct dependency on the cytoskeleton integrity. Tissue stiffness was decreased by Cytochalasin B [384] and increased tissue stiffness correlated with increased phosphorylation of the regulatory light chain of myosin II [385]. A study with neonatal and adult rat CF showed by applying isotonic biaxial load that matrix compaction decreased with increasing external load [372], however cell and matrix contribution were not discriminated. In the same study, it was demonstrated that biaxial loading in a sheet-like tissue provoked an irregular distribution of strain variation between the attached borders and the free central region of the construct [372]. The non-uniformity of tissue deformation specially in the end areas where the tissue is clamped to anchorage points or force transducers, has inherent implications for the interpretation of the results [353]. One way to overcome this limitation is the use of tissues with a dog-bone configuration or with a ring-shape.

Ring-shape engineered tissues are commonly used constructs prepared by mixing cells with a collagen-hydrogel and pouring around a ring-shaped mould with a central fixed rod, where it is let to gel and further cultivated [353]. An alternative is to transfer the ring-shaped tissue to spacers consisted of two fixed and non-bendable steel rods separated by a distance to maintain the internal open space of the rings [379]. Both options have not yet been directly compared. Nonetheless, for the parameters analysed, both seem to present similar trends on tissue behaviour. For applying constant or cyclic tensile stretch measurements, in this model the ends do not need to be statically clamped. Instead, the tissues are held in bars (anchorage points and/or force transducers). Although it still comprises compression areas around the loading bars, it allows a more uniform strain variation along the tensile arms while applying axial stretch for measuring mechanical and viscoelastic properties [353]. Uniaxial stretch measurements are complex and allow retrieving different parameters, including ultimate strength, yield strain, ultimate strain, resilience and toughness. Experimentally, all these parameters are affected by the stretch rate, rest period, stretch amplitude and the number and magnitude of preconditioning cycles. Experimental artefacts can be minimized by using preconditioning protocols and maintaining constant stretch rates and rest periods [376]. Similar to floating discs and microspheres, these ring-shape tissues compact over-time, reflected by a decrease in volume [242, 379]. Tissue compaction was shown to be hampered by TGF-β receptors blockade and further enhanced by TGF-β stimulus, at least up to the third day of culture [242]. Compaction was also shown to be a reversible process, but only during the first days of tissue formation, when the collagen fibrils are just held in place by the cells, before the collagen fibrils become stabilized by cross-linking [374]. Increasing compaction over time is accompanied by increasing matrix stiffness, as shown by uniaxial stretch

measurements, and the increase of tissue force along the time is, at least in part, dependant on integrins [374]. As found for soft quasi-3D lattices [241], the cell alignment in 3D tissues is preferential organised in the direction of the stretch [374, 379]. Several studies using this system have been emphasizing individual cellular and matrix mechanical contributions. Alike natural tissues, engineered tissues show a non-linear viscoelastic behaviour. This means that stress exponentially increases with strain increase, while there is a linear dependence of stiffness on force at a given strain [375, 379]. Cellular and matrix mechanical contributions can be discriminated, for example, by stimulating cellular contractile forces, disrupting F-actin fibres and removing cells from the matrices with detergents, allowing better testing of mechanical and functional properties of the tissues. By this, it was shown that the cellular-dependent stiffness (active component) increases with stretching frequency and decreases with stretch amplitude [375, 379]. Moreover, uniaxial cyclic stretch measurements have shown that cellular-dependent tissue stiffness is independent on cell density above a threshold density [375]. On the other hand, the stiffness conferred by the matrix (passive component) increases approximately exponentially with strain and with cell number, since additional cell-contributed matrix is expected to occur over-time [375]. This is supported by the observation that in two hours the cell-remodelled matrix (passive component – measured after decellularization) already presents higher stiffness comparing to collagen matrices that have not been populated with cells [374]. Moreover, at higher stretch strains the passive matrix component has a larger contribution for the tissue stiffness over the active cellular component [379]. In line, ultimate strength and stiffness of the passive component is increased by non-enzymatically crosslink of the collagen matrix [375, 386]. Thus, the decreasing ultimate strength of the tissue at every stretch cycle [374, 379] is associated with changes in the

structure of the collagen fibrils rather than being dependent on the cellular component [374]. In a more recent study [180], ring-shaped engineered tissues have been produced with CF or with cardiac myofibroblasts, selected according to SMA expression. Comparing to CF populated tissues, myofibroblasts produced tissues with greater compaction. Besides, the myofibroblasts-remodelled matrix had a higher stiffness and hysteresis, the energy dissipated due to stretch resistance [180]. The restoring force of embedded myofibroblasts at a constant strain after stretch reduces over-time to a level that is higher than the force at the beginning of the stretch. In contrary, the CF force increases minimally after stretch. In line with its increasing contractile force, the contribution of the active component to stretch resistance is notable with myofibroblasts, while CF barely contribute to it [180]. Contrary to findings in valvular fibroblasts cultured atop soft hydrogels or native valve matrix which preserved native phenotype of the cells [238], embedded CF in ring-shaped tissues around a central rod converted to myofibroblasts after three to four days which then contracted the matrix to a similar extent as in tissues initially produced with myofibroblasts [180]. However, different culture conditions, tissue architecture, and stiffness assessment prevent direct comparisons and linear extrapolations. Nevertheless, according to the mathematical model of Elson and colleagues it seems that increasing tissue stiffness due to CF contractility-mediated matrix compaction positively feedback to CF which began to transdifferentiate into myofibroblasts [180]. The model has not yet been experimentally proven. Ring-shaped tissues showed, nonetheless, to have the potential to attenuate over-time the myofibroblast phenotype acquired in cells while cultured in non-compliant stiff 2D substrates before embedment, shown by a decrease in the percentage of SMA-expressing cells [242].

The ring-shaped model around a single stiff pole has been implemented in our research

group. Using a mixture of rat CF from the ventricle and rat tail collagen type I, the constructs have been named engineered connective tissues (ECT). The group has demonstrated the ECT applicability to perform gain and loss of function experiments as well as small molecule studies while evaluating the impact on the viscoelastic properties of the tissues [281, 286, 370, 387]. Moreover, our group has shown that RhoA activity impacts viscoelastic properties of tissues [281, 286]. By using adenoviral transduction to overexpress p63RhoGEF it was found that increased RhoA activity increased tissue stiffness, which positively correlated with increased SMA and CTGF levels [286]. The overexpression of phosphodiesterase 2 (PDE2), which mediates cyclic adenosine monophosphate (cAMP) hydrolysis, accelerated CF transdifferentiation into myofibroblast in 2D culture, showing increased SMA and CTGF levels. When overexpressed in 3D cultures, PDE2 led to an increase of tissue stiffness [387]. In ECT produced with female CF/myofibroblasts, treatment with 17β-estradiol down-regulated COL1A1 and COL3A1 and tissue compaction was reduced without impacting stiffness. On the other hand, in male ECT 17β-estradiol increased COL1A1 and COL3A1 and induced higher tissue compaction and stiffness [370].

Microtissue suspended in multiple micropillars is a newly developed method established by Asmani and colleagues [388]. It involves preparing a sheet-like tissue, containing lung fibroblasts and collagen, suspended in a structure with multiple micropillars. These lung microtissues were used to model biomechanical events occurring during lung fibrosis and predict anti-fibrosis drug efficacy [388]. In line with the findings from Knezevic and colleagues [372], this study showed that microtissues had a non-uniform stress distribution. A higher stress concentration and collagen and SMA expression was observed in the areas surrounding the micropillars comparing to the areas between the micropillars. Further, it was shown that micropillars with higher

stiffness led to increased stress accumulated around the micropillars [388]. As shown by the group, tissues in micropillars allowed assessing tissue contractile force through the deflection of the micropillars according to cantilever bending theory [388]. Similar systems of flexible micropillars or flexible poles can be used for culturing of ring-shaped tissues [389], but it has so far not been used for homogeneous CF tissues.

These studies suggest that mechanical cues of engineered tissues influence mechanical properties of the cells and cell behaviour. Simultaneously, cell mechanical properties feedback with traction forces to the ECM, influencing tissue behaviour. Moreover, the structures holding the tissues seem to directly impact tissue and cell behaviour. Together, engineered tissues show the potential to provide mechanical conditions necessary to generate and study different phenotypes of CF and transdifferentiation mechanisms, eventually replicating key features of a range of pathologies, including fibrosis. Furthermore, they have the great potential to aid drug screening and the discovery of drug targets.

2. Preliminary data and aims of the project

2.1. Preliminary data

Previous results of our research group on a project focused on the impact of ROCK signalling on the behaviour of CF cultivated in 3D using pan-ROCK inhibitors contributed to build the scope of the study presented in this project-based dissertation.

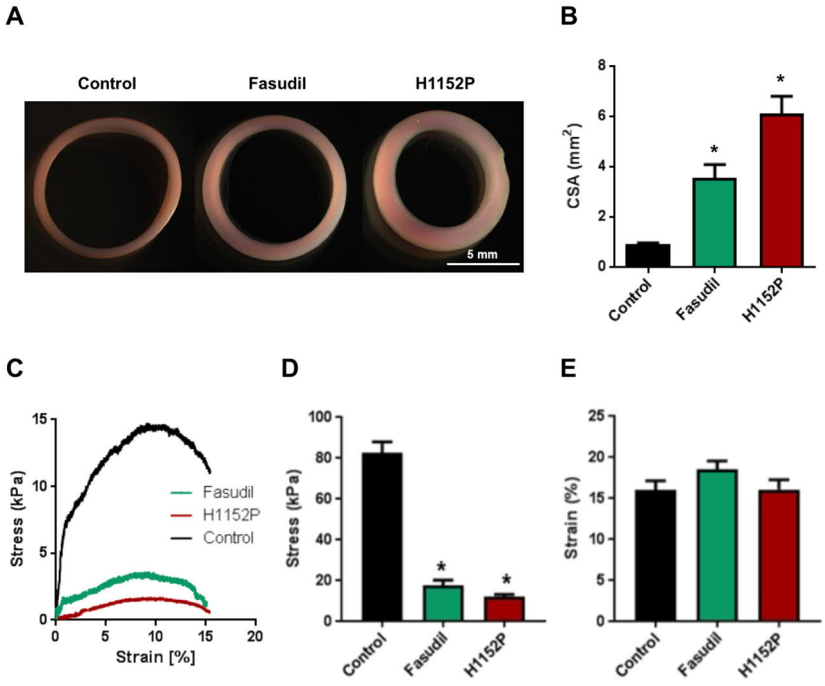

Figure 6. ROCK inhibition reduces compaction and stiffness of rECT [390].
rECT were generated with normal rat cardiac fibroblasts (NRCF) and collagen I and were cultured for 5 days in the absence (Control) or presence of 10 µM Fasudil or 3 µM H1152P. **A)** Representative images of rECT are shown. **B)** The cross sectional areas (CSA) were determined by image analysis. Given are the means+SEM of 13 to 15 individual tissues from 3 independent experiments. Differences were analysed by 1-way ANOVA with Dunnett's *post hoc* test for multiple comparisons, *p<0.05 vs. Control. **C)** Representative stress-strain curves from destructive tensile measurements are shown. **D)** The Young's moduli were calculated based on the obtained stress-strain curves. Given are the means+SEM of 9-13 rECT from 3 independent experiments. Differences were evaluated by 1-way ANOVA with Dunnett's *post hoc* test for multiple comparisons, *p<0.05 vs. Control. **E)** The strain to failure point was extracted from the obtained rheology data. Given are the means+SEM of 13-17 rECT from 3 independent experiments.

Two inhibitors with the same isoquinolin chemistry acting as adenosine triphosphate (ATP) analogues were used: Fasudil, a clinically approved ROCK inhibitor, and its more potent and specific homologue H1152P [351]. Originally, the ECT were

generated with neonatal rat CF and rat tail collagen I (rECT) and were cultured for 5 days in the presence or absence of Fasudil (10 µM) or H1152P (3 µM). It was found that both inhibitors interfered with the rECT compaction, demonstrated by an increase in the CSA (**Figure 6A,B**). Moreover, the stiffness of the rECT, given by the Young's modulus, was reduced by both inhibitors (**Figure 6C,D**) and no effect was found on the tissues' extensibility, namely on the ultimate strain (**Figure 6E**).

In order to identify potential causes for the changes observed in the biomechanical analyses, a series of qPCR analyses were performed. Especially, genes playing a role in ECM constitution and regulation were here in focus. It was found that both ROCK inhibitors showed inhibitor effects on the gene expression of the collagen cross-linker *Lox* and the fibrosis inducer hyaluronan synthase 2 (*Has2*). Moreover, H1152P also significantly inhibited the transcription of the elastase *Mmp12*, and increased matrix metalloproteinase 2 (*Mmp2*) and *Rock2* expression (**Figure 7**).

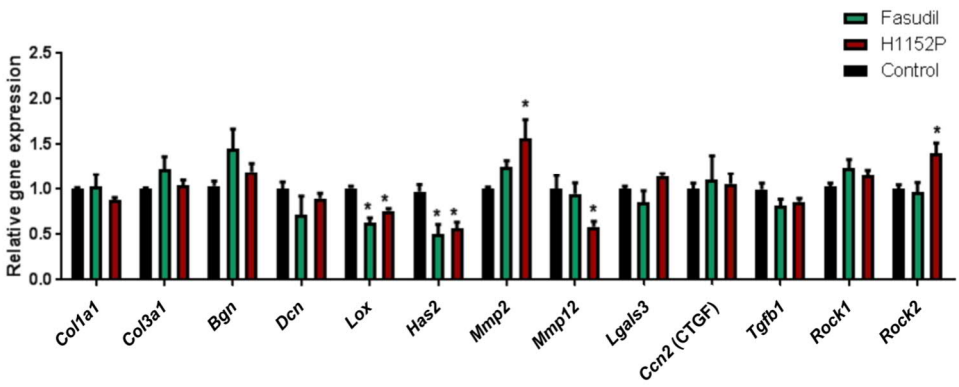

Figure 7. ROCK inhibition regulates gene expression in rECT [390].
rECT were generated with normal rat cardiac fibroblasts (NRCF) and collagen I and were cultured in the absence (Control) or presence of 10 µM Fasudil or 3 µM H1152P. After 5 days in culture, RNA was isolated from rECT and subjected to qPCR analysis. In total RNA from 3 to 8 independent samples were analysed. All values were normalized to the mean of the housekeeping genes *Pbgd* and *Gusb*. Bar graph depicts means+SEM and the differences were evaluated for each individual gene by 1-way ANOVA with Dunnett's *post hoc* test for multiple comparisons, *p<0.05 vs. Control.

2.2. Aims

The above-described preliminary work strongly suggested that parameters such as mechanical properties of the tissues and regulation of genes implicated in extracellular matrix regulation might be connected. However, the mechanisms through which ROCK inhibitors led to the results described above needed further clarification.

Moreover, as the measured stiffnesses of the rECT were found to be about 10 times higher under control condition than the reported values for healthy mammalian hearts [391, 392], creating an additional model resulting in tissues with stiffnesses closer to physiological values should be established. This model should then be used to compare its effects on biomechanical tissue properties, cell characteristics, and gene expression pattern with the already established model.

To this end, the main goals of this study were to:

- Characterize the effects of the ROCK inhibitors by using 2D and 3D cultures (rECT) assisted by the application of different inhibitors that allows identifying molecular players involved in the ROCK-dependent regulation of tissue formation and its mechanical properties.
- Translate the approach to a human engineered connective tissue (hECT) model using primary cells from the healthy human heart.
- Explore time-dependency and external stiffness influence on the regulation of molecular mechanisms that may play a role in the CF phenotypic switching and determine the biomechanical properties outcome on hECT.
- Compare molecular profiles between the hECT model and human heart samples using transcriptome analysis.

- Generate and validate a platform with medium throughput of the needed test assessments to foster a better understanding of the biology of CF and that would allow for comparative drug actions testing.

3. Material and Methods

3.1. Material

3.1.1. Animals

The animals were provided by the central animal facility of the UMG.

Table 1. Animals.

Rat strain	Age	Application
Wild type Wistar-Kyoto	0-3 days	Heart/cell isolation

3.1.2. Primary cells

The cells used for this work were isolated directly from tissue and have a finite lifespan and limited expansion capacity. Rat cells were isolated in house and human cells were purchased form Lonza. Specifications can be found in the following table.

Table 2. Primary cell lines.

Cell type	Abbreviation	Source (supplier)	Application
Neonatal rat cardiac fibroblasts from the ventricle	NRCF	Fresh isolation from Wistar-Kyoto neonatal hearts (0-3 days)	2D culture, rECT generation, RNA, IB, microscopy
Normal human cardiac fibroblasts from the ventricle	hCF	Non-failing heart, caucasian male, 53 years-old, 27741 LOT NO.: 0000421712 (Lonza #CC-2904)	2D culture, hECT generation, RNA, RNA-Seq, IB, microscopy

3.1.3. Reagents

Several substances, compounds, and mixtures (chemical or biological substances) were

used in this study. The tables below provide all the reagents as well as their suppliers and catalogue numbers. For mixtures prepared in house, the composition is individually given in the following. For cell culture purposes, mixtures were sterilized by using Vacuum Filtration Systems (Corning) or syringe filters (Sarstedt).

3.1.3.1. Supplied reagents, buffers and media

The following section comprises fine chemicals used for several applications as basic components of solutions prepared in house, drugs used with a pharmacological purpose to inhibit specific proteins or cellular processes in our cells and tissues, and general and cell culture specific reagents, buffers, media and additives ready to use or to supplement pre-made supplies. The following tables list the products, manufacturer and respective catalogue numbers.

Table 3. Fine chemicals (divers applications).

Product	Supplier	Catalogue number
β-Mercaptoethanol (β-ME)	AppliChem	A1108.0100
4',6-Diamidin-2-phenylidol (DAPI)	Roche	10236276001
Absolute ethanol	BD Bioscience	354052
Acetic acid	Carl Roth	KK62.1
Acrylamide[§] solution 30% (Rotiphorese gel 30)	Carl Roth	3029.1
Agarose	Carl Roth	A0385
Ammonium persulfate (APS)	AppliChem	141138
Bovine serum albumin (BSA)	Sigma-Aldrich	A3311-50G
Bromophenol blue	Sigma-Aldrich	B8026
Dimethyl Sulfoxide (DMSO)	Sigma-Aldrich	D2650
Ethylenediaminetetraacetic acid (EDTA)	Carl Roth	8043.2

List continued on next page

Table 3: Continued from previous page

Glycerol	AppliChem	A0970
Glycine	AppliChem	A3707
H_2O nuclease free	Life Technologies	AM9938
Hydrochloric acid (HCl)	Sigma-Aldrich	H1758
Hoechst 33342	Life Technologies	H3570
Liquid Nitrogen (N_2)	Air Liquide	-
Magnesium Chloride ($MgCl_2$)	Sigma-Aldrich	M8266
MED610 polymer	Stratasys	OBJ-02260
Methanol	Carl Roth	8388.6
N,N,N',N'-Tetramethyl ethylenediamine (TEMED)	Merck	1.10732.0100
Paraformaldehyde (PFA)	Sigma-Aldrich	P6148
Phalloidin (TRITC-labelled)	Sigma-Aldrich	P1951
Ponceau S	Sigma-Aldrich	P3504
Propidium iodide (PI)	Sigma-Aldrich	P4864
Sodium Chloride (NaCl)	Thermo Fisher Scientific	AM9759
Sodium deoxycholate (NaOH)	Sigma-Aldrich	30970
Sodium dodecyl sulfate (SDS) grained	AppliChem	A7249,0500
Tris	AppliChem	A1086
Tris-base	Sigma-Aldrich	T1503
Tris-hydrochloride (Tris-HCl)	Carl Roth	9090.3
Triton x-100	Carl Roth	3051.2
Tween 20	Carl Roth	9127

Table 4. Drugs (active pharmaceutical compounds).

Product	**Supplier**	**Catalogue number**
3-Aminopropionitrile fumarate (BAPN)	Sigma-Aldrich	A3134

List continued on next page

Table 4: Continued from previous page

Brefeldin-A (BFA)	Sigma-Aldrich Cayman	B6542 11861
CCG-203971 (CCG)	Sigma-Aldrich	SML1422
H1152P dihydrochloride	Biomol – AdipoGen[*] Tocris Bioscience[#]	SYN-1221 2414
Latrunculin-A (Lat-A)	Enzo Fife Sciences	BML-T119-0100
Staurosporine	Roche	11 055 682 001

[*#] Stock solutions are indicated accordingly (Table 11).

Table 5. Buffers, reagents and supplements ready to use (divers applications).

Product	**Supplier**	**Catalogue number**
Blocking solution – Roti-Block 10×	Carl Roth	A151.2
Blocking solution – Roti-ImmunoBlock 10×	Carl Roth	T144.1
Bradford reagent – Roti-Quant 5×	Carl Roth	K015.3
BSA purified solution (10 mg/mL)	BioLabs	B9001S
DNA ladder – peqGOLD Ultra Low Range II	Peqlab	25-4010
DNA/RNA dye – Midori Green Advanced	Nippon	MG04
Enhanced chemiluminescent (ECL) horseradish peroxidase (HRP) substrate – SuperSignal West Femto	Thermo Fisher Scientific	34096
Enhanced chemiluminescent (ECL) horseradish peroxidase (HRP) substrate – Lumi-Light Plus	Roche	12 015 196 001
FACSClean – cleaning solution	BD Biosciences	340345
FACSFlow – sheath fluid	BD Biosciences	342003
FACSRinse – maintenance solution	BD Biosciences	340346
Fixative agent – Roti-Histofix, 4% PFA stabilized with methanol	Carl Roth	P087.1
Master mix for PCR and gel loading – 2× GoTaq G2 Green Master Mix	Promega	M782B
Master mix for qPCR – 5× HOT FIREPol EvaGreen qPCR Mix Plus ROX	Solis Biodyne	08-24-00020

List continued on next page

Table 5: Continued from previous page

Phosphate buffered saline (PBS) 10×, pH 7.4, -Ca^{2+}, -Mg^{2+}	Gibco	70011-036
Protease inhibitor cocktail – cOmplete Tablets EDTA free EASY pack	Roche	04 693 159 001
Protein extraction reagent – CytoBuster	Millipore	71009
Protein marker – Roti-Mark Standard	Carl Roth	T851.2
Protein marker – Roti-Mark Tricolor	Carl Roth	8271.1
Protein marker – Spectra Multicolor Broad Range Protein Ladder	Thermo Fisher Scientific	26623

Table 6. Cell culture reagents (buffers, media, reagents and supplements).

Product	**Supplier**	**Catalogue number**
CASY Ton	CASY OLS	5651808
Collagen Type I (bovine) in 0.01 M HCl (medical grade)	LLC Collagen Solutions	CB-024
Collagen Type I (rat tail)	Corning/BD Biosciences	354236
Collagenase I	Sigma-Aldrich	SCR-103
Dissociation reagent – Accutase Solution	Merk Millipore	SCR005
Dissociation reagent – TrypLE Express	Gibco	12604039
Dissociation reagent – Trypsin (0.05%)	Gibco	25300-054
Dissociation reagent – Trypsin (2.5%)	Gibco	15090-046
DNAse I	Calbiochem	260913
Dulbecco's Modified Eagle Medium (DMEM) powder, high glucose	Gibco	12100061
Dulbecco's Modified Eagle Medium (DMEM), high glucose, GlutaMAX™ Supplement	Gibco	61965026
Dulbecco’s phosphate buffered saline (DPBS), pH 7.1, +Ca^{2+}, +Mg^{2+}	Gibco	14040091
Dulbecco’s phosphate buffered saline (DPBS), pH 7.2, -Ca^{2+}, -Mg^{2+}	Gibco	14190169

List continued on next page

Table 6: Continued from previous page

Fetal bovine serum (FBS)	Gibco	10270-106
Fibroblast Growth Medium 3 KIT	PromoCell	C-23130
Fibroblast Basal Medium 3		C-23230
SupplementPack		C-39350
Basic Fibroblast Growth Factor – recombinant human (rH)		C-30310
Fetal Calf Serum (FCS)		C-37340
Insulin – recombinant human (rH)		C-31010
L-Glutamine (200 nM)	Gibco	25030-123
Penicillin (10000 U/mL)/ Streptomycin (10000 µL/mL)	Gibco	15140130
Percoll	GE Healthcare Life Sciences	17-0891-01

3.1.3.2. Solutions, buffers and media composition – preparation in house

Several solutions, buffers and media were either fully prepared in house or prepared by supplementing ready to use supplied products. All formulations are described in the following tables according to their application.

Table 7. Composition of media and buffers for cells and tissues-handling.

Type of mixture	Composition/Supplementation		Application
Calcium and bicarbonate free Hanks with HEPES (CBFHH)	NaCl	137 mM	Isolation of neonatal rat cardiac fibroblasts (NRCF)
	KCl	5.4 mM	
	$MgSO_4$. 7 H_2O	0.81 mM	
	KH_2PO_4	0.44 mM	
	Na_2HPO_4 . 2 H_2O	0.34 mM	
	Glucose	5.6 mM	
	HEPES, pH 7.4	20 mM	
	pH 7.4 with NaOH in $_{dd}H_2O$		
Non-cardiomyocytes medium (NCM)	DMEM (1 g/L glucose)	88% (v/v)	Isolation of neonatal rat cardiac fibroblasts (NRCF)
	FCS (inactivated, 30 min at 56°C)	10% (v/v)	
	L-Glutamine	2 nM	
	Penicillin/ Streptomycin	100 U/mL / 100 µg/mL	
NRCF growth media	DMEM GlutaMAX (4.5 g/L glucose)	89% (v/v)	Culture of NRCF
	FBS	10% (v/v)	
	Penicillin/ Streptomycin	100 U/mL / 100 µg/mL	

List continued on next page

Table 7: Continued from previous page

NRCF freezing media	NRCF growth medium DMSO FBS (surplus)	80% (v/v) 10% (v/v) 10% (v/v)	Cryopreservation of NRCF
FGM3 growth media	Fibroblast Basal Medium 3 FCS Basic Fibroblast Growth Factor (rH) Insulin (rH) Penicillin/ Streptomycin	500 mL 10% (v/v) 1 ng/mL 5 µL/mL 100 U/mL / 100 µg/mL	Culture of hCF
hCF freezing media	FGM3 growth media DMSO FCS (surplus)	80% (v/v) 10% (v/v) 10% (v/v)	Cryopreservation of hCF
10× DMEM	DMEM powder $_{dd}H_2O$	1.34 g 10 mL	
2× DMEM	DMEM 10× FBS (rECT) or FCS (hECT) Penicillin/ Streptomycin $_{dd}H_2O$	20% (v/v) 20% (v/v) 200 U/mL / 200 µg/mL 58% (v/v)	ECT preparation
DNAse I solution	DNAse I in $_{dd}H_2O$	1 mg/mL	
Accutase mix	Accutase solution Trypsin (2.5%) DNAse I solution (1 mg/mL)	97.7% (v/v) 0.0075% 20 µg/mL	ECT dissociation
Collagenase solution	Collagenase I FBS DPBS $+Ca^{2+}$, $+Mg^{2+}$	2 mg/mL 20% (v/v) 80% (v/v)	
10% FBS in DPBS	FBS DPBS $-Ca^{2+}$, $-Mg^{2+}$	10% (v/v) 90% (v/v)	

Table 8. Buffers for agarose gel electrophoresis (qPCR product amplicon length).

Buffer/solution	**Composition/Supplementation**	
TAE buffer (50×)	Tris-base, pH 8 EDTA Acetic acid	2 mM 50 mM 1 M
TAE buffer (1×)	TAE buffer (50×) in $_{dd}H_2O$	2% (v/v)
2% Agarose gel	Agarose DNA dye (Midori Green) in TAE buffer (1×)	2% (w/v) 5 µL/100 mL

Table 9. Buffers for cell staining/immunostaining (microscopy and flow cytometry).

Buffer/solution	**Composition/Supplementation**	
4% PFA solution	Paraformaldehyde NaOH (10M) PBS 10× ($-Ca^{2+}$, $-Mg^{2+}$) pH 7.4 with HCl in $_{dd}H_2O$	4% (w/v) 1 mM 10% (v/v)

List continued on next page

Table 9: Continued from previous page

75% Ethanol	Ethanol (≥99%) in $_{dd}H_2O$	75% (v/v)
Blocking buffer (microscopy)	Roti-immunoblock 10× in $_{dd}H_2O$	10% (v/v)
Permeabilization buffer (microscopy)	Triton X-100 PBS 10× (-Ca^{2+}, -Mg^{2+}) pH 7.4 with HCl in $_{dd}H_2O$	0.2% (v/v) 10% (v/v)
Permeabilization/ blocking buffer (flow cytometry)	BSA FBS Triton-X 100 PBS 10× (-Ca^{2+}, -Mg^{2+}) in $_{dd}H_2O$	1% (w/v) 5% (v/v) 0.5% (v/v) 10% (v/v)

Table 10. Solutions and buffers prepared for protein analysis.

Type of mixture	Composition/Supplementation		Application
10% SDS[#]	Sodium dodecyl sulfate in $_{dd}H_2O$	10% (w/v)	General
Lysis buffer	Cytobuster cOmplete (20x)	95% (v/v) 5% (v/v)	Protein extraction
Protease inhibitors (20x)	cOmplete $_{dd}H_2O$	1 tablet 500 µL	
Laemmli sample buffer (4x)	Glycerol Tris SDS Bromophenol blue β-ME (added freshly) pH 7.4 with HCl in $_{dd}H_2O$	50% (v/v) 0.3 M 6% (w/v) 0.01% (w/v) 20% (v/v)	Sample denaturation
10% APS[$]	Ammonium persulfate in $_{dd}H_2O$	10% (w/v)	SDS PAGE
1.0M Tris-HCl[¥]	Tris-HCl pH 6.8 with HCl in $_{dd}H_2O$		
1.5M Tris-HCl[*]	Tris-HCl pH 8.8 with HCl in $_{dd}H_2O$		
Resolving gel[a] 6%	Tris-HCl[*] Acrylamide[§] SDS[#] APS[$] TEMED pH 8.8 in $_{dd}H_2O$	0.375 M 6% (w/v) 0.1% (w/v) 0.1% (w/v) 0.061% (v/v)	
Resolving gel[a] 8%	Tris-HCl[*] Acrylamide[§] SDS[#] APS[$] TEMED pH 8.8 in $_{dd}H_2O$	0.375 M 8% (w/v) 0.1% (w/v) 0.1% (w/v) 0.054% (v/v)	

List continued on next page

Table 10: Continued from previous page

Resolving gel[a] 10%	Tris-HCl[*] Acrylamide[§] SDS[#] APS[$] TEMED pH 8.8 in $_{dd}H_2O$	0.375 M 10% (w/v) 0.1% (w/v) 0.1% (w/v) 0.047% (v/v)	SDS PAGE
Resolving gel[a] 12%	Tris-HCl[*] Acrylamide[§] SDS[#] APS[$] TEMED pH 8.8 in $_{dd}H_2O$	0.375 M 12% (w/v) 0.1% (w/v) 0.1% (w/v) 0.04% (v/v)	
Stacking gel[a] 5%	Tris-HCl[¥] Acrylamide[§] SDS[#] APS[$] TEMED pH 6.8 in $_{dd}H_2O$	0.127 M 5% (w/v) 0.1% (w/v) 0.1% (w/v) 0.1% (v/v)	
Running buffer (10×)	Tris-Base Glycine SDS in $_{dd}H_2O$	250 mM 1.92 M 1% (w/v)	
Running buffer (1×)	Tris-Base Glycine SDS pH 8.3 with HCl in $_{dd}H_2O$	25 mM 0.192 M 0.1% (w/v)	
Tansfer buffer (10×)	Tris Glycine in $_{dd}H_2O$	250 mM 1.92 M	Electrophoretic transfer
Transfer buffer (1×)	Tris Glycine Methanol (added freshly) in $_{dd}H_2O$	25 mM 0.192 M 20% (v/v)	
Blocking buffer (Roti-block 1×)	Roti-block 10× in $_{dd}H_2O$	10% (v/v)	Blot membrane blocking
Ponceau S staining buffer	Ponceau S Glacial acetic acid in $_{dd}H_2O$	0.2% (w/v) 3% (v/v)	Blot membrane staining
Tris buffered saline solution 10× (TBS 10×)	Tris NaCl pH 7.4 with HCl in $_{dd}H_2O$	0.2 M 1.5 M	Washing and antibodies incubation
Tris buffered saline solution – Tween (TBST)	Tris NaCl pH 7.4 with HCl Tween-20 in $_{dd}H_2O$	20 mM 0.15 M 0.1% (v/v)	

[a] Gel composition is presented with final concentrations. For its preparation, the marked (*$#§¥) pre-made solutions were used.

3.1.3.3. Media supplementation for treatment groups

For each application, seeding densities and appropriate culture vessels are indicated in the correspondent section. The following table presents the chemicals and the concentration used for cell and tissue treatments.

Table 11. Drug and chemical treatment.

Drug/chemical	Stock concentration	Working concentration	Vehicle
H1152P	3 mM* / 10 mM#	300 nM and 3 µM	DMSO
Lat-A	105 µg/mL	7 ng/mL	DMSO
BAPN	30 mM	100 µM	$_{dd}H_2O$
CCG-203971	50 mM	50 µM	DMSO
BFA	500 µg/mL	5 µg/mL	DMSO
Staurosporine	1 mM	3 µM	DMSO

*# According to the supplied products (Table 4).

The vehicle (or diluent) of each chemical was used as the corresponding control. Vehicles were used at a maximum of 0.1% (v/v). For the comparison of multiple chemical treatments, all treatment groups including the control were tested containing the same amount of every vehicle being used. To assure complete homogeneous distribution of the additives before use, growth media and treatment/vehicle were mixed 20 to 30 min prior. Duration of the treatments and periodicity of media change are noted in each specific section.

3.1.3.4. Kits

When working with kits, mixtures were prepared according to manufactures' instructions and are shortly described within the procedures on the methods section, and thus are not specifically discriminated in this section. The kits used are listed below.

Table 12. Kits.

Product	Supplier	Catalogue number
Annexin V-FLUOS Staining Kit	Roche	11 858 777 001
Neonatal Heart Dissociation Kit, mouse and rat	Miltenyi Biotec	130-098-373
RevertAid First Strand cDNA Synthesis Kit	Thermo Fisher Scientific	K1622
Rneasy Mini Kit	Qiagen	74106
Silicone elastomer kit (Sylgard 184)	Dowsil	1673921

3.1.3.5. Antibodies

The different primary and secondary antibodies which were used for immunoblotting (IB) are listed below. Primary antibodies were reactive to both rat and human species. Polyacrylamide gel percentage used for analysis of each protein and antibodies' dilutions are indicated in the table.

Table 13. Primary antibodies.

Antibody	Host/Clone	Supplier	Catalogue number	Polyacrylamide gel	Dilution
α-Tubulin	Mouse/ B-5-1-2 monoclonal	Sigma-Aldrich	T5168	6-12%	1:2000
β-Actin	Mouse/ AC-15 monoclonal	Sigma-Aldrich	A5441	8-12%	1:2000
GAPDH	Mouse/ 6C5 monoclonal	Zytomed Systems	RGM2-6C5	8-12%	1:10.000
LOX	Rabbit/ polyclonal	Origene Abnova	TA337077 PAB12403	12%	1:2000 1:1000
POSTN	Mouse/ F-10 monoclonal	Santa Cruz	sc-398631	8-10%	1:1000
ROCK1	Mouse/ 46 monoclonal	BD Biosciences	611137	6-8%	1:500

List continued on next page

Table 13: Continued from previous page

ROCK2	Rabbit/ polyclonal	Santa Cruz	sc-5561	6-8%	1:200
SMA	Mouse/ 1A4 monoclonal	Sigma-Aldrich	A 5228	10-12%	1:2500

Table 14. Secondary antibodies.

Antigen	Host/conjugate	Supplier	Catalogue number	Dilution
IgG mouse	Rabbit/ Peroxidase	Sigma-Aldrich	A9044	1:10.000
IgG rabbit	Goat/ Peroxidase	Sigma-Aldrich	A9169	1:40.000

3.1.3.6. Primers

The primers used for qPCR are spanning primers and were designed to span or flank at least one intron. The FASTA sequences were extracted from Ensembl [393] and used to find the primer sequences with the support of Primer-BLAST tool of the National Center for Biotechnology Information (NCBI) [394]. The following tables indicate the sequences of forward (Fw) and reverse primers (Rv) for rat and human gene sequences, and the respective amplicon size. The primer specificity and amplicon size were validated (*section 3.2.4.5.*).

Table 15. qPCR primers for rat gene sequences used in this study.

Gene	Sequence (5' to 3')		Amplicon length (bp)	Melting (^{o}C) temperature
Bng	Fw	GCTCCGGAACATGAACTGCA	95	60.96
	Rv	GGTAGTTGAGCTTCAGGCCAT		60.07
Col1a1	Fw	ACGCCATCAAGGTCTACTGC	159	60.11
	Rv	ACTCGAACGGGAATCCATCG		59.90
Col3a1	Fw	CCATGACTGTCCCACGTAAGCAC	109	63.55
	Rv	GGAGGGCCATAGCTGAACTGAAAAC		63.84
Ccn2	Fw	CCGGGTTACCAATGACAATA	204	55.13
	Rv	CACACCCCACAGAACTTAGC		58.48

List continued on next page

Table 15: Continued from previous page

Dcn	Fw	GCTATTCCTCAAGGTCTGCC	152	58.04
	Rv	CTGCCATTTTCCACAACGGT		59.33
Gusb	Fw	TACTTCAAGACGCTGATCGCC	167	60.47
	Rv	ATCACCTCCAGATGCCCGTA		60.40
Has2	Fw	CTGGGCAGAAGCGTGGATTA	126	60.11
	Rv	AACATCTCCCCCAACACCTC		59.30
Hprt	Fw	CCTCCTCAGACCGCTTTTT	91	57.37
	Rv	AACCTGGTTCATCATCGCTAA		57.37
Lgals3	Fw	AGCCCAACGCAAACAGTATCA	180	60.54
	Rv	TGAATGGTTTGCCGCTCTCA		60.25
Lox	Fw	GCTGCACCATTTCACCGTATTAG	70	60.24
	Rv	GTCCAAACACCAGGTACTGCTT		60.75
Mmp2	Fw	TCCCCCGATGCTGATACTGA	150	60.11
	Rv	CCGCCAAATAAACCGGTCCTT		61.22
Mmp12	Fw	GGTACCAGAGCCACACTATC	150	57.11
	Rv	TCCTGCCTCACATCGTACCT		60.32
Pbgd	Fw	CCTGAAACTCTGCTTCGCTG	208	59.20
	Rv	CTGGACCATCTTCTTGCTGAA		57.94
Rock1	Fw	GGTGAAACACCAGAAGGAGCTGAA	123	63.03
	Rv	TTTGCACGCAACTGCTCAATATCAC		63.04
Rock2	Fw	TTCCCAACCAACTGTGAGGC	178	60.47
	Rv	ACAACAGATTCTTTGCCGATGATA		58.81
Tgfb1	Fw	AGAGCCCTGGATACCAACTA	206	57.13
	Rv	TGTTGGTTGTAGAGGGCAAG		57.73

Table 16. qPCR primers for human gene sequences used in this study.

Gene		**Sequence (5’ to 3’)**	**Amplicon length (bp)**	**Melting (^{o}C) temperature**
ACTA2 (SMA)	Fw	AGAACATGGCATCATCACCA	229	57.19
	Rv	GCGTCCAGAGGCATAGAGAG		59.69
CCDC80	Fw	TCCCTGGAGAACTTCCTATCC	60	55.33
	Rv	AGCAGAGATCACCAGCAACC		60.04
COL1A1	Fw	GTTCAGCTTTGTGGACCTCC	123	58.76
	Rv	TGTACGCAGGTGATTGGTGG		60.32
COL6A1	Fw	CTGGGCGTCAAAGTCTTCTC	71	58.57
	Rv	GTGGCGATGATGCTCAGAC		58.69
CYR61 (CCN1)	Fw	AAGAAACCCGGATTTGTGAG	77	55.95
	Rv	GCTGCATTTCTTGCCCTTT		57.08
DDIT3 (CHOP)	Fw	AAGGCACTGAGCGTATCATGT	105	59.79
	Rv	TGAAGATACACTTCCTTCTTGAACAC		59.29
DNAJA1	Fw	TGGTGCAACAAGAAAACTGG	101	57.04
	Rv	GGCAATTGGGACAGCACT		57.90
DNAJB9	Fw	CATGAAGTACCACCCTGACAAA	89	59.00
	Rv	CATCTGAGAGTGTTTCATATGCTTC		59.00

List continued on next page

Table 16: Continued from previous page

EIF2AK3 (PERK)	Fw Rv	CCAGCCTTAGCAAACCAGAG TCTTGGTCCCACTGGAAGAG	82	58.54 58.65
GUSB	Fw Rv	CGCCCTGCCTATCTGTATTC TCCCCACAGGGAGTGTGTAG	91	59.40 61.60
HSP90AA1	Fw Rv	TGACCATTCCATTATTGAGACCT CAGATCCTTCACAGACTTGTCG	73	57.80 58.75
HSP90B1	Fw Rv	CTGGAAATGAGGAACTAACAGTCA TCTTCTCTGGTCATTCCTACACC	94	58.45 59.23
HSPA1A	Fw Rv	AAGGACCGAGCTCTTCTCG GGTTCCCTGCTCTCTGTCG	82	58.81 59.78
HSPA5	Fw Rv	TGTTACAATCAAGGTCTATGAAGGTG CAAAGGTGACTTCAATCTGTGG	125	60.00 59.00
HSPA8	Fw Rv	CATCAACCCTGATGAAGCTGT GTGACATCCAAGAGCAGCAA	105	58.28 58.47
HSPB1	Fw Rv	TCCCTGGATGTCAACCACTT GATGTAGCCATGCTCGTCCT	111	58.56 59.61
HSPH1	Fw Rv	TTTCACCATCTCTACGGCATC CACTGTTGTCTTGCTGGACATT	143	57.82 59.38
LOX	Fw Rv	CAAGGGACATCAGATTTCTTACC CCATACTGTGGTAATGTTGATGAC	82	56.92 57.64
LUM	Fw Rv	CGAAAGCAGTGTCAAGACAGTAA GGCCACTGGTACCACCAA	100	59.20 59.16
PDGFRA	Fw Rv	GCTCTTTACTCCATGTGTGGGA ATTAGGCTCAGCCCTGTGAGA	127	60.03 60.62
PDIA4	Fw Rv	AAGATCGATGCAACCTCAGC GTGGGGTAGCCACTCACATC	62	58.34 60.11
POSTN	Fw Rv	GAACCAAAAATTAAAGTGATTGAAGG TGACTTTTGTTAGTGTGGGTCCT	76	56.26 59.80
SULF1	Fw Rv	CCAATGCTTCCCAACACATA GCAGCATTGGTCCTGTGTACT	90	55.99 60.61
TCF21	Fw Rv	AACGACAAATACGAGAACGGGT CTCCAGGTACCAAACTCCAAGG	154	60.29 60.29
THBS1	Fw Rv	GGTGCTGCAGAATGTGAGGT ACCACGTTGTTGTCAAGGGT	111	60.61 60.03
TUBB	Fw Rv	ATACCTTGAGGCGAGCAAAA TCACTGATCACCTCCCAGAAC	113	55.03 59.80

3.1.4. Consumables and durables

This section includes components of end products for single usage in various experiments, as well as laboratory ware material used to support of the work.

Table 17. Consumables.

Product	Supplier	Catalogue number
8-Strip PCR tubes (0.2 mL)	StarLab	I1402-2908
Cell culture dishes (⌀ 10 cm)	CytoOne/StarLab	CC7682-3394
Cell culture dishes (⌀ 15 cm)	CytoOne/StarLab	CC7682-3614
Cell culture flasks (T-75, T-175)	Sarstedt	83.3911.002 83.3912.002
Cell culture plates (6-, 12-, 24-multi well)	Greiner Bio-One	657160 665180 662160
Cell culture plates (24-multi well) Nunc delta surface	Thermo Fisher Scientific	142475
Cell scraper (16 cm)	Sarstedt	83.1832
Cryotubes Nunc (1.8 mL)	Thermo Fisher Scientific	377267
Filter System (PES, pore size 0.2 µm) (250, 500 mL)	Corning	431096 431097
Gloves (nitrile, powder free, small)	Corning/LabSolute	7 696 900
Mesh cell strainer (Nylon, pore size 40 µm)	BD Falcon	352340
MicroAmp Optical 384-Well Reaction Plate	Applied Biosystems	4309849
MicroAmp Optical Adhesive Film	Applied Biosystems	4311971
Microtest plate (96-well)	Sarstedt	82.1581
Mini-PROTEAN TGX Stain-Free Gels (10-well)	Bio-Rad	456-8093
Mini-PROTEAN TGX Stain-Free Gels (12-well)	Bio-Rad	456-8095
Nitrocellulose membrane Amersham Protran (pore size 0.2 µm)	GE Healthcare Life Sciences	GE10600001
Parafilm M	Sigma-Aldrich	P7793
Pasteur pipettes (230 mm)	Labsolute	7 691 061
Pipette filter tips (Biosphere 200 µL)	Sarstedt	70.760.211

List continued on next page

Table 17: Continued from previous page

Pipette filter tips (Sapphire low retention 200 µL)	Greiner Bio-One	739 288
Pipette filter tips (TipOne 10/20, 100, 1000 µL)	Starlab	S1120-3710 S1123-1740 S1122-1730
Pipette tips (10, 100/200 µL)	Sarstedt	70.1130 70.760.002
Pipette tips (Combitips advanced 0.5 mL)	Eppendorf	0030089421
Pipette tips (Multiflex for gel loading)	Sorenson BioScience	28480
Pipette tips (TipOne 1000 µL)	Starlab	S1112-1020
RnaseZap	Invitrogen	AM9780
Screening plate (48-multi well) TM5MED and TM4MED-TM9MED	myriamed GmbH	myrPlate-uniform myrPlate-gradient
Serological pipettes (25 mL)	Sarstedt	86.1685.020
Serological pipettes wide opening, sterile (10 mL)	Falcon	357504
Serological pipettes, sterile (2, 5, 10, 25 mL)	Sarstedt	86.1252.001 86.1253.001 86.1254.001 86.1685.001
Syringe – BD Discardit II 20 mL	BD Biosciences	300296
Syringe filter (PES, pore size 0.22 µm)	Sarstedt	83.1826.001
Transfer pipette	Sarstedt	68.1171
Tubes – round-bottom polystyrene (flow cytometry)	Falcon – Corning	352052
Tubes – round-bottom polystyrene with caps (flow cytometry)	Falcon – Corning	38007
Tubes (0.5, 1.5, 2.0 mL)	Sarstedt	72.699 72.690.001 72.691
Tubes (15, 50 mL)	Greiner Bio-One	188271 227261
Whatmann paper (3 mm)	Sigma-Aldrich	WHA3030917

Table 18. Durables.

Product	Supplier	Catalogue number
Dewar Carrying Flask – Type 27 B	KGW Isotherm	1212
Glass beaker (100, 250, 3000 mL)	Duran	BR91224-10EA BR912236-10EA BR91268-4EA
Glass bottles DIN thread (100, 250, 500, 1000, 2000, 5000 mL)	Duran	21 801 24 5 21 801 36 5 21 801 44 5 21 801 54 5 21 801 63 5 21 808 73 5
Glass measuring cylinder Class A (50, 100, 250, 500, 1000, 2000 mL)	Duran	21 390 17 06 21 390 24 02 21 390 36 04 21 390 44 03 21 390 54 08 21 390 63 01
Ice bucket (4L)	Corning	432123
Ice pan (9L)	Corning	432094
Magnetic Stirring Bar (PTFE-coated) L 10 mm, bar diam. 6 mm L 25 mm, bar diam. 6 mm L 60 mm, bar diam. 9 mm	Brand	 137113 137120 137140
Petri dishes (glass 60×20 mm)	Duran	2175541
Rack – Labtop cooler (-20°C)	Nalgene	5115-0012
Rack – Labtop cooler iceless	Nalgene	5115-0012
Rack – PCR 96-well	Sigma-Aldrich	R6901-5EA
Rack – reversible 96-well	Sigma-Aldrich	R6151-5EA
Screw cap GL 45, 2-ports GL 14	Duran	1129750
Silicone Versilic tubing (external ⌀ 4, internal ⌀ 2 mm, 60 shore A, ~2.2 MPa)	Th. Geyer	9205302
Silicone Versilic tubing (external ⌀ 3, internal ⌀ 1 mm, 60 shore A, ~2.2 MPa)	Th. Geyer	9205301
Silicone cord (⌀ 1 mm)	Th. Geyer	(discontinued)
Specimen container (urine cup)	Sarstedt	NC9867141

List continued on next page

Table 18: Continued from previous page

Timer 4 channel	Sper Scientific	810015
PTFE cylinders (external ⌀ 8, internal ⌀ 3.5 mm, 50 shore D, ~5.5 MPa)	UMG	Custom-made
PTFE cylinders (external ⌀ 16 mm, internal ⌀ 3.5 mm, 50 shore D, ~5.5 MPa)	UMG	Custom-made

3.1.5. Instruments and equipment

All instruments and equipment used in this study are listed in tables below.

Table 19. List of general instruments and electronic equipment.

Device	Type/model	Manufacturer
Autoclave	VX-150	Systec
Centrifuges		
Bench top microcentrifuge	5417R	Eppendorf
Bench top with Deepwell rotor A-2-DWP	5804R	Eppendorf
Bench top with rotor S-4-104	5810R	Eppendorf
Bench top with rotor TV-750	Heraeus Megafuge 40R	Thermo Scientific
Mini-centrifuge/vortex with rotors R-1.5, R-0.5/0.2 and SR-16	FVL-2400N Combi-spin	Eppendorf
Drying oven	Ecocell 404 - ECO line	MMM Medcenter Einrichtungen GmbH
Freezers		
Tall Upright Freezer	Confort GP 4013	Liebherr
Tall Upright Freezer	Confort	Liebherr
Tall Upright Freezer	Profi line	Liebherr
Tall Upright Freezer	Economic-super	Bosch
Freezing container	Mr. Frosty	Nalgene
Fridges		
Upright Refrigerator	Profi line FKS 5000	Liebherr
Upright Refrigerator	Profi line GKv 4310	Liebherr
Table Refrigerator	T 1400	Liebherr

List continued on next page

Table 19: Continued from previous page

Heating block plus adapter plate for 0.5 mL tubes	Termomixer confort	Eppendorf
Heating cabinet	Custom-made	UMG
pH multimeter, level 1	3856B inoLab	WTW
Pipettes		
Bottle top dispenser (10 mL)	Dispensette	BrandTech
Multipette	Plus	Eppendorf
P2.5 (0.1-2.5 µL)	Research plus	Eppendorf
P10 (0.5-10 µL)	Research plus	Eppendorf
P10 (1-10 µL)	Pipetman L	Gilson
P20 (2-20 µL)	Reference	Eppendorf
P100 (10-100 µL)	Research plus	Eppendorf
P100 (10-100 µL)	Pipetman L	Gilson
P200 (20-200 µL)	Pipetman L	Gilson
P1000 (100-1000 µL)	Research plus	Eppendorf
Pipette controller	Accu-jet pro	BrancTech
Pipette controller	Pipetus	Hirschmann Laborgeräte
Scales		
Electronic microscale	AX224	Sartorius
Electronic scale	Pt600	
Electronic semi-microbalance	R160P	
Portable toploading balance	AZ612 M-Power	
Shakers		
3D rocker motion (10° tilt angle)	Duomax 1030	Heidolph
Horizontal reciprocating linear motion	3016	GLF
Orbital motion	Vibramax	Heidolph
Stirrers		
Magnetic heating stirrer	RCT basic	IKA Labortechnik
Magnetic heating stirrer	RCT basic IKAMAG	
Ultrapure water system	Milli-Q Direct	Merk
Vacuum pump	Labport mini series	KNF
Vortexer	VF2	W.Krannich
Water bath	2764	Eppendorf

Table 20. List of specialized instruments and electronic equipment.

Device	Type/model	Manufacturer
3D printer	objet connex350	Stratasys
Waterjet	Powerblast	Balco
Automated cell imager	Cellavista High End System V 3.1.	SynenTec (Innovatis)
Light source (brightfield)	LED	
Camera	Monochrome interlined CCD	
Objective 2x	Olympus UPLFLN 2x (NA 0.08, WD 6.2, FN 26,5)	
Objective 4x	Olympus UPLFLN 4x (NA 0.13, WD 17, FN 26.5)	
Objective 10×	Olympus UPLFLN 10x (NA 0.3, WD 10, FN 26.5)	
Objective 20x	Olympus UPLFLN 20x (NA 0.5, WD 2.1, FN 26.5)	
Objective 40x	Olympus UPLFLN 40x (NA 0.75, WD 0,51, FN 26.5)	
Excitation sources	UV 395-nm LED 470 to 620-nm	
Excitation filters (UV) 395 to 400-nm	FF01-377/50	
Emission filter Hoechst/DAPI	FF01-452/45	
Emission filter FITC/GFP	FF01-530/43	
Emission filter YFP	FF01-542/27	
Emission filter Cy3	FF01-585/40	
Emission filter Texas Red	FF01-628/32	
Emission filter Cy5	FF01-692/40	
Blot roller	8.4 cm-wide PTFE roller with stainless steel handle	Thermo Scientific
Blotting chamber	Mini Trans-Blot Cell	Bio-Rad
Casting stand clamp kit with casting frames, casting stand gaskets, spacer plates with 1.0 mm integrated spacers, short plates, 10-well combs, and gel releasers	Mini-PROTEAN Tetra Cell Casting Module	Bio-Rad
Cell counter and analyser	CASY Model TTC	Roche
Cell dissociation sieve – tissue grinder	CD1-1KT	Sigma
Chemiluminescence imager	ChemiDoc MP	Bio-Rad

List continued on next page

Table 20: Continued from previous page

Clean benches		
Biological Safety Cabinet – vertical flow	Safe 2020 1.5 Class II	Thermo Scientific
Biological Safety Cabinet – horizontal flow	HERAguard HPH 9	
Electrophoresis chambers		
Vertical unit (protein analysis)	Mini-PROTEAN Tetra Cell, 4-gel	Bio-Rad
Horizontal unit (cDNA analysis)	Perfect Blue Maxi L	Peqlab
Fast Real-Time PCR system with 384-well block module	7900HT	Applied Biosystems
Fine surgical instruments		
Fine curved forceps #7	91197-00	FST by Dumont
Standard Scalpel Handle #4 Solid	10004-13	
Super fine tip forceps #5SF	11252-00	
Mini forceps #M5S	11200-14	
Scissors Vannas-Tübingen straight	15003-08	
Surgical sharp-blunt curved scissors	14004-14	
Surgical sharp-blunt straight scissors	14001-14	
Student surgical straight scissors	91402-12	
Fine scissors Wagner straight sharp	14068-12	
Student fine curved sharp scissors	91461-11	
Haemostats Kelly straight serrated	13018-14	
Flow cytometer	LSRII SORP	BD Biosciences
Laser 561-nm, 50mW (D, 505 LP, 530/30, FITC)	Sapphire, Coherent	
Laser 405-nm, 100mW (B, blank, 440/40, Pacific Blue)	Cube, Coherent	
Laser 355-nm, 20mW (B, blank, 450/50, DAPI/Hoechst)	Genesis, Coherent	
Full-spectrum spectrophotometer	Nanodrop ND 1000	peqLab
Gel caster unit for electrophoresis	Mini Sub-Cell GT	Bio-Rad
Gel documentation system	GelDoc XR	Bio-Rad
Gradient thermal cycler PCR	5331 MasterCycler	Eppendorf
Incubator	C200	Labotec

List continued on next page

Table 20: Continued from previous page

Inverted fluorescence microscope setup	IX81	Olympus
Light source	Xenon-Arc burner MT10_D	
Microscope controller	IX2-UCB-2	
Air Conditioning Unit	ACUO4E-0023	
Camera	CAM-XM10-T	
Objective 4x	UPlanFLN4xPh	
Objective 10×	UPlanFLN10×Ph	
Objective 20x	UPlanFLN20xPh	
Excitation filter 360-nm	DAPI BP 403/12	
Excitation filter 492-nm	FITC BP 492/18	
Excitation filter 572-nm	TxRed BP 572/23	
Emission filter blue detection	U/B/G triple-band pass	
Emission filter green detection	U/B/G triple-band pass	
Emission filter red detection	U/B/G triple-band pass	
Inverted transmitted-light microscope	Primovert 491206-0001-000	Zeiss
Objective 4x	Plan-Achromat 4x/0.10 for Primo	
Objective 10×	Plan-Achromat 10×/0.25 for Primo	
Ocular 10×	Eyepiece WF 10x/20 Br. foc. for Primo	
Microplate reader	Flex Station 3	MDS Analytical Technologies
Multi-well plate recording device	Costume-made*	UMG
with camera	MC2586	Mikrotron
Power supply		
Unit (protein analysis)	Power PAC HD	Bio-Rad
Unit (low voltage – cDNA analysis)	Power Pack P25	Biometra
Rheometer	RSA-G2	TA Instruments
Arm adapter	Custom-made*	UMG
Bath chamber	Custom-made*	UMG
Hooks	Custom-made#	
Heating system (Arduino nano)	Custom-made*	UMG

List continued on next page

Table 20: Continued from previous page

Sample disruption device	TissueLyser II	
Adapter set (2×24)	TissueLyser adapter set	Qiagen
Stainless steel beads (⌀ 5 mm)	69989	
Stereoscope	Lumar.V12	
Power unit	EMS-2/SYCOP	
Objective 0.8x	NeoLumar S 0.8xFL	Zeiss
Camera	AxioCam MRc	
Halogen light source	KL2500 LCD	
Stereoscope	M80	
Cold light source	KL200 LED	
Transmitted light base	MDG33	Leica
Stage heating system	MATS-TypeTL	
Objective 1.0x	ACHRO	
Oculars 10×/23	Leica 10450023	
Tissue dissociator	gentleMACS	
C Tubes	130-093-235 gentleMACS C Tubes 130-093-237	Miltenyl Biotec

* Dr. Tim Meyer, is the author of the indicated devices.
# Item designed by Dr. Tim Meyer and Gabriela L. Santos.

3.1.6. Software

Several software programs were used to record and analyse most of the data. Arduino was coded in house to support the heating system attached to the bath chamber of the rheometer. The table below lists all the software packages and their manufacturers.

Table 21. List of software programs.

Software/version	Manufacturer	City/State	Country
FACS DIVA™ software	BD Biosciences	Heidelberg	Germany
GraphPad Prism 6 & 7	GraphPad Software Inc.	La Jolla, CA	USA
ImageJ	NIH	Bethesda, MD	USA
Microsoft Office	Microsoft Corporation	Redmond, WA	USA

List continued on next page

Table 21: Continued from previous page

Quantity One 4.6.5	Bio-Rad	Hercules, CA	USA
SDS 2.4	Applied Biosystems	Carlsbad, CA	USA
Xcellence pro	Olympus	Muenster	Germany
AxioVision	Carl Zeiss	Jena	Germany
Image Lab	Bio-Rad	Hercules, CA	USA
ND-1000 V3.8.1	NanoDrop Technologies	Wilmington, DE	USA
Soft Max Pro5.4	Molecular Devices	San Jose, CA	USA
Cellavista 2.2	SynenTec	Elmshorn	Germany
Trios	TA Instruments	New Castle, DE	USA
Flowing Software 2.5.1	Perttu Terho, Turku Bioscience	Turku	Finland
microDisplay 5.4.1.2	Silicon Software	Mannheim	Germany
Arduino 1.8.5	Arduino AG	Boston, MA	USA

3.2. Methods

3.2.1. Animal care and housing

Wild type Wistar-Kyoto rats were bred and housedin line with the guidelines (§4 Absatz 3 Deutsches Tierschutzgesetz) of the institutional animal care and use committee Niedersächsisches Landesamtes für Verbraucherschutz und Lebensmittelsicherheit (LAVES, Germany). All animals were housed at the animal facility of the University Medical Center Göttingen, at a constant controlled temperature (22±2 °C) and humidity (55±5 %), under a 12:12 h light/dark circadian cycle with access to food and water *ad libitum*.

3.2.2. Cell culture – cell and tissue biology procedures

All the work involving cell culture was performed according to standard sterile techniques and safety rules. The material and reagent solutions used for all cell work were sterile. A class II biological safety cabinet, with HEPA (High-efficiency particulate air) filtered laminar airflow was used to handle the cell culture work, ensuring the blower was running for at least 10 min prior use. All surfaces, as working bench, bottles, tubes, packages of sterile material and devices were sterilized with 70% ethanol in a sterile hood, immediately before initiating the work. With no exception, all steps within this section entailing direct air exposure of cell culture reagents or cells were performed inside a sterile hood.

All reagent solutions were stored and handled according to manufacturer's instructions. To adjust its temperature, except when specifically stated otherwise, the reagent solutions were placed at room temperature for at least 30 min before use.

NRCF were cultured in sterile supplemented DMEM GlutaMAX as indicated in **Table 7**, hereafter referred as NRCF growth medium. Normal human cardiac fibroblasts from

the ventricle (hCF) were cultured in sterile supplemented Fibroblast Growth Media 3 as indicated in **Table 7**, hereafter referred as FGM3 growth medium or just FGM3. Media was always prepared at least 30 min before use to assure complete homogeneous distribution of the components and supplements. Unless otherwise stated, volumes of growth media, washing buffer and dissociation solution for various size culture vessels were used according to **Table 22**. Cell cultivation was carried in a humidified incubator at 37°C and 5% CO_2.

Control of viability, cell diameter and cell counting for analysis or specific seeding numbers were assessed by electrical current exclusion using the Casy TTS system as described in *section 3.2.2.4*.

Table 22. Various sizes of culture vessels and corresponding volumes (mL).

Vessel Type	Washing Solution (DPBS)	Dissociation Solution	Growth Media
10 cm dish	6	4	10
15 cm dish	15	10	25
6-well plate	1	0.7	3
12-well plate	0.4	0.3	2
24-well plate	0.2	0.2	1
T-75 flask	8	5	13
T-175 flask	18	12	30

3.2.2.1. Isolation of primary neonatal rat cardiac fibroblasts (NRCF)

3.2.2.1.1. Cardiac cells isolation

NRCF were isolated using the Neonatal Heart Dissociation Kit, according to the manufacturer's instructions. In brief, forty Wistar rats from postnatal day zero to day three (P0-P3), following euthanasia by decapitation, were submitted to partial thoracotomy to expose the heart. Pressure was applied between the shoulder blades

towards the chest, thereby forcing the heart pass the ribs for scalpular dissection. The excised hearts were placed into ice cold CBFHH buffer to remove excessive blood. Into a new dish containing CBFHH buffer, the atria, vascular pedicle and remaining connective tissue were dissected, and the remaining ventricles were washed twice to remove remaining blood using CBFHH buffer. The ventricles were subsequently sliced into roughly 1 mm^3 pieces and further minced into smaller fragments. The total volume of mincing buffer and tissue pieces was distributed into two gentleMACS C tubes and topped with 2.5 mL per tube of digesting enzymes mixture prepared beforehand as follows: for 40 neonatal rat hearts, after incubating 125 µL Enzyme P with 4.6 mL Buffer X for 5 min at 37°C of, a second mixture of 50 µL Buffer Y, 25 µL Enzyme A and 200 µL Enzyme D was added to the first). Tissue dissociation was carried by three cycles of a two-step procedure: enzymatic digestion for 15 min at 37°C and mechanical dispersion on a gentleMACS dissociator using the gentleMACS program htumor3.01. Dislodged cells in the gentleMACS C tubes were collected in 20 mL of NKM medium and passed resuspended through 250 µm pore stainless steel mesh into a 50 mL tube, in order to remove undigested tissue and debris clumps. The flow-through was centrifuged at 60 ×g, for 20 min at 4°C, and collected cells were resuspended in NKM medium. In order to avoid cell damaging, cell suspensions were always transferred/resuspended using a 10 mL serological pipette with wide opening.

3.2.2.1.2. Cardiac fibroblasts fraction purification – Percoll density gradient centrifugation.

The cell suspension was further processed to purify the fraction of CF by a two-step discontinuous Percoll gradient. Four 15 mL centrifugation tubes were prepared with a two-layer gradient, consisting of 4 mL transparent 65% Percoll solution underneath a

3 mL phenol red-containing 45% Percoll solution, according to manufacturer's instructions. Cell suspension prepared previously was sediment a second time at 300 ×g for 5 min at room temperature. Collected cells were resuspended in 8 mL 1× DPBS containing 100 U/mL penicillin and 100 µg/mL streptomycin. The cell suspension was finally loaded onto the gradient as the top layer, and immediately centrifuged at 1400 ×g and 4°C for 45 min, using standard acceleration conditions and deceleration speed 0, with a swing bucket rotor. NRCF enriched fraction could subsequently be removed from the newly formed layer on top of the red-coloured Percoll phase as represented in **Figure 8**.

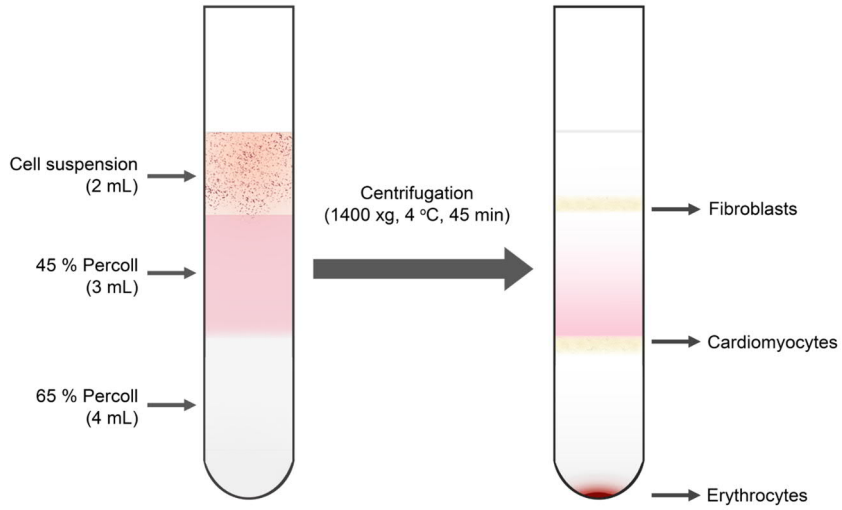

Figure 8. Schematic representation of Percoll density gradient separation of cells. (Original illustration, Gabriela L. Santos)

Collected material was pooled, diluted with 4 volumes in NRCF growth medium and centrifuged at 300 ×g for 5 min and 4°C, for removing any traces of Percoll. The cell pellet was resuspended in NRCF growth medium and cell number and viability were assessed. NRCF enriched fraction was then seeded at a density 5.52×10^4 viable cells per cm^2 on 15 cm diameter cell culture dishes with 0.2 mL/cm^2 of NRCF growth medium and incubated for 45 min in a humidified incubator (37°C, 5% CO_2). In this conditions, mainly CF are able to attach to the culture dish surface [395]. The plates

were then firmly tapped whereby the unattached cardiomyocytes, smooth muscle and endothelial cells could be removed with three following washing steps. Fresh medium was added and changed every second day thereafter. Subcultivation procedures can be found in the *section 3.2.2.2.*

3.2.2.2. Two-dimensional (2D) culture of cardiac fibroblasts and experiments

3.2.2.2.1. Proliferating cardiac fibroblasts

3.2.2.2.1.1. Sub-cultivation of cardiac fibroblasts

Cell density was controlled by light microscopy. Once achieved confluency of 70-90% (approximately within 4-5 days), cells were passaged onto new vessels, typically 15 cm dishes for NRCF and T-75 or T-175 flasks for hCF. For that, medium was aspirated from the vessel, ~0.1 mL/cm^2 DPBS was added to it and the vessel carefully rocked for 15 s to wash the cells. After removing the DPBS by aspiration, ~0.07 mL/cm^2 dissociation reagent (0.25% trypsin for NRCF and TrypLE for hCF) was used to detach the cells. Followed a 3 to 5 min incubation at 37°C (NRCF) or room temperature (hCF) until cells detached from the culture surface. Detachment was monitored under an inverted light microscope. The side of the vessel was gently tapped to loosen eventual remaining attached cells. Enzymatic activity of dissociation reagent was neutralized with addition of 1:1 NRCF or FGM3 growth medium volume, respectively. The cells were dispersed by carefully pipetting up and down with a 10 mL serological pipette and cell number and viability were measured as described in *section 3.2.2.4*. For subsequent 2D experiments, methods description continuous on *section 3.2.2.2.1.2*. For subsequent 3D experiments, methods description continuous on *section 3.2.2.3.3*. To maintain a proliferative culture, cells were plated in new cell culture vessels at a seeding density of 2.76×10^4 cells per cm^2 (NRCF) and 1.6×10^4 cells per cm^2 (hCF) in a total volume of

~0.17 mL/cm^2 prewarmed NRCF or FGM3 growth media, respectively. After gently rocking each culture vessel to evenly distribute the cells, those were directly placed in a 37°C, 5% CO_2 humidified incubator for cell attachment. Medium was replaced 16-24 h after seeding, and every second day thereafter.

3.2.2.2.1.2. Plating and treating cardiac fibroblasts

NRCF were used at passages P2 and P3, and hCF were used at passages P4 and P5. Cells were passaged at least once between isolation (NRCF) or thawing (hCF) and the start of an experiment. When 80% confluency was reached, proliferating cells were detached according to the subcultivation method described in *section 3.2.2.2.1.1*. Cells were then seeded with NRCF or FGM3 growth media according to **Table 23** and **Table 24**, respectively.

Table 23. Seeding number of NRCF and application for cell culture experiments.

Culture vessel	Seeding number	Application
15 cm dish	2.0×10^6	Cell lysates (protein isolation) [a]
10 cm dish	5.0×10^5	Cell lysates (protein isolation) [a]
6 cm dish	3.0×10^5	Flow cytometry
6-well plate	1.4×10^5	Cell lysates (nucleic acid isolation) [a]
12-well plate	4.0×10^4	Adhesion and Apoptosis
24-well plate	1.0×10^4	Proliferation (microscopy)

[a] Seeding numbers were adjusted accounting for cell loss/ in some treatment groups, so that by the end of the treatment period a uniform protein and RNA yields were readily obtainable from all groups.

Cells treatment was initiated 24 h after seeding with growth medium supplemented with the corresponding drug or its diluent as a control, and replaced every other day thereafter, unless noted otherwise. Total growth media volumes were used according to **Table 22** and used chemicals and correspondent concentrations are described in **Table 11**. Further specifications for cell proliferation, adhesion, apoptosis and bi-

nucleation/cell area assays are noted in the respective *sections 3.2.2.2.2., 3.2.2.2.3., 3.2.2.2.4.,* and *3.2.2.2.5.* For cell cycle analysis cells were cultured/treated for 5 days. After treatment, cells were detached identically to what is described for the subcultivation method (*section 3.2.2.2.1.1.*) and resuspended in DPBS containing 5% FCS for immediate cell number, viability and diameter assessments as described in *section 3.2.2.4.,* and further fixed as described in *section 3.2.2.5.* For protein and RNA isolation, the cells were treated for 48 hours or 5 days, and the harvesting procedures after treatment are described in *sections 3.2.3.1.* and *3.2.4.1.*, respectively.

Table 24. Seeding number for hCF and application for cell culture experiments.

Culture vessel	Seeding number	Application
10 cm dish	7.5×10^5	Cell lysates (protein isolation) [a]
T-75 flask	2.5×10^5	Flow cytometry
6-well plate	1.2×10^5	Cell lysates (nucleic acid isolation) [a]
12-well plate	5.0×10^4	Adhesion
24-well plate	5.0×10^3	Proliferation/ bi-nucleation (microscopy)

[a] Seeding numbers were adjusted accounting for cell loss/ in some treatment groups, so that by the end of the treatment period a uniform protein and RNA yields were readily obtainable from all groups.

3.2.2.2.1.3. Freezing cardiac fibroblasts

In order to preserve cell viability after thawing, cells were frozen at low passage number, P0 and P1 for NRCF, and from P1 to P3 for hCF. Before freezing, cells were kept in culture for a maximum of 3-4 and 5-6 days, respectively. Second consideration was harvesting the cells when culture reaches about 80% confluency, so that the cells are in the logarithmic growing phase when processed for cryopreservation.

Cells were detached likewise as described in the subcultivation methods (*section 3.2.2.2.1.1.*). After the dissociation reagent being neutralized, the cells were dispersed by carefully pipetting up and down with a 10 mL serological pipette and transferred into a centrifugation tube. Cell number and viability were measured and the tube

containing the cells was subsequently centrifuged for 5 min at 300 ×g, room temperature. The pelleted cells were carefully resuspended in cryopreservation growth medium (see **Table 7**), prepared freshly beforehand, in order to have single cell suspension with 4×10^6 - 8×10^6 cells/mL (NRCF) or 1×10^6 - 2×10^6 cells/mL (hCF). Cell suspension was afterwards transferred into appropriate cryovials (1 mL/vial). An optimal cooling rate of -1°C/min is pivotal to achieve the best possible recovery post-thawing. Thereby, an isopropanol freezing container (Mr. Frosty) was used. The cryovials were immediately inserted in a room temperature Mr. Frosty and placed at -80°C for 4-6 h (NRCF) or 12-20 h (hCF). After, the cryovials were transferred directly to a -152°C freezer for long-term storage.

3.2.2.2.1.4. Thawing cardiac fibroblasts

Beforehand, a culture vessel (typically 15 cm dish for NRCF, and T-75 or T-175 flasks for hCF) was prepared with ~0.17 mL/cm^2 of prewarmed NRCF or FGM3 growth medium, respectively. For thawing purposes was ensured that (independently on the vessel format) the used volume of growth medium was at least 9 times the cryopreserved cell suspension volume in order to reduce the percentage of DMSO to a maximum of 1%. At a time, a cryopreserved vial of cells was taken from -152°C storage and the vial cup turned a quarter to relieve air pressure, then re-tightened. The cells were quickly thawed by placing the lower half of the vial in a 37°C water bath for approximately 2 min, with slow circular motion until when only a small amount of ice was left in the vial. Using a 2 mL serological pipette, cells were subsequently resuspended thrice and transferred to the culture vessel previously prepared with the corresponding growth medium. Starting cultures were seeded at a density of 2.76×10^4-5.52×10^4 cells/cm^2 (NRCF) or 7.0×10^3 cells/cm^2 (hCF). The culture vessel was gently

rocked to evenly distribute the cells, and placed in a 37°C, 5% CO_2 humidified incubator for cell attachment. Medium was replaced 24 h after seeding to remove all traces of DMSO, and every second day thereafter until they reached 70-90% confluency, according to the subsequent subcultivation method (*section 3.2.2.2.1.1.*).

3.2.2.2.2. Proliferation assay

NRCF and hCF proliferation was evaluated over a time-course of 6 or 3 days, respectively. Treatments were conducted according to *section 3.2.2.2.1.2.* For this particular assay, the treatment started 24 h after seeding and the growth media with treatment/vehicle were replaced thereafter on a daily basis. At days 0, 1, 2 and 3 or 6, counting from the 24 h after seeding, cells were washed once with PBS and fixed with 0.1 mL/cm^2 of 4% PFA solution for 15 min at room temperature. After two washes with PBS, cells were kept in the same buffer at 4°C until following measurement. To analyse the cell number, cells were stained with 0.1 mL/cm^2 of 10 µg/mL Hoechst 33342 in PBS for 30 min at room temperature on a 3D rocker shaker, protected from light. Three more washes with PBS followed and finally cell nuclei number was assessed by automated counting using the cell imager Cellavista system. For analysis, it was used a modified procedure of the manufacturer's standard procedure 'Cell Nuclei Experiment'. In short, Nunc delta surface 24-multi well plate type was defined onto the software according manufacturer's instructions. Using the application 'cell nuclei type V1.0', the samples were excited by a UV 395-nm source, using a 452/45-nm filter via a 395-nm-cutoff dichroic mirror and through a 4× objective. For automated quantitative purposes light intensity was used at 100% with 350 ms exposure time and gain 24×, and offset adjusted between -0.12 to -0.14 to allow optimal sharpness of the cell nuclei

for accurate counting. Changes in cell number were calculated relatively to the estimated cell number measured on day zero.

3.2.2.2.3. Adhesion assay

NRCF were seeded in 6-well plates and treated as described in *section 3.2.2.2.1.2*. After 24 h of treatment, cells were then re-plated into 12-well plates (**Table 23**), with uncoated or collagen type I-coated culture surface. Multi-well plates were coated by incubating 0.1 mL/cm^2 of 50 µg/cm^2 collagen type I in DPBS for 1 h at 37°C, followed by one wash with DPBS and let to dry. After seeding, at 0, 20, 40 and 60 min ten bright-field images per condition were acquired using the time-lapse function with a 10× objective (auxiliary magnification factor kept at 1×) of the Olympus IX81 inverted fluorescence microscope setup, equipped with a humidified climate chamber set to 37°C and 5% CO_2. The number of adhered cells was manually accessed using ImageJ and expressed in percentage relative to the number of seeded cells.

3.2.2.2.4. Annexin V/propidium iodide staining assay for apoptosis analysis

The treatment of NRCF was carried as described in *section 3.2.2.2.1.2.*, with the exception that 24 h after seeding, cells were pre-conditioned for 24 h with reduced serum (2%)-containing NRCF growth medium before initiating the 48 h treatment with H1152P and respective control. As an additional positive control, NRCF were treated with 3 µM staurosporine in NRCF medium only during the last 3 h of the 48 h of treatment period. After the treatment, media containing treatments was discarded and cells were washed twice with DPBS. NRCF were immediately stained using the kit Annexin V-FLUOS Staining according to the manufacturer's instructions. Briefly, cells were incubated with 0.1 mL/cm^2 of 1:50 Annexin V-Fluorescein (FLUOS), 1:50

propidium iodide (PI) and supplemental 10 µg/mL Hoechst 33342 in HEPES buffer, for 15 min at room temperature, in the dark, on a 3D rocker shaker. Staining solution was replaced by HEPES buffer and stained cells were imaged using a 10× objective (auxiliary magnification factor 1.6×) on the Olympus IX81 inverted fluorescence microscope setup, equipped with a humidified climate chamber set to 37°C and 5% CO_2. Annexin V-Fluorescein, PI and Hoechst 33342 stainings were imaged by using the bandpass filter set for FITC (lamp intensity 2 and 420 ms exposure time), Texas Red (lamp intensity 1 and 3100 ms exposure time) and DAPI (lamp intensity 2 and 110 ms exposure time), respectively. Cells were manually counted with the support of ImageJ software. Apoptotic cells binding Annexin V-Fluorescein showed green staining in the plasma membrane. Necrotic cells that have lost membrane integrity showed co-staining with PI (red) throughout the nucleus and a halo of Fluorescein (green staining) on the cell surface. Total amount of cells was accessed by cell nuclei stained with Hoechst 33342. Percentage of apoptotic and necrotic cells was calculated for 'Annexin V-Fluorescein positive/PI negative' and 'Annexin V-Fluorescein positive/PI positive' cells together divided by the total amount of cells.

3.2.2.2.5. Bi-nucleation and cell area analysis in 2D cultures

The treatment of NRCF was carried as described in *section 3.2.2.2.1.2.* After 48 h, the cells were washed with PBS and fixed with 4% PFA solution for 15 min. For hCF, the samples prepared in *section 3.2.2.2.2.* were used. In both cases, cells were incubated for 3 min in permeabilization buffer. Followed an incubation in blocking buffer for 1 h, on a 3D rocker shaker, at room temperature. Actin cytoskeleton was stained with 0.5 µg/mL FITC-labelled phalloidin and the nuclei of NRCF were additionally stained with 1 µg/mL DAPI in PBS. Staining took place for 1 h at room temperature on a 3D

rocker shaker and protected from light. Finally, the cells were washed thrice with PBS and imaged on the Olympus IX81 inverted fluorescence microscope setup, using a 10× objective (auxiliary magnification factor kept at 1×). FITC-labelled phalloidin and DAPI stainings were imaged by using the bandpass filter set for FITC (lamp intensity 2 and 420 ms exposure time) and DAPI (lamp intensity 2 and 110 ms exposure time), respectively. Bi-nucleated cells were counted and cell size analysis was performed with the free hand tool of ImageJ.

3.2.2.3. Three-dimensional (3D) cultures of cardiac fibroblasts and experiments

3.2.2.3.1. Stiff moulds – mounting, shape and dimensions

Ring-shaped casting moulds, in this thesis also referred as stiff moulds, where prepared in glass 60 mm diameter petri dishes. The method for the production of the moulds was adapted from Zimmermann *et al.* (2002) [396] and is graphically summarized in **Figure 9**. The tubings used in the assembly are listed on **Table 18**. In short, a 2 mm thick layer of polydimethylsiloxane (PDMS) and curing agent, prepared according to the Sylgard 185 silicon elastomer kit's manufacturer, was poured into the petri dish and let harden for 24 h at 70°C to create a silicon bed. PTFE cylinders were placed onto the silicon bed to serve as spacers while a second layer of silicon mixture was poured into the culture dish around the cylinders. After hardening of the silicone, the PTFE spacers were removed leaving hollow cavities. One silicon tube/cord was concentrically glued with silicone mixture to the bottom of each cavity. Those served to hold removable rods (poles) which *per se* yielded ring-shaped wells. For reuse, the moulds were washed with water, autoclaved at 121°C and reused multiple times. To assure maintenance of its chemical and mechanical performance, the PDMS poles were often replaced.

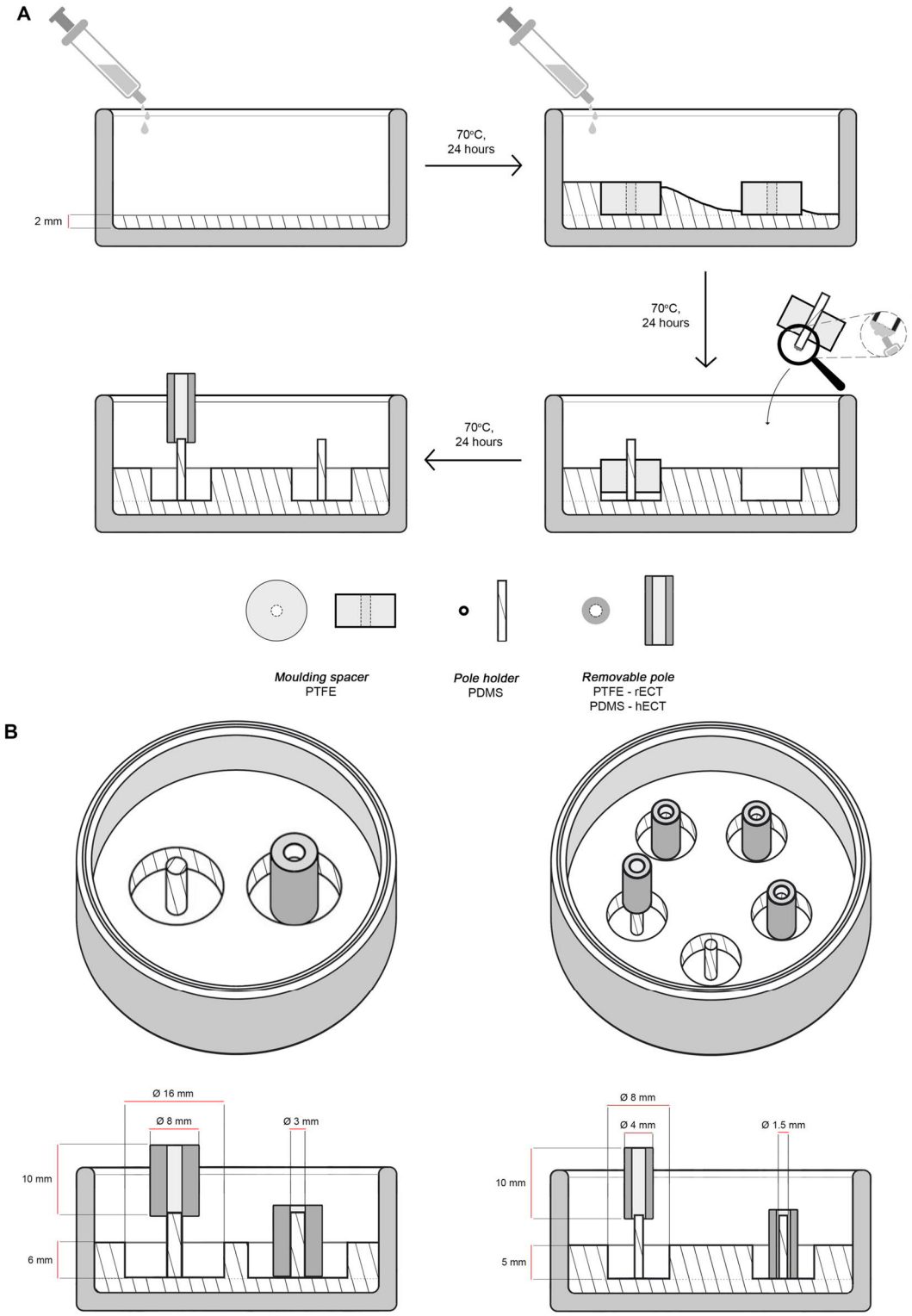

Figure 9. Schematic representation of the casting moulds assembly.
A) Ring-shaped moulds were made by imprinting polytetra-fluoroethylene (PTFE) molding spacers (16 mm diameter, rECT, or 8 mm diameter, hECT) in polydimethylsiloxane (PDMS, silicone) poured into glass dishes (diameter 60 mm). After cure of the PDMS, a hollow cavity was formed. A PDMS pole holder (3 mm diameter, rECT, or 1.5 mm diameter, hECT) was fixed concentrically with silicon mixture and used to hold removable poles (8 mm diameter PTFE tubes, rECT, and 4 mm diameter silicone tubes, hECT) [366]. **B)** Technical drawings of casting mould assembly for 2 rECT with 900 µL volume (left) and 5 hECT with 180 µL volume (right). The dimensions of all components of the moulds are itemized. (Original illustration, Gabriela L. Santos)

3.2.2.3.2. Flexible moulds – shape and dimensions

The flexible casting moulds consist of a 48 multi-well plate format. It was developed at the Institute of Pharmacology and Toxicology by Tim Meyer [397], patented by University Medical Center Göttingen (DE102016110328B3) and it is marketed by myriamed GmbH.

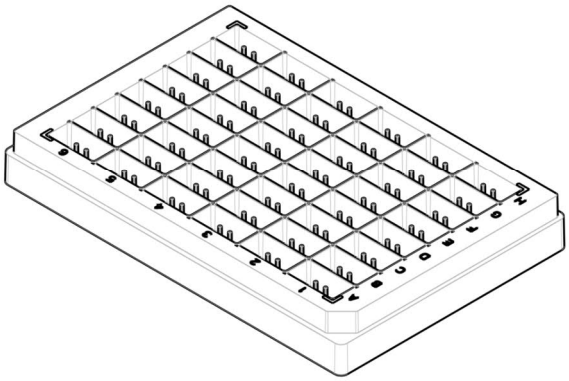

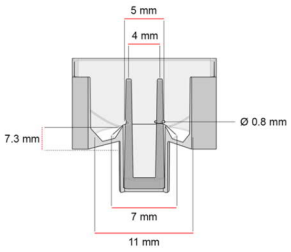

Material	dForce (mN/mm)	Non-stretched Force (mN)
TM4	0.7	0.5
TM5	1.5	0.7
TM6	2.4	0.8
TM7	3.3	1.2
TM8	8.1	1.7
TM9	12.2	1.9

Figure 10. Technical drawing of the multi-well plate for casting of hECT.
Multi-well screening plate for generation of 48 hECT with 180 µL volume. Each well comprises an upwardly open annular channel, delimited at an outer circumference by a wall that allows a total volume capacity of at least 500 µL to the full well. The inner circumference thereof is delimited by a shorter wall that holds two retaining elements (brighter dye-containing poles) at the plate main body. The flexible poles have a free horizontal distance to one another and are elastically connected at the base. Different material composition of the poles defines specific poles stiffnesses. The patent of the plate is assigned to UMG (DE102016110328B3) [397] and it is a product of myriamed GmbH. (Adapted from original illustration provided by Dr. Tim Meyer.)

Each well comprises an upwardly open annular channel, delimited at an outer circumference by a wall that allows a total volume capacity of at least 500 µL to the full well. The inner circumference thereof is delimited by a shorter wall that holds two retaining elements at the plate main body. Those are the flexible poles with a free horizontal distance to one another and are elastically connected at the base. Different material composition provides the poles with specific spring constants for fine-tuning tissue properties and are depict in **Figure 10**.

3.2.2.3.3. Generation of engineered connective tissues (ECT)

As described in the literature, collagen fibrillogenesis and gelation greatly depend on ionic strength, pH and temperature. Optimal gelation occurs at physiologic conditions and thus adjusting these parameters is crucial and highly time sensitive for tissue preparation. To avoid early collagen gelation, all reagent solutions necessary for this method are required to be ice-cold including the material such as pipette tips, serological pipettes and tubes. Concentrated DMEM is necessary to counteract changes in osmolarity of the collagen pre-gel solution and to increase the ionic strength. Therefore, filtered 2× DMEM was prepared beforehand according to **Table 7**. It is also important to note that the pH of collagen hydrogels is dependent on factors as neutralization agent to acid-solubilized collagen, buffer type and preparation, dilution ratio of collagen in hydrogel, and even absolute collagen concentration, and it impacts collagen matrixes assembly [398, 399]. Thereby, pH titration is fundamental and must be verified for each individual collagen batch before establishing a standard cell-collagen hydrogel master mix composition. The gelation process of the acid-solubilised collagen ensues once the ionic content is increased by the addition of DMEM and the pH is neutralized. This process of collagen self-assembly is also highly dependent on temperature, which affects fiber bundling and pore size of the collagen network [400]. Therefore, the tissue preparation process must be thoroughly fast to avoid gelation at sub-optimal temperature. This may ultimately influence the cell component and thereupon the structure and mechanical properties of the tissues.

3.2.2.3.3.1. Rat engineered connective tissues (rECT)

After isolation, NRCF from a 2D culture at P2 (*section 3.2.2.2.1.1.*) were used to generate rECT. Cells were harvested according to the subcultivation methodology

described in *section 3.2.2.2.1.1.*, and after cell number and viability measurement as described in *section 3.2.2.4.*, the cell suspension was centrifuged for 5 min at 300 ×g and 4°C. Pelleted cells were resuspended in NRCF growth medium and kept on ice until further use. Note that the volume of NRCF growth medium for resuspension varies according not only to the total number of cells pelleted, but also to the concentration of the collagen stock. Calculations were made considering a total volume of 900 µL per rECT. Detailed composition of the cell-collagen hydrogel can be found in **Table 25**.

Table 25. Composition of cell-collagen hydrogel for rECT.

Master mix components	**Volume per rECT (µL)**	**Volume per rECT (µL)**	**Volume per rECT (µL)**
1.2 mg rat tail collagen (3.81 mg/ml in 0.02 N acetic acid) [a]	314.96	–	–
1.2 mg rat tail collagen (3.96 mg/mL in 0.02 N acetic acid) [b]	–	303.03	–
1.2 mg rat tail collagen (3.00 mg/mL in 0.02 N acetic acid) [b]	–	–	400
2× DMEM	314.96	303.03	400
0.1 N NaOH [c]	51.3	49.36	65.15
1.7×10^6 cells (Cell suspension 7.77×10^6/mL) [d]	218.78	–	–
1.7×10^6 cells (Cell suspension 6.95×10^6/mL) [d]	–	244.58	–
1.7×106 cells (Cell suspension 48.78×10^6/mL) [d]	–	–	34.85
Total volume per rECT [e]	900	900	900

[a] Self-prepared rat tail collagen solution supplied by the host institution.
[b] Commercial rat tail collagen solution used alternatively to the prepared in house.
[c] To neutralise the pH to 7.4..
[d] Resuspended cells in NRCF growth medium.
[e] Extra volume (~15%) facilitates pipetting exact volumes of the viscous ECT mixture.

To proceed with the cell-collagen hydrogel preparation on ice, 1.2 mg rat tail collagen type I (purified in-house or commercial) per rECT were buffered with equal volume of 2× DMEM. The pH was neutralized with 0.1 N NaOH, using the color transition from yellow to red of phenol red as an indicator. Then the calculated volume of NRCF

growth medium containing 1.7×10^6 NRCF per rECT was added dropwise and in circular motion to the buffered collagen hydrogel, ensuring a homogeneous dispersion of cells without forming foam. The mixture was finally cast into circular self-made moulds (**Figure 9**) and allowed to harden for 45 min to 1 h in a humidified incubator at 37°C and 5% CO_2. Thereafter, 5 mL of NRCF growth medium with or without treatment was added to each glass dish containing two casting moulds and the tissues were cultured for 5 days. The medium with or without additives was changed every day. For the specific treatments, used concentrations are outlined in **Table 11**.

3.2.2.3.3.2. Human engineered connective tissues (hECT)

The cell-collagen hydrogel for hECT casting was prepared similarly but not identical to the rECT as described above. In short, hCF from 2D cultures at P4 were harvested according to the subcultivation methodology described in *section 3.2.2.2.1.1.,* when 80% confluency was reached. After cell number and viability were measured as described in *section 3.2.2.4.*, the cell suspension was centrifuged for 5 min at 300 ×g and 4°C. Collected cells were then resuspended in FGM3 according to **Table 26** and kept on ice until further use. Collagen hydrogel mixture was prepared on ice by buffering 0.3 mg bovine collagen type 1 per tissue with equal volume of 2× DMEM and neutralizing its pH with 0.2 N NaOH until phenol red transitioned from yellow to red. Dropwise and in circular motion, the prepared cell suspension (corresponding to 0.75×10^6 CF per tissue) was then added to the collagen hydrogel mixture. The final volume of the mixture was 180 µL per tissue. Detailed composition of the cell-collagen hydrogel (master mix) can be found in **Table 26**.

The cell-collagen hydrogel was swiftly pipetted into two types of casting moulds, stiff (**Figure 9**) and flexible (**Figure 10**). Because the flexible casting mould displays two

Table 26. Composition of cell-collagen hydrogel for hECT.

Master mix components	Volume per hECT (µL)	Volume per hECT (µL)	Volume per hECT (µL)	Volume per hECT (µL)
0.3 mg bovine collagen (6.10 mg/mL in 0.01 N acetic acid) [a]	49.18	–	–	–
0.3 mg bovine collagen (6.49 mg/mL in 0.01 N acetic acid) [a]	–	46.23	–	–
0.3 mg bovine collagen (6.84 mg/mL in 0.01 N acetic acid) [a]	–	–	43.86	–
0.3 mg bovine collagen (6.91 mg/mL in 0.01 N acetic acid) [a]	–	–	–	43.42
2× DMEM	49.18	46.23	43.86	43.42
0.2 N NaOH [b]	3.33	3.13	2.97	2.94
0.75×10^6 cells (Cell suspension 9.588×10^6/mL) [c]	78.31	–	–	–
0.75×10^6 cells (Cell suspension 8.888×10^6/mL) [c]	–	84.42	–	–
0.75×10^6 cells (Cell suspension 8.400×10^6/mL) [c]	–	–	89.31	–
0.75×10^6 cells (Cell suspension 8.311×10^6/mL) [c]	–	–	–	90.23
Total volume per hECT [d]	180	180	180	180

[a] Commercial bovine collagen (Collagen Solutions) was used from different lots along the time.
[b] To neutralise the pH to 7.4.
[c] Resuspended cells in FGM3 medium.
[d] Proportional extra volume of each component (~15%) facilitates pipetting exact volumes of the viscous ECT mixture.

flexible poles elastically interconnected, they allow tissue contraction over time. For that reason, the tissues are subjected to a lower tension (**Figure 11**A) comparing to the ones prepared in stiff moulds. Tissues prepared in circular self-made moulds with a stiff central and uncompressible rod encounter higher resistance that prevents them from contracting further. Therefore, in the stiff mould tissues are under higher tension forces (**Figure 11**B). After casting of the cell-collagen hydrogel into the moulds, the tissues were allowed to solidify for 45 min to 1 h in a humidified incubator at 37°C and 5% CO_2. Then, FGM3 was added with the respective additives and changed thereafter every second day, for a period of 1 or 5 days. For the specific treatments, used concentrations are outlined in **Table 11**.

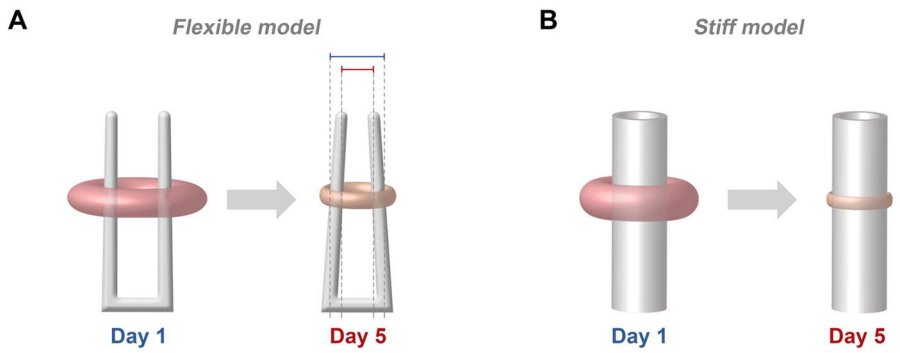

Figure 11. Schematic representation of tissue compaction and contraction according to flexible and stiff models.
A) Flexible model comprises tissues cast in moulds with two flexible poles that for its ability to deflect allows not only tissue compaction but also further contraction over 5 days. The traces indicate the variation in the distance of the pole between day 1 (blue) and day 5 (red). **B)** Stiff model comprises tissues cast in moulds with a stiff central unbendable rod that besides tissue compaction does not allow for further contraction over 5 days. (Original illustration, Gabriela L. Santos)

3.2.2.3.4. Compaction analysis of ECT – cross-sectional area and volume

Tissue compaction starts after gelation of the collagen and describes changes triggered by cell-driven compression of the matrix and by remodelling of the matrix due to secreted factors. This parameter is assessed by determining the cross-sectional area (CSA) and volume of the tissues. At day 1 or day 5, tissues were transferred from the casting moulds to a DPBS-containing multi-well plate and macroscopic images of top and side views of the ECT were taken with a Stereo Lumar.V12 stereomicroscope.

Horizontal line scan analysis of the tissue diameters was performed at a minimum of 3 positions (for rigid tissues) or 6 positions (for flexible tissues) per imaging plane, using ImageJ. The mean diameters of the tissues were calculated (d_t, the mean diameter of the top view plane, and d_s, the mean diameter of the side view plane, as schematized on **Figure 12** and the CSA was calculated according to the elliptic area equation: $CSA=\pi\times(d_t/2)\times(d_s/2)$. The volume of each ECT was calculated by multiplying its averaged CSA by its full length, which was measured from top view plane as the central ECT perimeter, using ImageJ.

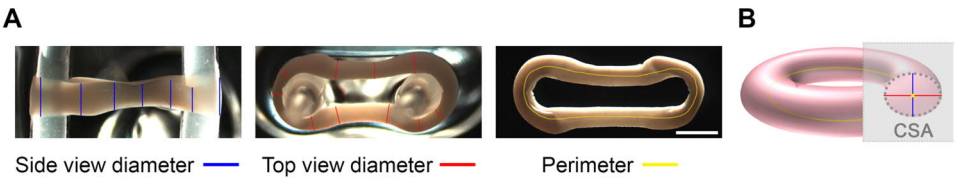

Figure 12. Cross-sectional area (CSA) and volume analysis approach.
A) Macroscopic images (Stereo Lumar.V12, Zeiss) of top and side views of an ECT and correspondent example of line scan analysis of the tissues' diameters and perimeter, using ImageJ. Scale bar = 1 mm. Diameters are depicted in blue (side view diameters) and red (top view diameters) and perimeter depicted in yellow. **B)** Schematic representation of the cross-sectional plane of an ECT depicting in blue the side view diameter which is calculated from the mean of all line lengths measured on the side view plane and top view diameter in red which is calculated from the mean of all line lengths measured on the top view plane. (Original illustration, Gabriela L. Santos)

3.2.2.3.5. Contraction analysis of ECT

The tissues prepared in flexible moulds were daily imaged on a multi-well plate recording device (**Figure 13**). This hardware was developed by Dr. Tim Meyer (Institute of Pharmacology and Toxicology, University Medical Center Göttingen).

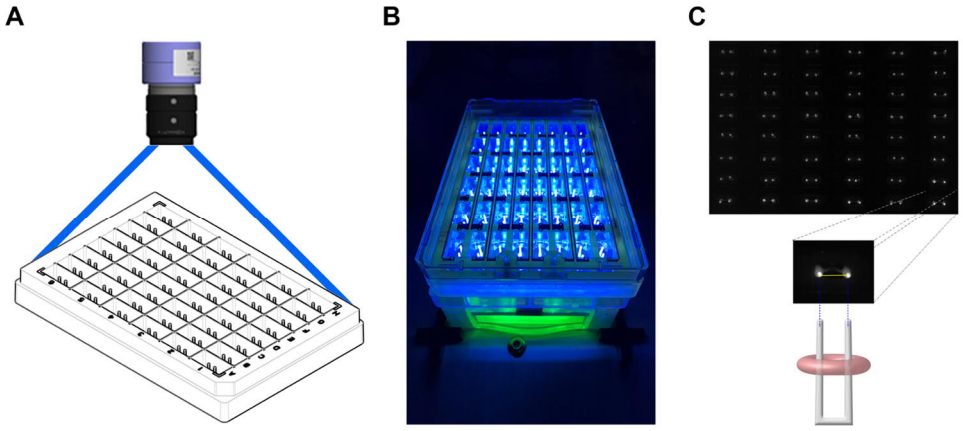

Figure 13. Schematic overview of assessment of contractility according to pole bending.
A) Set up for high resolution image recordings from a custom-made multi-well plate recording device [401]. **B)** Multi-well screening plate under UVA-light excitation. **C)** Record of the tip of brighter dye-containing poles displayed with microDisplay 5.4.1.2 software (top) and distance measurement (yellow line) using ImageJ software (bottom). (Figure 13A adapted from original illustration provided by Dr. Tim Meyer.)

The recording device is a high resolution special purpose image hardware with an integrated UVA light source, which allows short and long-term analysis under sterile

and non-perturbing conditions. As the poles contain a brighter dye, the UVA light leads to an increase of the contrast allowing to record with high precision the position of the poles, with a camera MC2586 (Mikrotron) (**Figure 13C**). The image processing was done with microDisplay 5.4.1.2 software. Distance between the poles was subsequently measured using ImageJ from daily records. hECT contraction is given by the variation of poles' distance. The poles are deflected by the tissues and the decline in distance reflects the tissue contraction. Therefore, contraction was calculated as the inverted variation in distance between the poles comparatively to the initial distance at day zero.

3.2.2.3.6. Destructive tensile strength measurement and stress strain analysis

To assess viscoelastic properties of ECT destructive tensile strength measurements with an RSA-G2 rheometer were performed. The ECT were loaded onto two custom-made hooks in a 37°C tempered organ bath filled with DPBS as demonstrated in **Figure 14**. Tissues were stretched uniaxially at a constant linear rate of approximately 1% of their initial length per second, until the point of rupture. Therefore, rECT were stretched at a constant speed of 0.05 mm/s, and hECT were stretched at 0.03 mm/s.

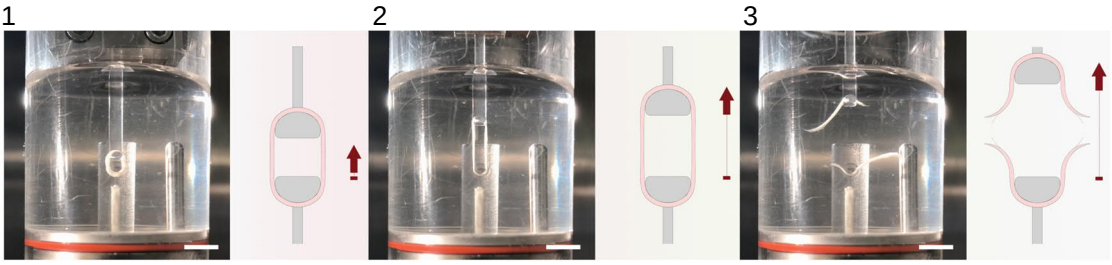

Figure 14. Experimental set-up for rheological destructive tensile measurement of ECT and schematic representation of the uniaxial stretch.
Rheological destructive tensile measurement on a RSA-G2 rheometer represented in three phases: **1,** loaded ECT at initial length, L_0, **2,** axial tensile stretch at 0.03 mm/s, and **3,** failure point post ultimate strain. Arrows indicate the direction of the stretch. Scale bar = 5 mm. (Original illustration, Gabriela L. Santos)

To calculate the given parameters from the destructive tensile strength measurements, for each ECT, the measured force values (mN) were divided by the determined CSA to

obtain stress values (kPa) and these were plotted against the gap in millimeters (distance between the upper and lower hook) in GraphPad Prism 7. On the resultant curve, the beginning of the toe region was manually identified, corresponding to the initial length of the tissue immediately before the stretch ensues, L_0. The strain values were calculated by the equation $(L_{total}-L_0)/L_0$ in which L_{total} is the total gap at every measuring point. The stress value at L_0 was used for background subtraction. Transformed values were then re-plotted creating the final stress-strain curve.

A typical stress-strain curve as the ones obtained for ECT displays three regions: toe region, elastic region and plastic region. The upper limit of the elastic region corresponds to the Yield point and the plastic region is comprised between the Yield point and the failure point. The failure point corresponds to a sudden drop in stress due to the rupture of the tissue (**Figure 15**). For each obtained curve, the slope of the linear part of the elastic region was determined by linear regression on GraphPad Prism 7, and corresponds to the Young's modulus. This is also known as elastic modulus, which is a mechanical property that measures the stiffness of the tissue. The maximum stress and ultimate strain, characterized by the highest stress reached and the strain at which the stress suddenly drops, respectively, were manually retrieved from each curve. The resilience and toughness were calculated using the function area under the curve (AUC) of GraphPad Prism 7, up to the Yield point and to the failure point, respectively. The baseline was set to zero and only the peaks above the baseline which are at least 10% of the distance from minimum to maximum Y were considered to compute the AUC by the trapezoidal method. Due to the material-dependent variations in the absolute values, comparisons were only made between conditions which had been tested in parallel.

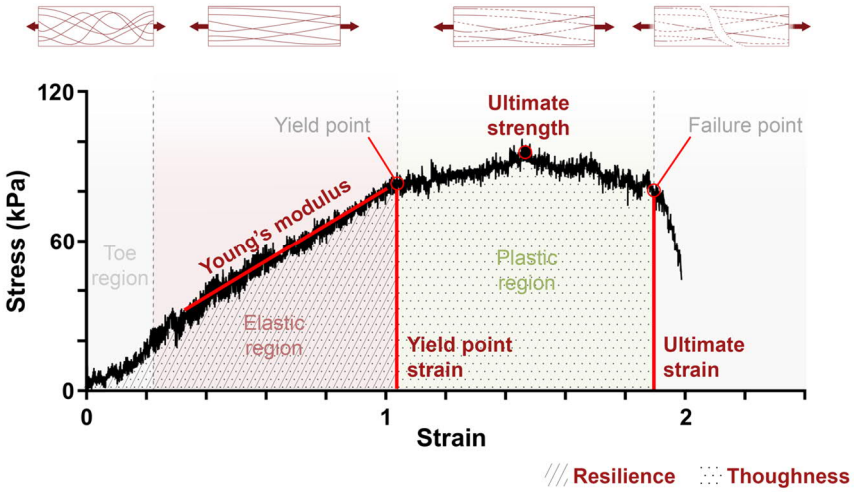

Figure 15. Stress-strain diagram of an ECT showing the main measured parameters.
The stress-strain curve presents three regions: toe, plastic and plastic. The upper limit of the elastic region corresponds to the yield point and the plastic region is comprised between the Yield point and the failure point. The slope of the linear phase of the elastic region corresponds to the Young's modulus of tissue stiffness. The ultimate strength corresponds to the maximum tensile stress a tissue can withstand. Due to fiber microfracturing, the stress decreases until the tissue reaches the failure point. This occurs at the ultimate strain (maximum extensibility) where a sudden drop in stress is observed due to the rupture of the tissue. Resilience corresponds to the energy (kJ/m^3) absorbed by the tissue before permanent deformation and is given by the area under the curve (AUC) up to the yield point strain. Toughness corresponds to the total energy the tissue can absorb until rupture, and is given by the AUC up to the ultimate strain. A schematic stretch of the fiber within the tissue is presented along with the strain variation. (Original illustration, Gabriela L. Santos)

3.2.2.3.6.1. 3D printing of hooks for destructive tensile strength measurements

The hooks used to load onto the ECT for destructive tensile strength measurements were printed on a Connex350 3D printer using the biocompatible MED610 polymer according to the sketch presented on **Figure 16**.

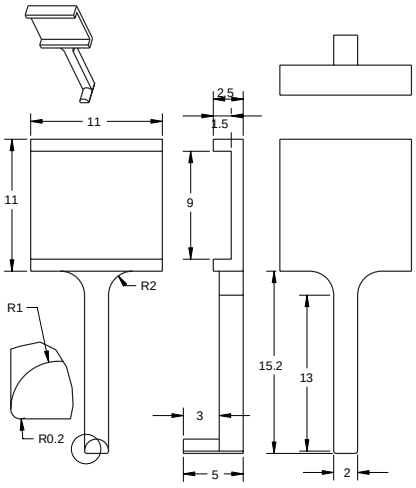

Figure 16. Loading hooks for rheological tests.
A technical drawing of the hooks is schematized with dimensions presented in millimetre. (Illustration provided by Dr. Tim Meyer.)

After printing, the support material was sprayed off using a Balco Powerblast waterjet. Hooks were incubated for 15 minutes in isopropanol to dissolve traces of support material, sprayed again, rinsed, and soaked in water for at least 5 days to bleed out leftovers from the polymerization process. Hooks were then sterilized by UV. This procedure was carried in collaboration with Dr. Tim Meyer (Institute of Pharmacology and Toxicology, University Medical Center Göttingen).

3.2.2.3.7. Dissociation of ECT for single cells re-isolation

To isolate single cells from ECT, tissues cultured/treated for one or five days were placed in 12-well plates and individually incubated in 1 mL collagenase solution at 37°C for 2-3 h (rECT) or 1-2 h (hECT). The supernatants were transferred to 15 mL collection tubes and kept on ice. The residual tissue fragments left were washed with 1 mL/well of DPBS without calcium to remove traces of serum, and further incubated in 1 mL/well accutase mix for 20 min at 37°C. The DPBS used for washing was pooled with the respective supernatants previously collected. After the incubation in accutase mix, residual tissues were mechanically dispersed by pipetting and enzymatic activity was inhibited by adding 2 mL DPBS containing 5% FBS. Each suspension of 3 mL containing the released cells was respectively pooled into the 15 mL collection tube with the previously collected volumes. The collection tubes were further centrifuged at 300 ×g for 5 min at 4°C, and pelleted cells were next resuspended in 1 mL of DPBS containing 5% FBS.

Cell suspensions were used immediately for cell number, viability and diameter assessments as described in *section 3.2.2.4.*, and further fixed and analysed as described in *section 3.2.2.5.*

3.2.2.4. Cell number, viability and diameter assessment

Measurement of cell number, viability and cell diameter used for experimental analysis, quality control or specific seeding numbers were assessed by electrical current exclusion and pulse area analysis using the Casy TTS system. Throughout the measuring period, cells dispersed either in growth media or in 5% FBS containing-DPBS were kept on ice. A program with specific settings was created individually for NRCF and hCF according to the manufactures instructions, to allow a standardization of the measurements. According to the Casy programs designed, 10 µL suspended NRCF or 20 µL hCF were added to 10 mL of Casy Tone buffer for measurement. Data are presented as absolute values.

3.2.2.5. Flow cytometry – cell cycle and cell markers analysis

After measurements on Casy TTS system (*section 3.2.2.4.*), harvested cells from 2D cultures (*section 3.2.2.2.1.2.*) and isolated cells from ECT (*section 3.2.2.3.7.*) where centrifuged at 300 ×g for 5 min at 4°C. On that note, all centrifugation steps within this section were performed under these same settings. After centrifugation, each sample of NRCF was fixed in 1 mL of the fixative agent Roti-Histofix for 5 min at room temperature and each sample of hCF in 1 mL of -20°C cold 70% ethanol for at least 30 min. The fixatives were added dropwise to the pelleted cells on a vortex mixer. The samples were stored up to one month in 1 mL DPBS at 4°C (for Roti-Histofix-fixed cells) or in 70% ethanol at 4°C (for cells fixed in the same agent). Flow cytometry analysis was performed earliest 16 h after fixation with 70% ethanol to give time for degraded DNA to diffuse out of the cells and thus give more reproducible separation between the pre-G_1 and G_1 peaks [402]. Before flow cytometry analysis, stored samples were washed once by centrifuging, discarding the supernatant and resuspending the

cells in DPBS. Samples were kept on ice for 20 min, to allow rehydration of those fixed and stored in ethanol. Cells were further strained using a 40 µm nylon mesh cell strainer to remove clumped cells and thus permit staining without excessive background and avoid clogging the flow cytometer. After a centrifugation step, cells were incubated with 0.6 mL permeabilization/blocking buffer per sample, for 10 min at 4°C. After a centrifugation step and discarding supernatant, each sample was incubated in the dark at room temperature for 30 min using 0.2 mL permeabilization/blocking buffer containing 10 µg/mL Hoechst 33342. Subsequently, cells were washed twice by centrifuging and discarding supernatant and lastly resuspended in 0.4 mL PBS each for analysis. Using a BD LSRII SORP Cytometer, a hierarchical gating strategy was applied. First gate for main population of cells was based on pulse processing, by gating the parameter forward scatter area (FSC-A) versus sideward scatter area (SSC-A). A subsequent gate was based on DNA signal area versus the parameter FSC-A allowing for exclusion of cell debris. Consecutively, the elimination of doublet cells was achieved by gating the parameter DNA signal width versus the parameter FSC-A. Cycle phases (bandpass filter 440/40-nm, Pacific Blue) were acquired and gated within the hierarchical strategy described (**Figure 17**). For proper quantitative DNA analysis, a greater resolution during acquirement is critical. Therefore, at least 10,000 events per sample were acquired within the gating strategy designed at a flow rate lower than 200 events per second using FACS DIVA software. Flowing software was used for analysis. For cell cycle presentation as column graphs only phases G_0/G_1, S and G_2/M were considered and thus presented as percentage of the total number of cells (events) acquired within those three phases.

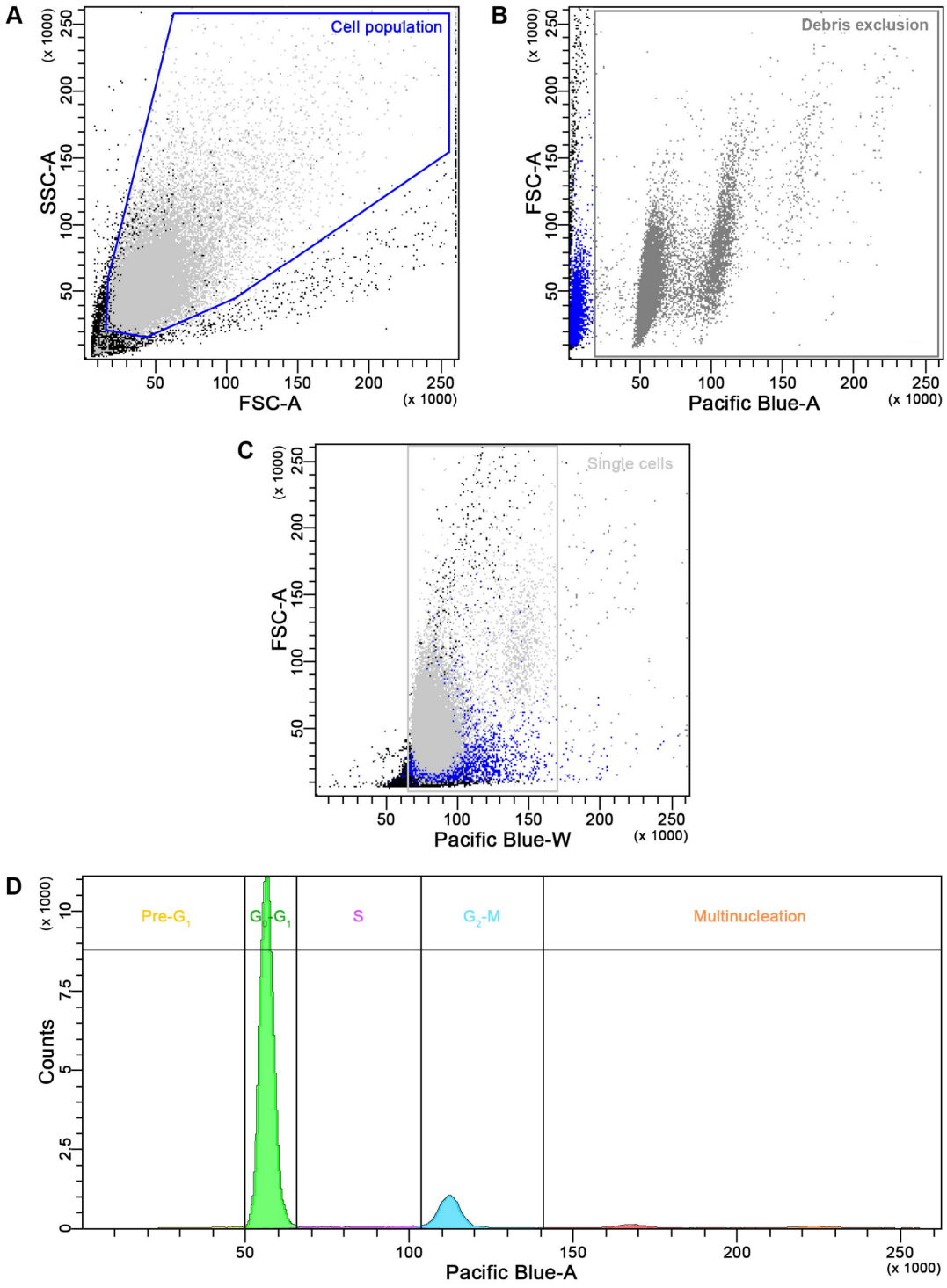

Figure 17. Hierarchical gating strategy for flow cytometry analysis.
To define the population of interest, it was set a **A)** main cell population gate based on pulse processing, by gating the parameter forward scatter area (FSC-A) versus sideward scatter area (SSC-A). To exclude the cell debris still included in the selected population, a **B)** debris exclusion gate was applied based on DNA signal area versus FSC-A. **C)** Single cells gate was defined under the previous gates to allow for elimination of doublet cells by gating the parameter DNA signal width versus the parameter FSC-A. **D)** Cell cycle phases (450/50-nm Pacific Blue) were acquired and gated within the hierarchical strategy implemented.

3.2.3. Biochemical procedures

3.2.3.1. Protein extraction

As cell lysis starts taking place, proteolysis and denaturation of proteins ensue. Therefore, to efficiently slow down these events, samples were kept on ice or at 4°C at all times. Lysis buffer was always freshly prepared by supplementing CytoBuster Protein Extraction Reagent with protease inhibitors cOmplete EASY pack according to manufacturer's indications. The gentle non-ionic composition of CytoBuster Reagent is indicated as being suitable for efficient extraction of soluble proteins from mammalian cells and compatible with the Bradford assay. The following procedures for preparation of whole cell and tissue lysates are a modification of the manufacturer's protocol.

3.2.3.1.1. Preparation of whole cell lysates from 2D adherent cells

For the preparation of whole lysates for protein isolation, adherent cells were harvested by washing twice with ice-cold DPBS and approximately 150 µL per 10^6 cells of lysis buffer was added directly to the culture vessel. The cells were scraped off the plates and the cell lysates were directly collected in appropriate tubes, followed by a 5 min incubation on ice. Mechanic lysis was further applied by gently pipetting up and down for complete homogenization. After a centrifugation step at 28500 ×g, 4°C for 20 min, the cleared supernatants (protein extract) were transferred into new 1.5 mL collection tubes and protein concentrations were subsequently assessed as described in *section 3.2.3.2*. After concentration measurement, lysis buffer was used to adjust protein concentration so that all samples from the same set had equal concentration. In order to avoid freeze-thaw cycles, a fraction of each sample was separately aliquoted, snap frozen in liquid nitrogen and placed at -80°C for long term storage, while the other part

was prepared according to *section 3.2.3.3.* for subsequent application.

3.2.3.1.2. Preparation of whole tissue lysates from ECT

After one or five days of culture/treatment, ECT were shortly washed with DPBS after culture and the excess of DPBS absorbed using a clean cloth. Tissues were then placed into 2 mL microcentrifuge tubes, snap frozen in liquid nitrogen and stored at -80°C until further use. For protein extraction, each sample was constituted by a pool of 3 ECT. ECT were allowed to thaw on ice in the presence of 200 µL (per rECT) or 75 µL (per hECT) lysis buffer for 15 min. A single stainless steel 5 mm diameter bead was added to each tube and mechanic lysis of ECT was applied in 2-3 cycles of 90 s at 30 Hz by using TissueLyser. Beads were removed from the tubes after a short spin and tubes were further centrifuged at 28500 ×g, 4°C for 20 min (rECT) or at 12000 ×g, 4°C for 15 min (hECT). The cleared supernatant (protein extract) was transferred into new 1.5 mL collection tubes. One part was separately aliquoted, snap frozen in liquid nitrogen and placed at -80°C for long term storage, while the other part was prepared according to *section 3.2.3.3.* for subsequent application.

For whole tissue lysates from ECT the classical methods to access protein concentration, such as Bradford assay, are technically difficult to implement due to the high amount of collagen in the ECT. Thus, a run-test was issued beforehand and the loading volumes for further protein analysis, were adjusted according to Ponceau S staining (*section 3.2.3.6.*). Intensity quantification of the lanes from the Ponceau S stained blot membranes was performed using Image Lab software. Lanes were manually selected and all bands including faint bands were detected. Band intensities were totalled for each lane. The relative protein amount of the cell lysates form ECT was calculated based on the lanes intensity using Microsoft Excel 2016. Samples

dilution was then readjusted using a mixture of 3 parts of lysis buffer to 1 part of 4× Laemmli sample buffer, for equal loading volumes.

Stainless steel beads used for tissue homogenization were washed between procedures. After rinsing thoroughly with water, beads where incubated in 0.1 M HCl for at least 1 h at room temperature to degrade any biological material and avoid cross-contamination in future preparations. Beads were thoroughly rinsed with distilled water and further with 100% ethanol, and let up to dry before use or storage.

3.2.3.2. Protein concentration determination using Bradford assay

Protein concentrations of whole cell lysates were determined using a colorimetric protein assay originally described by Bradford [403] and further standardized by Harmmond and Kruger [404, 405]. Here is briefly described the method using Bradford reagent Roti-Quant 5× according to the manufacturer's adapted instructions. The samples were prepared for protein concentration analysis by mixing, 190 or 195 µL of $_{dd}H_2O$ and 10 or 5 µL of sample, respectively, and briefly vortexed. Simultaneously, bovine serum albumin (BSA) standards were prepared by serial dilutions in a range from 0 to 100 µg/mL, from a BSA purified solution (10 mg/mL). Along with standards, the samples were pipetted, in triplicates, into a 96-well plate and topped with 200 µL of Roti-Quant (1× v/v in $_{dd}H_2O$). The plate containing mixtures was incubated at room temperature in the dark for 5 min. The absorbance at 595 nm was measured using the spectrophotometric microplate reader FlexStation3 and the protein concentration of the cell lysates was calculated based on the standard curve using Microsoft Excel 2016.

3.2.3.3. Preparation of samples for protein analysis

In order to assist the unfolding of proteins, protein extracts prepared as described in *sections 3.2.3.1.1.* and *3.2.3.1.2.* were supplemented with Laemmli sample buffer (3

parts of protein extracts to 1 part of 4× Laemmli sample buffer). Laemmli sample buffer contains ionic detergent sodium dodecyl sulfate (SDS) and freshly added β-mercaptoethanol (β-ME) to assure negatively charged and desaturated proteins which can then separate by electrophoretic mobility proportionally to their molecular weights [406, 407]. To fully achieve protein denaturation, immediately before loading the samples for protein separation, those were heated at 95℃ for 5 min, cooled down on ice and shortly spun down. For later use, non-heated samples were stored at -20℃.

3.2.3.4. Protein separation by sodium dodecyl sulfate polyacrylamide gel electrophoresis (SDS-PAGE)

The separation of denatured proteins is possible due to sodium dodecyl sulfate-polyacrylamide gel electrophoresis (SDS-PAGE). This technique evolved from the widely known Laemmli system (1970) [407] and combines the use of a detergent and a discontinuous buffer system. For PAGE, two different chemically inert gel matrixes which act as a molecular sieve were formed by copolymerization of acrylamide and *N*,*N'*-methylenebisacrylamide [408] catalysed by the combined action of ammonium persulfate (APS) and tetramethylethylenediamine (TEMED) [409]. On top, a stacking gel that due to its bigger pore size and acidity arranges protein samples to enter the resolving gel. This second gel, due to its small pore size and basicity, allows separation of proteins. Briefly, using the Bio-Rad casting stand clamp kit, 5.6 mL of resolving gel solution was prepared according to the composition described in **Table 10**, poured between 1 mm thick gel glass plates and covered with isopropanol to settle the gel surface and prevent air bubbles. After the polymerization of the gel (approximately 20 to 30min), the excess isopropanol was drained and 2.5 mL of stacking gel (composition described in **Table 10**) was poured on top of the resolving gel. A desired multi-well

comb was promptly inserted into the stacking gel which was then allowed to polymerize for approximately 10 min. To facilitate band sharpness, the height of the stacking gel was 2× the height of the well. The polymerized gel was used after 2 h of polymerization to ensure maximum reproducibility of pore size, or stored in a wet environment at 4°C to avoid dehydration and used up to one week. In order to achieve optimal acrylamide polymerization and increase reproducibility [410], buffers and monomer gel solutions were allowed to equilibrate to room temperature before initiating the catalysis with APS and TMED. In particular cases, 4-20% Mini-PROTEAN TGX Stain-Free Protein 12 well or 10 well gels were used.

To run the SDS-PAGE, vertical electrophoresis Bio-Rad Mini-PROTEAN system was set up with gels. The electrophoresis cells were filled with 1× running buffer and the combs removed from the gels with subsequent rinsing of the wells with the same buffer. Equal amounts of protein samples (10-50 µg), prepared as described in *section 3.2.3.3.*, were loaded into the wells along with a molecular weight standard. Total volumes of 20 µL or 30 µL were used on the precast polyacrylamide gels and 25 µL on the self-made 10-well gels. The volume per well of the molecular weight standard, was prepared by adding 2 µL of one of the protein markers indicated in **Table 5** and lysis buffer containing 1× Laemmli sample buffer up to the referred volumes for the specific acrylamide gels. Within the stacking gel, the electrophoresis was run at an initial constant voltage of 80 V and switched to constant 180 V when samples were in the resolving gel and run until samples reached the bottom of the gel, indicated by the tracking dye, bromophenol blue, which migrates at the leading edge [406].

3.2.3.5. Electrophoretic transfer (Immunoblotting)

Following SDS-PAGE, electrophoretic transfer adapted from standardized protocols

[411, 412] was carried. In short, run gels were disassembled from the gel glass plates or precast moulds, stacking gels were cut off (if necessary) and the resolving gels were equilibrated at room temperature in transfer buffer 1×. Amersham Protran nitrocellulose membranes were briefly rinsed in 1× transfer buffer and the transfer sponges and sheets of Whatman paper were also soaked in transfer buffer 1×. Using the Bio-Rad blotting chamber system Mini Trans-Blot Cell according to the manufacturer's instructions, the transfer sandwich was assembled on a plastic transfer cassette completely immersed in transfer buffer 1× to avoid trapping air bubbles. The transfer assembly was carried by placing a soaked sponge on the bottom half of the plastic transfer cassette followed by two sheets of wet Whatman paper, gel on top of the papers, wet nitrocellulose membrane on top of the gel avoiding any air bubbles and placing again two sheets of wet Whatman paper. Air bubbles eventually formed while assembling transfer stacks were gently removed by using a blot roller. Finally, a wet transfer sponge was placed on top. The top half of the transfer cassette was locked in place and the transfer sandwich was placed in the blotting chamber filled with ice-cold transfer buffer 1× while ensuring the correct orientation. A cold ice pack was also placed in the tank to avoid excessive heating of the transfer buffer. The proteins were transferred from gel onto nitrocellulose membrane at constant 100 V for 1 h.

3.2.3.6. Immunodetection

After complete electrophoretic transfer of proteins onto nitrocellulose membranes, the transfer sandwich was disassembled and the membranes were stained with Ponceau S. Briefly, blot transfer membranes were washed once with $_{dd}H_2O$ for 5 min. Followed an incubation with 1% (v/v) acetic acid and 0.1% (w/v) Ponceau S up to 5 min at room temperature, on a horizontal reciprocating linear shaker (40 rpm). Excess Ponceau S

stain was removed with several changes of $_{dd}H_2O$ for 30 s to 1 min each, until the background had a very slight pink tinge and the protein bands were still easily detected. Membranes were kept wet and a digital record of the protein pattern was conducted by the Chemidoc MP. Adjustment of samples' concentration according the Ponceau S staining is described in *section 3.2.3.1.2*.

After the documentation of the Ponceau S staining, the membranes were distained with three TBST washing steps of 10 min, at room temperature and on a horizontal reciprocating linear shaker (40 rpm). After confirming an equal sample loading, even transfer, and that any bubbles had prevented protein from transfer to the membrane, those were cut according to the molecular weight of the specific proteins and blocked with 1× Roti-block for 1 h at room temperature, on a horizontal reciprocating linear shaker (40 rpm). It followed one wash step with TBST before probing the membranes with specific primary antibodies diluted in TBST (in some cases supplemented with 5% 1× Roti-block) by overnight incubation at 4°C on an orbital shaker (350 rpm). Incubation with the appropriate HRP-conjugated secondary antibodies was preceded and followed by three washing steps with TBST. The secondary antibodies were diluted in TBST (and in some cases supplemented with 5% 1× Roti-block) and the incubation took place on a horizontal reciprocating shaker (40 rpm) for 1 h at room temperature. Finally, secondary antibodies chemiluminescent signals were detected using ECL technology. For highly abundant proteins as loading control proteins or SMA Lumi Light was used, whereas for lower expressed proteins the more sensitive reagent SuperSignal West Femto Maximum Sensitivity Substrate was preferred. For band density quantification, excess of TBST was drained and membranes were exposed to ECL and directly analysed in a Bio-Rad ChemiDoc MP Imaging System. Immunoblots shown in the figures are representative for immunoblots obtained from at least three

different biological experiments.

Note that the washing procedure within this section was performed by rinsing the membranes with TBST, followed by at least one incubation in TBST for 5 min on a horizontal reciprocating linear shaker (40 rpm) at room temperature. Number of washing steps are mentioned above for each specific application. Specific antibodies and correspondent working dilutions are described in *section 3.1.3.5*.

3.2.4. Molecular biology

3.2.4.1. RNA isolation

Total RNA was isolated from cells or ECT with QIAshredder spin columns and the Qiagen RNeasy Mini Kit according to manufacturer's protocols. The lysis buffer RLT was supplemented with 0.1% β-ME. Although its effectivity is debated [413], β-ME was used to irreversibly inactivate RNases enzyme functionality due to its reducing properties [414].

For the preparation of whole lysates for RNA isolation from adherent cells, these were harvested by washing twice with ice-cold DPBS and adding 350 µL per $<5\times10^6$ cells of supplemented RLT directly to the culture vessel. The cells were scraped off and the cell lysate was directly collected into 1.5 mL tubes, followed by an incubation of 2 min at room temperature.

For the preparation of whole lysates for RNA isolation from ECT, these must have been shortly washed with DPBS after culture and the excess of DPBS absorbed using a clean cloth. Alternatively, ECT subjected to destructive tensile measurements could be used. Tissues were then placed into 2 mL microcentrifuge tubes, snap frozen in liquid nitrogen and stored at -80°C until further use. Each sample was constituted by a pool of 2 to 3 ECT. For RNA extraction, ECT were allowed to thaw and incubate for 5-20

min at room temperature in the presence of 175 µL per ECT of supplemented RLT.

In both cases, after the incubation in supplemented RLT, samples were disrupted by pipetting up and down until complete homogenization and incubated for further 3 min at room temperature. One volume of 70% ethanol was added to each lysate and mixed gently by pipetting to precipitate RNA. Each lysate was transferred to a RNeasy Mini spin column placed in 2 mL receiver tube. Columns were centrifuged at 8000 ×g, for 20 s at room temperature and the flow-through discarded. The columns were further washed once with 700 µL of buffer RW1 and twice with 500 µL of buffer RPE. Washing steps were done by centrifugation at 8000 ×g, for 20 s at room temperature. The membranes carrying RNA were dried by centrifuging columns placed in clean 2 mL receiver tubes at full speed for 1 min at room temperature. The RNA was eluted into RNAse-free 1.5 mL collection tubes by adding 20 µL of nuclease-free water. After an incubation of 1 min at room temperature, columns were centrifuged at 8000 ×g for 1 min. The RNA concentration was determined as described in *section 3.2.4.2.* and the RNA was either used immediately (*section 3.2.4.3.*) or frozen at -80°C.

3.2.4.2. Determination of nucleic acid concentration

The amount and quality of the RNA was assessed with a NanoDrop spectrophotometer. Sample absorbances against nuclease-free water blank were measured at 260 nm and 280 nm to check the quality of nucleic acids and as a secondary measure absorbances at 260 nm and 230 nm wavelengths were also checked. Briefly, 1 µL of nuclease-free water or sample was applied to the NanoDrop pedestal, the arm was closed and the sample concentrations and absorbances were measured. The results of nucleic acid concentration determinations were then registered and the samples were either used immediately (*section 3.2.4.3.*) or stored at -80°C.

3.2.4.3. RNA reverse transcription into cDNA

For qPCR, 350 to 1000 ng of the isolated total RNA was transcribed into cDNA with the RevertAid cDNA synthesis kit from Thermo Fischer Scientific using $OligodT_{18}$ primers according to manufacturer's instruction. Briefly, all reaction components were thawed on ice and each reaction was prepared by mixing 350, 500 or 1000 ng of RNA with 1 µL $OligodT_{18}$ primers and nuclease-free water up to 12 µL in PCR strips and incubated at 65°C for 5 min, chilled on ice and spun down. Each reaction was further complemented with 4 µL of 5X reaction buffer, 1 µL RiboLock RNase Inhibitor, 2 µL dNTP Mix and 1 µL RevertAid M-MuLV RT. The total 20 µL reaction mix was vortexed and spun down briefly. The reaction mix was then incubated in a thermal cycler using the following protocol: reverse transcription at 42°C for 60 min, reverse transcriptase inactivation at 65°C for 5 min and holding at 4°C indefinitely. Part of the synthesized cDNA was diluted in nuclease-free water in a ratio of 1:10.5, 1:15 or 1:30, accordingly to the starting RNA amount. All cDNA samples were stored at -20°C until used for qPCR.

3.2.4.4. Quantitative real-time polymerase chain reaction

Quantitative real-time polymerase chain reaction (qRT-PCR or in short qPCR) was performed using equal amounts of cDNA (synthesized as described in *section 3.2.4.3.*) and the 5× HOT FIREPol EvaGreen qPCR mix. Reaction volumes were pipetted into 384-well plates and qPCR performed on the Applied Biosystems ViiA 7 system. For each set of samples, a pool of cDNA was made to establish a standard curve for each primer pair. Standard curves were generated using a logarithmic progression of dilutions from cDNA pools. At least 3 points of the series 1:3, 1:10, 1:30, 1:100 and 1:300 were used. All primers' sequences used for amplification are given in the **Table**

15 and **Table 16**. Reactions were carried out in at least three technical replicates. Per gene and per sample, each 10 µL reaction volume per well in a 384-well plate contained 2 µL of 5× HOT FIREPol EvaGreen qPCR mix, 0.25 µL of each forward and reverse primers (2.5 pmol from each) and proportionally diluted cDNA template in nuclease-free water up to 7.5 µL. The plate was sealed with adhesive seal, spun briefly at 600 ×g for 1 min. A fast thermal cycling protocol was applied on a ViiA 7 real-time PCR system according to the 5× HOT FIREPol EvaGreen qPCR mix manufactures' indications: initial denaturation and polymerase activation at 95°C for 15 min, amplification for 40 cycles with steps of denaturation at 95°C for 15 s, annealing at 58°C (human primers) or 62°C (rat primers) for 20 s and elongation at 72°C for 40 s. Melt-curve analyses were carried out for all runs at steps of 95°C for 15 s, 60°C for 15 s and 95°C for 15 s, to test for multiple peaks in a single amplicon product. The reaction was carried out with ROX as a passive reference and standard detector for SYBR green. Data analyses were carried out using the SDS software v2.4 for the Applied Biosystems 7900HT Fast Real-Time PCR System using the standard curve method. Data was exported as Microsoft Excel files for further analyses. All values were normalized either by the two housekeeping genes β-tubulin (*TUBB*) and β-glucuronidase (*GUSB*), or by porphobilinogen deaminase (*PBGD*) and *GUSB*, or *PBGD* and hypoxanthine phosphoribosyltransferase 1 (*HPRT*). The information is given in every bar graph.

3.2.4.5. Primer specificity and amplicon size

To validate the primers, specificity and amplicon size were verified for amplified qPCR probes by agarose gel electrophoresis. Gels were prepared by melting 2% agarose in Tris-acetate-EDTA (TAE) buffer. Immediately before loading into the casting mould, 5µL of Midori Green DNA dye were mixed with 100 mL of agarose-TAE volume

(**Table 8**). For better resolution of the signal, gels were poured up to 1 cm thickness and let to polymerise for approximately 30 min. qPCR products of each primer pair were separately pooled. For loading, each qPCR product pool was mixed with equal amount of 2× GoTaq G2 Green Master Mix to a total volume of 40 µL. Negative controls of the qPCR (no template) were tested in parallel. The peqGOLD ultra low range DNA ladder II was used to check the amplicons size. The electrophoresis was carried at 100 V for 10-20 min in TAE buffer.

3.2.4.6. RNA-sequencing

Total RNA-sequencing (RNA-seq) was performed in biological triplicates with each individual sample consisting of a pool from 3 different hECT to minimize biological variation by Dr. Gabriela Salinas-Riester at the NGS Integrative Genomics Core Unit (NIG), a core facility of the University Medical Center Goettingen. Data pre-processing was done by Dr. Orr Shomroni (NIG). Total RNA was extracted according to *section 3.2.4.1.* and quantified as described in *section 3.2.4.2*. The procedure was performed at NIG is shortly described below. Therefore, specific materials, reagents and instruments are not listed in this thesis.

Quality and integrity of RNA was assessed with the Fragment Analyzer from Advanced Analytical by using the standard sensitivity RNA Analysis Kit (DNF-471). All samples selected for sequencing exhibited an RNA integrity number over 8. Libraries were performed using a modified strand-specific, massively-parallel cDNA sequencing (RNA-Seq) protocol from Illumina, the TruSeq Stranded Total RNA (Cat. No. RS-122-2301). For accurate quantitation of cDNA libraries, the QuantiFluor™dsDNA System from Promega, a fluorometric based system was used. The size of final cDNA libraries was determined by using the dsDNA 905 Reagent Kit (Fragment Analyzer from

Advanced Bioanalytical) exhibiting a sizing of 300 bp in average. Libraries were pooled and sequenced on an Illumina HiSeq 4000 Illumina generating 50 bp single-end reads (30-40 Mio reads/sample). Sequence images were transformed with Illumina software BaseCaller to BCL files, which was demultiplexed to fastq files with bcl2fastq v2.17.1.14. The sequencing quality was asserted using FastQC (version 0.11.5) [415]. Sequences were aligned to the reference genome *Homo sapiens* (hg38 version 89) [416] using the STAR aligner (version 2.5.2a) [417] allowing for 2 mismatches within 50 bases. Subsequently, read counting was performed using featureCounts (version 1.5.0–p1) [418]. Read counts were analysed in the R/Bioconductor environment (version 3.4.2) [419] using the DESeq2 package (version 1.16.1) [420]. Read counts were normalised per kilobase of transcript per million mapped reads (RPKM). Candidate genes were filtered using an absolute log2 fold-change >1 and FDR-corrected p-value <0.05. Gene annotation was performed using *Homo Sapiens* entries via biomaRt R package (version 2.32.1) [421]. Further analyses based on RNA sequencing are specified in *section 3.2.5*.

3.2.5. Bioinformatics

3.2.5.1. Principal component analysis (PCA)

Principal components (PC) were calculated in ClustVis [422]. PC were used to visualize how the samples cluster for the most variably expressed genes: all genes with RPKM ≥ 1 and a difference in RPKM between flexible and stiff hECT from day one and day 5 ≥ 1 were included in the analysis.

3.2.5.2. Venn diagram

The Venn diagram was generated from log2-fold changed genes with nVenn [423].

3.2.5.3. Gene ontology analysis (GO)

The gene ontology (GO) analysis was performed with David [424], GoRilla [425], Panther [426, 427] and String [428]. For David, GOrilla and Panther a reference list was used which comprised all genes detected in the hECT. GO terms detected by all four programs are shown with the false discovery rate (FDR) given by Panther.

3.2.5.4. Heat maps

For the generation of heat maps the RPKM values normalized by the mean of all samples per gene were used. The heat maps were generated with GraphPad Prism 7 or ClustVis.

3.2.5.5. Pathway analysis

Differential expressed genes (DEGs) were interpreted using the Reactome Knowledgebase [429]. A dataset of Ensembl gene identifiers and fold changes was uploaded for Core Analysis.

3.2.6. Statistics

Unless otherwise indicated, results were analysed using Microsoft Excel 2016 and GraphPad Prism 6 and 7. Graphs are presented as mean values of absolute numbers or normalized to experimental controls and depict corresponding standard errors of the mean for at least three biological replicates. Most data were analysed by one- or two-way ANOVA with Tukey's or Dunnett's *post hoc* tests for multiple comparisons, or by 2-sided unpaired t-test assuming normal distribution. A p-value <0.05 was considered as significant. The performed tests are specified in the respective figure legends.

4. Results

4.1. ROCK inhibition regulates cardiac myofibroblasts function in 2D cultures and rECT

4.1.1. ROCK inhibition alters NRCF spreading and cell cycle progression in 2D cultures

Preliminary results showed that ROCK inhibition with Fasudil or H1152P interfered with the ability of CF to form compact and stiff rECT (**Figure 6**). Additionally, gene expression analysis revealed that the ROCK inhibitors regulated the transcription of genes involved in collagen modification and/or regulation (**Figure 7**). In order to understand the mechanisms by which ROCK inhibitors led to the obtained data in 3D cultures, expanded 2D culture experiments were performed. Therefore, the rat CF were treated with 300 nM and 3µM H1152P, which is more potent and specific than Fasudil. To understand if the impediment of rECT compaction caused by ROCK inhibition (**Figure 6A,B**) is potentially dependent on changes in cell spreading, microscopy images of Phalloidin-labeled NRCF (**Figure 18A**) were used to determine the cell surface area after 48 h of culture. The analyses revealed that 300 nM H1152P was sufficient to significantly increase the cell area, and 3 µM was without further effect (**Figure 18B**). This increase was not, however, due to a change in overall cell size as shown by the identical cell diameters in all conditions, measured by electrical current exclusion of suspended cells (**Figure 18C**). Defective or delayed adhesion could a further explanation of the failing rECT compaction. Therefore, the influence of H1152P on cell adhesion to plastic or collagen-coated surfaces was investigated. Adhesion to collagen-coated surfaces was, as expected, faster than that to uncoated plastic. Besides, ROCK inhibition was shown to not interfere with cell adhesion to collagen or plastic

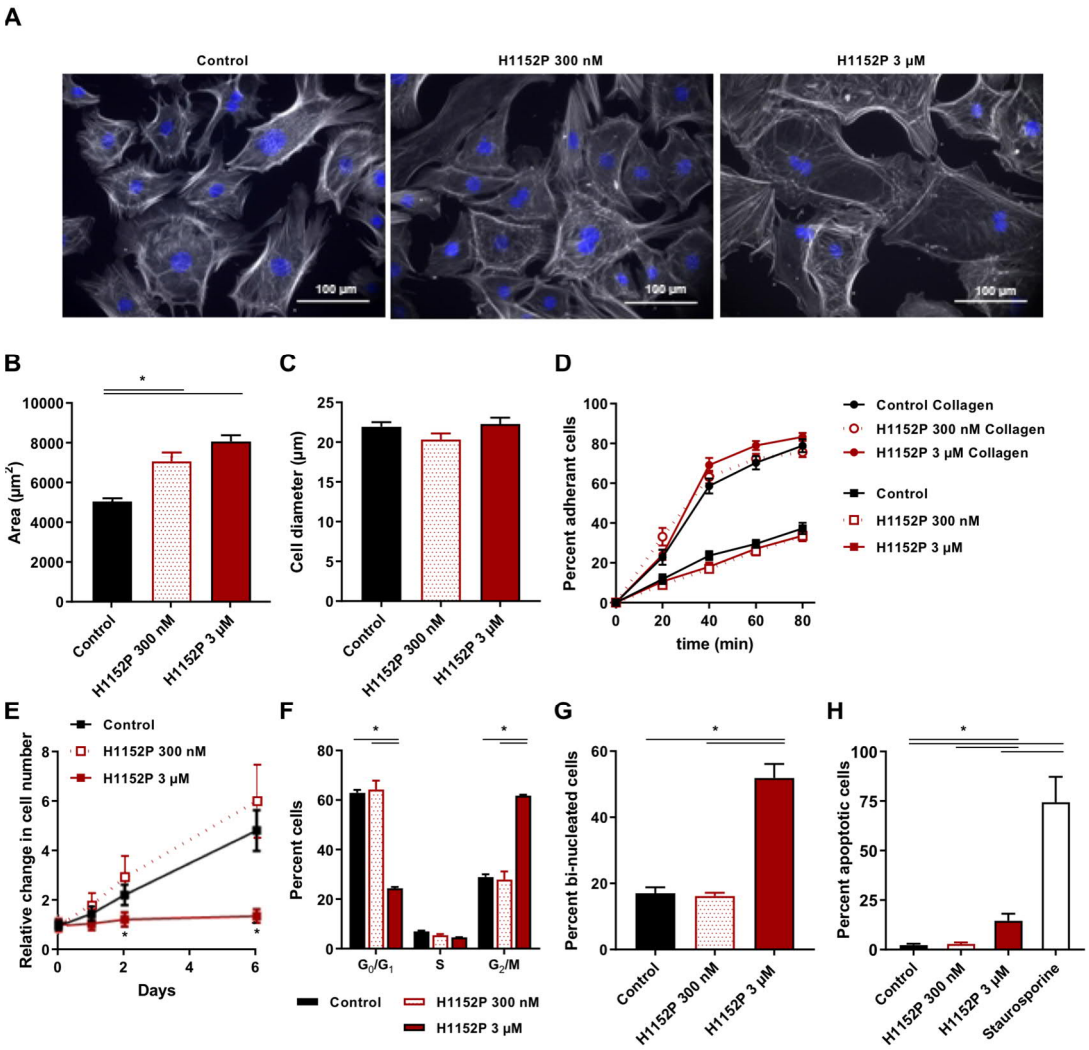

Figure 18. ROCK inhibition alters NRCF cell shape and cell cycle progression in 2D culture.
NRCF were treated with the indicated concentration of H1152P and subjected to the respective analyses. **A)** The treated NRCF were fixed after 48 h and stained with FITC-phalloidin (gray) and DAPI (blue). Images were taken with a fluorescence microscope, 20x objective. Shown are representative merges of both channels. **B)** Based on the FITC-phalloidin images the areas of attached cells were determined. Given are the means+SEM of 3 independent experiments. The differences were evaluated by 1-way ANOVA with Tukey's *post hoc* multiple comparisons test, *p<0.05. **C)** The treated NRCF were detached and the cell diameters were determined by electrical current exclusion. Given are the means+SEM of 3 independent experiments. **D)** The pre-treated, detached NRCF were seeded in 12-well plates in the absence or presence of a collagen I coat. Images were taken every 20 min and the percentage of attached cells was determined. Given are the means±SEM of 3 independent experiments. **E)** The NRCF were seeded in cell culture plates, treated with the indicated concentrations of H1152P and fixed 24 h after seeding (Day 0) as well as 1, 2 and 6 days later. The nuclei were stained with DAPI and counted automatically. Given are the means±SEM of 5-6 independent experiments. The differences were evaluated by 2-way ANOVA, *p<0.05 vs. Control. **F-G)** The NRCF were treated for 48 h, detached, fixed, stained and subjected to flow cytometry analysis. The numbers of cells in different cell cycle phases **(F)** and of bi-nucleated cells **(G)** were analysed. Given are the means+SEM of 4-6 independent experiments. Significant changes were assessed by **(F)** 2-way ANOVA with Tukey's *post hoc* test for multiple comparisons or **(G)** 1-way ANOVA with Tukey's *post hoc* multiple comparisons test, *p<0.05. **H)** The NRCF were treated for 48 h as indicated and apoptotic cells were identified by a life cell Annexin V/propidium iodide (PI) stain. The percentages of apoptotic cells are given as means+SEM of 3 independent experiments. The differences were evaluated by 1-way ANOVA with Tukey's *post hoc* multiple comparisons test (*p<0.05).

tissue culture surfaces (**Figure 18D**). Moreover, an impairment in cell proliferation could contribute to the observed effects in 3D cultures. For this purpose, automated cell nucleus counting was used. Over a six-day period, a complete blockage in cell number increment was evident with 3 µM H1152P, while 300 nM H1152P had no considerable impact compared to control (**Figure 18E**). Cell cycle analysis carried out by flow cytometry corroborated these results (**Figure 18F**). The lower concentration of H1152P did not affect cell cycle progression, whereas a 3-fold increase was observed for cells in G2/M phase when treated with 3 µM H1152P, arguing for a significant decrease in cell cycle activity. Flow cytometry analysis also revealed that there was a significant increase in number of binucleated cells after the treatment with 3 µM H1152P, but not with 300 nM (**Figure 18G**). To understand if these findings could be related to changes in cell death, a combined incubation with Annexin V and PI was used to assess apoptosis. Staurosporine, a broad-spectrum kinase inhibitor widely recognised as an apoptosis inducer was used as a positive control, resulting in an apoptosis induction by about 75% in 2D NRCF. In comparison, the 300 nM H1152P was without effect compared to control, and 3 µM H1152P increased the apoptosis rate from 2.3% under basal condition to 14.6% (**Figure 18H**).

4.1.2. ROCK inhibition reduces the transcription of fibrosis-associated genes in 2D NRCF

Next, the impact of ROCK inhibition was tested at the transcription level for adaptive time-dependent regulation of pro-fibrotic gene expression. For that, 2D cultures of NRCF were tested after 48 h and 5 days of treatment with H1152P. The direct effect on ROCK1 and ROCK2 expression was verified for control. Transcription levels showed, in particular with 3 µM H1152P, a significant up-regulation of *Rock2* at 48 h, while *Rock1* was not significantly altered. After 5 days, the effect shifted to a significant

down-regulation of both isoforms, where 300 nM H1152P was sufficient to reduce *Rock1* transcription, but *Rock2* showed significant changes only with 3 µM H1152P (**Figure 19A,B**). At protein level only the moderate increase in ROCK2 after 48 h was consistent with the RNA data (**Figure 19C,D**).

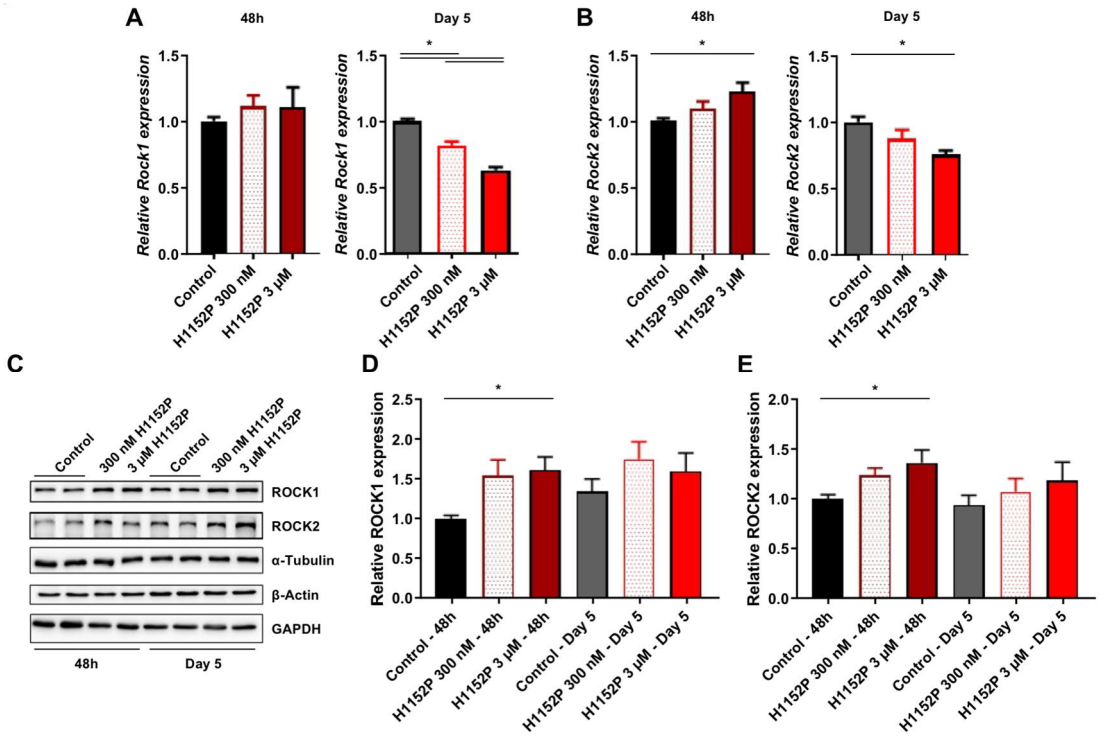

Figure 19. ROCK expression regulation in 2D NRCF cultures.
RNA and protein were extracted from NRCF treated for 48 h and 5 days with 300nM or 3µM H1152P and subjected to qPCR and immunoblot analyses. The transcripts and protein levels of ROCK1 **(A, D)** and ROCK2 **(B, E)** were analysed. **A-B)** The qPCR values were normalized to the mean of the housekeeping genes *PBGD* and *HPRT* and are given relative to control. In total RNA from 4 independent experiments were analysed. Shown are the means+SEM. The differences were evaluated by 1-way-ANOVA with Tukey's *post hoc* test for multiple comparisons, *p<0.05. **C)** Representative immunoblots of ROCK1, ROCK2 and of the housekeeping proteins α-Tubulin, β-Actin and GAPDH are shown. **D-E)** Protein levels were normalized by the housekeeping proteins and are given relative to control 48h as means+SEM of 4 independent experiments. The differences were accessed by 1-way-ANOVA with Tukey's *post hoc* test for multiple comparisons within each group (time), *p<0.05.

In line with the 3D data (**Figure 7**), the RNA levels of both *Col1a1* and *Col3a1* genes were not regulated by H1152P (**Figure 20A,B**). *Has2* and *Mmp2* were down- and up-regulated, respectively, in 2D after 5 days, which resembled the 3D data. The regulation of *Has2*, but not of *Mmp2* was concentration-dependent. Both genes displayed a slow onset in regulation as there was no difference after 48 h detectable (**Figure 20C,D**). *Mmp12* showed in 2D culture an opposite regulation to the rECT, with a significant

increase in its expression. Although it was increased significantly after 48h treatment with 300nM H1152P, the effect of the ROCK inhibition was more pronounced after 5 days treatment with 3 µM H1152P (**Figure 20**E).

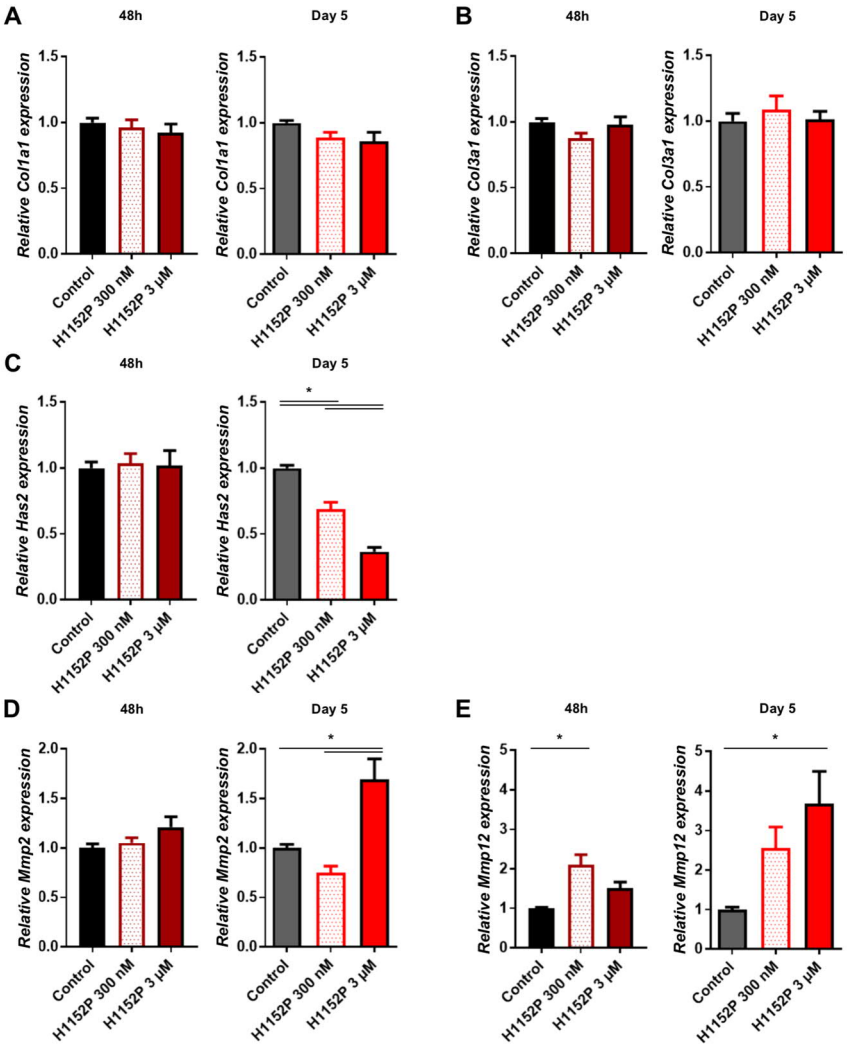

Figure 20. Impact of ROCK inhibition on pro-fibrotic genes in 2D NRCF cultures.
RNA was extracted from NRCF treated for 48 h and 5 days with 300 nM or 3 µM H1152P and subjected to qPCR analysis. The following transcripts were analysed: *Col1a1* **(A)**, *Col3a1* **(B)**, *Has2* **(C)**, *Mmp2* **(D)** and *Mmp12* **(E)**. All qPCR values were normalized to the mean of the housekeeping genes *Pbgd* and *Hprt* and are given relative to control. In total RNA from 4 independent experiments were analysed. Shown are the means+SEM. The differences were evaluated by 1-way-ANOVA with Tukey's *post hoc* multiple comparisons test, *p<0.05.

According to the essential role of ROCK in actin-myosin regulation [430], genes regulated by changes in actin mechanics like *Lox* and *Acta2* (SMA) were of special interest. *Lox* transcription in 2D was found to be, not only analogously regulated to rECT after 5 days, but also to be concentration-dependently reduced by H1152P at both

time points (**Figure 21A**). *Acta2* (SMA) showed a similar regulation pattern as *Lox* on RNA level. In the presence of 3 µM H1152P at day 5, the decline in transcription was comparable in 2D and 3D cultures (**Figure 21B,C**). Protein analysis revealed that LOX expression was concentration-dependently reduced after 48 h. After 5 days, basal LOX expression was significantly lower than after 48 h and the effect of H1152P was not as profound as at the earlier time point (**Figure 21D,E**). SMA protein levels also declined in a concentration-dependent manner after 48 h, but not after 5 days. In contrast to LOX regulation, SMA expression was by trend increased after 5 days compared to 48 h under basal condition (**Figure 21D,F**).

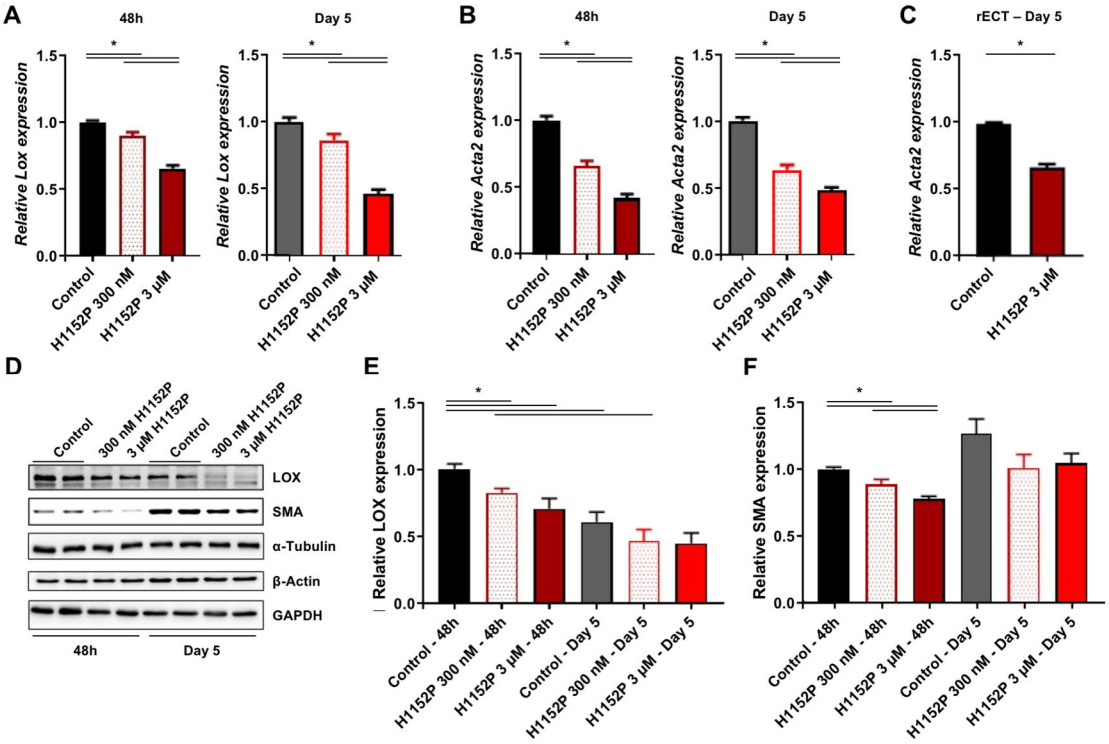

Figure 21. ROCK inhibition regulates LOX and SMA expression in 2D NRCF cultures.
RNA and protein were extracted from NRCF treated for 48 h and 5 days with 300 nM or 3 µM H1152P and subjected to qPCR and immunoblot analyses. The transcripts and protein levels of LOX **(A, D, E)** and SMA **(B, D, E)** were analysed. The *Acta2* (SMA) transcription was additionally analysed in rECT **(C)**. **A-C)** All qPCR values were normalized to the mean of the housekeeping genes *Pbgd* and *Hprt* and are given relative to control. In total RNA from 4 independent experiments were analysed. Shown are the means+SEM. The differences were evaluated by 1-way ANOVA or an unpaired t-test (rECT), *p<0.05. **D)** Representative immunoblots of LOX, SMA and of the housekeeping proteins α-Tubulin, β-Actin and GAPDH are shown. **E-F)** Protein levels were normalized by the housekeeping proteins and are given relative to control 48 h as means+SEM of 4 independent experiments. Differences were analysed by 1-way ANOVA with Tukey's *post hoc* test for multiple comparisons for each time point individually (*p<0.05); and by 1-way ANOVA with Tukey's *post hoc* test for multiple comparisons between all samples (#p<0.05).

4.1.3. ROCK inhibition in rECT reduces LOX expression

As changes in RNA do not necessarily translate into changes in proteins, we also validated by immunoblot the expression of LOX, ROCK1 and ROCK2 which in preliminary experiments (**Figure 7**) were consistently regulated by 10 µM Fasudil and 3 µM H1152P at the transcription level.

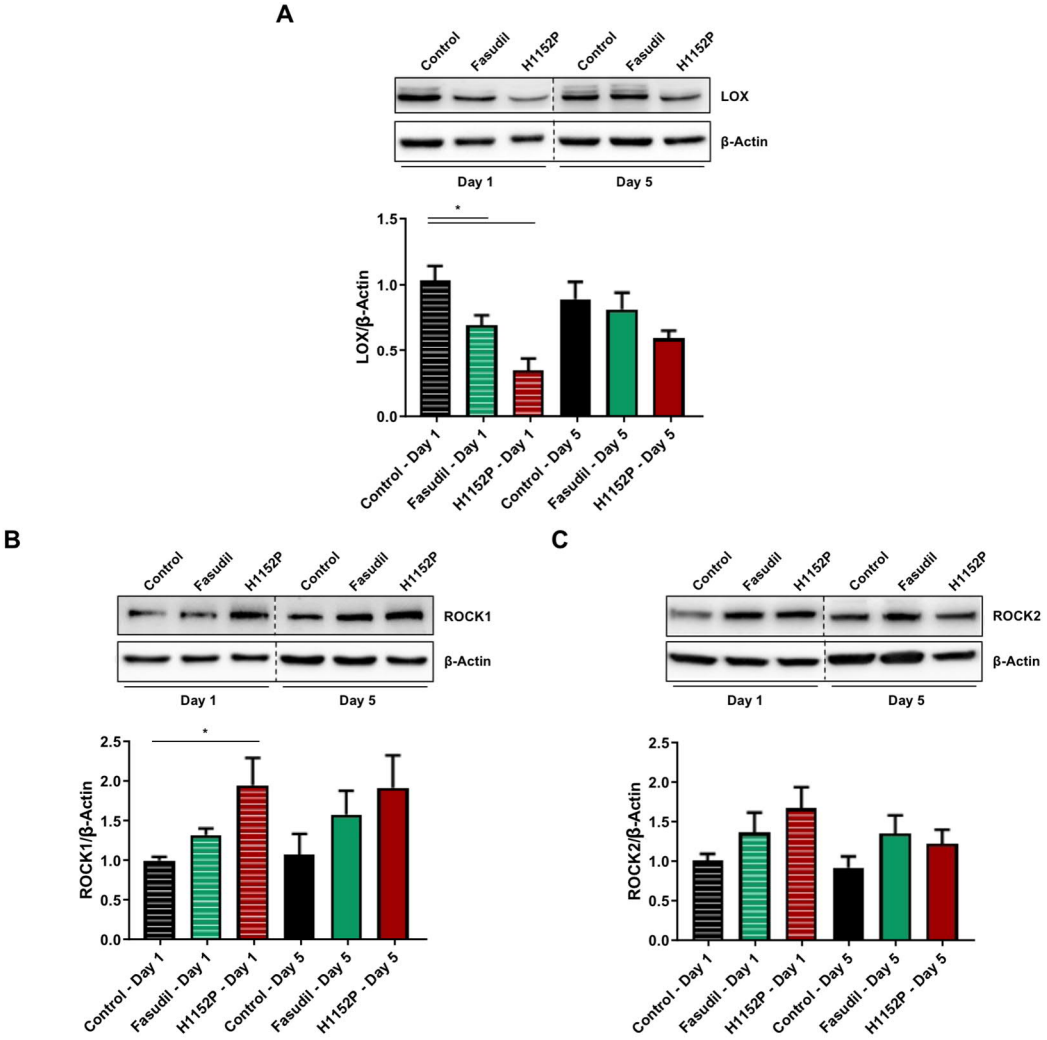

Figure 22. ROCK inhibition regulates LOX expression in rECT.
rECT were generated with NRCF and collagen I and were cultured in the absence (Control) or presence of 10 µM Fasudil or 3 µM H1152P. **A-C)** After 1 day and 5 days of treatment rECT were homogenized and protein levels of LOX **(A)**, ROCK1 **(B)** and ROCK2 **(C)** were detected by immunoblot analyses. Shown are representative immunoblots (upper panels) and the quantification of 3 independent experiments in which at least 7 rECT were investigated. The data is given normalized by β-actin and relative to Control - Day 1 as mean+SEM. Differences were evaluated by 1-way ANOVA with Dunnett's *post hoc* test for multiple comparisons for each time-point individually (*p<0.05 vs. Control).

To investigate possible time-dependent regulations, we again performed analysis for protein expression in rECT after 1 and 5 days of treatment with both inhibitors (**Figure**

22). Protein levels of LOX were significantly reduced in rECT after 1 day of treatment with both ROCK inhibitors, with H1152P presenting a stronger effect. After 5 days of treatment, the changes were not as prominent as after 1 day (**Figure 22A**). For control, the effects of the inhibitors on the protein levels of ROCK1 and ROCK2 were tested. The isoform ROCK1 was only significantly increased by H1152P after 1 day (**Figure 22B**), while ROCK2 showed no significant changes in its protein level at any condition (**Figure 22C**).

4.1.4. LOX inhibition resembles the effect of ROCK inhibition on rECT stiffness

Based on the obtained expression data and the published regulation and role of LOX in ECM remodelling, LOX came into focus in this study.

First, the effect of LOX inhibition by β-aminopropionitrile (BAPN) was studied in parallel and in combination with H1152P in the rECT model. Similar to the preliminary results, ROCK inhibition by 3 µM H1152P led to a significant 3.7-fold increase in CSA over control. Differently, treatment with BAPN had no effect on the CSA and it did not enhance the inhibitory effect of H1152P when combined (**Figure 23**A,B). Although BAPN did not affect tissue compaction, it led to a 57.6% reduction in tissue stiffness, close to the 73.4% stiffness decrease caused by ROCK inhibition. The combined application of the two inhibitors resulted in a stiffness reduction by 88.8%, which was not significantly different from single treatments with BAPN or H1152P (**Figure 23C,D**). To verify that the observed changes were independent of cell loss, cells were re-isolated from the tissues. According to what was observed in the preliminary data, H1152P did not affect viable cell number in rECT. Similarly, BAPN did not impair cell viability and cell yield was comparable in all groups (**Figure 23E-F**). Analysis of the cell cycle on cells re-isolated from tissues showed that only treatment groups that

included H1152P led to an increased number of cells at the G2/M phase. The control group had 12.2% of its cells in the G2/M phase while H1152P treatment resulted in a significant accumulation of 15.5% and the combination of BAPN and H1152P of 18.6% of the cells in this stage (**Figure 23**G).

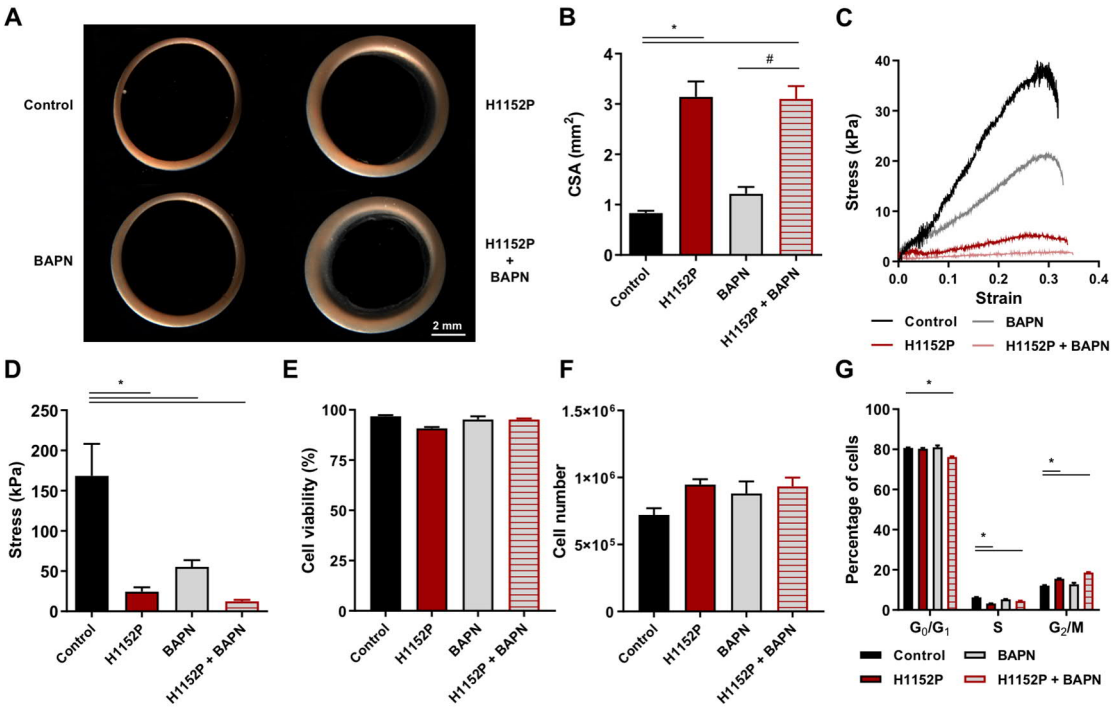

Figure 23. LOX inhibition resembles the effect of ROCK inhibition on rECT.
rECT were generated with NRCF and collagen I and were cultured for 5 days in the absence (Control) or presence of 3 µM H1152P and/or 100 µM BAPN. **A)** Representative images of rECT are shown. **B)** The cross sectional areas (CSA) were determined by image analysis. Given are the means+SEM of 12 individual tissues from 4 independent experiments. Differences were analysed by 1-way ANOVA with Dunnett's *post hoc* test for multiple comparisons (*p<0.05 vs. Control, #p<0.05 vs. H1152P+BAPN). **C)** Representative stress- strain curves from destructive tensile measurements are shown. **D)** The Young's moduli were calculated based on the obtained stress-strain curves. Given are the means+SEM of 12 individual tissues from 4 independent experiments. Differences were analysed by 1-way ANOVA with Dunnett's *post hoc* test for multiple comparisons, *p<0.05 vs. Control. **E-F)** The NRCF were re-isolated from rECT and the viability **(E)** and cell number **(F)** were measured by electrical current exclusion. Given are the means+SEM of 3 independent experiments. **G)** Cell cycle distribution was analysed by flow cytometry in re-isolated, fixed and stained cells. Given are the percentages of cells at G_0/G_1, S and G_2/M stages as means+SEMs of 4 independent experiments measured each in 3 technical replicates, *p<0.05 vs. Control was assessed by 2-way ANOVA with Dunnett's *post hoc* test for multiple comparisons.

Next, gene expression analysis was performed using rECT treated for 5 days with H1152P, BAPN or the combination of both inhibitors. Interestingly, unlike ROCK inhibition, treatment with BAPN did not change *Lox* and *Acta2* (SMA) transcription levels in rECT (**Figure 24A,B**). *Col1a1* was again found to be unregulated by H1152P

alone, but was moderately increased in the presence of H1152P and BAPN (**Figure 24E**). *Has2* and *Mmp12* were consistently down-regulated by H1152P, independent if BAPN was present or not (**Figure 24F,G**). Interestingly, the RNA level of the major pro-fibrotic cytokine TGF-β was not altered by H1152P, but was significantly increased as a result of LOX inhibition by BAPN (**Figure 24H**).

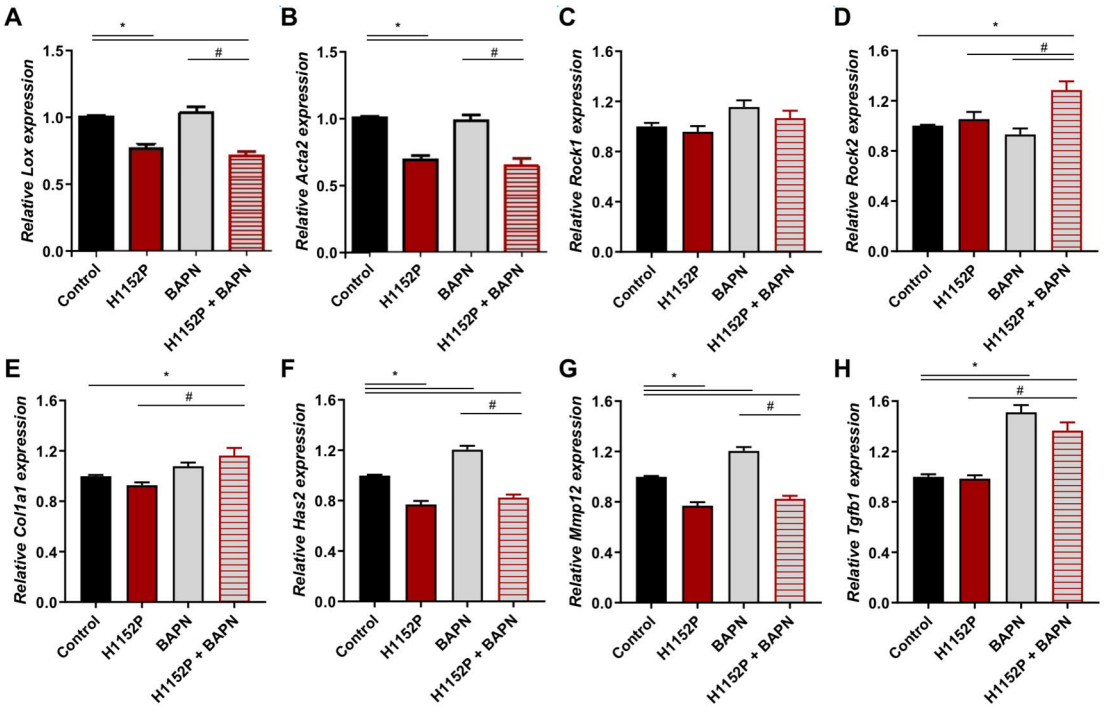

Figure 24. Impact of LOX inhibition at the transcription level on rECT.
rECT were generated with NRCF and collagen I and were cultured for 5 days in the absence (Control) or presence of 3 µM H1152P and/or 100 µM BAPN. RNA was isolated from a total of 12 rECT and expression levels of the genes *Lox* **(A)**, *Acta* (SMA) **(B)**, *Rock1* **(C)**, *Rock2* **(D)**, *Col1a1* **(E)**, *Has2* **(F)**, Mmp12 **(G)** and *Tgfb1* (TGF-β) **(H)** were analysed by qPCR. All values are normalized to the mean of the housekeeping genes *Pbgd* and *Hprt*. Shown are the means+SEM and the differences were evaluated by 1-way ANOVA with Dunnett's *post hoc* test for multiple comparisons (*$p<0.05$ vs. Control, #$p<0.05$ vs. H1152P+BAPN).

Taken together, the differences observed in the regulation of the investigated factors seemed to point to two distinct mechanisms: LOX and SMA appear to be direct ROCK targets, the time-delayed regulation of MMP2 and HAS2 points to a secondary regulating mechanism, and MMP12 may be regulated by mechanosignalling, which is expected to be very different between 3D and 2D cultures. Therefore, the project followed focusing on the path that seemed to be the closest to a direct ROCK-dependent regulation.

4.1.5. Inhibition of actin polymerization and MRTF translocation reduced rECT compaction and stiffness as well as LOX expression

As mentioned before, LOX expression was suggested to be regulated by the actin-regulated MRTF/SRF transcription complex. To validate whether this mechanism plays a role in LOX regulation in the rECT model, the influences of the actin polymerisation inhibitor Lat-A and the MRTF translocation inhibitor CCG-203971 were tested on the mechanical properties of rECT and LOX expression.

Both treatments reduced the rECT compaction, denoted by the significant increase in CSA (**Figure 25A,B**). Both inhibitors also decreased the stiffness of the tissues compared to control (**Figure 25C,D**). Both parameters were more efficiently reduced by Lat-A than by CCG-203971. Neither Lat-A nor CCG-203971 had an influence on the ultimate strain (**Figure 25E**). Subsequent analysis of LOX expression revealed further that Lat-A and CCG-203971 led to a significant reduction of LOX protein in rECT after 5 days of treatment. Moreover, the data revealed that the onset in transcriptional inhibition was faster when the MRTF translocation was suppressed compared to the actin polymerization inhibition as already after 1 day of treatment with CCG-203971, but not with Lat-A LOX levels were significantly reduced compared to control (**Figure 25F,G**).

In summary, inhibition of actin polymerization and MRTF translocation resulted in similar changes in tissue morphology and mechanical properties as found for ROCK inhibition. Together with the results from LOX transcription analyses, this data supported the hypothesis that ROCK regulates LOX expression via the actin/MRTF/SRF pathway.

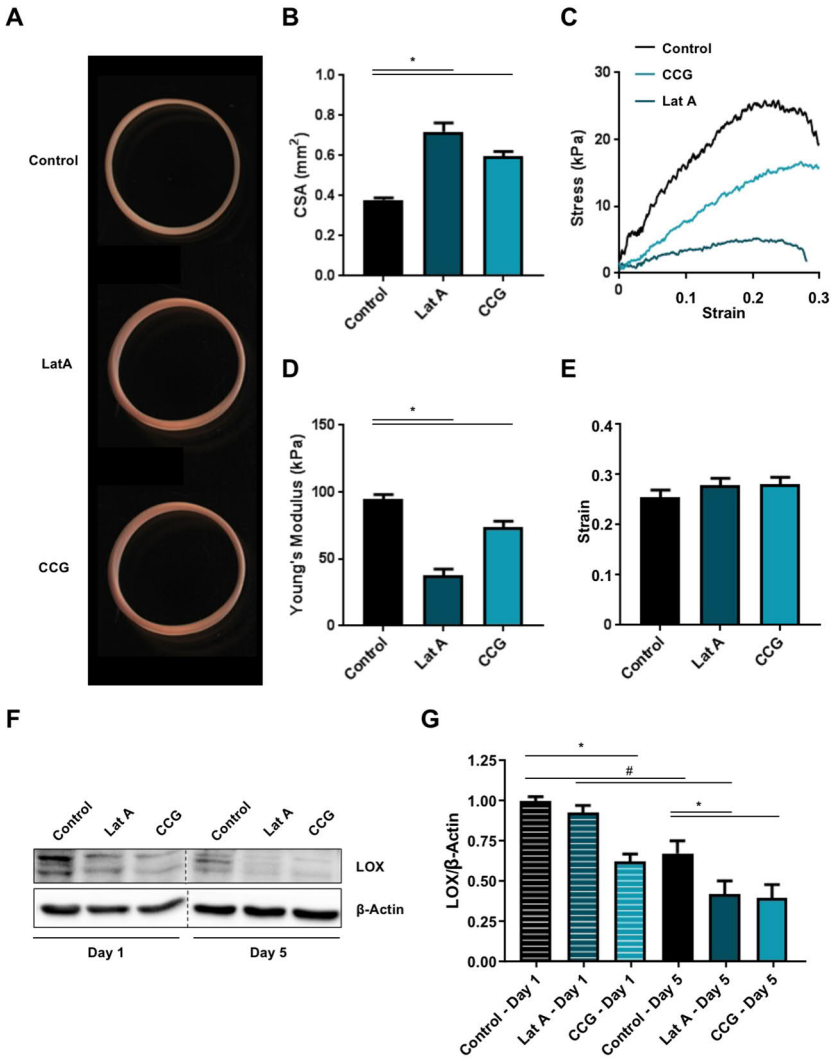

Figure 25. Inhibition of actin polymerization and MRTF translocation reduced rECT compaction and stiffness as well as LOX expression.

rECT were generated with NRCF and collagen I and were cultured for 5 days in the absence (Control) or presence of 7 ng/ml Lat-A or 50 µM CCG-203971 (CCG). **A)** Representative images of rECT are shown. **B)** The cross sectional areas (CSA) were determined by image analysis. Given are the means+SEM of 16 individual tissues from 3 independent experiments. Differences were analysed by 1-way ANOVA with Dunnett's *post hoc* test, *p<0.05 vs. Control. **C)** Representative stress-strain curves from destructive tensile measurements are shown. **D-E)** The Young's moduli **(D)** and the strain to failure point **(E)** were extracted from the obtained stress-strain curves. Given are the means+SEM of 16 individual tissues from 3 independent experiments. Differences were analysed by 1-way ANOVA with Dunnett's *post hoc* test, *p<0.05 vs. Control. **F-G)** Proteins were extracted from rECT treated for 1 or 5 days and subjected to immunoblot analysis. Shown are representative immunoblots of LOX and β-actin **(F)**. LOX expression was normalized to β-actin expression and is given relative to Control - Day 1. The values are means+SEM of 4 independent experiments **(G)**. Differences were analysed by 1-way ANOVA with Dunnett's *post hoc* test for multiple comparisons for each day individually (*p<0.05 vs. Control); and by 1-way ANOVA with Tukey's *post hoc* test for multiple comparisons between all samples (#p<0.05).

4.2. The distinct response of human cardiac fibroblasts to mechanical stimuli and the establishment of a physiological or pathological phenotype in hECT

4.2.1. Contribution of the dynamics between the environmental stiffness and the cellular behaviour to the hECT function

Impact of environmental stiffness on the stiffness of hECT

It was hypothesized that the feedback of the casting moulds' mechanical structure on the hECT has important implications for the development of their own biomechanical properties. Two types of moulds for hECT casting were used to test this hypothesis. One contained two flexible poles made of TM5MED and was therefore called the flexible model, while the stiff model consisted of a mould containing only a stiff central silicon rod. The same volumes of a collagen-cell mixture were used in both moulds and the tissues were cultivated under the same conditions over 5 days (**Figure 26A**). To rule out the influence of the cell content on tissue formation, a cell-free collagen matrix was prepared in flexible moulds as a control. The cross-sectional areas (CSA) and tissue volumes were calculated from measurements made from lateral and top view macroscopic images taken on the fifth day of culture. While the non-populated collagen matrix did not compact, hCF effectively led to compaction of the matrix regardless of the mould used (**Figure 26A-C**). However, when directly compared, hECT from stiff moulds were found to compact significantly more than those prepared in flexible moulds, demonstrating a 30.6% lower CSA (**Figure 26B**) and 23.6% lower volume (**Figure 26C**). From stress-strain analyses, of which representative curves are shown in **Figure 26D**, the retrieved Young's moduli revealed that the tissues prepared in flexible (16.9±0.8 kPa) moulds were not significantly stiffer than non-populated collagen matrix (8.5±0.9 kPa). However, the tissues prepared in stiff moulds (69.8±4.5 kPa) were 4.1- and 8.2-fold stiffer than flexible hECT and the collagen matrix, respectively

(**Figure 26E**). The stiffer hECT could also withstand higher stress as shown by the 6.7-fold change increase in ultimate tensile strength over collagen tissues and 2.3-fold change over flexible hECT (**Figure 26F**). Despite similar stiffnesses, hECT prepared in flexible moulds proved to be significantly stronger withstanding 3.0 times more stress than non-populated collagen matrix (**Figure 26**F). When comparing the two parameters, it was confirmed that the Young's moduli and the ultimate strengths are positively correlating (R^2=0.76) (**Figure 26G**). On the other hand, the stiffer hECT proved to have a less elastic behaviour compared to the flexible ones, as shown by its 29.8% shorter yield point strain which was more comparable to the non-populated collagen matrix (**Figure 26H**). Unlike the correlation with ultimate strength, the Young's modulus described a non-linear relation with the yield strain (**Figure 26I**). To integrate and understand the meaning of this relationship, the resilience of the tissues (area under the curve up to the yield point strain) was calculated. The hECT from stiff moulds presented higher resilience, indicating that it absorbed higher amount of energy that the hECT from flexible moulds, while they were elastically deformed. Contrary, non-populated collagen matrix showed a significantly lower resilience compared to both hECT models, independently of the used mould material and geometry (**Figure 26J**). The stiffer hECT also showed a 31.6-45.3% shortening of the ultimate strain compared to the other two tissues (**Figure 26K**). The Young's modulus and the ultimate strain showed to also have a non-linear relationship (R^2=0.66) (**Figure 26L**), which prompted to investigate the toughness (area under the curve up to the ultimate strain) of the tissues. Interestingly, flexible and stiff tissues had approximately the same measured toughness, which was approximately 3-fold significantly higher than that found for non-populated collagen matrix (**Figure 26M**). In summary, both hECT had the ability to absorb the same amount of energy, during the elastic phase and in total,

but the hECT generated in stiff moulds are stiffer, stronger and less extensible than the flexible hECT. To ease the presentation of the data ahead, based on the mechanical properties of the tissues, those prepared in flexible moulds (TM5MED) will hereinafter be referred to as flexible hECT model and those prepared in stiff moulds referred to as stiff hECT model.

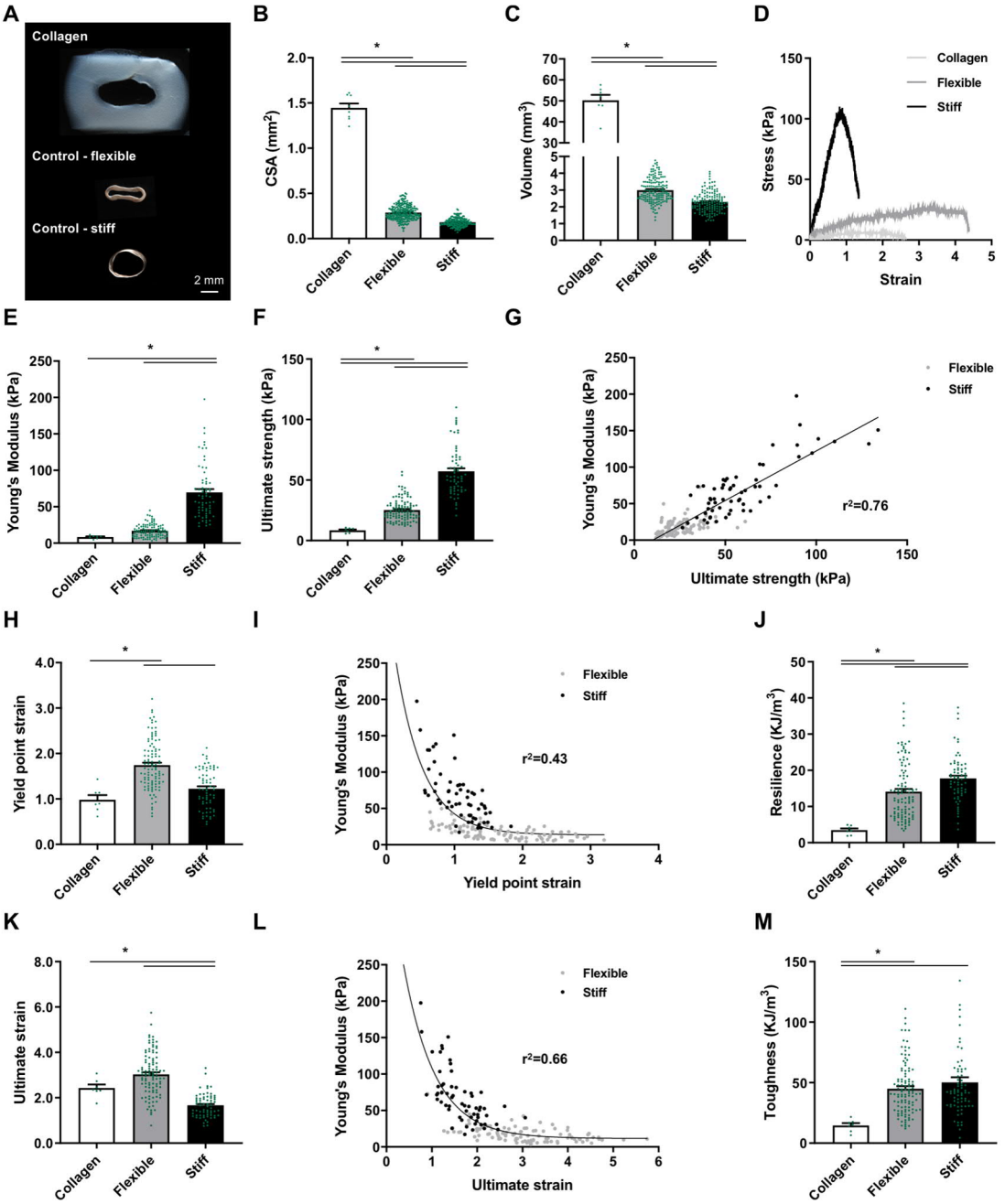

Figure 26. The environmental stiffness determines the stiffness of hECT.
hECT generated with human cardiac fibroblasts and collagen I and were cultured for 5 days on flexible (TM5MED) and stiff casting moulds. An additional control (Collagen) was prepared without cells in the flexible moulds. **A)** Representative macroscopic images of tissues after 5 days in culture are presented. Scale bar = 2 mm. The **B)** cross sectional areas (CSA) and the **C)** volumes of hECT were calculated

(Caption continued on next page)

(Figure 26: caption continued from previous page)
based on measurements of the side and top view macroscopic images. The tissues were subjected to destructive tensile strength measurements. **D)** Representative stress-strain curves of hECT prepared in flexible or stiff moulds and with collagen only are shown. The mechanical parameters **E)** Young's moduli and **F)** ultimate strength are shown. **G)** Scatterplot is showing the linear relationship between the Young's modulus and the ultimate strength. The **H)** Yield point strain and **I)** its non-linear relationship with the Young's moduli are shown. The **J)** resilience was calculated from area under the curve (AUC) up to the yield point strain. The **K)** ultimate strain and **L)** its non-linear relationship with the Young's moduli are shown. The **M)** toughness was calculated from AUC up to the ultimate strain. Values in **B-C** are depicted as means+SEM together with the single data points, n=8 (Collagen), n=176-257 (hECT) for CSA and n=7 (Collagen), n=145-167 (hECT) for volumes. Values in **E**, **F**, **H**, **J**, **K** and **M** were retrieved from stress-strain analysis and are depicted as means+SEM together with the single data points, n=7 (Collagen), n=64-110 (hECT). Scatterplots **(G**, **I**, **L)** show single points for the flexible (grey dots, n=104) and stiff (black dots, n=61-68) hECT. **G)** The relationship between both parameters was analysed by linear regression. The goodness of fit is given by the R^2-value. **I, L)** The relationship between parameters was analysed by a one phase decay equation; the goodness of fit is given by the R^2-value. Significant changes (*$p<0.05$) in **B**, **C**, **E**, **F**, **H**, **J**, **K** and **M** were assessed by 1-way ANOVA with Tukey's *post hoc* test for multiple comparisons.

The hECT model response to narrow variations in environmental stiffnesses

It was confirmed that the mechanical environment determines the biomechanical properties of hECT. Further investigation on whether this interaction could be fine-tuned was essential for understanding how sensitive hCF are to the mechanical environment. Using the flexible hECT model enabled testing poles with different stiffnesses in a 48-multi well plate, hereinafter referred to as gradient plate. The simultaneously tested poles had spring constants ranging from 0.7 to 12.2 mN/mm (**Figure 27A**). The plate was imaged every day during the time-course of five days, under UVA light to detect the poles containing optical brightener (**Figure 27B**). The distances between the poles were measured to determine tissue contraction (**Figure 27C,D**). All tissues reached their maximum point of contraction after 3 to 4 days in culture, regardless of the pole stiffness. As expected, hECT showed greater contraction when using poles of more flexible material and gradually decreased with increasing spring constants (**Figure 27D**). The CSA and tissue volumes after 5 days of culture were determined from macroscopic images as previously described. Tissues in all

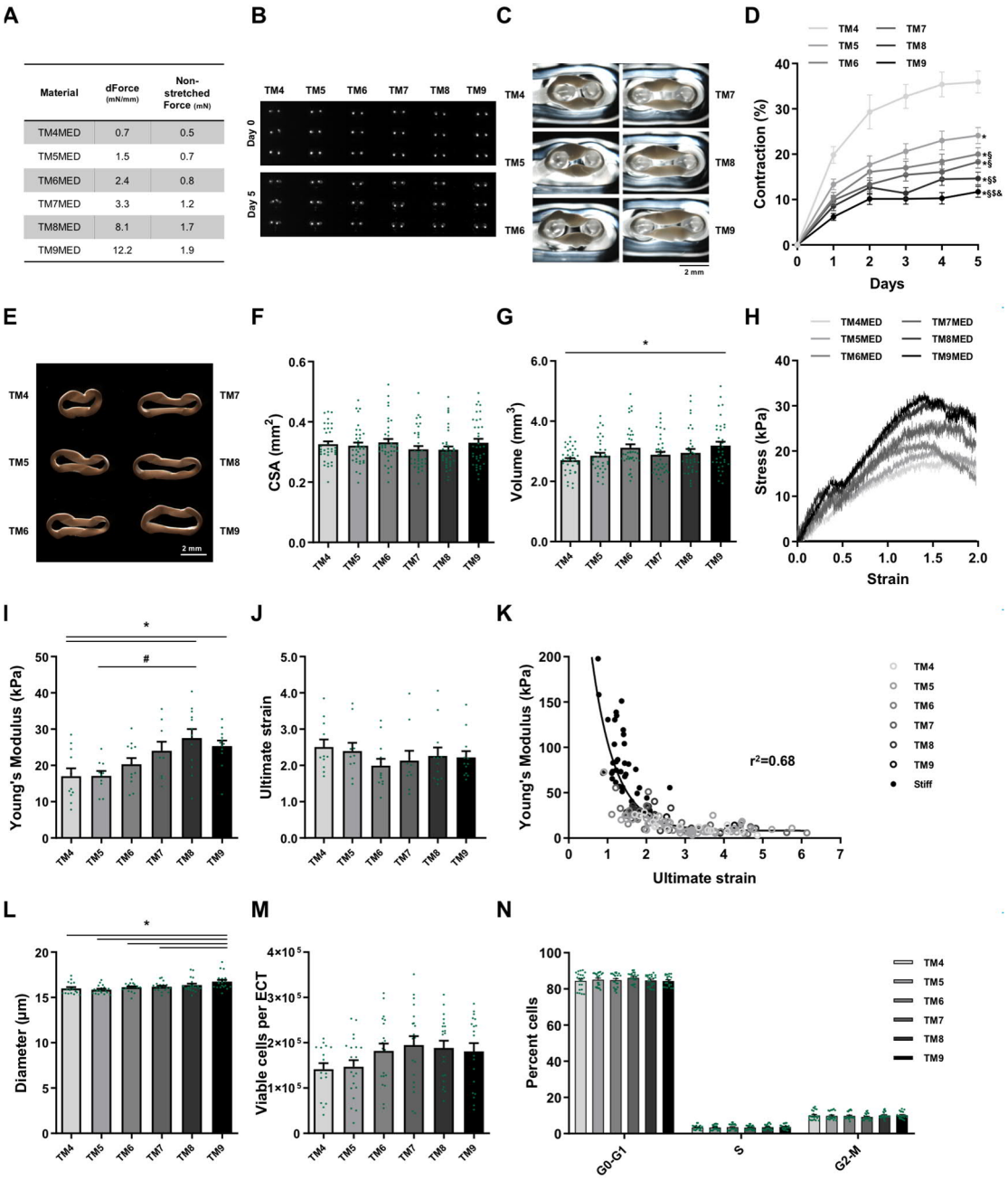

Figure 27. Narrow variations in environmental stiffness are sufficient to determine the hECT contraction and stiffness.

hECT generated with human cardiac fibroblasts and collagen I were cultured for 5 days in moulds containing flexible poles with gradually increasing stiffnesses (TM4MED-TM9MED) and cultured for 5 days. **A)** Material parameters of the poles are given. **B)** Representative imaging of the brighter dye-containing poles at day 0 and day 5 used for poles' deflection measurement are shown. **C)** Representative images of hECT placed in moulds after 5 days are shown. Scale bar = 2 mm. **D)** Tissue contraction was calculated based on pole deflection over a period of 5 days. Values are given as means±SEM, n=36, $p<0.05$ *vs. TM4, §vs. TM5, $vs.TM6, &vs. TM7 at day 5 assessed by 1-way ANOVA with Tukey's *post hoc* test for multiple comparisons. **E)** Representative macroscopic images of hECT as used for dimensional measurements are shown. Scale bar = 2 mm. **F)** Cross sectional areas (CSA) calculated from macroscopic images are presented. Values are given as means+SEM together with the single data points, n=36-37. **G)** Calculated volumes of the hECT after 5 days in culture are given as means+SEM, n=35-37, *$p<0.05$ vs. TM4 assessed by 1-way ANOVA with Dunnett's *post hoc* test for multiple comparisons. Tissues were subjected to destructive tensile strength measurements, from which **H)** representative

(Caption continued on next page)

(Figure 27: caption continued from previous page)
stress-strain curves of hECT are presented. The **I)** Young's moduli and the **J)** ultimate strain values were retrieved from the stress-strain analyses. The values are depicted as means+SEM together with the single data points, n=9-12, significant changes were assessed by 1-way ANOVA with Dunnett's (*p<0.05 vs. TM4) and Tukey's (#p<0.05) *post hoc* tests for multiple comparisons. **K)** Scatterplot demonstrating the non-linear relationship between the Young's modulus and the ultimate strain of all hECT (TM4MED-TM9MED) including the stiff tissues are given. A one phase decay equation was used for analysis; the goodness of fit is given by the R^2-value. The cells werere-isolated from hECT and **L)** cell diameter and **M)** number of viable cells were measured by current exclusion technology. Shown are the means+SEM with the single data points, n=16-20, *p<0.05 vs. TM9 assessed by 1-way ANOVA with Dunnett's *post hoc* test for multiple comparisons.re-isolated cells from the hECT were fixed and flow cytometry analysis was performed. **N)** The percentages of cells in different cell cycle phases are presented, n=20-22 hECT.

groups showed the same CSA independent of the pole stiffness (**Figure 27E,F**). Tissues generated with the stiffer poles (TM9MED) presented higher volumes compared to the ones of flexible poles (TM4MED) (**Figure 27G**). Stress-strain analysis revealed that the Young's moduli of tissues gradually increased with the stiffness of the poles, ranging from 17 to 27.5 kPa. These differences became significant for TM8MED and TM9MED in comparison with TM4MED (**Figure 27H,I**). The range of the pole stiffnesses was not sufficient to denote changes in tissue extensibility, as indicated by the unchanged ultimate strain (**Figure 27J**). Despite this, the Young's moduli and ultimate strains found on these tissues fitted to the before described non-linear relationship (**Figure 27K**). The diameter and cell viability were determined on cells isolated from hECT after 5 days of culture. The increase in cell size was constant from the most flexible towards the stiffest poles, becoming significant for TM9MED in relation to TM4-, TM5- and TM6MED poles (**Figure 27L**). The number of viable cells isolated was similar among the different poles used (**Figure 27M**). Flow cytometry analysis showed that the cell cycle activity was also unchanged. In all groups more than 80% of the cells were found in G0/G1 phase (**Figure 27N**). Taken together, it was proven that the cells embedded in hECT are sensitive to slight differences in the pole stiffness, wherein the range tested was sufficient to generate a tissue stiffness gradient. Notwithstanding, the range used had a minimal influence on the morphology of hECT,

and no impact on tissue extensibility or on the cell cycle activity of the embedded cells.

Role of the actin cytoskeleton and the secretory pathway on the hECT function

Cells naturally exert contractile forces through their actomyosin cytoskeleton which may have implications for the mechanical remodelling of the ECM. But the ECM also undergoes remodelling due to factors secreted by the cells [172]. To test the influence of the actin cytoskeleton and of the secretory pathway, hECT were prepared in flexible (TM5MED) and stiff moulds and treated with the actin polymerisation inhibitor, Lat-A, and the inhibitor of the secretion pathway, Brefeldin A (BFA). Both treatments reduced the hECT compaction in both model systems as indicated by the significant increase in CSA (**Figure 28A,B**). Lat-A treatment led to an increase of the CSA over controls by about 1.6-fold and 1.8-fold in the flexible and stiff model, respectively. The treatment with BFA had a more pronounced impact causing an increase of 4.4 and 4-fold, respectively. As already observed in the previous section, hECT produced in stiff moulds proved to be more compact than those produced in flexible moulds. This was also true for the hECT treated with Lat-A or BFA. The contraction of the tissues cultures in the flexible moulds was assessed during the 5 days of culture. In the absence of any drug, the contraction increased sharply until day 2 and moderately until day 5 where it reached 37.3% contraction. Lat-A significantly affected tissue contraction from day one and the maximum contraction obtained on day five was only about half (17.9%) of that observed in control. Compared to Lat-A, BFA had a significantly higher inhibiting effect on tissue contraction, where 5% was the maximum contraction achieved over time (**Figure 28C**). Interestingly, the observed difference of Lat-A and BFA on tissue contraction in flexible moulds was not reflected in a different decrease in their stiffness (**Figure 28D**). Rheological measurements performed on day 5 showed

that inhibition of actin polymerization and secretion only led to a significant reduction of stiffness in tissues prepared in stiff moulds, and it was identical between Lat-A and BFA with 57.1% and 54.7% of reduction over control, respectively (**Figure 28D**). The differences in magnitude between the measured stiffness in tissues produced in stiff and flexible moulds was confirmed once more. For both hECT prepared in flexible and stiff moulds, the Lat-A treatment did not impact tissue elasticity (yield point strain) nor extensibility (ultimate strain). In contrast, the use of BFA led to a moderate reduction of the strains at the yield and failure points, but only in flexible hECT (**Figure 28E-F**).

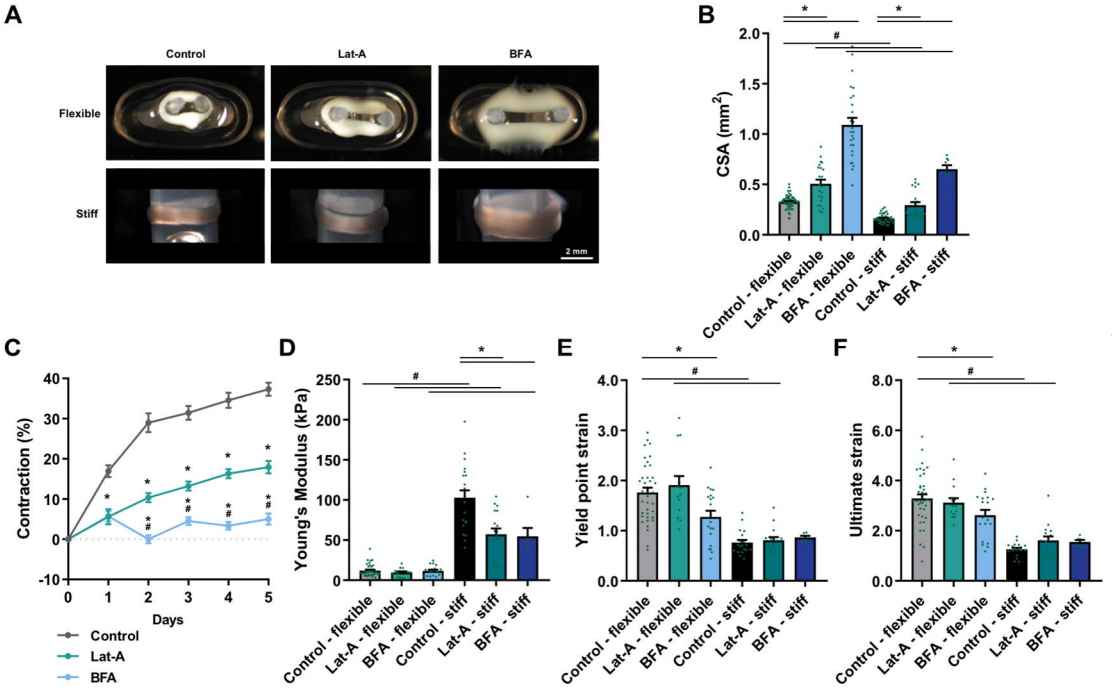

Figure 28. Inhibition of the actin polymerisation and the secretory pathway impacts the hECT compaction, contraction and stiffness.

hECT generated with human cardiac fibroblasts and collagen I were cultured for 5 days on flexible (TM5MED) and stiff casting moulds in the presence or absence of 7 ng/mL Latrunculin-A (Lat-A) or 5 µg/mL Brefeldin-A (BFA). **A)** Representative images of control and treated hECT placed in flexible and stiff moulds after 5 days are shown. Scale bar = 2 mm. **B)** Cross sectional areas (CSA) were calculated from macroscopic images. Values are given as means+SEM together with the single data points, n=22-57 (hECT from flexible moulds) and n=9-39 (hECT from stiff moulds). **C)** Tissue contraction was calculated based on pole deflection over a period of 5 days. Values are given as means±SEM, n=30-53. Significant changes were assessed by 2-way ANOVA with Dunnett's (*p<0.05 vs. Control) and Tukey's (#p<0.05 vs. Lat-A) *post hoc* tests for multiple comparisons. Tissues were subjected to destructive tensile strength measurements. The **D)** Youngs' moduli, **E)** yield point strain and **F)** ultimate strain values were retrieved from the stress-strain analyses. The values are depicted as means+SEM together with the single data points, n=14-38 (hECT from flexible moulds) and n=6-20 (hECT from stiff moulds). Significant changes in **C** and **D-F** were assessed by 1-way ANOVA with Dunnett's *post hoc* test for multiple comparisons within each mould type (*p<0.05 vs. Control); and by 1-way ANOVA with Tukey's *post hoc* test for multiple comparisons between all samples (#p<0.05).

Taken together, both inhibitors resulted in similar effects. Tissue compaction and contraction were clearly influenced by blocking the secretion and the contractile action of the cytoskeleton, although cell secretion seemed to have a greater contribution than the actin-network integrity. These two mechanisms do not seem to be responsible for leading to major changes in tissue elasticity and extensibility, but their contribution to hECT stiffness outcome seems to become more critical when the tissues encounter increasing environmental stiffness.

4.2.2. Understanding the ROCK-LOX axis – the hECT model and its potential as a platform for drug testing

Effect of ROCK inhibition on the tissue compaction, contraction, stiffness, viability, cell cycle and proliferation

The results from rECT produced in stiff moulds pointed to a strong anti-fibrotic potential of pharmacological ROCK inhibition, which was in part due to a regulation of the collagen cross-linker enzyme LOX expression. Therefore, ROCK inhibition was tested next side-by-side in the flexible and stiff hECT models. First, the effect of two concentrations of H1152P (300 nM and 3 µM) was investigated on tissue contraction over the time-course of 5 days in the flexible model. Similar as demonstrated before, the contraction of the control hECT reached its maximum at around day 3 and reached a maximum of 28.1%. In contrast, both concentrations of the ROCK inhibitor H1152P completely prevented the contraction from the beginning on (**Figure 29A,B**). Next, the CSA was determined from macroscopic images of the tissues 5 days after casting. The relative increases in CSA were in both models concentration-dependent and were 1.47- and 1.61-fold with 300 nM H1152P, and 2.12- and 2.92-fold with 3 µM H1152P in relation to the flexible and stiff controls, respectively (**Figure 29C,D**). Comparative

rheological analyses showed that 300 nM H1152P was not sufficient to significantly affect the tissue stiffness regardless of the used mould. In contrast, 3 µM H1152P significantly reduced the Young's moduli by 36% and 56% in the flexible and stiff models, respectively (**Figure 29E**). Tissue elasticity was concentration-dependently affected in the flexible model and inconsistently regulated in the stiff model (**Figure 29F**). Tissue extensibility was unaffected by ROCK inhibition (**Figure 29G**).

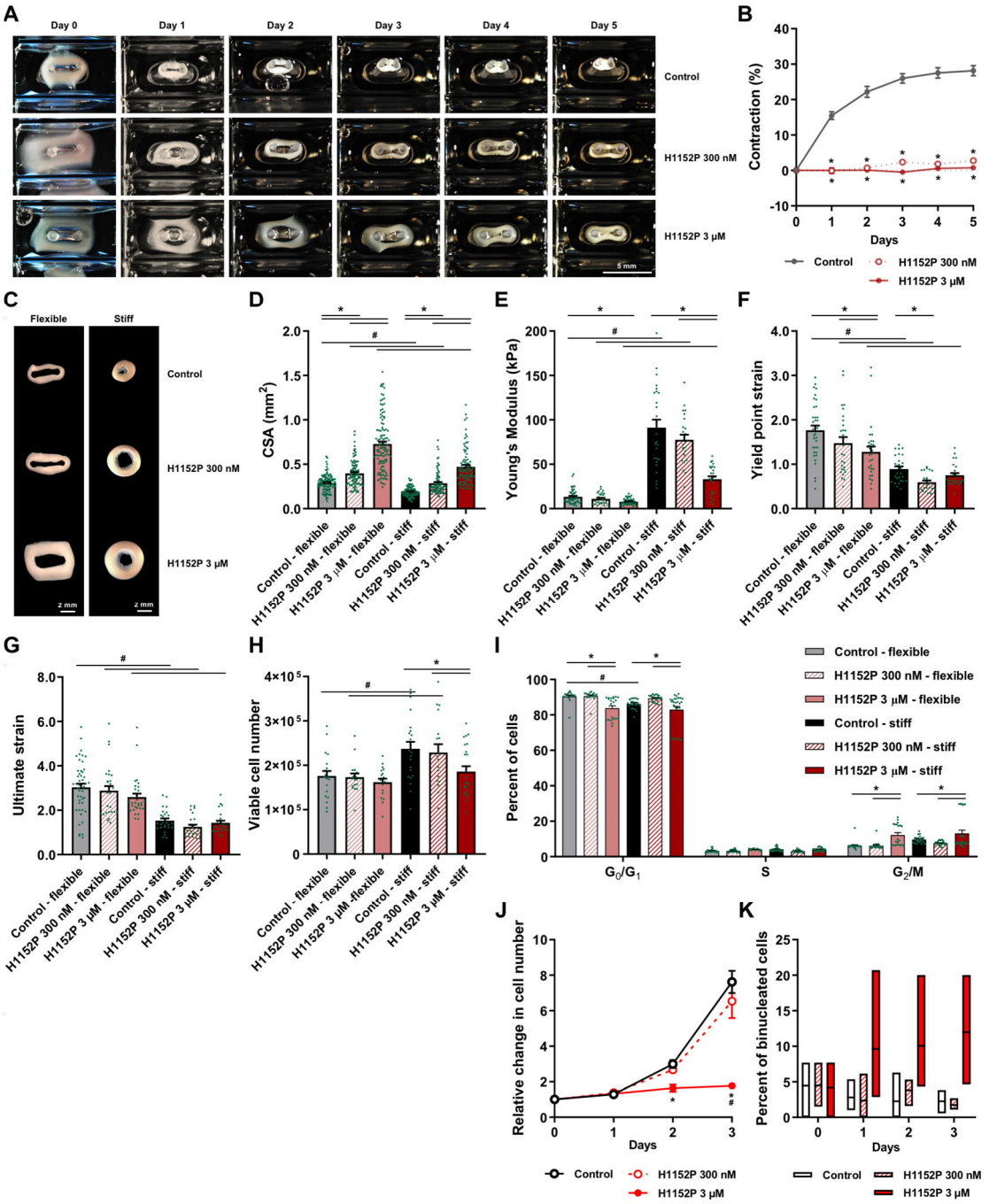

(Figure 29. Caption continued on next page)

(Figure 29: caption continued from previous page)

Figure 29. ROCK inhibition impacts the mechanical properties of hECT and the viability, cell cycle activity and proliferation of the cells.
hECT generated with human cardiac fibroblasts (hCF) and collagen I were cultured in flexible (TM5MED) and stiff moulds for 5 days in the presence or absence of 300 nM and 3µM H1152P. **A)** Representative images of control and treated hECT placed in flexible moulds over a time of 5 days are presented. Scale bar = 5 mm. **B)** Tissue contraction was calculated based on pole deflection in flexible moulds over a period of 5 days and values are given as means±SEM, n=110-116, *p<0.05 vs. control assessed by 2-way ANOVA with Tukey's *post hoc* test for multiple comparisons. **C)** Representative macroscopic images of control and treated hECT from flexible and stiff moulds at day 5 are shown. Scale bars = 2 mm. **D)** Cross sectional areas (CSA) calculated based on macroscopic images are presented. Values are given as means+SEM together with the single data points (n=97-118 hECT from flexible moulds and n=83-94 hECT from stiff moulds). Tissues were subjected to destructive tensile strength measurements and the **E)** Youngs' moduli, **F)** yield point strain and **G)** ultimate strain values were retrieved from the stress-strain analyses. The values are depicted as means+SEM together with the single data points (n=29-48 hECT from flexible moulds and n=23-27 hECT from stiff moulds). Cells werere-isolated from hECT and **H)** number of viable cells was measured by current exclusion technology (n=18-20 hECT from flexible moulds and n=18-23 hECT from stiff moulds). **D-H)** Significant changes within each mould type were assessed independently by 1-way ANOVA with Tukey's *post hoc* test for multiple comparisons (*p<0.05); and differences between all samples were assessed by 1-way ANOVA with Tukey's *post hoc* test for multiple comparisons (#p<0.05). **I)** The cells re-isolated from hECT were fixed and flow cytometry analysis was performed. Percentages of cells in different cell cycle phases are presented (n=21-26 hECT). Significant changes for comparisons within each mould type were assessed independently by 2-way ANOVA with Tukey's *post hoc* test for multiple comparisons (*p<0.05); and differences between all samples were assessed by 2-way ANOVA with Tukey's *post hoc* test for multiple comparisons (#p<0.05). For 2D analysis, **J-K)** hCF were seeded in cell culture plates, treated in the presence or absence of 300 nM and 3µM H1152P and fixed 24 h after seeding (Day 0) as well as 1, 2 and 3 days later. **J)** Cell proliferation was assessed by automatic counting of DAPI-stained nuclei. Given are the relative changes in means±SEM of quadruplicates from 3 independent experiments. The differences were evaluated by 2-way ANOVA with Tukey's *post hoc* test for multiple comparisons (n=3, p<0.05 *vs. Control and $^{\#}$vs. 300 nM H1152P). The **K)** percent of binucleated cells shown was measured from images of FITC-phalloidin- and DAPI-stained cells taken with a 10x objective and a fluorescence microscope (preliminary data obtained from 10 technical replicates).

Next, in order to identify if H1152P impacts cell viability, the cells were isolated from the hECT and the number of viable cells analysed by current exclusion technology. In the flexible model, H1152P had no impact on cell viability. In the stiff model, 20.8% less viable cells could be isolated from the hECT treated with 3 µM H1152P compared to control. The number of cells obtained in that treatment group was however the same as in the same group from the flexible model. In general, a higher number of viable cells isolated could be isolated from stiff hECT (**Figure 29H**). Next, the cell cycle activity of the isolated cells was determined using flow cytometry. The corresponding analysis showed that only the high concentration of H1152P led to changes in the cell

cycle and these occurred in a similar way regardless of the model used. In this condition a reduction in the percentage of cells in G0/G1 phase cells was detectable, which was accompanied by an increase in the percentage of cells in G2/M phase. The amount of S-phase cells did not change significantly between the different treatment groups. Interestingly, more cells were found to be in G0/G1 phase in the flexible compared to the stiff model under control conditions (**Figure 29I**).

To further asses the influence of 3 µM H1152P on the mitogenic behaviour of human CF, cell proliferation was evaluated over 3 days in 2D cultures. As previously demonstrated for NRCF (**Figure 18E**), 300 nM H1152P had no effect on hCF proliferation, while 3 µM H1152P completely prevented it (**Figure 29J**). As a supplementary control, some samples were examined by microscopy to check for the presence of binucleated cells. Similar to the results in NRCF (**Figure 18G**), an obvious increase of binucleated cells from day 1 on was observed due to treatment with 3 µM H1152P (**Figure 29K**).

In this section, it was specifically demonstrated with the hECT model that H1152P not only act as a powerful contraction inhibitor, but also decreased the compaction, the stiffness and the elasticity of the tissues in the flexible and stiff models with minor differences.

LOX expression in the hECT

As in rECT, LOX was identified as potential target of ROCK, the influence of the ROCK inhibitor on LOX expression in flexible and stiff hECT was analysed next by qPCR. In the absence of a ROCK inhibitor, *LOX* expression was significantly higher in stiff compared to flexible tissues. Importantly, it was even higher in 2D cultured cells which supports the idea that *LOX* gene transcription is stiffness dependent (**Figure 30A**). In line with the data obtained in the rat model, in flexible hECT *LOX* levels were

reduced by 27.7% and in stiff hECT by 36.8% after 5 days of treatment with 3 µM H1152P (**Figure 30B,C**).

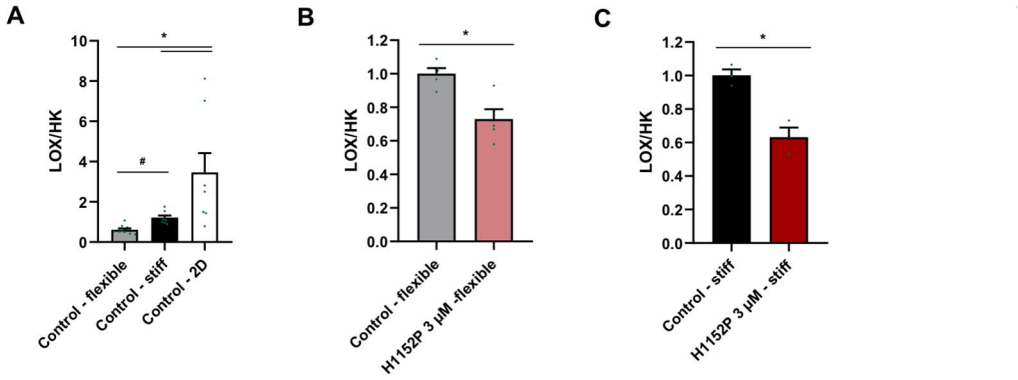

Figure 30. LOX expression is stiffness-dependent and down-regulated by ROCK inhibition in hECT. hECT generated with human cardiac fibroblasts (hCF) and collagen I were cultured in flexible (TM5MED) and stiff moulds for 5 days in the presence or absence of 3µM H1152P. 2D cultured hCF, which served as input for the hECT, were analysed in addition. RNA from pools of 2 hECT each and from hCF monolayers was isolated and qPCR analysis performed. **A)** Comparison of *LOX* gene expression between hECT (n=8-10, 21-29 hECT from 8-10 independent experiments) and 2D cultured hCF (n=8) is shown. The differences between hECT and 2D hCF were evaluated by 1-way ANOVA with with Dunnett's *post hoc* test for multiple comparisons (*p<0.05 vs. 2D). The differences between hECT prepared in flexible and stiff moulds was analysed by unpaired t-test (#p<0.05). The effect of H1152P on *LOX* gene expression was analysed in **B)** hECT from flexible moulds (n=5, 16 hECT from 5 independent experiments) and in **C)** hECT from stiff moulds (n=3, 8 hECT from 3 independent experiments). *LOX* expression is given relative to the controls and the differences were evaluated by unpaired t-test, *p<0.05. All qPCR values were normalized to the housekeeping (HK) gene *GUSB* and shown are the means+SEM with the single points of each averaged independent experiment.

Effect of LOX inhibition on the tissue compaction, contraction and stiffness

To further confirm the role of LOX on the tissue function, 100 µM of the specific inhibitor BAPN was used to treat the hECT in both models. BAPN did not lead to changes in the CSA in comparison to their respective controls (**Figure 31A,C**), corroborating the results previously described for rECT. LOX inhibition had also no impact on hECT contraction in the flexible model (**Figure 31B**). Stress-strain analysis demonstrated that BAPN treatment resulted in a similar reduction of the Young's moduli by 37.9% and 31.2% in the flexible and stiff hECT model, respectively (**Figure 31D**). The yield point strain and the ultimate strain were unaltered by BAPN treatment

(**Figure 31E,F**). Taken together, BAPN inhibition affected the tissue stiffness in hECT, and every other parameter was unaltered.

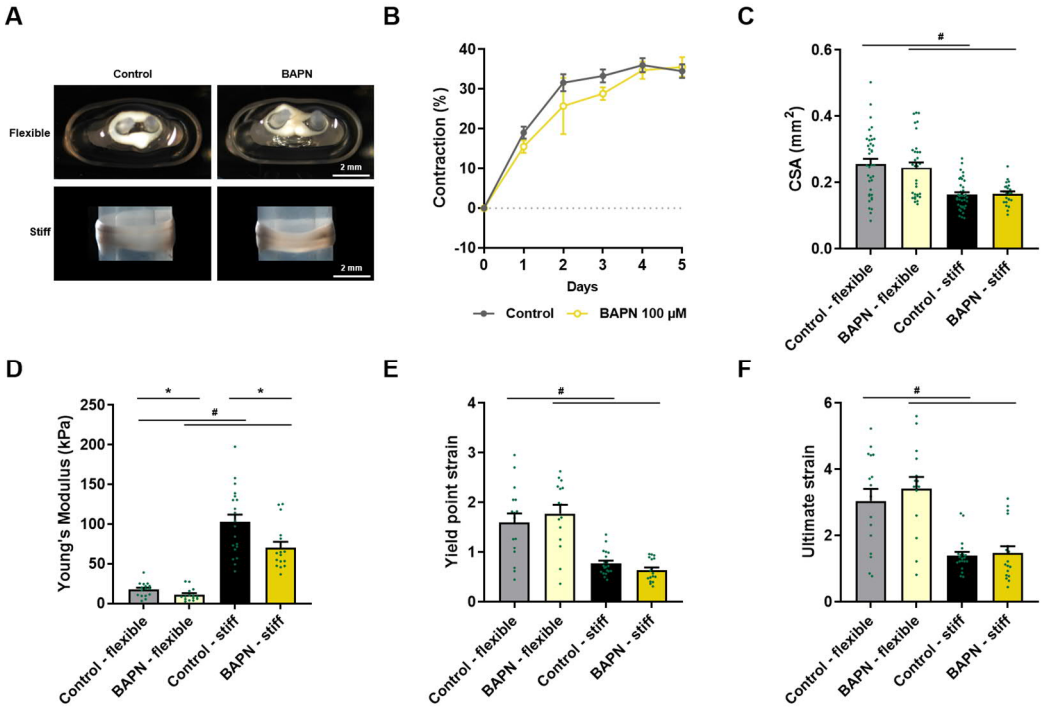

Figure 31. LOX inhibition impacts the hECT stiffness but not tissue compaction and contraction. hECT generated with human cardiac fibroblasts and collagen I were cultured for 5 days on flexible (TM5MED) and stiff casting moulds in the presence or absence of 100 µM β-aminopropionitrile (BAPN). **A)** Representative images of control and treated hECT placed in flexible and stiff moulds after 5 days are shown. Scale bar = 2 mm. **B)** Tissue contraction was calculated based on pole deflection over a period of 5 days and the values are given as means±SEM, n=31-59. **C)** Cross sectional areas (CSA) was calculated from macroscopic images and the values are given as means+SEM together with the single data points, n=22-37 (hECT from flexible moulds) and n=23-39 (hECT from stiff moulds). Tissues were subjected to destructive tensile strength measurements and shown are the **D)** Youngs' moduli, **E)** yield point strain and **F)** ultimate strain values, which were retrieved from stress-strain analyses. The values are depicted as means+SEM together with the single data points, n=15-16 (hECT from flexible moulds) and n=17-20 (hECT from stiff moulds). Significant changes in **D-F** were assessed by unpaired t-test within each mould type (*p<0.05); and by 1-way ANOVA with Tukey's *post hoc* test for multiple comparisons between all samples (#p<0.05).

4.2.3. The effect of 3D environment on the pronounced myofibroblast phenotype reversion in hECT-embedded cells

Influence of environmental stiffnesses on the viability, size and cell cycle activity of hECT-embedded cells

The stress-strain analyses, presented in the paragraphs before, demonstrated that the environmental stiffness fundamentally influences the hECT properties under control

conditions. First data on the cell status in the different hECT showed that the external stiffness can control cell size (**Figure 27L**), cell viability (**Figure 29H**), cell cycle activity (**Figure 29I**) and gene expression (**Figure 30A**). This prompted the following detailed analysis of different cellular parameters in the flexible (TM5MED) and stiff model one and five days after tissue generation.

Before the cells were isolated, the CSA of the hECT were determined. In both models, the CSA decreased between day one and day five, and as demonstrated before the tissues were more compact when prepared in stiff than in flexible moulds (**Figure 32**A).

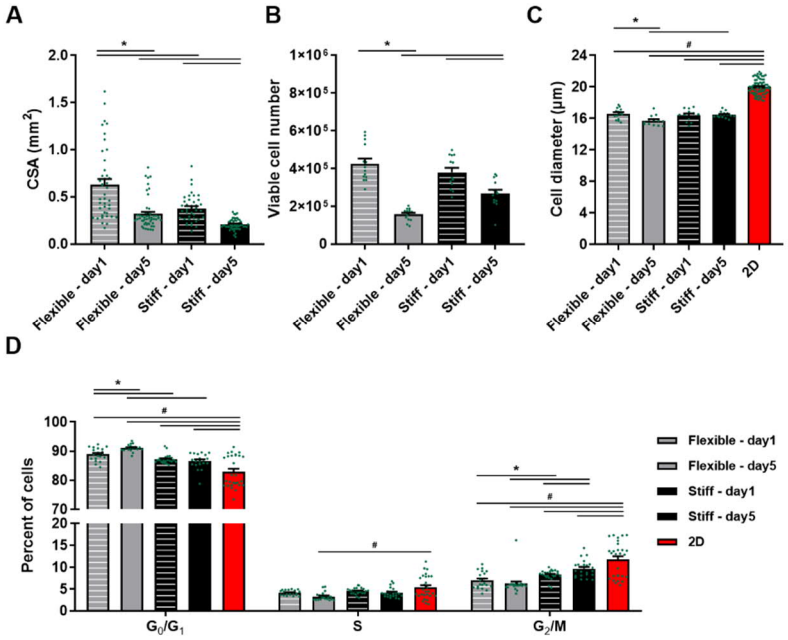

Figure 32. High environmental stiffness influences the cell size, viability and cell cycle activity in hECT-embedded and 2D cultured hCF.

hECT generated with human cardiac fibroblasts (hCF) and collagen I were cultured for 1 and 5 days on flexible (TM5MED) and stiff casting moulds. hCF cultured for 5 days in a 2D format, which served as input for the hECT were used as an additional control. **A)** Cross sectional areas (CSA) were calculated from macroscopic images after 1 and 5 days and values are given as means+SEM together with the single data points (n=42-51 hECT from flexible moulds and n=40-55 hECT from stiff moulds). Cells were re-isolated from hECT after 1 or 5 days and 2D cultured hCF harvested and analysed by current exclusion technology. Shown are the **B)** number of viable cells (n=13-14) and **C)** cell diameter (n=13-71). The graphs depict means+SEM together with the individual data points. Differences between hECT samples were assessed by 1-way ANOVA with Tukey's *post hoc* test for multiple comparisons (*p<0.05). Comparison to 2D cultured hCF was assessed by 1-way ANOVA with Dunnett's *post hoc* test for multiple comparisons (#p<0.05 vs. 2D). **D)** Cell cycle analysis of re-isolated cells from hECT and hCF harvested from 2D cultures was performed by flow cytometry. The percentages of cells in different cell cycle phases are presented as means+SEM together with the individual data points (n=9-10 hECT and n=28 2D). Differences between hECT samples were assessed by 2-way ANOVA with Tukey's *post hoc* test for multiple comparisons (*p<0.05). Comparison to 2D cultured hCF was assessed by 2-way ANOVA with Dunnett's *post hoc* test for multiple comparisons (#p<0.05 vs. 2D).

After cell isolation, analyses by current exclusion and flow cytometry were performed. After one day, approximately 4.2×10^5 viable cells could be isolated from both hECT types (**Figure 32B**). At the fifth day, however, a substantial loss of viable cells was observed in both models. This loss was more pronounced in the flexible hECT model, from which only 1.6×10^5 viable cells could be isolated compared to the 2.4×10^5 viable cells isolated from stiff hECT (**Figure 32B**). In addition to cell viability, the diameters of the isolated cells were determined. For control, 2D cultured cells were used. The measurements revealed that the 3D matrix-embedded cells were independent of the condition substantially smaller than the cells cultured in 2D. By comparing the two 3D models, no differences in cell size was found at day 1. However, at day 5, the cells of the flexible hECT were significantly smaller as the cells of the stiff hECT (**Figure 32C**). Comparative cell cycle analyses demonstrated that the cell cycle activity of the hCF embedded in a 3D matrix was in all conditions lower than that of 2D cultured hCF. The cells which showed the lowest cell cycle activity, were the cells obtained from flexible hECT after 5 days of culture. The cells with the highest activity were those obtained from stiff hECT after 5 days of culture (**Figure 32D**).

The influence of environmental stiffnesses on the expression of the myofibroblast markers SMA and periostin in hECT

So far, the influence of the environmental stiffness on cell viability, size and cell cycle activity could be demonstrated. Next, its effect on the expression of the myofibroblast markers SMA (gene *ACTA2*) and POSTN was investigated. Therefore, flexible and stiff hECT and 2D cultured cells with a clear myofibroblast phenotype were used for qPCR and immunoblot analyses. In agreement with the other cellular parameters shown above, the RNA and protein levels of SMA was in all hECT conditions lower than in

2D cultured cells (**Figure 33A,B**). In addition, although the transcriptional levels of SMA in the flexible hECT model were unchanged during the culture time, the SMA protein level was higher on the first day and decreased by about 70% during the following four days. In the stiff hECT model, SMA protein was lower on the first day compared to flexible hECT, and by tendency increased over the following four days (**Figure 33B,C**). The qPCR analysis confirmed the increase from day one to day five on RNA level (**Figure 33A**). As a result, after five days of culture, the SMA protein level was 2.3-fold higher in stiff hECT compared to the flexible hECT (**Figure 33B,C**).

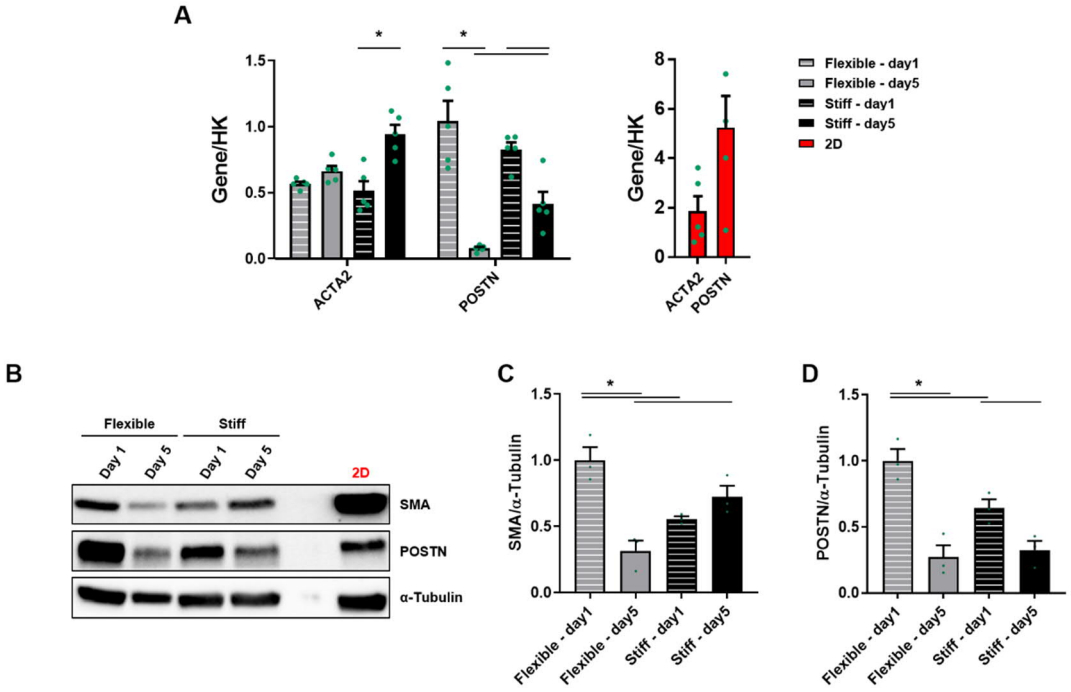

Figure 33. Lower 3D environmental stiffness regulates expression of pro-fibrotic proteins.
hECT generated with human cardiac fibroblasts (hCF) and collagen I were cultured for 1 and 5 days on flexible (TM5MED) and stiff casting moulds. hCF cultured for 5 days in a 2D format, which served as input for the hECT were used as an additional control. Homogenates of pools with at least 2 hECT (RNA) or 3 hECT (protein) each and of 2D cultured hCF were used for RNA and protein analyses by qPCR and immunoblotting, respectively. **A)** qPCR analysis for *ACTA2* (SMA) and *POSTN* are presented as means+SEM with the individual data points, n=4 (4 independent experiments, each with a pool of 2-3 hECT), *p<0.05 was assessed by 1-way ANOVA with Tukey's *post hoc* test for multiple comparisons. 2D cultured hCF were used in addition (right graphs), n=5. All qPCR values were normalized to the mean of the housekeeping (HK) genes *TUBB* and *GUSB*. **B)** Representative immunoblots of SMA, POSTN and α-Tubulin are shown. The quantification of **C)** SMA and **D)** POSTN shown for hECT was normalized by the housekeeping protein α-Tubulin and is given relative to hECT from flexible mould at day 1 (Flexible - day1). Graphs depict means+SEM with the individual data points, n=3 (9 hECT from 3 individual experiments), *p<0.05 assessed by 1-way ANOVA with Tukey's *post hoc* test for multiple comparisons. (Contribution: Alisa DeGrave assisted with the pipetting of part of the qPCR experiments, which were conceived, established, and supervised by Gabriela L. Santos.)

Differently from *SMA*, *POSTN* was significantly reduced in both flexible and stiff models over time. In the flexible hECT the mRNA levels markedly decreased, but only moderately in stiff hECT (**Figure 33A**). Compared to the stiff model, POSTN protein levels were higher at day one in the flexible model and showed a 73% decrease from day one to day five. At day five, the measured protein levels in the stiff hECT was equivalent to the one in flexible hECT model (**Figure 33B,C**). In 2D cultured cells, the *POSTN* RNA level was higher compared to both hECT models (**Figure 33A**), although the protein level was not obviously higher (**Figure 33B**).

Effect of ROCK inhibition on the pro-fibrotic marker SMA in hECT

The effect of ROCK inhibition on SMA expression was demonstrated for rECT. Therefore, the effect of H1152P should be next investigated for hECT.

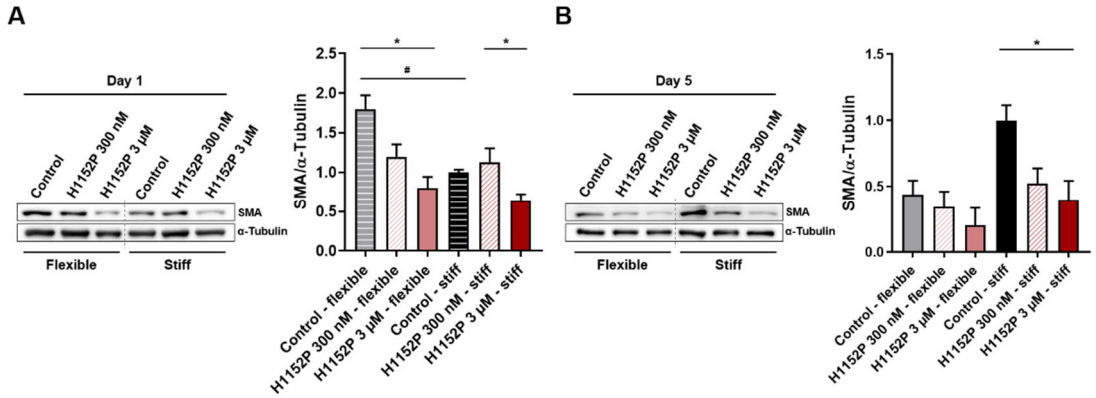

Figure 34. ROCK inhibition in hECT regulates the expression of pro-fibrotic protein SMA.
hECT generated with human cardiac fibroblasts and collagen I were cultured in flexible (TM5MED) and stiff moulds for 1 and 5 days in the presence or absence of 300 nM and 3µM H1152P. Homogenates of pools with 3 hECT each were used for protein analysis by immunoblotting. **A)** Representative immunoblots of SMA and α-Tubulin expression at day 1 are shown in the left panel, and the quantification (right panel) is given normalized by the housekeeping protein α-Tubulin. **B)** Representative immunoblots SMA and α-Tubulin expression at day 5 are shown in the left panel, and the quantification (right panel) is given normalized by the housekeeping α-Tubulin. The graphs depict means+SEM with the individual data points, n=3 (9 hECT from 3 individual experiments). Significant changes within each mould type were assessed independently by 1-way ANOVA with Tukey's *post hoc* test for multiple comparisons (*p<0.05); and comparisons between all samples were assessed by 1-way ANOVA with Tukey's *post hoc* test for multiple comparisons (#p<0.05).

Stiff and flexible hECT treated with 300 nM or 3 µM H1152P for one and five days were used for immunoblot analysis. At day one, there was a concentration-dependent

decline in SMA levels in flexible hECT. In contrast, in stiff hECT only 3 µM H1152P was sufficient to reduce SMA levels. On day 5, H1152P showed no more significant effect in flexible hECT, but diminished SMA expression in stiff hECT (**Figure 34A,B**).

4.2.4. The hECT as a disease model

Transcriptome landscape of hECT – the phenotypic switching

The results obtained up to this point with the flexible and the stiff hECT models suggested that the environmental properties are instructive for the development of different cellular phenotypes. To further investigate the differences between the two models, RNA-seq of flexible and stiff tissues one and five days after generation was performed. The samples will henceforth be called F1, S1, F5 and S5, where F stands for flexible hECT, S for stiff hECT, and the numbers for days of culture.

Sequencing was performed from 3 independent experiments, each consisting of a RNA pool from three hECT. After initial data processing, including normalization of reads per kilobase of transcript per million mapped reads (RPKM) for comparing gene coverage values, a principal component analysis (PCA) was performed. That enabled a comprehensive and unbiased look on how the different testing groups clustered according to their variability based on differential expressed genes (DEGs). Using the first two components, it was found that flexible and stiff hECT from day one are more similar as they are closely clustered (F1 and S1), while F5 vs. F1, S5 vs. S1, and S5 vs. F5 showed higher degrees of dissimilarity. Especially the segregation between S5 vs. F5 in PC2 reflected the differences between the biomechanical properties of the tissues (**Figure 35A**). By extracting the DEGs (log2-fold change ≥ 1, padj ≤ 0.03) from each comparison of interest (F5 vs. F1, S5 vs. S1, S1 vs. F1, S5 vs. F5), it was found that the highest variance was between S5 and F5 in which 1603 genes were differentially

regulated (647 up- and 956 down-regulated) (**Figure 35B,C**). The variance between F5 and F1 followed with 739 up- and 808 down-regulated transcripts, and between S5 and S1 with 689 up- and 723 down-regulated transcripts. As already suggested by the PCA, the lowest variance was found for the comparison S1 vs. F1 with 215 up- and 260 down-regulated transcripts. The DEGs analysis using quasi-proportional Venn diagrams, showed a surprising overlap of 292 up-regulated transcripts in both S5 vs. S1 and S5 vs. F5, which reflected 42.4% and 45.1% of all up-regulated transcripts on each comparison, respectively (**Figure 35B**).

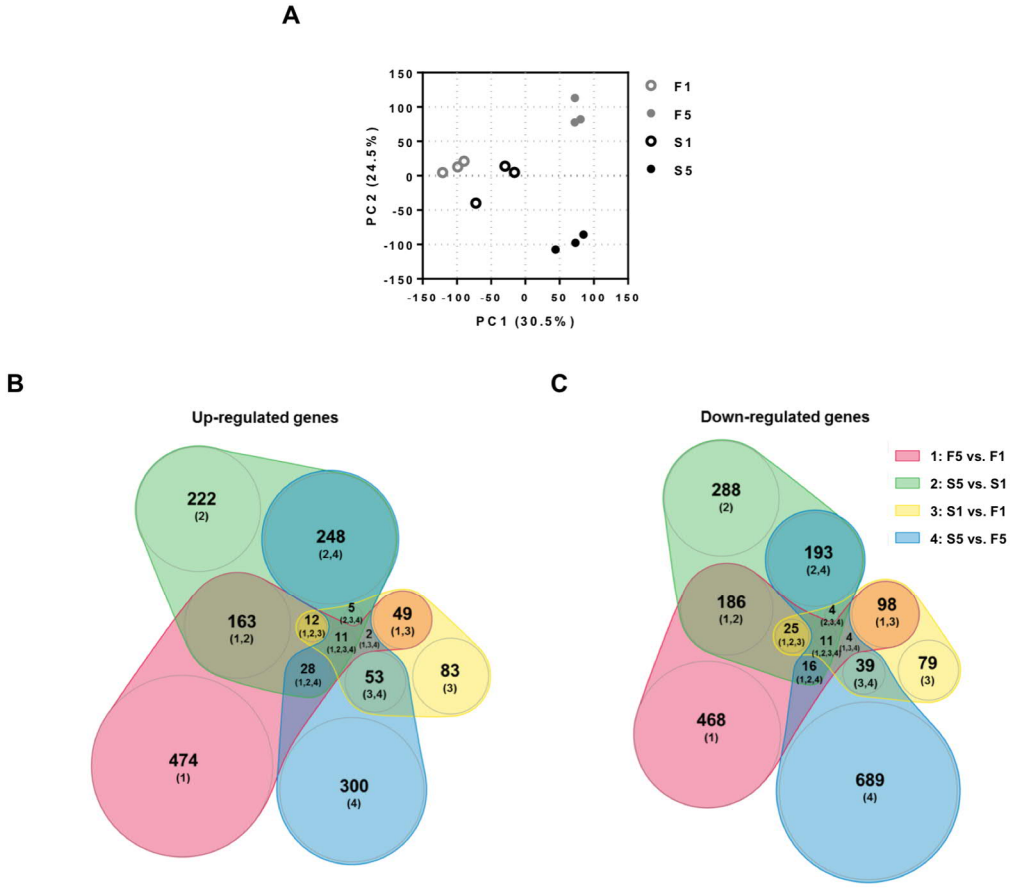

Figure 35. Transcriptome analysis overview evidences extent of variation between the hECT types according to differential regulated genes.
hECT generated with human cardiac fibroblasts and collagen I were cultured for 1 and 5 days on flexible (TM5MED) and stiff casting moulds. Sample groups were named as F1, F5, S1 and S5 accordingly. RNA was isolated from 3 independent experiments, each with a pool of 3 hECT, sequenced and normalized for sequencing depth (RPKM). **A)** Principal component analysis performed on ClustVis was used to visualize how the samples cluster for the most variably expressed genes. Those with RPKM ≥ 1 were included in the analysis. Differentially expressed genes (DEGs) were identified based on a log2-fold change ≥1 or ≤-1 and with a padj ≤0.03. The quasi-proportional Venn diagrams show the overlaps in gene regulation for **B)** up-regulated genes and **C)** down-regulated genes. Colour code for comparisons: Pink F5 vs. F1, Green S5 vs. S1, Yellow S1 vs. F1 and Blue S5 vs. F5.

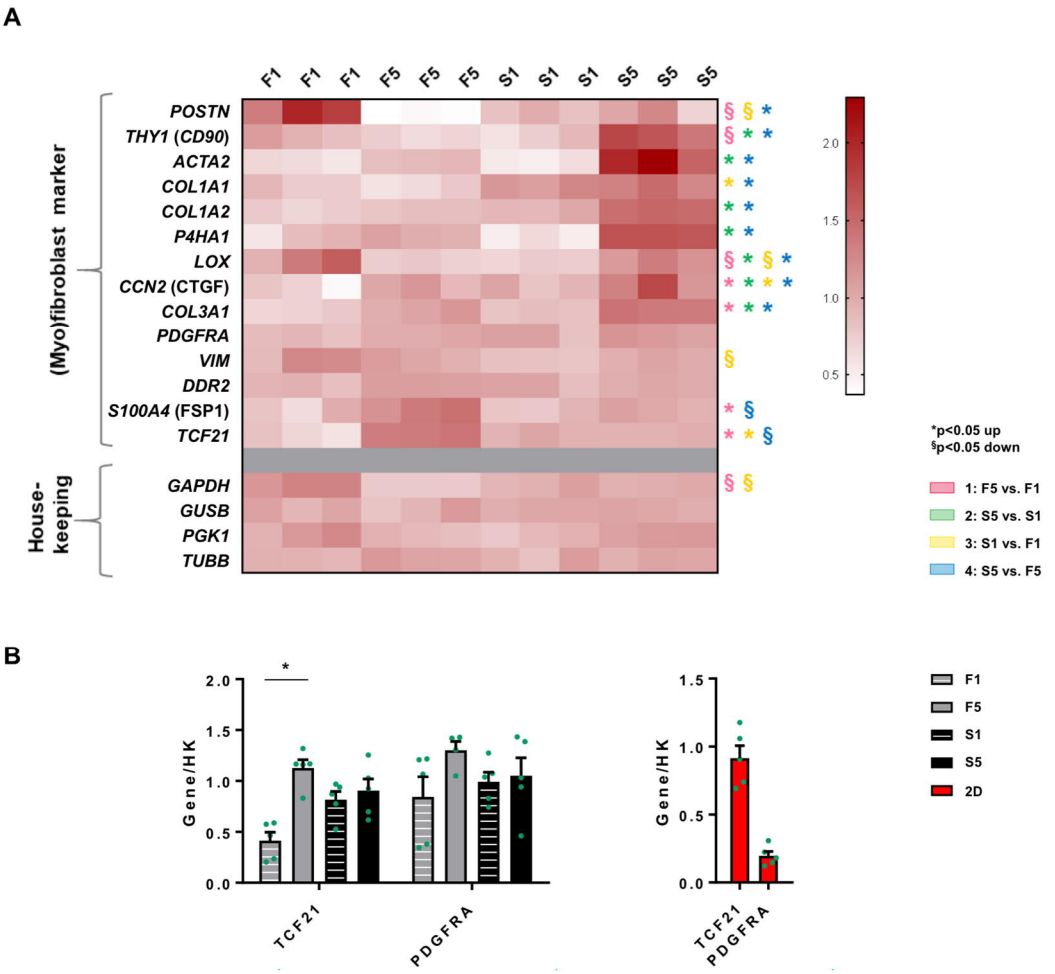

Figure 36. Environmental stiffness influences the transcription of genes that have been used to identify or characterize cardiac (myo)fibroblasts.
hECT generated with human cardiac fibroblasts (hCF) and collagen I were cultured for 1 and 5 days on flexible (TM5MED) and stiff casting moulds. Sample groups were named as F1, F5, S1 and S5 accordingly. RNA was isolated from 3 independent experiments, each with a pool of 3 hECT, sequenced and normalized for sequencing depth (RPKM). Genes with RPKM ≥ 1 were considered and differentially gene expression analysis (DEGs) performed based on a log2-fold change ≥1 or ≤-1 and with a padj ≤0.03. **A)** Heat map of RPKM values shows relative gene expression of published myofibroblast and fibroblast markers between F1, F5, S1 and S5 sample groups. Only genes belonging to the DEGs group were considered. Significant changes between the RPKM values were identified by 1-way ANOVA with Tukey's *post hoc* test for multiple comparisons (*up-regulation and §down-regulation with $p<0.05$ Pink F5 vs. F1, Green S5 vs. S1, Yellow S1 vs. F1 and Blue S5 vs. F5). **B)** qPCR analysis for validation of the detected changes in gene expression of *TCF21* and *PDGFRA* in hECT. The values are presented as means+SEM with the individual data points given, n=4 (4 independent experiments, each with a pool of 2-3 hECT), *$p<0.05$ was assessed by 1-way ANOVA with Tukey's *post hoc* test for multiple comparisons. hCF cultured for 5 days in a 2D format, which served as input for the hECT, were used as an additional control (right graphs), n=5. All qPCR values were normalized to the mean of the housekeeping (HK) genes *TUBB* and *GUSB*. (Contribution: Alisa DeGrave assisted with the pipetting of part of the qPCR experiments, which were conceived, established, and supervised by Gabriela L. Santos.)

Guided by the hypothesis that the two models of hECT present different phenotypes, first the transcription patterns of genes that have been used to identify or characterize cardiac (myo)fibroblasts [203, 431] was investigated. Strikingly, proposed myo-

fibroblast markers such as *ACTA2* (SMA), *THY1* (CD90), *COL1A2*, *P4HA1*, *LOX*, *CCN2* (CTGF), and *COL3A1* showed higher RNA levels in stiff hECT at day five compared to day one (S5 vs. S1). On the other hand, the transcription of *POSTN*, *THY1* and *LOX* lowered in flexible hECT at day five compared to day one (F5 vs. F1). The highest number of myofibroblasts markers differentially regulated, which additionally included COL1A1, was found when comparing stiff and flexible hECT at day five (S5 vs. F5). Interestingly, the CF marker *TCF21* was higher on flexible hECT day five (F5 vs. F1), but maintained lower and unchanged levels in stiff hECT (S5 vs. F5 and S5 vs. S1). The *PDGFRA* and *DDR2* fibroblast genes were unchanged, as were the housekeeping genes *GUSB*, *PGK1*, and *TUBB* (**Figure 36A**). Some of the observed changes were validated by qPCR, where RNA from cardiac myofibroblasts of 2D cultures was used as an additional control. The increase in *TCF21* transcription in flexible hECT between the first and fifth day was validated. The transcription of the *PDGFRA* receptor was confirmed to be constant between the models, but interestingly it was considerably lower in 2D cultured cells (**Figure 36B**). Previous qPCR analysis of *SMA* and *POSTN* (**Figure 33A**) were in line with the changes observed in the RNA-seq analysis.

To aid the interpretation of the transcriptome dataset of the different tissues, a highly stringent Gene Ontology (GO) analysis was performed by comparing the results obtained with four different classification tools (Panther, David, GOrilla, String). Only the GO-terms that were detected by the four programs with -log FDR ≥ 3 according to the Panther analysis were considered. The highest probabilities were found for down-regulated genes in F5 vs. F1 which were significantly enriched for *ECM organization* (GO:0030198), and for up-regulated genes in S5 vs. F5 which were significantly enriched for *response to unfolded protein* (GO:0006986) (**Figure 37A**).

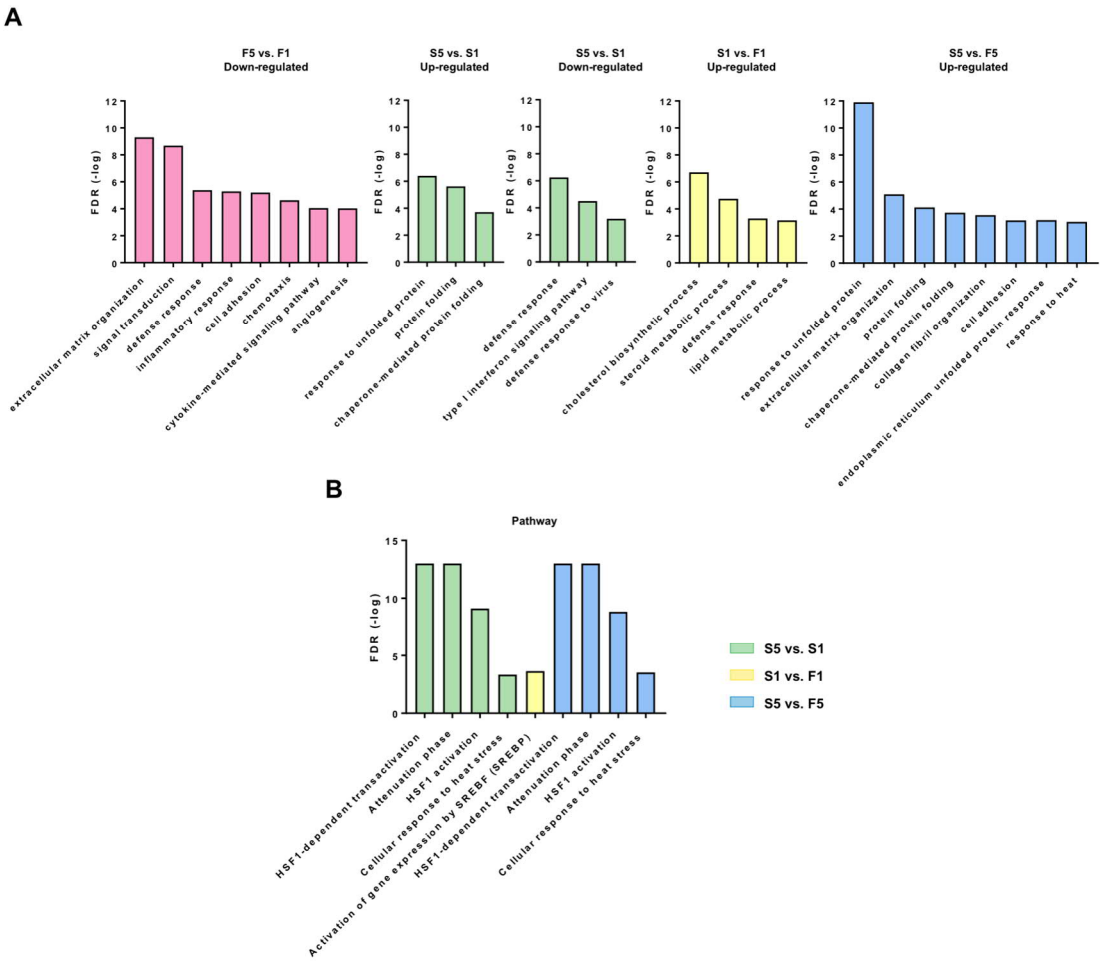

Figure 37. Environmental stiffness in hECT determines the regulation of processes mainly related to ECM organization, protein folding and response to unfolded proteins.
hECT generated with human cardiac fibroblasts and collagen I were cultured for 1 and 5 days on flexible (TM5MED) and stiff casting moulds. Sample groups were named as F1, F5, S1 and S5 accordingly. RNA was isolated from 3 independent experiments, each with a pool of 3 hECT, sequenced and normalized for sequencing depth (RPKM). Genes with RPKM ≥ 1 were included in the analysis. Differentially expressed genes (DEGs) were identified based on a log2-fold change ≥ 1 or ≤ -1 and with a padj ≤ 0.03 and used for the following analyses. **A)** Comparative gene ontology (GO) analysis shows the enriched GO terms commonly detected by the online tolls Panther, String, GOrilla and David, with a -log FDR>3 according to Panther. **G)** Pathway analysis performed with Reactome shows the main enriched activated pathways. Bars colour stand for comparisons: Pink F5 vs. F1, Green S5 vs. S1, Yellow S1 vs. F1 and Blue S5 vs. F5.

Up-regulated genes of the cluster *response to unfolded protein* were also vastly represented in S5 vs. S1 indicating that the induction of these genes was specific for the stiff hECT model (**Figure 37A**). Next, pathway analysis with Reactome investigated enrichment for biologically relevant pathways and functions. An enrichment of the *Heat shock factor 1 (HSF1)-dependent transactivation* pathway (R-HSA-3371571) in stiff tissues (S5 vs. S1 and S5 vs. F5) was identified (**Figure 37B**),

which was in line with the increased transcription of genes belonging to GO *response to unfolded protein*.

In **Figure 38A**, the volcano plot presents the overall distribution of all genes according to their log2-fold change and -log padj. The DEGs with a log2-fold change ≥1, padj ≤0.03, are highlighted and were considered for further analysis. The top genes by p-values that were identified in the clusters associated to the GO terms *protein folding, response to unfolded protein* and *response to topologically incorrect proteins* are labelled in **Figure 38B**, and the ones identified in the cluster associated to *ECM organization* are labelled in **Figure 38C**.

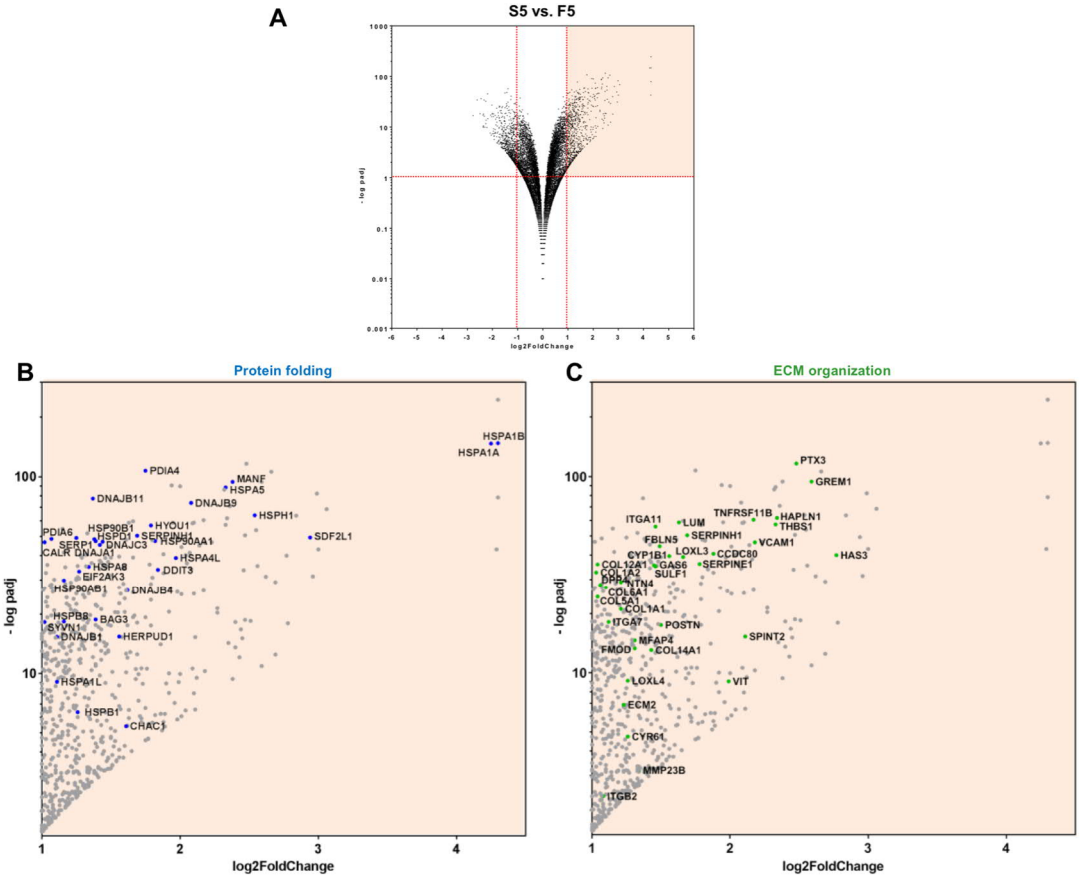

Figure 38. Volcano plot depicts the top up-regulated genes in stiff hECT in the context of protein folding and ECM organization.
hECT were generated with human cardiac fibroblasts and collagen I and cultured for 5 days on flexible (TM5MED) and stiff casting moulds. Sample groups were named as F5 and S5 accordingly. RNA-sequencing data from 3 independent experiments, each with a pool of 3 hECT, was adjusted for sequencing depth (RPKM) and used for differentially expressed genes (DEGs) analysis. Genes with RPKM ≥ 1 were considered. **A)** The volcano plot depicts differences in gene transcription for S5 vs. F5. The top DEGs identified based on a log2-fold change ≥1 and with a padj ≤0.03 (orange square) are separately depict for clusters related to **B)** protein folding and to **C)** extracellular matrix organization.

A differential network analysis was used to compare the set of inter-connections of over-expressed genes between stiff and flexible hECT after a period of five days in culture. The DEGs from that dataset were used to construct a protein-protein interaction (PPI) network via the online database STRING (**Figure 39**).

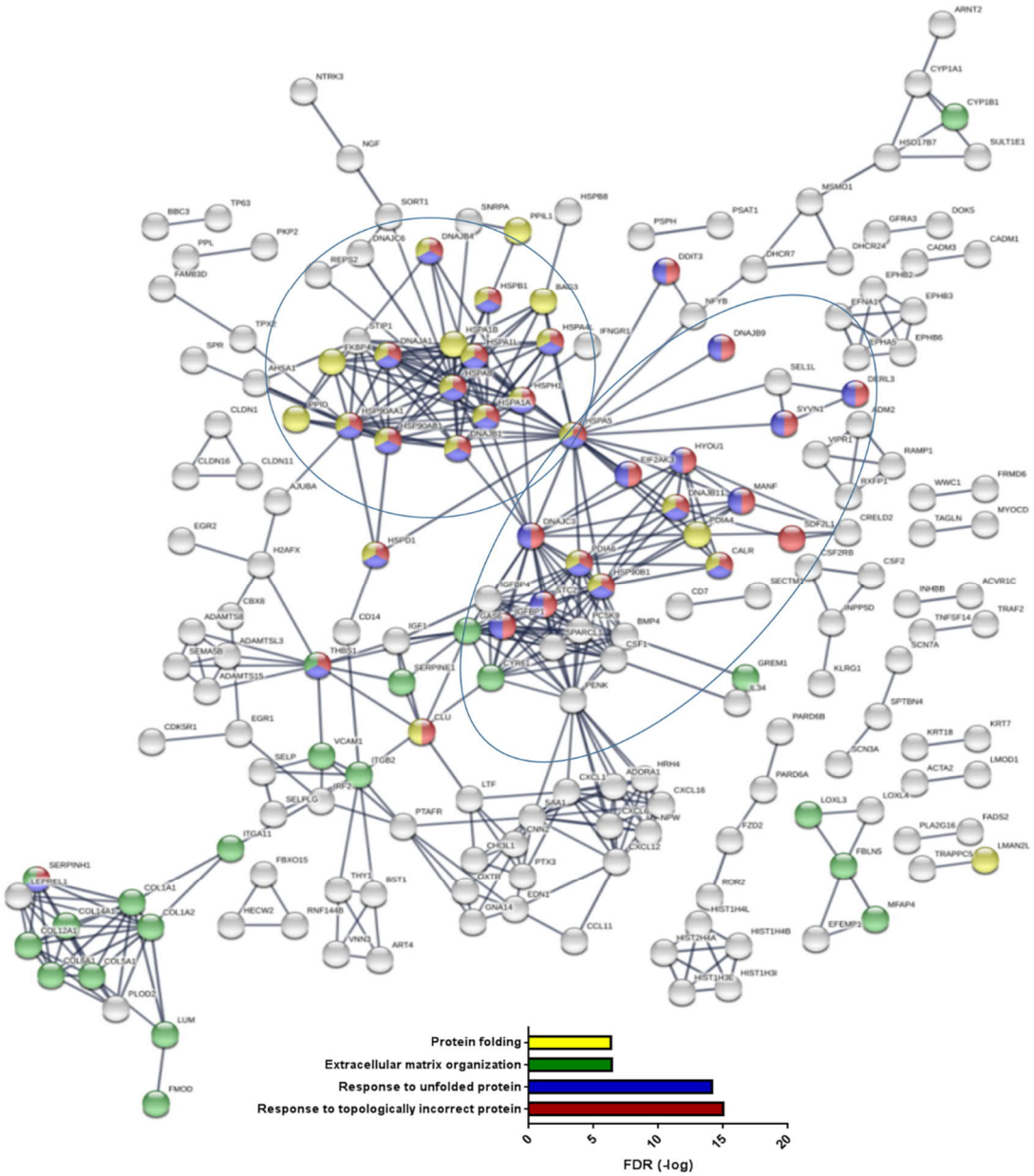

Figure 39. Differential network analysis depicts the clustering of up-regulated genes in stiff hECT in the context of protein folding and ECM organization according to their inter-connections.
hECT generated with human cardiac fibroblasts and collagen I were cultured for 5 days on flexible (TM5MED) and stiff casting moulds. Sample groups were named as F5 and S5 accordingly. RNA-sequencing data from 3 independent experiments, each with a pool of 3 hECT was adjusted for sequencing depth (RPKM) and used for differentially expressed genes (DEGs) analysis. Genes with RPKM ≥ 1 were considered. String analysis (confidence level >0.9, disconnected nodes are not shown) shows the clustering of the up-regulated genes (S5 vs. F5, log fold-change ≥ 1, padj ≤ 0.03). Colour scheme represents the GO term membership.

The genes were screened by calculating the number of interconnections between encoded proteins. Genes belonging to the GO terms *protein folding*, *response to unfolded protein* and *response to topologically incorrect proteins* could be divided into two sub-clusters. The larger cluster predominantly comprised genes that encode proteins involved in protein folding in the cytosol, whereas the smaller gene cluster included genes which play a role in protein folding in the endoplasmic reticulum (ER) and in the unfolded protein response like *DDIT3* (coding gene for CHOP) and *EIF2AK3* (coding gene for PERK). Genes belonging to the GO term *ECM organization* were organized in a distinctly separate cluster.

Furthermore, unsupervised hierarchical clustering of the expression profiles for the DEGs included in the above mentioned clusters is respectively shown in **Figure 40A** (*protein folding*, *response to unfolded protein* and *response to topologically incorrect proteins*) and **Figure 40B** (*ECM organization*). The heat maps presenting the relative changes in gene transcription reveal the distinct transcriptomic signature of stiff hECT at day five compared to flexible hECT or to short-term cultured flexible and stiff hECT. In this network were found several key heat shock family members belonging to the process of protein folding in the cytosol. Besides, the genes from UPR modulators *EIF2AK3* and *DDIT3* and elements involved in the process of protein folding in the endoplasmic reticulum (ER) such as the ER chaperones *HSPA5* and *HSP90B1*, the co-chaperone *DNAJB9* and the catalytic enzyme *PDIA4* were also found (**Figure 38B**, **Figure 40A**). In the ECM organization cluster, other than *POSTN*, were found ECM components such as *COL1A1* and the collagen organizers *LUM* and *LOX*, the matricellular factor *CYR61* (CCN1), the TGF-β1 responsive Thrombospondin-1 (*THBS1*) and Sulfatase 1 (*SULF1*), and the cell adhesion promoter *CCDC80* (**Figure 38C** and **Figure 40B**). From the identified genes, *THBS1* and *SERPINH1* are associated

with both over-represented GO terms.

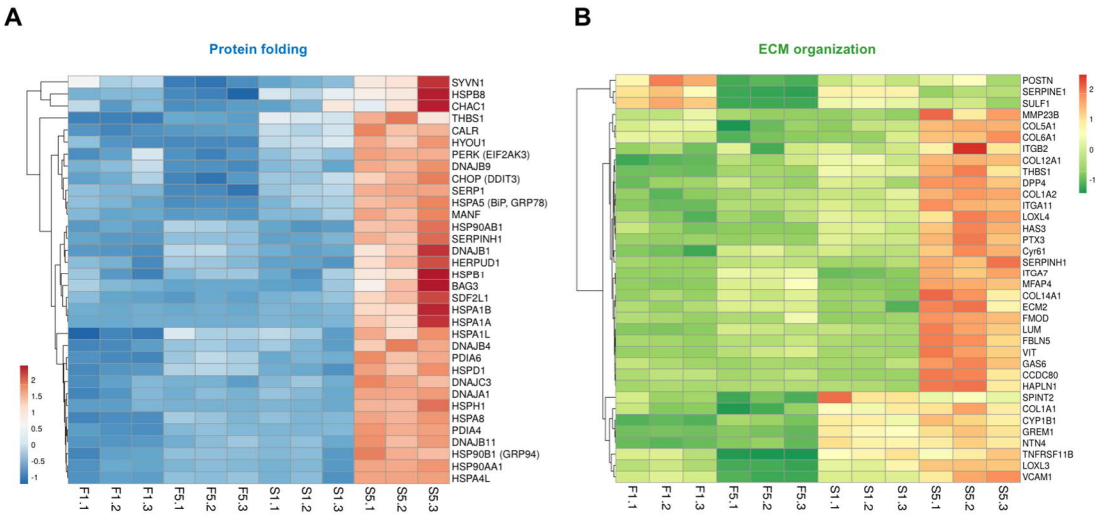

Figure 40. Transcriptome analysis shows the environmental stiffness influence in gene transcription in the context of protein folding and ECM organization.
hECT generated with human cardiac fibroblasts and collagen I were cultured for 1 and 5 days on flexible (TM5MED) and stiff casting moulds. Sample groups were named as F1, F5, S1 and S5 accordingly. RNA-sequencing data from 3 independent experiments, each with a pool of 3 hECT was adjusted for sequencing depth (RPKM) and used for differentially expressed genes (DEGs) analysis. Genes with RPKM ≥ 1 were considered. Heat maps were generated with ClustVis and depict clustering and relative changes in expression of the identified genes (log2 fold-change ≥1, padj ≤0.03) belonging to the GO-terms **A)** *protein folding* and **B)** *extracellular matrix organization.*

It was of interest to further validate the gene levels of such key players by qPCR assay. Gene levels were tested for hECT from independent experiments and additionally for cells from 2D cultures and it was possible to largely confirm the major regulations found in the RNA-seq analysis. From the selected genes, it was shown that many of those involved in protein folding in the cytosol and in the ER are expressed at a similar level in cells cultivated in 2D and in stiff hECT of day five (**Figure 41A,C**). Curiously, the two genes involved in the UPR signalling (*DDIT3* and *EIF2AK3*) and *PDIA4* showed lower transcription levels in 2D cells compared to the stiff hECT of day five (**Figure 41B,C**). Significantly or by trend, the genes of the UPR and ER protein folding sets were less expressed in flexible hECT from day five compared to stiff hECT from the same day (**Figure 41B,C**). The same holds true for the cytosolic chaperones *HSPA1A*, *HSP90AA1* and *HSPH1* (**Figure 41A**).

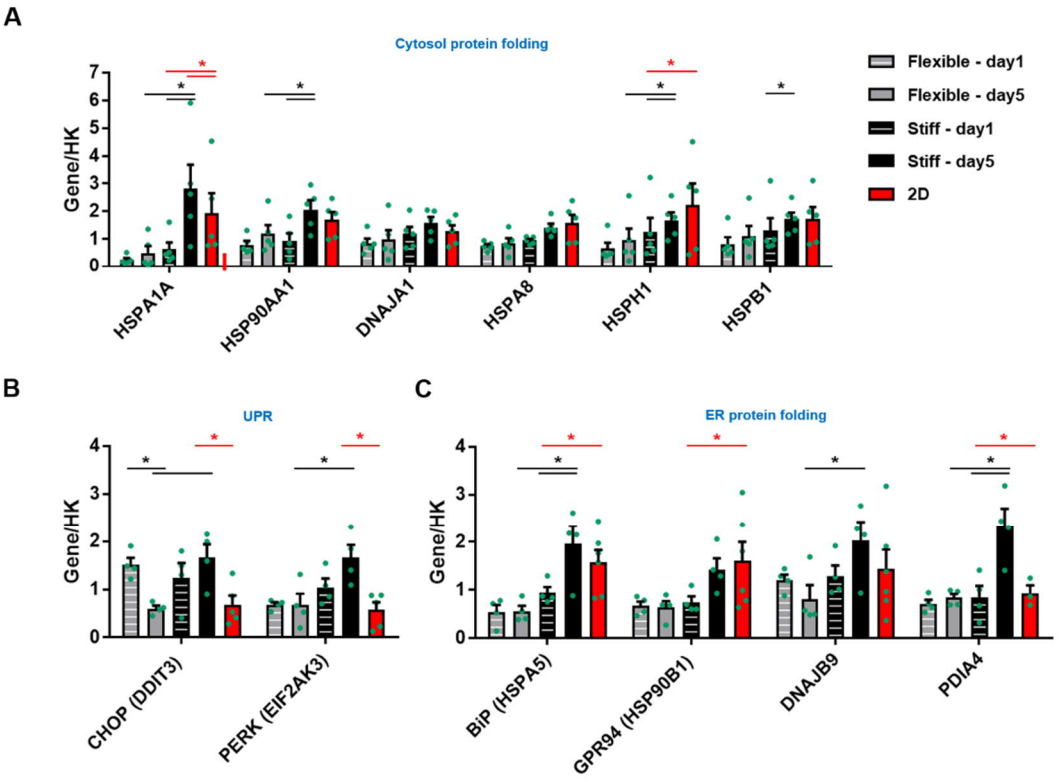

Figure 41. qPCR analysis shows the environmental stiffness influence in gene transcription in the context of protein folding and ECM organization.
hECT generated with human cardiac fibroblasts (hCF) and collagen I were cultured for 1 and 5 days on flexible (TM5MED) and stiff casting moulds. Sample groups were named as F1, F5, S1 and S5 accordingly. hCF cultured for 5 days in a 2D format, which served as input for the hECT, were used as an additional control. RNA was isolated from pools of 2-3 hECT or hCF monolayers and used for qPCR analysis. Changes in gene expression are presented for exemplary genes involved in **A)** protein folding in the cytosol, **B)** unfolded protein response (UPR), and in **C)** protein folding in the endoplasmic reticulum (ER) and protein folding. All qPCR values were normalized to the mean of the housekeeping (HK) genes *TUBB* and *GUSB*. Shown are the means+SEM with the single data points, n=4-5, *p<0.05 assessed by 2-way ANOVA with Tukey's (between hECT conditions) and Dunnett's (to 2D) *post hoc* tests for multiple comparisons. Black stars depict differences within the F1, F5, S1 and S5 groups, red stars depict differences between the 2D data and the hECT conditions. (Contribution: Alisa DeGrave assisted with the pipetting of part of the qPCR experiments, which were conceived, established, and supervised by Gabriela L. Santos.)

Most of the extracellular matrix genes tested were expressed in a comparable way between cells cultivated in 2D and in stiff hECT of day five, and significantly less expressed in flexible hECT of the same day. Only *CCDC80* presented higher levels in 2D cells compared to the stiff hECT of day five. From this set, *SULF1* levels were shown to reduce in flexible hECT compared to stiff hECT at day five (**Figure 42**). The same was true for *DDIT3* in the UPR signalling set of genes (**Figure 41**). This analysis also revealed that the 3D environment under stiff conditions was particularly inductive

for the transcription of genes such as *HSPA1A*, *DDIT3*, *EIF2AK3* and *PDIA4*, arguing for a differential gene regulation between 2D and 3D environments.

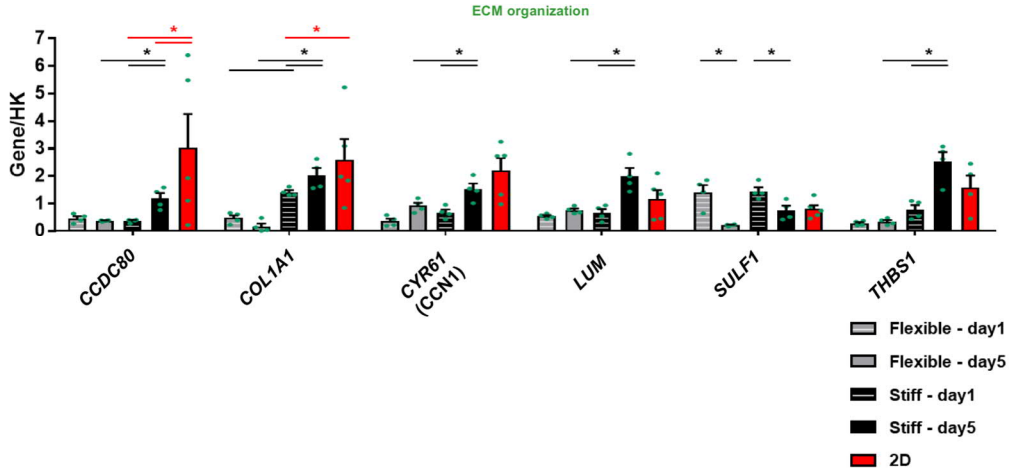

Figure 42. qPCR analysis shows the environmental stiffness influence in gene transcription in the context of protein folding and ECM organization.
hECT generated with human cardiac fibroblasts (hCF) and collagen I were cultured for 1 and 5 days on flexible (TM5MED) and stiff casting moulds. Sample groups were named as F1, F5, S1 and S5 accordingly. hCF cultured for 5 days in a 2D format, which served as input for the hECT, were used as an additional control. RNA was isolated from pools of 2-3 hECT or hCF monolayers and used for qPCR analysis. Changes in gene expression are presented for exemplary genes involved in extracellular matrix (ECM) organization. All qPCR values were normalized to the mean of the housekeeping (HK) genes *TUBB* and *GUSB*. Shown are the means+SEM with the single data points, n=4-5, *p<0.05 assessed by 2-way ANOVA with Tukey's (between hECT conditions) and Dunnett's (to 2D) *post hoc* tests for multiple comparisons. Black stars depict differences within the F1, F5, S1 and S5 groups, red stars depict differences between the 2D data and the hECT conditions. (Contribution: Alisa DeGrave assisted with the pipetting of part of the qPCR experiments, which were conceived, established, and supervised by Gabriela L. Santos.)

Comparative transcriptome analysis – flexible and stiff hECT model versus healthy and diseased myocardium

The results obtained with hECT led to the hypothesis that differential stiffness [354-357] and transcription profiling in flexible versus stiff hECT reproduces the differences of healthy and diseased myocardium, proposing it as model for cardiac fibrosis. To test this hypothesis, the differentially expressed genes between flexible and stiff hECT at day five were compared to those identified in a RNA-seq analysis of 14 non-failing (NF) heart samples and 50 samples from end-stage HF (37 dilated cardiomyopathy (DCM), 13 ischemic cardiomyopathy (ICM)) [432].

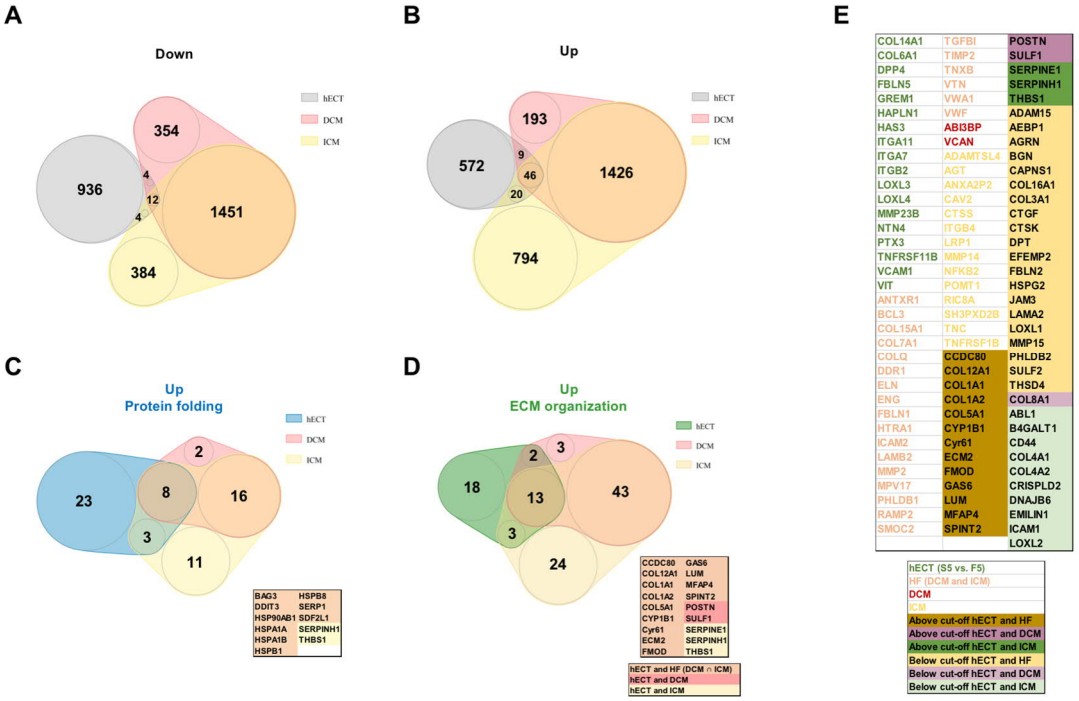

Figure 43. Overlap of differentially expressed genes in stiff vs. flexible hECT and failing vs. non-failing human heart tissues.
RNA-sequencing analysis of 3 independent experiments was performed in RNA extracted from pools of 3 hECT generated with human cardiac fibroblasts and collagen I on flexible (TM5MED) and stiff casting moulds. Differentially expressed genes (DEGs) in stiff vs. flexible hECT after 5 days in culture (S5 vs. F5, log2-fold change ≥1, padj≤0.03) were compared to DEGs in 37 human dilated cardiomyopathy (DCM) samples and 13 human ischemic myopathy (ICM) samples vs. 14 non-failing (NF) sample (log2-fold change ≥1, padj≤0.05 [432]). Quasi-proportional Venn diagrams (nVenn) illustrate the overlap of **A)** down-regulated and **B)** up-regulated genes. The overlaps of up-regulated genes in hECT (S5 vs. F5) and human heart samples (DCM vs NF, ICM vs. NF) within the context of the GO terms **C)** protein folding and **D)** extracellular matrix (ECM) organization are shown. **E)** List shows all 106 up-regulated genes belonging to the GO term *ECM organization* identified either in hECT (S5 vs F5) or human heart samples (DCM vs NF, ICM vs. NF, based on log2-fold change >1, padj<0.05). Genes labelled as "above cut-off" were regulated by log2-fold change >1, padj<0.03 in the hECT (S5 vs F5). Genes labelled as below cut-off" include the additional regulated genes in the hECT (S5 vs F5) with a log2-fold change >1, padj<0.05.

Because the human myocardium is a complex mixture of various cell types, it was not surprising to see that the overlap of DEGs was minor between hECT and human heart samples (**Figure 43A,B**). The global overlaps showed 20 down- and 95 up-regulated genes between stiff vs. flexible hECT and healthy vs. diseased human heart samples. However, a sub-analysis of the identified genes assigned to the GO terms *protein folding, response to unfolded protein* and *response to topologically incorrect proteins* (depicted in **Figure 43E**) and *ECM organisation* (depicted in **Figure 43I**) revealed in comparison to diseased heart a substantial overlap of up-regulated genes (**Figure**

43C,D). Proportionally, the genes assigned to *ECM organization* showed a higher degree of similarity. This was evidenced by the 18 out of 36 genes increased in stiff hECT based on cut-off of log2-fold change ≥1 and padj <0.03, which were similarly regulated in DCM, ICM or in both diseases (log2-fold change ≥1, padj ≤0.05) (**Figure 43D**). Furthermore, of the remaining 70 regulated genes in the HF samples (3 in DCM, 24 in ICM, 43 in DCM and ICM) belonging to this GO term (**Figure 43D**), 31 genes below the cut-off (log2-fold change <1) in stiff hECT were also found to be significantly (padj <0.03) over-expressed (**Figure 43E**).

Considering the diversity of cell populations included in human heart samples, the degree of similarity in gene regulation between the hECT model and human heart samples was explored [203, 431]. The reads per kilobase of transcript per million mapped reads (RPKM values) from hECT of day five and from the human heart samples published by Sweet et al. 2018 (data set GSE116250) [432] were used to compare the expression of a selection of genes from pro-fibrotic/myofibroblast markers and fibroblast markers (*POSTN*, *THY1*, *ACTA2*, *COL1A1*, *COL1A2*, *P4HA1*, *LOX*, *CCN2*, *COL3A1*, *PDGFRA*, *VIM*, *DDR2*, *S100A4* and *TCF21*) [203, 431] (**Figure 44**). All the referred pro-fibrotic/myofibroblast genes (*POSTN*, *THY1*, *ACTA2*, *COL1A1*, *COL1A2*, *P4HA1*, *LOX*, *CCN2* and *COL3A1*) were found to be higher expressed in stiff hECT comparing to flexible hECT. From those, however, *THY1* and *ACTA2* showed to be overall higher expressed in the human heart samples compared to the only fibroblasts-containing hECT samples. Differently, RPKM values of collagens and LOX were proportionally higher in hECT than in human heart samples. POSTN, *P4HA1* and *CCN2* (CTGF) showed RPKM values in the same order of magnitude between hECT and human heart samples, but only *POSTN* and *CCN2* were commonly higher regulated in stiff vs. flexible hECT and in HF vs. non-failure.

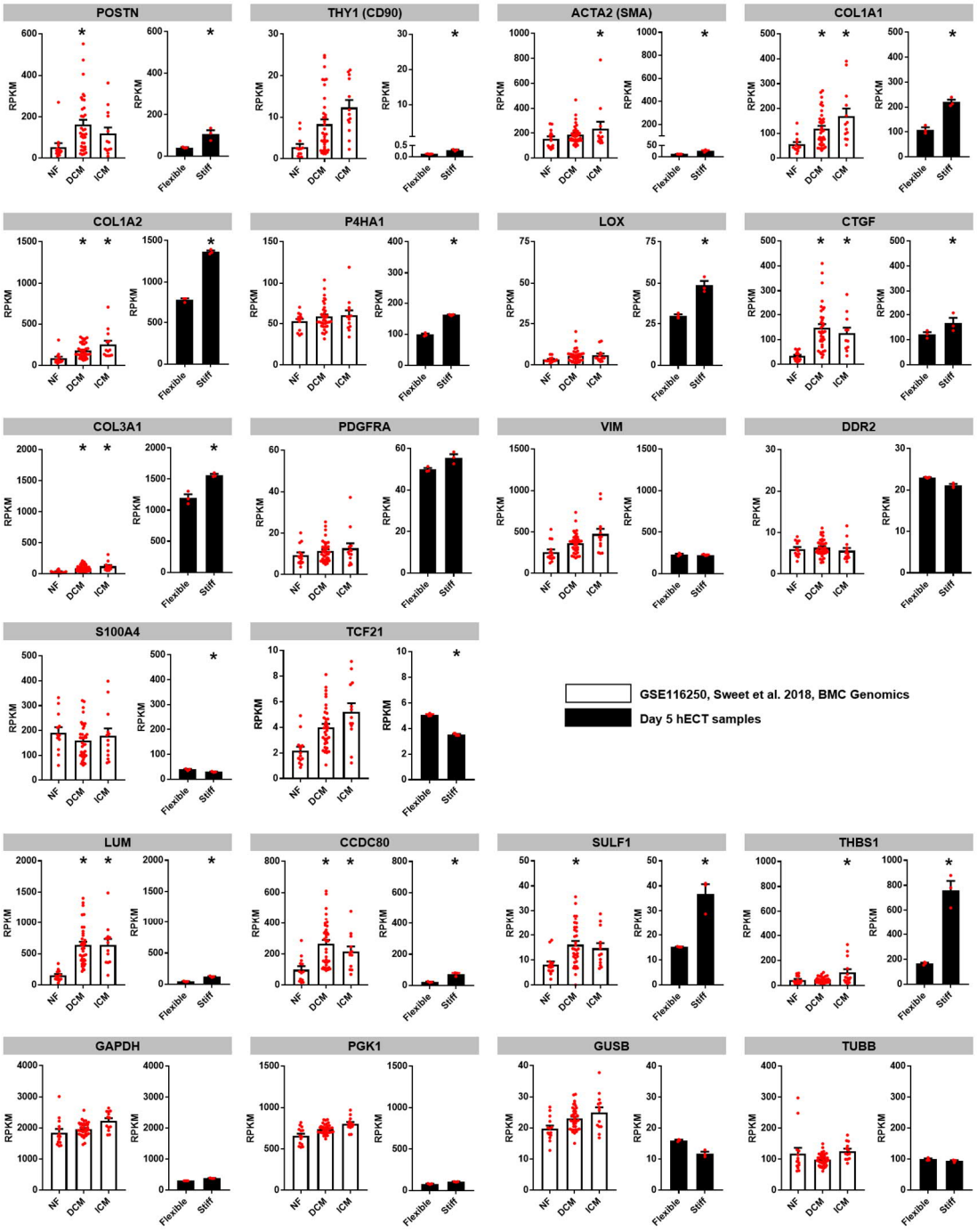

Figure 44. Selected differential expressed genes show a comparable regulation between the hECT model and human heart samples.

RNA-sequencing analysis of 3 independent experiments was performed in RNA extracted from pools of 3 hECT generated with human cardiac fibroblasts and collagen I and cultured for 5 days in flexible (TM5MED) and stiff casting moulds. Presented are the RPKM values of human heart samples (left panels, white) and hECT (right panels, black) of published pro-fibrotic markers, fibroblast markers and housekeeping genes. The RPKM values of the human heart samples and the statistical analysis were taken from the GSE116250 data set published by Sweet et al. 2018 [432]. The graphs depict means+SEM with single data points. Human heart samples: non failing (NF) n=14, dilated cardiomyopathy (DCM) n=37, ischemic cardiomyopathy (ICM) n=13. hECT samples from day 5: Flexible n=3, Stiff n=3. *p<0.05 vs. NF was assessed by 1-way ANOVA with Tukey's *post hoc* test for multiple comparisons, or vs. Flexible assessed by an unpaired t-test.

The *PDGFRA*, *VIM* and *DDR2* fibroblast genes were unchanged in stiff hECT vs. flexible hECT and in HF vs. non-failure samples. *PDGFRA* and *DDR2*, but not *VIM*, showed higher RPKM values in hECT compared to human heart samples. *S100A4* (FSP1) and *TCF21* genes were suggested as fibroblasts markers specially in developing tissues [115, 167, 202, 433]. Those were found to be significantly higher expressed in flexible hECT compared to stiff hECT, but no significant regulation was observed in human heart samples. Unlike *S100A4* (FSP1), *TCF21* RPKM values were similar between human heart samples and hECT. RPKM values of the genes *LUM*, *CCDC80*, *THBS1* and *SULF*, which belong to the GO term *ECM organization*, were also analysed. They were found to be higher expressed in both stiff vs. flexible hECT and HF vs. non-failure samples. However, the RPKM values of *LUM* and *CCDC80* were lower in hECT compared to human heart samples. Interestingly, while the RPKM values for *THBS1* and *SULF1* had more similar order of magnitude between human heart samples and flexible hECT, the rigid hECT compared to those showed disproportionately higher RPKM values. The *GAPDH*, *GUSB*, *PGK1*, and *TUBB* housekeeping genes were unchanged for both hECT and human heart samples.

Overall, the collected data demonstrated that cells in flexible and stiff hECT displayed clear transcriptomic differences. In particular, myofibroblast markers and genes involved in protein folding and ECM organization were found to be more highly expressed in stiff hECT cells. The comparison between both transcriptome analyses suggests substantial resemblances of the transcription patterns within the GO term *ECM organization* between hECT and the human heart samples. Moreover, as RPKM are a unit of transcript expression normalized for sequencing depth, it can be suggested that in the heart the expression of collagens, *LOX*, *PDGFRA*, *DDR2*, *THBS1* and *SULF1* seems to be undertaken preferentially by the (myo)fibroblasts fraction.

5. Discussion

Cardiac fibrosis is a factor that significantly contributes to the progression of HF. The complex nature of fibrosis still lacks a more comprehensive understanding, delaying the development of effective pharmacological therapies that target the involved cell populations and their pathological contribution to cardiac fibrosis progression. One of the main limitations of research on the biology of cardiac fibroblasts and their pathological derivatives is the shortage of representative human models. Cardiac fibrosis has been more widely studied in animal models [434, 435]. With the possibility of creating transgenic models and applying *in vivo* techniques, they are indispensable tools for evaluating the resulting cardiac phenotypes and for understanding the molecular changes underlying the development and progression of the disease. Besides, they are undoubtedly necessary to bridge molecular strategies from the bench to therapeutic application in patients. However, these models are highly complex hampering the study of biological processes in different cardiac cell types individually. The extensive intercellular communication in mammalian models is not suitable, for example, to study the effect of a certain protein in a specific cell type without interfering with auto, para- and sometimes endocrine effects. Thus, mammalian models do not adequately support the study of particular cellular processes involved in cardiac fibrosis such as CF proliferation and contractility, as well as the production, compaction and remodelling of the ECM. Another aspect is the non-applicability of mammalian models for exhaustive drug screening, limited not only by the complexity of the organisms but also by the limit of possible parallel testing. These constraints have encouraged many researchers to investigate the behaviour of cardiac fibroblasts in 2D cultures. However, conventional 2D cell culture systems cannot reliably mimic the process of cardiac

fibrosis as they are oversimplified systems with an unnatural stiff substrate and lack an embedding ECM. Fibroblasts are highly perceptual cells and therefore, their behaviour is strongly influenced by the biochemical and mechanical characteristics of the environment. The unnatural stiffness of the substrate in 2D cultures, which is five orders of magnitude higher than the healthy myocardium [354-357], leads to a fast phenotypic switch. Cardiac fibroblasts spontaneously undergo transdifferentiation when they are isolated from the heart and expanded in 2D cultures, exhibiting then a myofibroblast phenotype [172, 184, 239, 352, 358, 359]. It is in this context that the relevance of 3D models emerges to bridge the gap between cell culture and animal models, particularly, when applied to the investigation of cardiac fibrosis. Studies spanning around four decades of research have been exploring the tissue engineering field [353, 436]. Although lacking the full *in vivo* complexity, fibroblast-based tissue engineering has been established to study cellular responses in a more physiologically relevant environment. Several studies have demonstrated that engineered tissues can be prepared from cardiac fibroblasts to study cellular plasticity, matrix mechanics and sex-differences in cardiac fibrosis, and tissues prepared from virally transduced cells allowed loss- and gain-of function studies [240, 242, 281, 286, 370, 379, 382, 387, 437]. However, they were mostly sourced from rats and chickens and in rare cases from other species such as mice and humans.

The presented work demonstrates the feasibility of the ECT model to advance the research field of cardiac fibrosis. The ECT is a straightforward approach which can be produced in short time and by using a low number of cells from different origins and maturation states. Due to its composition and structure, the ECT model is suitable for functional and mechanistic readouts, and also constitutes a versatile tool with the potential for studying several pharmacological substances and concentrations in

parallel. The ECT model produced from neonatal rat cardiac fibroblasts [281, 286, 370, 387], here referred as rECT, was used for a systematic investigation into the effects of ROCK inhibition on the biomechanical properties of rECT and for the validation of the significance of ROCK-dependent signalling processes, like the actin-MRTF-LOX regulation. Moreover, the limited availability of reliable human tissue models, prompted to the development of a human 3D model, the hECT, to study human CF plasticity and mechanical aspects of cardiac fibrosis. This model was scaled to a smaller volume format allowing a greater cost-effectiveness of the material *versus* the experimental output and fostering comparability of multiple experimental approaches. In this study it was also shown that the hECT has the advantage of providing a comparative model because it has the capability of controlling the phenotype of CF through modifications of the physical properties of the tissue mould. ROCK inhibition was also tested in the context of human engineered tissues, benefiting from the availability of the different mechanical conditions which assisted the investigation of differential effects of ROCK inhibition.

5.1. Effect of the environmental stiffness on the biomechanical properties of hECT

Cardiac fibroblasts, likewise all type of fibroblasts, are known to be mechanosensitive. Through an interactive process, when fibroblasts undergo augmented external environment stiffness, G-actin assembles into F-actin polymers forming contractile stress fibres, resulting in an intracellular tension increase. Consequently, mechanosensitive pathways including the MRTF/SRF activation induce the expression of typical myofibroblast genes including *ACTA2* (encoding for SMA), *CCN2* (encoding for CTGF), *COL1A1* and *LOX*. By this means, CF transdifferentiate into

myofibroblasts, which feed back to the external environment with increased traction forces and an enhanced expression of extracellular matrix components and modulators [242, 352, 359, 383, 388]. This interplay framed the hypothesis that in 3D cultures the mechanical characteristics and architecture of the tissue moulds could drive specific cellular responses and determine the biomechanical tissue properties.

The cells used for the preparation of the tissues were previously expanded in 2D culture. Henceforth, hECT were prepared from expectably differentiated cardiac myofibroblasts expressing SMA and POSTN (**Figure 33A,B**). Once transitioned to 3D conditions, myofibroblasts were exposed to high and low environmental stiffness by respectively preparing tissues in moulds with a single uncompressible stiff rod (stiff model) or with two flexible poles (flexible model). Similar to previous studies [242, 374, 379], time-dependent matrix compaction of hECT (**Figure 29A, Figure 32A**) was at least in part directly mediated by the cellular component as demonstrated by the significantly reduced CSA and volume of the flexible and stiff hECT models comparing to non-populated collagen matrix (**Figure 26A-C**). In line with the studies from Wakatsuki and colleagues [374], the higher tissue compaction observed in the stiff compared to the flexible model was associated with a higher tissue stiffness (**Figure 26B-E**). In the flexible model, the obtained stiffness was in the range of that documented for the healthy myocardium (8-10 kPa), while in the stiff model it corresponded to the diseased myocardium (25-100 kPa) [354-357].With the aid of a gradient plate composed of flexible poles with different spring constants, the hECT model has enabled to further discriminate between compaction (CSA decrease) and contraction (pole deflection). The compaction of the tissues cultured on flexible poles with rather low stiffnesses varying within a short range, was minimally or not impacted by the external forces that the moulds exert on the tissues (**Figure 27F**). Contrastingly,

as softer the poles were, higher was the level of tissue contraction (**Figure 27D**). In contrast to the observation between flexible and stiff hECT models, the net variation between CSA and arm's length in the gradient flexible model showed that compaction and contraction do not necessarily correlate positively with stiffness. The inverse variation between contraction and tissue stiffness in the flexible model (**Figure 27D,I**) rather indicates that tissue stiffness increases when the tissue is prevented from contracting, and varies positively with incremental resistance exerted by the poles against tissue contraction. The same principle is plausible for the stiff model in which contraction is fully prevented. Moreover, as shown with the gradient plate, the increase in environmental stiffness (**Figure 27A**) and in tissue stiffness (**Figure 27I**) do not maintain a linear relationship, suggesting that the tissue stiffness of the stiff model may not be achievable using flexible poles. Thus it was raised the question of whether, beyond stiffness, the geometry of the mould may be instrumental in determining the maximum achievable tissue stiffness. This assumption is supported by a study showing that pulmonary microtissues produced in moulds with micropillars presented an uneven distribution of stress. The area of the tissue directly surrounding a micropillar showed higher signs of stress, including an increased collagen expression than the areas between the micropillars [388]. This probably also applies to the hECT prepared in flexible moulds, where the stress around the two poles is supposedly higher than in the arms region. Supportive of this possibility is the observation that the thickness of the hECT around the two poles was lower than in the arm region. The tissues produced in the stiff mould, which are ring shaped and in which the tissues are uniformly in contact with the surface of a single stiff rod, can be equated in mechanical terms to the area of the tissue located in the region of the poles in the flexible mould. Considering that this area of the poles corresponds only to about 25 to 30% of the total length of the tissues

produced in flexible moulds, this could explain why they have an overall lower stiffness than those produced in stiff moulds. Thus, even when two non-bendable poles of highest stiffness would be used, suspended tissues in such moulds would probably not reach the same stiffness level as those generated around a single rod in stiff moulds.

Similarly to other studies using engineered tissues [180, 375, 379], hECT showed a non-linear viscoelastic behaviour. The hECT viscoelastic curves showed three distinct regions, toe, elastic, and plastic. The toe and the plastic regions follow a non-linear response, while the elastic region shows a linear relationship between stress and strain. Stiffness is given by the slope of the linear phase on the elastic region, thus indicating that the model follows a linear dependence of stiffness on stress at a given strain. By comparing stiffness with ultimate strength, a linear relationship is indicated (**Figure 26G**), showing that as stiffer as the hECT is, the tissue can withstand more stress while being stretched before disrupting (**Figure 26F**).

But besides tissue stiffness given by the Young's modulus, other viscoelastic parameters are relevant for tissue quality and necessary to assess with respect to cellular behaviour and tissue mechanical properties under functional and pathological conditions. Moreover, these parameters should be taken into consideration when the impact of a pharmacological treatment is tested. For example, the yield strain describing the length of the elastic phase (**Figure 26H**) and the ultimate strain describing the extensibility of the tissues (**Figure 26K**) were found to be significantly lower in stiff compared to flexible tissues. From the mechanical perspective, at lower strains collagen fibres have a more lose architecture and thus are able to bear almost no load, leaving the contribution to the tissue elasticity to the cellular component. Because the stiff hECT and the non-populated collagen showed a similar yield point (**Figure 24H**), it can be suggested that the shortening of the elastic phase in the stiff model might be due

to matrix remodelling such as cross-linking. On the other hand, at higher load conditions the then more aligned collagen fibres start bearing the load, leading therefore to an increasing tissue stiffness [438]. A shortened elastic phase under high load conditions would make the myocardium however more susceptible to microtraumata, which would trigger reparative fibrosis. If cardiac fibrosis shortens the yield strain of the myocardium is still not known, but that microtraumata could induce fibrotic processes in the heart has been discussed as one cause of fibrosis in the hearts of athletes [439]. In the hECT model, the yield strain showed an inverse relationship with the stiffness (**Figure 24I**), indicating that the stiffer hECT have less elasticity while the less stiff hECT from the flexible model have higher elasticity. An inverse relationship between stiffness and elasticity has been already shown for various tissue types including scarred skin versus normal skin and for the uterus after cesarean section [440-442]. Moreover, the inverse relationship shown for the ultimate strain and stiffness (**Figure 26L**) indicates that stiffer hECT are likely to disrupt faster during load, while softer hECT from the flexible model are more extensible. Together, this suggests that the stiff hECT is more susceptible to microtraumata. Since the stiff hECT model is likely to present higher levels of matrix remodelling, this component is also likely to bear more load during stretch from lower to higher strain conditions. This could be the reason for the stiff tissue model to absorb more energy during the elastic phase (resilience) (**Figure 26J**), even if stiffer hECT are less elastic than the flexible hECT.

5.2. Role of the actin cytoskeleton and the secretory pathway on the hECT function

Compaction was demonstrated to be primarily modulated by the cell cytoskeleton contractility and by generated traction forces on the collagen fibrils [369, 371, 374, 380,

381, 383]. Also, in the hECT model hampering the actin dynamics through inhibition of actin polymerisation by Lat-A significantly reduced tissue compaction in both flexible and stiff models, and reduced tissue contraction in the flexible model (**Figure 28B,C**), suggesting that both processes are dependent on the dynamics of the cytoskeleton. Together with the aforementioned results, this could indicate that at a low range of external tension as in the flexible model, the small variation in the stiffness of the poles present in the gradient plate is not sufficient to greatly impact cell contractility and thus alter matrix compaction. As tissue stiffness has been shown to depend more on the passive component (remodelled matrix) than on the cells [374], the results obtained in the gradient plate could suggest that increased external stiffness starts by influencing cells to change towards a more secretory status modulating matrix composition and stiffness before stimulating a more contractile cell phenotype.

In line with the non-linear relation between environmental and tissue stiffness observed in the hECT models, at a much higher threshold of environmental stiffness where contraction is entirely prevented (stiff model), the increased tissue compaction observed in the stiff model could then occur in consequence of increased cell contractility and increased traction forces. This cellular behaviour has been shown to happen in response to highly stiff lattices [247, 363], and is known to lead to the activation of mechanoresponsive signalling pathways associated with myofibroblasts transdifferentiation [236, 247]. It is therefore reasonable to suggest that a high environmental stiffness as found in the stiff model may induce further cell activation, which results in an enhanced contractile phenotype, by this feeding back positively towards enhanced secretion/matrix remodelling through mechanosignalling pathways activation. The consequence is an enhanced tissue stiffness (see *section 5.3.2.*).

The association of both components (matrix remodelling and cell cytoskeleton

contractility/tension), resultant in enhanced tissue stiffness, could at least in part explain the non-linear relation between environmental and tissue stiffnesses. In line, there was evidence that the actin dynamics becomes predominantly instrumental at higher stiffnesses as the inhibition of actin polymerisation reduced tissue stiffness in the stiff model but had no impact in the flexible model (**Figure 28D**). These findings are resonant with the model developed by Elson and colleagues which showed that in stiffer tissues, populated with myofibroblasts, both passive (matrix) and active (cells) components contribute to the total stiffness, while in softer tissues, populated with fibroblasts, the cellular component does not contribute to the total stiffness [180]. The comparison between the non-populated collagen matrix and the flexible hECT model showing rather similar stiffnesses is also in line with their model, and further supports the premise that in the flexible model the embedded cells may have a less secretory phenotype than in the stiff hECT model.

To test the impact of secretion in the mechanical properties of the tissues, hECT were treated with BFA. Inhibition of protein trafficking/secretion reduced both tissue compaction and contraction (**Figure 28A-C**) to a higher extent than the effect induced by actin polymerization inhibition. The enhanced effect could be explained by a combination of the potential effects of BFA on ECM secretion and cell adhesion. For example, elastin and fibronectin, both ECM components secreted by fibroblasts [139-142], have been shown to have a permissive effect on cell-mediated collagen matrices compaction [443-445]. Moreover, through disturbances of the Golgi apparatus, BFA can block maturation and trafficking of FA-associated proteins including β1-integrin and focal adhesion kinase (FAK) to the cellular membrane, potentially causing cell detachment and abolishing traction forces [446]. Notwithstanding, blockade of the secretory pathway did not influence tissue stiffness in the flexible hECT model, but led

to a stiffness decrease in the stiff model. Wakatsuki and colleagues showed that in a ring-shaped tissue cultured around a single stiff rod, 2 hours were sufficient for myofibroblasts to remodel the matrix, as the stiffness of the then decellularised matrix was already stiffer than matrices which have been never populated [374]. On one hand, the missing effect of Lat-A and BFA on tissue stiffness emphasises that in tissues prepared in the flexible moulds the tissue stiffness is mainly dependent on a poorly remodelled ECM structure and not mediated by cellular tension forces. On the other hand, the impact of the inhibitors on the stiffness of tissues prepared in the stiff moulds stresses the fact that under stiffer environmental conditions tissue stiffness most prominently depends on cell tension and enhanced secretion.

5.2.1. The impact of actin polymerization inhibition on tissue mechanical properties is recapitulated by the inhibition of MRTF nuclear import

The mechanisms whereby cells adjust to strain and stress involve mechanotransduction pathways. The dynamics of the actomyosin cytoskeleton is particularly involved in the mechanical regulation of gene transcription. One of the important pathways in the regulation of gene transcription involves the co-transcriptional factor MRTF [249, 250]. As discussed above, Lat-A impacted tissue compaction in both flexible and stiff models, while it only reduced tissue stiffness in the stiff hECT model (**Figure 28B,D**). Because the tissues compaction is primarily modulated by the cell cytoskeleton contractility and generated traction forces [369, 371, 374, 380, 381, 383], and tissue stiffness depends rather on the passive component (remodelled matrix) [374], it was raised the hypothesis that the differentiated effect of Lat-A on the stiffness of the flexible and stiff hECT could be related to modulation of actin-dependant mechanotransduction pathways. By formation of F-actin fibres, the pool of G-actin

monomers decreases, which releases MRTF out of the G-actin binding, and enhances its nuclear translocation [249, 250]. MRTF nuclear localization coupled with SRF activity is known to promote the transcription of genes involved in myofibroblast phenotype switch and functionality, such as *ACTA2* (SMA), *CCN2* (CTGF) and *COL1A2* [208, 264, 265]. With the aid of the rECT model, which mechanically and architecturally corresponds to the hECT stiff model and similarly presents a mean stiffness around 10 times higher than the reported values for healthy mammalian hearts [391, 392], the effect of MRTF nuclear import inhibition on tissue mechanical properties was tested. Similar to the effect of actin polymerization inhibition on stiffness of both hECT and rECT stiff models, the inhibition of MRTF translocation by CCG-20397 recapitulated the effect of Lat-A, inhibiting tissue compaction and decreasing tissue stiffness in the stiff rECT model. These results strongly support that the enhanced cellular responses driven by increasing environmental tension/stiffness, which further positively feedback towards increasing tissue stiffness in the ECT model, may occur through actin-MRTF/SRF-dependent mechanotransduction signalling pathway.

5.3. Drug testing in the hECT model – the potential therapeutic effect of ROCK inhibition based on tissue mechanical properties

As of undoubtable importance, mechanosignalling, bridging adjustments to strain and stress between cells and environment, constitutes an interesting target for an anti-fibrotic therapy.

ROCK as upstream regulators of actin dynamics and actomyosin cytoskeleton contractility [251, 253-255], playing a role in cardiac fibroblast migration and

proliferation [281-285] and in the regulation of fibrosis-associated genes [277, 285-289], along with their increased activity in several CVD including MI and HF [292-298], are of clinical relevance and thus very attractive targets for anti-fibrotic therapy. It is expected that a therapeutic intervention with ROCK will reduce the stiffness of the fibrotic myocardium. Restoring its elasticity would be a further asset for the therapy. Therefore, the basic requirements for anti-fibrotic drugs to be tested in hECT are a decrease in Young's modulus and it should, at least, not negatively affect the yield strain and ultimate strain of the tissues. A decrease in elasticity and extensibility could result in structural disintegration of the myocardium *in vivo*. As ROCK is involved in the regulation of cytoskeleton dynamics, expectedly its inhibition impacted tissue compaction in both stiff and flexible hECT models (**Figure 29D**). More importantly, treatment of hECT with the ROCK inhibitor H1152P caused a reduction in tissue stiffness, particularly marked in the stiff hECT model. It failed to prolong the elastic phase of the stiff tissues, but at least did not cause a detrimental impact on it or on tissue extensibility (**Figure 29E-G**). The fact that ROCK have pleiotropic functions including the regulation of cellular contraction, morphology, polarity, cell division, and gene expression [253], its balanced activity is expectably crucial for cell and tissue integrity. In particular, its physiological role has already been shown to be critical in maintaining the contractility of the normal heart [447]. Thus, in the flexible hECT model which in control conditions corresponds to the stiffness of a healthy heart, the decrease in tissue stiffness accompanied by yield strain decrease caused by H1152P lauds the detrimental effect of ROCK inhibition in physiological conditions. The complete abolishment of tissue contractility by H1152P treatment in the flexible hECT model (**Figure 29B**) is in line with other publications [242, 383, 448] and supports that hypothesis. Thus, the beneficial effect of ROCK inhibition observed under high tension environmental

conditions argues for a pathologic ROCK activity augmentation in stiff tissues. In line are the studies from Truebestein and colleagues, describing ROCK as a molecular ruler possibly controlled by the cytoskeletal tension [259]. According to their findings, it could be proposed that the high tension created by the stiff mould leads to a direct activation of ROCK independent of RhoA by mechanically guiding ROCK coiled-coil orientation and by forcing it to interact with their substrates. This potential mechanism argues for a dependency of the beneficial effect of ROCK inhibition observed in the stiff hECT model on the potentially augmented ROCK activity in stiff tissues. To further validate this hypothesis, a potential increase in ROCK activity should be validated, e.g. by measuring the levels of MYPT1 phosphorylation.

5.3.1. Cellular processes underlying the therapeutic effect of ROCK inhibition

To explore the molecular mechanisms by which ROCK inhibition may exert a therapeutic effect, cellular processes known to be regulated by ROCK were also assessed in this thesis.

It was shown by Wakatsuki and colleagues that the Young's modulus of the passive component (remodelled-matrix) increased with cell number. As more cells present in a tissue as more reorganization of the matrix is executed by the cells [375]. Accordingly, it was possible to rule out that the decrease in stiffness caused by H1152P in the flexible model was a consequence of cell loss, as the same number of viable cells could be re-isolated from control and H1152P-treated flexible hECT (**Figure 29H**). Also the inhibitory effect on tissue compaction and contraction was not a consequence of a change in cell number. Moreover, ROCK inhibition did not alter the capacity of cell adhesion to collagen in 2D cultures of NRCF (**Figure 18D**), emphasising that the consequences of ROCK inhibition on 3D matrix compaction and contraction were

dependant on cytoskeleton contractility and not on an impairment of FA formation. In line, the increase in cell spreading of 2D-cultured NRCF treated with H1152P indicates cytoskeleton relaxation due to ROCK inhibition (**Figure 18B**). On the other hand, a lower number of cells could be re-isolated from stiff hECT treated with H1152P compared to control (**Figure 29H**), but in the correspondent stiff rECT model the cell number was not affected by ROCK inhibition (**Figure 23F**). Cell cycle analysis in cells from hECT (**Figure 29I**) and rECT (**Figure 23G**), and in 2D-cultured NRCF (**Figure 18F**) showed an accumulation of cells in the G2/M phase. This could point to a cell cycle arrest blocking cells from division. In line, ROCK have been associated with the maintenance and positioning of the centrosome [449, 450] affecting the correct formation of spindles and also seem to regulate the progression through cytokinesis [451, 452]. This hypothesis is, at least in part, supported by the undoubted increase in binucleation and full prevention of cell proliferation of 2D-cultured hCF (**Figure 29J,K**) and NRCF (**Figure 18E,G**) treated with H1152P. Other studies have shown that ROCK inhibition had divergent stiffness-dependent effects on cell proliferation, whereby high proliferative and migratory capacity induced by substrate stiffness was abolished by ROCK inhibitors [453, 454]. Together, the results suggest that the therapeutic effect of ROCK inhibition in the stiff hECT model may be also associated to an inhibition of high stiffness-induced cell proliferation. Cell death cannot be totally excluded as H1152P induced apoptosis in 2D-cultured NRCF (**Figure 18H**). To rule out species- and culture substrata-dependent effects and further disclaim H1152P-induced cell death in treated hECT, analysis of the cellular apoptotic levels in embedded cells should be conducted.

5.3.2. Molecular mechanisms underlying the therapeutic effect of ROCK inhibition – axis ROCK-actin-MRTF/SRF-regulated LOX

In the previous project, on which this thesis was based, H1152P and Fasudil were used to treat rECT and both inhibitors fulfilled the requirement of reducing the tissue stiffness to values published for the normal rat heart [391]. The anti-fibrotic effect of ROCK inhibitors or ROCK deletion has been formerly attributed to a reduction in the expression of fibrosis-associated genes [455]. From the screening in rECT performed in the previous project, it was indicated that both ROCK inhibitors showed indeed inhibitory effects on the gene expression of e.g. the collagen cross-linker *Lox* and the fibrosis inducer *Has2*. Moreover, H1152P also significantly inhibited the transcription of the elastase *Mmp12*, and increased *Mmp2* transcription. In this thesis, in which H1152P was selected for the majority of the analyses due to its higher potency and specificity [351], it could be confirmed that H1152P treatment over five days similarly down-regulated *Has2* in 2D NRCF, however, *Mmp12* was inversely regulated compared to rECT (**Figure 20**). Additionally, LOX regulation was analysed herein in both the rat and human systems, and it was shown to be consistently downregulated by ROCK inhibition in 2D cultures and in flexible and stiff hECT and rECT (**Figure 21A,E**, **Figure 22A**, **Figure 30**). This is in line with previous reports, which have comparably shown that LOX transcription is down-regulated as a consequence of ROCK inhibition. For example, Y27632 reduced *Lox* RNA levels in NIH3T3 fibroblasts [456], Fasudil in astrocytes [457], and SLx-2119, a supposedly ROCK2-specific inhibitor, in human pulmonary smooth muscle cells as well as dermal fibroblasts [458]. Furthermore, *LOX* expression was higher in the stiff hECT model compared to the flexible hECT model (**Figure 30A**). The stiffness- and ROCK-dependent regulation of LOX observed, led to the hypothesis that LOX is not only

regulated by hypoxia-inducible factor 1-alpha [459, 460], peroxisome proliferator-activated receptor γ [461], SMAD 2/3 and activator protein 1 complexes [462], or by the nuclear factor I [463], but also by the ROCK-regulated, actin-dependent MRTF/SRF transcriptional complex [263, 464]. This hypothesis is in line with previously published ChIP- and RNA-sequencing studies showing that the MRTF/SRF transcriptional complex binds close to the *LOX* gene in a serum-dependent manner inducing its transcription dependent on actin [465]. The experiments using Lat-A and CCG-20397 in rECT, which have been discussed above, together with the results obtained with H1152P on hECT, clearly confirmed this hypothesis. Taken together, it was shown that inhibition of each actin polymerization, MRTF nuclear translocation, and ROCK activity have not only a comparable impact on tissue compaction and stiffness, but also on the height of LOX expression (**Figure 25**).

In order to see if an interference with LOX activity is sufficient to mimic the effect of ROCK inhibitors, the LOX inhibitor BAPN was used in this thesis. BAPN activity is, however, not restricted to LOX but acts also on the LOX-homologs LOX-like 1-4 [466, 467]. In rECT, the direct inhibition of LOX was shown to resemble the effect of ROCK inhibition on tissue stiffness (**Figure 23**). Using the hECT, it was possible to further explore comparatively the effects of LOX inhibition on other mechanical properties of the tissues (**Figure 31**). In contrast to H1152P, BAPN had no impact on tissue contractility in the flexible hECT model and did not affect tissue compaction in both the flexible and stiff models. These results are resonant with the findings described above (*section 5.1.*) and in line with published data indicating that tissue compaction/contractility is fundamentally dependent on the cellular component – cytoskeleton contractility and traction forces [369, 371, 374, 380, 381, 383]. The result of collagen cross-linking inhibition as a consequence of BAPN treatment further

stresses the hypothesis (discussed in *section 5.1*) that higher tissue compaction in the stiff hECT model is not resultant from enhanced matrix remodelling (deposition and cross-linking) by cells, but instead results from a more pronounced contractile cell phenotype in response to higher environmental stiffness. Moreover, BAPN indiscriminately decreased stiffness of both flexible and stiff hECT without affecting tissue elasticity and extensibility. The similar impact of cross-linking decrease on both flexible and stiff tissues is also in line with earlier findings indicating that tissue stiffness depends preferentially on the passive component [374]

In line with the model proposed by Elson and colleagues, in which stiffer tissues populated with myofibroblasts both passive (matrix) and active (cells) components have high contribution to the total stiffness, while in softer tissues populated with fibroblasts only the passive component contributes to the total stiffness [180], in the stiff hECT model the treatment with BAPN, which just affects the collagen cross-linking, did not lead to the same level of tissue stiffness decreased as obtained via ROCK inhibition. The anti-fibrotic effect of LOX inhibition is in line with published data from *in vivo* studies, showing that BAPN treatment reduced the left ventricular stiffness and collagen content in a volume overload rat model [468, 469], decreased the extent of cardiac fibrosis in rats under a high fat diet [470], and ameliorated cardiac fibrosis and ventricular dilatation in a MI mouse model [193].

Altogether, the presented findings proved for the first time the functionality of the ROCK-actin-MRTF/SRF-mediated LOX regulation pathway in the setting of fibrosis.

5.4. Phenotype inter-exchangeability

Despite many advances in in the field of tissue engineering and cell fate mediated by tension forces, it is still highly debated whether myofibroblasts can be reverted into

activated fibroblasts and even fibroblasts, or if they remain locked by their epigenetic memory [237, 471, 472]. Throughout the project there were several signs that the cellular phenotype altered depending on the external mechanical conditions. A key indicator for this was the observed change in cell cycle activity, as the 3D environment proved to reduce the proliferation capacity of myofibroblasts. In NRCF, the cell cycle activity showed a decrease of near 17% of proliferative cells, when NRCF were transferred from 2D cultures into a 3D environment (**Figure 18**, **Figure 23**). Similar, when human CF were embedded in hECT, the cells showed at any time a higher percentage of G_0/G_1 phase cells than 2D-cultured cells. Most interestingly, over-time, there was a reactivation of the cell cycle of cells embedded in stiff hECT, but not of cells residing in flexible hECT (**Figure 32D**). Considering that activated fibroblasts display an enhanced cell cycle activity [132, 173, 174, 187, 473, 474], and flexible tissues after 5 days of culture showed the lowest cycle activity of all conditions, it can be argued that these cells are closer to have a less activated phenotype.

Moreover, in line with findings demonstrating that fibroblasts are smaller in volume than myofibroblasts [475, 476], the transference of cells from 2D-substrates to 3D-matrixes, including the stiff and the flexible hECT models, showed that the cell diameter and thus the volume of the hCF incrementally decreased with decreasing external environmental stiffnesses (**Figure 32C**). Highly secretory cells naturally adapt their ER and Golgi apparatus volumes to cope with an increased cargo load. Such adaptation involves ER stress. The UPR component XBP1 was found to be sufficient to trigger ER stress, resulting in ER expansion and consequently cell volume increase [477, 478]. These evidences suggest that the difference in volume described between fibroblasts is likely to be dependent on the different secretory activities of both cell types. If that holds true, the highest cell volume at day five compared to the flexible

hECT could suggest that the myofibroblasts in the stiff hECT model have a higher secretory activity.

An additional indicator for the phenotypic reversion was a change in the expression of SMA. Although, SMA could be still detected in ECT, its expression in 3D was clearly lower compared to 2D cultured cells. Intriguingly, SMA expression was lowest in flexible hECT (**Figure 33**). An interference with the internal cell stiffness by ROCK inhibition, leading to reduction in SMA expression (**Figure 21B,C,F**, **Figure 34**) was shown to be sufficient to result in the same phenotypic changes as the lowering of the external stiffness. In hECT model, after five days of culture H1152P lowered SMA expression in the stiff hECT to the same level found in the flexible hECT in control conditions of the same day (**Figure 34**).

Taken together, this data suggested that the potential gradual reversibility of cardiac myofibroblasts into a at least less active fibroblast phenotype induced by lowering the external and internal stiffness is indeed possible.

5.4.1. Transcriptome profile of hECT

To gain further insight into the stiffness-dependent cellular remodelling, transcriptomic analyses were conducted to compare between cells from flexible and stiff hECT after one and five days of culture. An unbiased PC analysis of cells in flexible and stiff hECT showed a strikingly time-dependent and biomechanical-dependent segregation according to the mould type. Based on the DEG, the highest differences in the gene program were found to occur at day five between the flexible and stiff hECT models. The second highest variance was found within the flexible hECT between day one and day five. In line with the above described indications of a phenotypic reversion, profound transcriptional differences in typical cardiac myofibroblast markers were

found in 2D-cultured cells, and cells residing in stiff and flexible hECT.

The regulation of myofibroblast marker POSTN [116] clearly demonstrated the dynamic fluctuation of the cellular phenotype in the hECT model (**Figure 33**, **Figure 36**). Its expression decreased strongly within 1 day after the 2D cultured cells were incorporated into the collagen matrix and continued to decrease in the following 4 days in both hECT models, but to a different extent. As with *POSTN*, other myofibroblast markers, including *ACTA2*, and *COL1A1* were higher expressed in stiff hECT than in flexible hECT after 5 days (**Figure 33**, **Figure 42**). The data also showed that the genes of originally defined (myo)fibroblast markers [203, 433, 479], such as *VIM*, *DDR2* and *S100A4* (FSP1), do not experience changes in their transcriptional level in the hECT model (**Figure 36A**). These results are consistent with the RNA sequencing data from non-failing human heart samples compared to samples from patients with DCM and ICM [432]. Furthermore, the most recently described fibroblast markers PDGFRA [119] and TCF21 [115] showed identical expression levels in flexible and stiff hECT after 5 days (**Figure 36B**). Overall, the observed expression pattern of (myo)fibroblast markers clearly showed that cells populating stiff hECT have a more pronounced myofibroblast phenotype compared to cells residing in flexible hECT. In any case, the myofibroblast phenotype was not as exaggerated as that of 2D cultured cells (**Figure 33A,B**, **Figure 36B**). However, it is not possible to clearly indicate whether the cells in the flexible tissues represent a phenotype that is closer to fibroblasts or activated fibroblasts. Considering the lower cycle activity discussed above, it can be argued that cells embedded in flexible hECT are closer to being non-activated fibroblasts.

By the RNA-sequencing analysis it was further possible to demonstrate that the gene program between cells embedded in flexible and in stiff hECT greatly differed not only in single genes, but also in gene clusters. Especially, gene clusters assigned to

extracellular matrix organization (*ECM organization*) and protein folding (*protein folding, response to unfolded protein* and *response to topologically incorrect protein*) showed intriguing differences, with all clusters being more prominently expressed in stiff compared to flexible hECT. Moreover, by the day-wise comparison, the data demonstrated that the difference in the cluster *response to unfolded protein* was exclusively based on an induction in the stiff hECT model and not by inverse regulation in both models (**Figure 37A**). A pathway analysis further indicated an enrichment in the *Heat shock factor 1 (HSF1)-dependent transactivation* pathway in the stiff hECT, supporting the specific regulation of the protein folding machinery in stiff hECT (**Figure 37B**). There is growing evidence that the UPR and thus the protein folding plays a crucial role in the process of transition of CF into myofibroblasts [480, 481]. In line with the hypothesis that cells in stiff hECT display a more pronounced myofibroblast phenotype then cells in flexible hECT, the two UPR genes *EIF2K3* (PERK) and *DDIT3* (CHOP) were found to be more than 2-fold higher in the stiff tissues (**Figure 41B**). It is important to note that the cells cultivated in 2D did not express as high *EIF2K3* (PERK) and *DDIT3* (CHOP) levels as cells in stiff hECT. However, for most of the genes tested that are involved in protein folding this did not happen, and comparable expression levels were found between 2D-cultured cells and cells from stiff hECT. The transient nature of the UPR in response to mild ER stress [482] might be a possible explanation. Since the cells are initially cultured in a 2D format, it is likely that the cells have adapted their protein folding machinery and ER size via the UPR, which allows them to keep proteostasis under the high secretory load in 2D. However, when transferred to soft environments and the secretory load declines, the cells likely adapt their endomembrane system and protein folding machinery. As discussed above, this results in cells with a smaller size. That the secretory load is highest in 2D cultured

cells, followed by cells in stiff and flexible hECT can be assumed due to the observed regulation of genes involved in ECM organization. The tested genes displayed either the highest expression in 2D cultured cells, like *POSTN*, or equally high expression levels in 2D cultured cells and cells from stiff hECT, like *COL1A1*, *CYR61*, *LUM*, and *THBS1*. In any case the expression of these genes was lowest in cells from flexible hECT. (**Figure 42**). Taken together, this data indicates that 2D cultured cells initially adapt to the softer environment in the hECT independent of the model, but then diverge over time according to the environmental stiffness. The higher expression of ECM genes in the stiff hECT indicates that matrix regulation is more pronounced under stiff conditions and that this adaptation results in a need of a reactivation of the protein folding machinery. This raises the question whether an inhibition of the ER adaptation could reduce the overt expression of matrix genes and thus prevent cardiac fibrosis.

5.4.2. Stiff hECT transcriptome profile resembles that of the failing human heart

Considering the mechanical characteristics and transcriptome profiles of the flexible and stiff hECT models defined in this thesis, it was investigated whether a parallelism of changes in gene expression between the hECT models and the healthy and diseased heart could be established. Not surprisingly, considering that fibroblasts make up a small percentage of heart cells [112], the overall overlap of the differently expressed genes was rather low. Despite the increasing number of fibroblasts-derived cells in HF resultant from CF activation, proliferation and myofibroblast differentiation [472], their contribution to the bulk transcriptome, even of the diseased heart, is probably low. For this reason, the analysis focused on genes that are mainly expressed or increased in myofibroblasts. Hence, the analysis included members of the GO term extracellular matrix organisation. Within this GO term, it was found that a considerable number of

genes are simultaneously higher expressed in the stiff hECT and in the diseased heart than in the flexible hECT and in the non-failing myocardium (**Figure 43**). A further comparison of the RPKM values of a selection of pro-fibrotic/myofibroblast markers and fibroblast markers demonstrated that not only the general regulation is similar, but also the height of their induction, suggesting that in the heart the expression of some of those genes (*COL1A1*, *COL1A*2, *COL3A1*, *LOX*, *PDGFRA*, *DDR2*, *THBS1* and *SULF1*) seems to be undertaken preferentially by the (myo)fibroblasts fraction (**Figure 44**). Taken together, the stiff hECT model resembles not only the biomechanical parameters of the diseased heart, but also its fibrotic gene pattern as it shows transcriptomic similarities with regard to the fraction of (myo)cardiac fibroblasts.

5.4. Conclusions and perspectives

The work of this thesis demonstrates that the ECT model is a versatile tool to model, understand and unravel fibrotic processes occurring in the human heart. It is the only model so far which allows to study the highly complex interplay between external and cellular biomechanics in an informative, multi-parametric way. The model helped to demonstrate that external stiffness, as occurring in the diseased heart, must be accounted as a stand-alone trigger for cardiac fibrosis progression and CF transdifferentiation. Moreover, the ROCK-MRTF-LOX pathway was identified as a potential anti-fibrotic target.

In summary, the ECT model opens new avenues for studies of mechanisms underlying human heart fibrosis and scarring and screening for anti-fibrotic drugs. However, to allow for professional screening further modifications of the model must be undertaken, especially with regard to the stiff hECT model. The small dish size hampers fast screening procedures and an adaptation to a multi-well format is indispensable.

Moreover, some parameters assessed with the flexible and stiff model are currently too tedious for a large compound screen. This includes the rheometric measurements requiring a high-throughput approach for fast screening, which is currently, however, not available. Additionally, important parameters, like the cell cycle analysis and marker expression show a need for automatization. In these cases, the use of fluorescent biosensors coupled with a high-throughput imaging platform would be an opportunity to not only speed up the analysis process, but also to allow for real-time assessments.

In addition to improvements in automatization, the effects of long-term cultures of the hECT is a pressing question. The most obvious question regards the homeostatic nature of the model. Is there at a certain time point an equilibrium between the cell and the matrix reached, or is the interplay between the cells and the matrix indeed resulting in a theoretical indefinite, self-perpetuating propagation of fibrotic processes. The respective experiments could also help to better characterize the nature of the cells in the flexible tissues as it can be postulated that if these cells are similar to quiescent healthy fibroblasts, the tissue properties and the gene profile of the cells should stabilize over time.

Finally, the model must be adapted allowing for the validation of the importance of genetic abnormalities in the setting of cardiac fibrosis. Primary human cardiac fibroblasts possess a restricted capacity for proliferation, therefore, genetic manipulations, like the stable induction of mutations, are not executable with these cells. The current progress in the generation of inducible pluripotent stem cell-derived cardiac fibroblasts is of invaluable importance [483]. First experiments with these cells demonstrated that their reaction on external stiffness is comparable to primary cells (data not shown in this thesis) and thus the prerequisite for future disease-related research is fulfilled.

References

1. Wain, H.M., et al., *Guidelines for human gene nomenclature.* Genomics, 2002. **79**(4): p. 464-70.
2. EMBL-EBI, et al. *International Protein Nomenclature Guidelines*. 2020 02-MAR-2020 [cited 2020; Available from: https://www.ncbi.nlm.nih.gov/genome/doc/internatprot_nomenguide/.
3. WHO, *Cardiovascular Diseases.* Available online at https://www.who.int/health-topics/cardiovascular-diseases/ - tab=tab.
4. Schaufelberger, M., et al., *Decreasing one-year mortality and hospitalization rates for heart failure in Sweden; Data from the Swedish Hospital Discharge Registry 1988 to 2000.* Eur Heart J, 2004. **25**(4): p. 300-7.
5. Mensah, G.A., et al., *Decline in Cardiovascular Mortality: Possible Causes and Implications.* Circ Res, 2017. **120**(2): p. 366-380.
6. Roger, V.L., et al., *Trends in heart failure incidence and survival in a community-based population.* JAMA, 2004. **292**(3): p. 344-50.
7. Joffe, S.W., et al., *Improved survival after heart failure: a community-based perspective.* J Am Heart Assoc, 2013. **2**(3): p. e000053.
8. Bueno, H., et al., *Trends in length of stay and short-term outcomes among Medicare patients hospitalized for heart failure, 1993-2006.* JAMA, 2010. **303**(21): p. 2141-7.
9. Mortality, G.B.D. and C. Causes of Death, *Global, regional, and national life expectancy, all-cause mortality, and cause-specific mortality for 249 causes of death, 1980-2015: a systematic analysis for the Global Burden of Disease Study 2015.* Lancet, 2016. **388**(10053): p. 1459-1544.
10. Mortality, G.B.D. and C. Causes of Death, *Global, regional, and national age-sex specific all-cause and cause-specific mortality for 240 causes of death, 1990-2013: a systematic analysis for the Global Burden of Disease Study 2013.* Lancet, 2015. **385**(9963): p. 117-71.
11. in *Cardiovascular Disability: Updating the Social Security Listings.* 2010: Washington (DC).
12. Burchfield, J.S., M. Xie, and J.A. Hill, *Pathological ventricular remodeling: mechanisms: part 1 of 2.* Circulation, 2013. **128**(4): p. 388-400.
13. Bluemke, D.A., *MRI of nonischemic cardiomyopathy.* AJR Am J Roentgenol, 2010. **195**(4): p. 935-40.
14. Hershberger, R.E., D.J. Hedges, and A. Morales, *Dilated cardiomyopathy: the complexity of a diverse genetic architecture.* Nat Rev Cardiol, 2013. **10**(9): p. 531-47.
15. Mestroni, L., et al., *Familial dilated cardiomyopathy: evidence for genetic and phenotypic heterogeneity. Heart Muscle Disease Study Group.* J Am Coll Cardiol, 1999. **34**(1): p. 181-90.
16. Maron, B.J. and M.S. Maron, *Hypertrophic cardiomyopathy.* Lancet, 2013. **381**(9862): p. 242-55.
17. McNally, E.M., J.R. Golbus, and M.J. Puckelwartz, *Genetic mutations and mechanisms in dilated cardiomyopathy.* J Clin Invest, 2013. **123**(1): p. 19-26.
18. Mestroni, L., et al., *Genetic Causes of Dilated Cardiomyopathy.* Prog Pediatr Cardiol, 2014. **37**(1-2): p. 13-18.

19. McMurray, J.J., et al., *ESC Guidelines for the diagnosis and treatment of acute and chronic heart failure 2012: The Task Force for the Diagnosis and Treatment of Acute and Chronic Heart Failure 2012 of the European Society of Cardiology. Developed in collaboration with the Heart Failure Association (HFA) of the ESC.* Eur Heart J, 2012. **33**(14): p. 1787-847.
20. Dickstein, K., et al., *ESC guidelines for the diagnosis and treatment of acute and chronic heart failure 2008: the Task Force for the diagnosis and treatment of acute and chronic heart failure 2008 of the European Society of Cardiology. Developed in collaboration with the Heart Failure Association of the ESC (HFA) and endorsed by the European Society of Intensive Care Medicine (ESICM).* Eur J Heart Fail, 2008. **10**(10): p. 933-89.
21. Katz, A.M. and E.L. Rolett, *Heart failure: when form fails to follow function.* Eur Heart J, 2016. **37**(5): p. 449-54.
22. Kırali, K.Ö., T.; Özgür, M., *Pathophysiology in Heart Failure.* Cardiomyopathies - Types and Treatments, ed. K. Kırali. 2017.
23. Roger, V.L., *Epidemiology of heart failure.* Circ Res, 2013. **113**(6): p. 646-59.
24. Rosamond, W., et al., *Heart disease and stroke statistics--2007 update: a report from the American Heart Association Statistics Committee and Stroke Statistics Subcommittee.* Circulation, 2007. **115**(5): p. e69-171.
25. Heron, M., *Deaths: Leading Causes for 2012.* Natl Vital Stat Rep, 2015. **64**(10): p. 1-93.
26. Anand, I.S.F., V.G., *Structural Remodeling in the Development of Chronic Systolic Heart Failure: Implication for Treatment.* Congestive Heart Failure and Cardiac Transplantation, ed. D.J.W. Garry, R.F.; Vlodaver, Z. 2017: Springer, Cham.
27. Kehat, I. and J.D. Molkentin, *Molecular pathways underlying cardiac remodeling during pathophysiological stimulation.* Circulation, 2010. **122**(25): p. 2727-35.
28. Hill, J.A. and E.N. Olson, *Cardiac plasticity.* N Engl J Med, 2008. **358**(13): p. 1370-80.
29. Maillet, M., J.H. van Berlo, and J.D. Molkentin, *Molecular basis of physiological heart growth: fundamental concepts and new players.* Nat Rev Mol Cell Biol, 2013. **14**(1): p. 38-48.
30. Weeks, K.L. and J.R. McMullen, *The athlete's heart vs. the failing heart: can signaling explain the two distinct outcomes?* Physiology (Bethesda), 2011. **26**(2): p. 97-105.
31. Bernardo, B.C., et al., *Molecular distinction between physiological and pathological cardiac hypertrophy: experimental findings and therapeutic strategies.* Pharmacol Ther, 2010. **128**(1): p. 191-227.
32. Piek, A., R.A. de Boer, and H.H. Sillje, *The fibrosis-cell death axis in heart failure.* Heart Fail Rev, 2016. **21**(2): p. 199-211.
33. Heineke, J. and J.D. Molkentin, *Regulation of cardiac hypertrophy by intracellular signalling pathways.* Nat Rev Mol Cell Biol, 2006. **7**(8): p. 589-600.
34. Ho, C.Y., et al., *Myocardial fibrosis as an early manifestation of hypertrophic cardiomyopathy.* N Engl J Med, 2010. **363**(6): p. 552-63.
35. Camici, P.G. and F. Crea, *Coronary microvascular dysfunction.* N Engl J Med, 2007. **356**(8): p. 830-40.

36. Shirani, J., et al., *Morphology and significance of the left ventricular collagen network in young patients with hypertrophic cardiomyopathy and sudden cardiac death.* J Am Coll Cardiol, 2000. **35**(1): p. 36-44.
37. Varnava, A.M., et al., *Hypertrophic cardiomyopathy: the interrelation of disarray, fibrosis, and small vessel disease.* Heart, 2000. **84**(5): p. 476-82.
38. Chin, C.W., et al., *Markers of left ventricular decompensation in aortic stenosis.* Expert Rev Cardiovasc Ther, 2014. **12**(7): p. 901-12.
39. Beltrami, C.A., et al., *Structural basis of end-stage failure in ischemic cardiomyopathy in humans.* Circulation, 1994. **89**(1): p. 151-63.
40. Everett, R.J., et al., *Assessment of myocardial fibrosis with T1 mapping MRI.* Clin Radiol, 2016. **71**(8): p. 768-78.
41. Doesch, C., et al., *Mitral annular plane systolic excursion is an easy tool for fibrosis detection by late gadolinium enhancement cardiovascular magnetic resonance imaging in patients with hypertrophic cardiomyopathy.* Arch Cardiovasc Dis, 2015. **108**(6-7): p. 356-66.
42. Dweck, M.R., et al., *Midwall fibrosis is an independent predictor of mortality in patients with aortic stenosis.* J Am Coll Cardiol, 2011. **58**(12): p. 1271-9.
43. Weidemann, F., et al., *Impact of myocardial fibrosis in patients with symptomatic severe aortic stenosis.* Circulation, 2009. **120**(7): p. 577-84.
44. Gulati, A., et al., *Association of fibrosis with mortality and sudden cardiac death in patients with nonischemic dilated cardiomyopathy.* JAMA, 2013. **309**(9): p. 896-908.
45. Halliday, B.P., et al., *Association Between Midwall Late Gadolinium Enhancement and Sudden Cardiac Death in Patients With Dilated Cardiomyopathy and Mild and Moderate Left Ventricular Systolic Dysfunction.* Circulation, 2017. **135**(22): p. 2106-2115.
46. Moreno, M.U., et al., *The Hypertensive Myocardium: From Microscopic Lesions to Clinical Complications and Outcomes.* Med Clin North Am, 2017. **101**(1): p. 43-52.
47. Barison, A., et al., *Myocardial interstitial remodelling in non-ischaemic dilated cardiomyopathy: insights from cardiovascular magnetic resonance.* Heart Fail Rev, 2015. **20**(6): p. 731-49.
48. Azevedo, C.F., et al., *Prognostic significance of myocardial fibrosis quantification by histopathology and magnetic resonance imaging in patients with severe aortic valve disease.* J Am Coll Cardiol, 2010. **56**(4): p. 278-87.
49. Briasoulis, A., et al., *Myocardial fibrosis on cardiac magnetic resonance and cardiac outcomes in hypertrophic cardiomyopathy: a meta-analysis.* Heart, 2015. **101**(17): p. 1406-11.
50. Almaas, V.M., et al., *Increased amount of interstitial fibrosis predicts ventricular arrhythmias, and is associated with reduced myocardial septal function in patients with obstructive hypertrophic cardiomyopathy.* Europace, 2013. **15**(9): p. 1319-27.
51. Dzeshka, M.S., et al., *Cardiac Fibrosis in Patients With Atrial Fibrillation: Mechanisms and Clinical Implications.* J Am Coll Cardiol, 2015. **66**(8): p. 943-59.
52. Ten Tusscher, K.H. and A.V. Panfilov, *Influence of diffuse fibrosis on wave propagation in human ventricular tissue.* Europace, 2007. **9 Suppl 6**: p. vi38-45.
53. Rottner, L., et al., *Catheter Ablation of Atrial Fibrillation: State of the Art and Future Perspectives.* Cardiol Ther, 2020. **9**(1): p. 45-58.

54. Garvanski, I., et al., *Predictors of Recurrence of AF in Patients After Radiofrequency Ablation.* Eur Cardiol, 2019. **14**(3): p. 165-168.
55. Akoum, N. and N. Marrouche, *Assessment and impact of cardiac fibrosis on atrial fibrillation.* Curr Cardiol Rep, 2014. **16**(8): p. 518.
56. Hirsh, B.J., R.S. Copeland-Halperin, and J.L. Halperin, *Fibrotic atrial cardiomyopathy, atrial fibrillation, and thromboembolism: mechanistic links and clinical inferences.* J Am Coll Cardiol, 2015. **65**(20): p. 2239-51.
57. Cochet, H., et al., *Pre- and intra-procedural predictors of reverse remodeling after cardiac resynchronization therapy: an MRI study.* J Cardiovasc Electrophysiol, 2013. **24**(6): p. 682-91.
58. Leong, D.P., et al., *Effects of myocardial fibrosis and ventricular dyssynchrony on response to therapy in new-presentation idiopathic dilated cardiomyopathy: insights from cardiovascular magnetic resonance and echocardiography.* Eur Heart J, 2012. **33**(5): p. 640-8.
59. Chen, Z., et al., *Focal But Not Diffuse Myocardial Fibrosis Burden Quantification Using Cardiac Magnetic Resonance Imaging Predicts Left Ventricular Reverse Modeling Following Cardiac Resynchronization Therapy.* J Cardiovasc Electrophysiol, 2016. **27**(2): p. 203-9.
60. Massoullie, G., et al., *Low fibrosis biomarker levels predict cardiac resynchronization therapy response.* Sci Rep, 2019. **9**(1): p. 6103.
61. Aoki, T., et al., *Prognostic impact of myocardial interstitial fibrosis in non-ischemic heart failure. -Comparison between preserved and reduced ejection fraction heart failure.* Circ J, 2011. **75**(11): p. 2605-13.
62. Paulus, W.J. and C. Tschope, *A novel paradigm for heart failure with preserved ejection fraction: comorbidities drive myocardial dysfunction and remodeling through coronary microvascular endothelial inflammation.* J Am Coll Cardiol, 2013. **62**(4): p. 263-71.
63. Kato, S., et al., *Prognostic significance of quantitative assessment of focal myocardial fibrosis in patients with heart failure with preserved ejection fraction.* Int J Cardiol, 2015. **191**: p. 314-9.
64. Gulati, A., et al., *Absence of Myocardial Fibrosis Predicts Favorable Long-Term Survival in New-Onset Heart Failure.* Circ Cardiovasc Imaging, 2018. **11**(9): p. e007722.
65. Eschalier, R., et al., *Extracellular matrix turnover biomarkers predict long-term left ventricular remodeling after myocardial infarction: insights from the REVE-2 study.* Circ Heart Fail, 2013. **6**(6): p. 1199-205.
66. Lopez-Andres, N., et al., *Association of galectin-3 and fibrosis markers with long-term cardiovascular outcomes in patients with heart failure, left ventricular dysfunction, and dyssynchrony: insights from the CARE-HF (Cardiac Resynchronization in Heart Failure) trial.* Eur J Heart Fail, 2012. **14**(1): p. 74-81.
67. Bulluck, H., et al., *Myocardial T1 mapping.* Circ J, 2015. **79**(3): p. 487-94.
68. Azevedo, P.S., et al., *Cardiac Remodeling: Concepts, Clinical Impact, Pathophysiological Mechanisms and Pharmacologic Treatment.* Arq Bras Cardiol, 2016. **106**(1): p. 62-9.
69. Cohn, J.N., R. Ferrari, and N. Sharpe, *Cardiac remodeling--concepts and clinical implications: a consensus paper from an international forum on cardiac remodeling. Behalf of an International Forum on Cardiac Remodeling.* J Am Coll Cardiol, 2000. **35**(3): p. 569-82.

70. Weber, K.T., Y. Sun, and E. Guarda, *Structural remodeling in hypertensive heart disease and the role of hormones.* Hypertension, 1994. **23**(6 Pt 2): p. 869-77.
71. Maron, B.J., S.E. Epstein, and W.C. Roberts, *Hypertrophic cardiomyopathy and transmural myocardial infarction without significant atherosclerosis of the extramural coronary arteries.* Am J Cardiol, 1979. **43**(6): p. 1086-102.
72. Chiong, M., et al., *Cardiomyocyte death: mechanisms and translational implications.* Cell Death Dis, 2011. **2**: p. e244.
73. Dorn, G.W., 2nd, *Apoptotic and non-apoptotic programmed cardiomyocyte death in ventricular remodelling.* Cardiovasc Res, 2009. **81**(3): p. 465-73.
74. Bialik, S., et al., *Myocyte apoptosis during acute myocardial infarction in the mouse localizes to hypoxic regions but occurs independently of p53.* J Clin Invest, 1997. **100**(6): p. 1363-72.
75. Dobaczewski, M., C. Gonzalez-Quesada, and N.G. Frangogiannis, *The extracellular matrix as a modulator of the inflammatory and reparative response following myocardial infarction.* J Mol Cell Cardiol, 2010. **48**(3): p. 504-11.
76. Holmes, J.W., T.K. Borg, and J.W. Covell, *Structure and mechanics of healing myocardial infarcts.* Annu Rev Biomed Eng, 2005. **7**: p. 223-53.
77. Richardson, W.J., et al., *Physiological Implications of Myocardial Scar Structure.* Compr Physiol, 2015. **5**(4): p. 1877-909.
78. Etoh, T., et al., *Myocardial and interstitial matrix metalloproteinase activity after acute myocardial infarction in pigs.* Am J Physiol Heart Circ Physiol, 2001. **281**(3): p. H987-94.
79. Yang, F., et al., *Myocardial infarction and cardiac remodelling in mice.* Exp Physiol, 2002. **87**(5): p. 547-55.
80. Fishbein, M.C., D. Maclean, and P.R. Maroko, *Experimental myocardial infarction in the rat: qualitative and quantitative changes during pathologic evolution.* Am J Pathol, 1978. **90**(1): p. 57-70.
81. Vanhoutte, D., et al., *Relevance of matrix metalloproteinases and their inhibitors after myocardial infarction: a temporal and spatial window.* Cardiovasc Res, 2006. **69**(3): p. 604-13.
82. O'Rourke, S.A., A. Dunne, and M.G. Monaghan, *The Role of Macrophages in the Infarcted Myocardium: Orchestrators of ECM Remodeling.* Front Cardiovasc Med, 2019. **6**: p. 101.
83. Frangogiannis, N.G., C.W. Smith, and M.L. Entman, *The inflammatory response in myocardial infarction.* Cardiovasc Res, 2002. **53**(1): p. 31-47.
84. Jugdutt, B.I., *Ventricular remodeling after infarction and the extracellular collagen matrix: when is enough enough?* Circulation, 2003. **108**(11): p. 1395-403.
85. Zeisberg, M. and R. Kalluri, *Cellular mechanisms of tissue fibrosis. 1. Common and organ-specific mechanisms associated with tissue fibrosis.* Am J Physiol Cell Physiol, 2013. **304**(3): p. C216-25.
86. Factor, S.M., et al., *Pathologic fibrosis and matrix connective tissue in the subaortic myocardium of patients with hypertrophic cardiomyopathy.* J Am Coll Cardiol, 1991. **17**(6): p. 1343-51.
87. Ginzton, L.E., et al., *Functional significance of hypertrophy of the noninfarcted myocardium after myocardial infarction in humans.* Circulation, 1989. **80**(4): p. 816-22.

88. Talman, V. and H. Ruskoaho, *Cardiac fibrosis in myocardial infarction-from repair and remodeling to regeneration.* Cell Tissue Res, 2016. **365**(3): p. 563-81.
89. Volders, P.G., et al., *Interstitial collagen is increased in the non-infarcted human myocardium after myocardial infarction.* J Mol Cell Cardiol, 1993. **25**(11): p. 1317-23.
90. Litwin, S.E., et al., *Contractility and stiffness of noninfarcted myocardium after coronary ligation in rats. Effects of chronic angiotensin converting enzyme inhibition.* Circulation, 1991. **83**(3): p. 1028-37.
91. Choudhury, L., et al., *Myocardial scarring in asymptomatic or mildly symptomatic patients with hypertrophic cardiomyopathy.* J Am Coll Cardiol, 2002. **40**(12): p. 2156-64.
92. Bujak, M., et al., *Essential role of Smad3 in infarct healing and in the pathogenesis of cardiac remodeling.* Circulation, 2007. **116**(19): p. 2127-38.
93. Nakamura, H., et al., *Induction of left ventricular remodeling and dysfunction in the recipient heart after donor heart myocardial infarction: new insights into the pathologic role of tumor necrosis factor-alpha from a novel heterotopic transplant-coronary ligation rat model.* J Am Coll Cardiol, 2003. **42**(1): p. 173-81.
94. Deten, A., et al., *Cardiac cytokine expression is upregulated in the acute phase after myocardial infarction. Experimental studies in rats.* Cardiovasc Res, 2002. **55**(2): p. 329-40.
95. Ono, K., et al., *Cytokine gene expression after myocardial infarction in rat hearts: possible implication in left ventricular remodeling.* Circulation, 1998. **98**(2): p. 149-56.
96. Irwin, M.W., et al., *Tissue expression and immunolocalization of tumor necrosis factor-alpha in postinfarction dysfunctional myocardium.* Circulation, 1999. **99**(11): p. 1492-8.
97. Weber, K.T., *Cardiac interstitium in health and disease: the fibrillar collagen network.* J Am Coll Cardiol, 1989. **13**(7): p. 1637-52.
98. Anderson, K.R., M.G. Sutton, and J.T. Lie, *Histopathological types of cardiac fibrosis in myocardial disease.* J Pathol, 1979. **128**(2): p. 79-85.
99. Chin, C.W.L., et al., *Myocardial Fibrosis and Cardiac Decompensation in Aortic Stenosis.* JACC Cardiovasc Imaging, 2017. **10**(11): p. 1320-1333.
100. Maron, B.J., et al., *Intramural ("small vessel") coronary artery disease in hypertrophic cardiomyopathy.* J Am Coll Cardiol, 1986. **8**(3): p. 545-57.
101. Dusenbery, S.M., et al., *Myocardial extracellular remodeling is associated with ventricular diastolic dysfunction in children and young adults with congenital aortic stenosis.* J Am Coll Cardiol, 2014. **63**(17): p. 1778-85.
102. Silver, M.A., et al., *Reactive and reparative fibrillar collagen remodelling in the hypertrophied rat left ventricle: two experimental models of myocardial fibrosis.* Cardiovasc Res, 1990. **24**(9): p. 741-7.
103. Tanaka, M., et al., *Quantitative analysis of myocardial fibrosis in normals, hypertensive hearts, and hypertrophic cardiomyopathy.* Br Heart J, 1986. **55**(6): p. 575-81.
104. Hinz, B., *Tissue stiffness, latent TGF-beta1 activation, and mechanical signal transduction: implications for the pathogenesis and treatment of fibrosis.* Curr Rheumatol Rep, 2009. **11**(2): p. 120-6.
105. Thiedemann, K.U., et al., *Connective tissue content and myocardial stiffness in pressure overload hypertrophy. A combined study of morphologic,*

morphometric, biochemical, and mechanical parameters. Basic Res Cardiol, 1983. **78**(2): p. 140-55.
106. Coronel, R., et al., *Electrophysiological changes in heart failure and their implications for arrhythmogenesis.* Biochim Biophys Acta, 2013. **1832**(12): p. 2432-41.
107. Dhanjal, T.S., et al., *Massive Accumulation of Myofibroblasts in the Critical Isthmus Is Associated With Ventricular Tachycardia Inducibility in Post-Infarct Swine Heart.* JACC Clin Electrophysiol, 2017. **3**(7): p. 703-714.
108. Rommel, K.P., et al., *Extracellular Volume Fraction for Characterization of Patients With Heart Failure and Preserved Ejection Fraction.* J Am Coll Cardiol, 2016. **67**(15): p. 1815-1825.
109. Su, M.Y., et al., *CMR-verified diffuse myocardial fibrosis is associated with diastolic dysfunction in HFpEF.* JACC Cardiovasc Imaging, 2014. **7**(10): p. 991-7.
110. Brutsaert, D.L., *Cardiac endothelial-myocardial signaling: its role in cardiac growth, contractile performance, and rhythmicity.* Physiol Rev, 2003. **83**(1): p. 59-115.
111. Nag, A.C. and R. Zak, *Dissociation of adult mammalian heart into single cell suspension: an ultrastructural study.* J Anat, 1979. **129**(Pt 3): p. 541-59.
112. Pinto, A.R., et al., *Revisiting Cardiac Cellular Composition.* Circ Res, 2016. **118**(3): p. 400-9.
113. Zhou, B., et al., *Genetic fate mapping demonstrates contribution of epicardium-derived cells to the annulus fibrosis of the mammalian heart.* Dev Biol, 2010. **338**(2): p. 251-61.
114. Munoz-Chapuli, R., et al., *The epicardium as a source of mesenchyme for the developing heart.* Ital J Anat Embryol, 2001. **106**(2 Suppl 1): p. 187-96.
115. Acharya, A., et al., *The bHLH transcription factor Tcf21 is required for lineage-specific EMT of cardiac fibroblast progenitors.* Development, 2012. **139**(12): p. 2139-49.
116. Snider, P., et al., *Origin of cardiac fibroblasts and the role of periostin.* Circ Res, 2009. **105**(10): p. 934-47.
117. Wessels, A., et al., *Epicardially derived fibroblasts preferentially contribute to the parietal leaflets of the atrioventricular valves in the murine heart.* Dev Biol, 2012. **366**(2): p. 111-24.
118. Tallquist, M.D. and J.D. Molkentin, *Redefining the identity of cardiac fibroblasts.* Nat Rev Cardiol, 2017. **14**(8): p. 484-491.
119. Smith, C.L., et al., *Epicardial-derived cell epithelial-to-mesenchymal transition and fate specification require PDGF receptor signaling.* Circ Res, 2011. **108**(12): p. e15-26.
120. Zhou, B., et al., *Epicardial progenitors contribute to the cardiomyocyte lineage in the developing heart.* Nature, 2008. **454**(7200): p. 109-13.
121. Cai, C.L., et al., *A myocardial lineage derives from Tbx18 epicardial cells.* Nature, 2008. **454**(7200): p. 104-8.
122. Olivey, H.E., et al., *Transforming growth factor-beta stimulates epithelial-mesenchymal transformation in the proepicardium.* Dev Dyn, 2006. **235**(1): p. 50-9.
123. Lie-Venema, H., et al., *Origin, fate, and function of epicardium-derived cells (EPDCs) in normal and abnormal cardiac development.* ScientificWorldJournal, 2007. **7**: p. 1777-98.

124. Visconti, R.P. and R.R. Markwald, *Recruitment of new cells into the postnatal heart: potential modification of phenotype by periostin.* Ann N Y Acad Sci, 2006. **1080**: p. 19-33.
125. Kovacic, J.C., et al., *Epithelial-to-mesenchymal and endothelial-to-mesenchymal transition: from cardiovascular development to disease.* Circulation, 2012. **125**(14): p. 1795-808.
126. Snider, P., et al., *Periostin is required for maturation and extracellular matrix stabilization of noncardiomyocyte lineages of the heart.* Circ Res, 2008. **102**(7): p. 752-60.
127. Ouanouki, A., S. Lamy, and B. Annabi, *Periostin, a signal transduction intermediate in TGF-beta-induced EMT in U-87MG human glioblastoma cells, and its inhibition by anthocyanidins.* Oncotarget, 2018. **9**(31): p. 22023-22037.
128. Hu, Q., et al., *Periostin Mediates TGF-beta-Induced Epithelial Mesenchymal Transition in Prostate Cancer Cells.* Cell Physiol Biochem, 2015. **36**(2): p. 799-809.
129. de Lange, F.J., et al., *Lineage and morphogenetic analysis of the cardiac valves.* Circ Res, 2004. **95**(6): p. 645-54.
130. Kisanuki, Y.Y., et al., *Tie2-Cre transgenic mice: a new model for endothelial cell-lineage analysis in vivo.* Dev Biol, 2001. **230**(2): p. 230-42.
131. Ali, S.R., et al., *Developmental heterogeneity of cardiac fibroblasts does not predict pathological proliferation and activation.* Circ Res, 2014. **115**(7): p. 625-35.
132. Moore-Morris, T., et al., *Resident fibroblast lineages mediate pressure overload-induced cardiac fibrosis.* J Clin Invest, 2014. **124**(7): p. 2921-34.
133. Armstrong, E.J. and J. Bischoff, *Heart valve development: endothelial cell signaling and differentiation.* Circ Res, 2004. **95**(5): p. 459-70.
134. Niessen, K., et al., *Slug is a direct Notch target required for initiation of cardiac cushion cellularization.* J Cell Biol, 2008. **182**(2): p. 315-25.
135. Tamariz, E. and F. Grinnell, *Modulation of fibroblast morphology and adhesion during collagen matrix remodeling.* Mol Biol Cell, 2002. **13**(11): p. 3915-29.
136. Hinz, B., et al., *The myofibroblast: one function, multiple origins.* Am J Pathol, 2007. **170**(6): p. 1807-16.
137. Souders, C.A., S.L. Bowers, and T.A. Baudino, *Cardiac fibroblast: the renaissance cell.* Circ Res, 2009. **105**(12): p. 1164-76.
138. Camelliti, P., T.K. Borg, and P. Kohl, *Structural and functional characterisation of cardiac fibroblasts.* Cardiovasc Res, 2005. **65**(1): p. 40-51.
139. Bosman, F.T. and I. Stamenkovic, *Functional structure and composition of the extracellular matrix.* J Pathol, 2003. **200**(4): p. 423-8.
140. Chapman, D., K.T. Weber, and M. Eghbali, *Regulation of fibrillar collagen types I and III and basement membrane type IV collagen gene expression in pressure overloaded rat myocardium.* Circ Res, 1990. **67**(4): p. 787-94.
141. Bashey, R.I., et al., *Growth properties and biochemical characterization of collagens synthesized by adult rat heart fibroblasts in culture.* J Mol Cell Cardiol, 1992. **24**(7): p. 691-700.
142. Fan, D., et al., *Cardiac fibroblasts, fibrosis and extracellular matrix remodeling in heart disease.* Fibrogenesis Tissue Repair, 2012. **5**(1): p. 15.

143. Tsuruda, T., L.C. Costello-Boerrigter, and J.C. Burnett, Jr., *Matrix metalloproteinases: pathways of induction by bioactive molecules.* Heart Fail Rev, 2004. **9**(1): p. 53-61.
144. Lindner, D., et al., *Differential expression of matrix metalloproteases in human fibroblasts with different origins.* Biochem Res Int, 2012. **2012**: p. 875742.
145. Ma, Y., et al., *Myofibroblasts and the extracellular matrix network in post-myocardial infarction cardiac remodeling.* Pflugers Arch, 2014. **466**(6): p. 1113-27.
146. Liu, Y., et al., *Surrounding tissues affect the passive mechanics of the vessel wall: theory and experiment.* Am J Physiol Heart Circ Physiol, 2007. **293**(6): p. H3290-300.
147. Pizzo, A.M., et al., *Extracellular matrix (ECM) microstructural composition regulates local cell-ECM biomechanics and fundamental fibroblast behavior: a multidimensional perspective.* J Appl Physiol (1985), 2005. **98**(5): p. 1909-21.
148. Flynn, B.P., et al., *Mechanical strain stabilizes reconstituted collagen fibrils against enzymatic degradation by mammalian collagenase matrix metalloproteinase 8 (MMP-8).* PLoS One, 2010. **5**(8): p. e12337.
149. Manso, A.M., S.M. Kang, and R.S. Ross, *Integrins, focal adhesions, and cardiac fibroblasts.* J Investig Med, 2009. **57**(8): p. 856-60.
150. Herum, K.M., et al., *The Soft- and Hard-Heartedness of Cardiac Fibroblasts: Mechanotransduction Signaling Pathways in Fibrosis of the Heart.* J Clin Med, 2017. **6**(5).
151. Mayalu, M.N., M.C. Kim, and H.H. Asada, *Multi-cell ECM compaction is predictable via superposition of nonlinear cell dynamics linearized in augmented state space.* PLoS Comput Biol, 2019. **15**(9): p. e1006798.
152. Ehrlich, H.P., G. Gabbiani, and P. Meda, *Cell coupling modulates the contraction of fibroblast-populated collagen lattices.* J Cell Physiol, 2000. **184**(1): p. 86-92.
153. Carver, W., et al., *Role of the alpha 1 beta 1 integrin complex in collagen gel contraction in vitro by fibroblasts.* J Cell Physiol, 1995. **165**(2): p. 425-37.
154. Schiro, J.A., et al., *Integrin alpha 2 beta 1 (VLA-2) mediates reorganization and contraction of collagen matrices by human cells.* Cell, 1991. **67**(2): p. 403-10.
155. Caulfield, J.B. and T.K. Borg, *The collagen network of the heart.* Lab Invest, 1979. **40**(3): p. 364-72.
156. Johnson, R.D. and P. Camelliti, *Role of Non-Myocyte Gap Junctions and Connexin Hemichannels in Cardiovascular Health and Disease: Novel Therapeutic Targets?* Int J Mol Sci, 2018. **19**(3).
157. Thomsen, M.B. and K. Calloe, *Human atrial fibroblasts and their contribution to supraventricular arrhythmia.* Physiol Rep, 2016. **4**(3).
158. Kohl, P. and D. Noble, *Mechanosensitive connective tissue: potential influence on heart rhythm.* Cardiovasc Res, 1996. **32**(1): p. 62-8.
159. Krenning, G., E.M. Zeisberg, and R. Kalluri, *The origin of fibroblasts and mechanism of cardiac fibrosis.* J Cell Physiol, 2010. **225**(3): p. 631-7.
160. Zeisberg, E.M., et al., *Endothelial-to-mesenchymal transition contributes to cardiac fibrosis.* Nat Med, 2007. **13**(8): p. 952-61.

161. Widyantoro, B., et al., *Endothelial cell-derived endothelin-1 promotes cardiac fibrosis in diabetic hearts through stimulation of endothelial-to-mesenchymal transition.* Circulation, 2010. **121**(22): p. 2407-18.
162. Ieronimakis, N., et al., *Coronary adventitial cells are linked to perivascular cardiac fibrosis via TGFbeta1 signaling in the mdx mouse model of Duchenne muscular dystrophy.* J Mol Cell Cardiol, 2013. **63**: p. 122-34.
163. Kramann, R., et al., *Perivascular Gli1+ progenitors are key contributors to injury-induced organ fibrosis.* Cell Stem Cell, 2015. **16**(1): p. 51-66.
164. Haudek, S.B., et al., *Bone marrow-derived fibroblast precursors mediate ischemic cardiomyopathy in mice.* Proc Natl Acad Sci U S A, 2006. **103**(48): p. 18284-9.
165. Mollmann, H., et al., *Bone marrow-derived cells contribute to infarct remodelling.* Cardiovasc Res, 2006. **71**(4): p. 661-71.
166. van Amerongen, M.J., et al., *Bone marrow-derived myofibroblasts contribute functionally to scar formation after myocardial infarction.* J Pathol, 2008. **214**(3): p. 377-86.
167. Kanisicak, O., et al., *Genetic lineage tracing defines myofibroblast origin and function in the injured heart.* Nat Commun, 2016. **7**: p. 12260.
168. Ruiz-Villalba, A., et al., *Interacting resident epicardium-derived fibroblasts and recruited bone marrow cells form myocardial infarction scar.* J Am Coll Cardiol, 2015. **65**(19): p. 2057-66.
169. van Wijk, B., et al., *Cardiac regeneration from activated epicardium.* PLoS One, 2012. **7**(9): p. e44692.
170. Zhou, B., et al., *Adult mouse epicardium modulates myocardial injury by secreting paracrine factors.* J Clin Invest, 2011. **121**(5): p. 1894-904.
171. Movat, H.Z. and N.V. Fernando, *The fine structure of connective tissue. I. The fibroblast.* Exp Mol Pathol, 1962. **1**: p. 509-34.
172. Tomasek, J.J., et al., *Myofibroblasts and mechano-regulation of connective tissue remodelling.* Nat Rev Mol Cell Biol, 2002. **3**(5): p. 349-63.
173. Fu, X., et al., *Specialized fibroblast differentiated states underlie scar formation in the infarcted mouse heart.* J Clin Invest, 2018. **128**(5): p. 2127-2143.
174. Mouton, A.J., et al., *Fibroblast polarization over the myocardial infarction time continuum shifts roles from inflammation to angiogenesis.* Basic Res Cardiol, 2019. **114**(2): p. 6.
175. Hinz, B., *Formation and function of the myofibroblast during tissue repair.* J Invest Dermatol, 2007. **127**(3): p. 526-37.
176. Humeres, C. and N.G. Frangogiannis, *Fibroblasts in the Infarcted, Remodeling, and Failing Heart.* JACC Basic Transl Sci, 2019. **4**(3): p. 449-467.
177. Frangogiannis, N.G., L.H. Michael, and M.L. Entman, *Myofibroblasts in reperfused myocardial infarcts express the embryonic form of smooth muscle myosin heavy chain (SMemb).* Cardiovasc Res, 2000. **48**(1): p. 89-100.
178. Kaur, H., et al., *Targeted Ablation of Periostin-Expressing Activated Fibroblasts Prevents Adverse Cardiac Remodeling in Mice.* Circ Res, 2016. **118**(12): p. 1906-17.
179. Cowling, R.T., et al., *Mechanisms of cardiac collagen deposition in experimental models and human disease.* Transl Res, 2019. **209**: p. 138-155.
180. Elson, E.L., et al., *A model for positive feedback control of the transformation of fibroblasts to myofibroblasts.* Prog Biophys Mol Biol, 2018. **144**: p. 30-40.

181. Woodcock-Mitchell, J., et al., *Alpha-smooth muscle actin is transiently expressed in embryonic rat cardiac and skeletal muscles.* Differentiation, 1988. **39**(3): p. 161-6.
182. Owens, G.K., *Regulation of differentiation of vascular smooth muscle cells.* Physiol Rev, 1995. **75**(3): p. 487-517.
183. Narikawa, M., et al., *Acute Hyperthermia Inhibits TGF-beta1-induced Cardiac Fibroblast Activation via Suppression of Akt Signaling.* Sci Rep, 2018. **8**(1): p. 6277.
184. Cho, N., S.E. Razipour, and M.L. McCain, *Featured Article: TGF-beta1 dominates extracellular matrix rigidity for inducing differentiation of human cardiac fibroblasts to myofibroblasts.* Exp Biol Med (Maywood), 2018. **243**(7): p. 601-612.
185. Serini, G., et al., *The fibronectin domain ED-A is crucial for myofibroblastic phenotype induction by transforming growth factor-beta1.* J Cell Biol, 1998. **142**(3): p. 873-81.
186. Cucoranu, I., et al., *NAD(P)H oxidase 4 mediates transforming growth factor-beta1-induced differentiation of cardiac fibroblasts into myofibroblasts.* Circ Res, 2005. **97**(9): p. 900-7.
187. Ivey, M.J., et al., *Resident fibroblast expansion during cardiac growth and remodeling.* J Mol Cell Cardiol, 2018. **114**: p. 161-174.
188. Pauschinger, M., et al., *Dilated cardiomyopathy is associated with significant changes in collagen type I/III ratio.* Circulation, 1999. **99**(21): p. 2750-6.
189. Pauschinger, M., et al., *Differential myocardial abundance of collagen type I and type III mRNA in dilated cardiomyopathy: effects of myocardial inflammation.* Cardiovasc Res, 1998. **37**(1): p. 123-9.
190. Mukherjee, D. and S. Sen, *Alteration of cardiac collagen phenotypes in hypertensive hypertrophy: role of blood pressure.* J Mol Cell Cardiol, 1993. **25**(2): p. 185-96.
191. Mukherjee, D. and S. Sen, *Alteration of collagen phenotypes in ischemic cardiomyopathy.* J Clin Invest, 1991. **88**(4): p. 1141-6.
192. Soufen, H.N., et al., *Collagen content, but not the ratios of collagen type III/I mRNAs, differs among hypertensive, alcoholic, and idiopathic dilated cardiomyopathy.* Braz J Med Biol Res, 2008. **41**(12): p. 1098-104.
193. Gonzalez-Santamaria, J., et al., *Matrix cross-linking lysyl oxidases are induced in response to myocardial infarction and promote cardiac dysfunction.* Cardiovasc Res, 2016. **109**(1): p. 67-78.
194. Lu, X., et al., *Smooth muscle alpha-actin expression in endothelial cells derived from CD34+ human cord blood cells.* Stem Cells Dev, 2004. **13**(5): p. 521-7.
195. Ando, J., et al., *Differential display and cloning of shear stress-responsive messenger RNAs in human endothelial cells.* Biochem Biophys Res Commun, 1996. **225**(2): p. 347-51.
196. Smith-Mungo, L.I. and H.M. Kagan, *Lysyl oxidase: properties, regulation and multiple functions in biology.* Matrix Biol, 1998. **16**(7): p. 387-98.
197. Green, R.S., et al., *Identification of lysyl oxidase and other platelet-derived growth factor-inducible genes in vascular smooth muscle cells by differential screening.* Lab Invest, 1995. **73**(4): p. 476-82.
198. Garrett, Q., et al., *Involvement of CTGF in TGF-beta1-stimulation of myofibroblast differentiation and collagen matrix contraction in the presence of mechanical stress.* Invest Ophthalmol Vis Sci, 2004. **45**(4): p. 1109-16.

199. Lipson, K.E., et al., *CTGF is a central mediator of tissue remodeling and fibrosis and its inhibition can reverse the process of fibrosis.* Fibrogenesis Tissue Repair, 2012. **5**(Suppl 1): p. S24.
200. Dorn, L.E., et al., *CTGF/CCN2 is an autocrine regulator of cardiac fibrosis.* J Mol Cell Cardiol, 2018. **121**: p. 205-211.
201. Zeisberg, E.M. and R. Kalluri, *Origins of cardiac fibroblasts.* Circ Res, 2010. **107**(11): p. 1304-12.
202. Kong, P., et al., *Lack of specificity of fibroblast-specific protein 1 in cardiac remodeling and fibrosis.* Am J Physiol Heart Circ Physiol, 2013. **305**(9): p. H1363-72.
203. Ivey, M.J. and M.D. Tallquist, *Defining the Cardiac Fibroblast.* Circ J, 2016. **80**(11): p. 2269-2276.
204. Braitsch, C.M., et al., *Differential expression of embryonic epicardial progenitor markers and localization of cardiac fibrosis in adult ischemic injury and hypertensive heart disease.* J Mol Cell Cardiol, 2013. **65**: p. 108-19.
205. Qian, L., et al., *In vivo reprogramming of murine cardiac fibroblasts into induced cardiomyocytes.* Nature, 2012. **485**(7400): p. 593-8.
206. Bogdanova, M., et al., *Inflammation and Mechanical Stress Stimulate Osteogenic Differentiation of Human Aortic Valve Interstitial Cells.* Front Physiol, 2018. **9**: p. 1635.
207. Zent, J. and L.W. Guo, *Signaling Mechanisms of Myofibroblastic Activation: Outside-in and Inside-Out.* Cell Physiol Biochem, 2018. **49**(3): p. 848-868.
208. Davis, J. and J.D. Molkentin, *Myofibroblasts: trust your heart and let fate decide.* J Mol Cell Cardiol, 2014. **70**: p. 9-18.
209. Booz, G.W. and K.M. Baker, *Molecular signalling mechanisms controlling growth and function of cardiac fibroblasts.* Cardiovasc Res, 1995. **30**(4): p. 537-43.
210. Powell, D.W., et al., *Myofibroblasts. I. Paracrine cells important in health and disease.* Am J Physiol, 1999. **277**(1): p. C1-9.
211. Kapoun, A.M., et al., *B-type natriuretic peptide exerts broad functional opposition to transforming growth factor-beta in primary human cardiac fibroblasts: fibrosis, myofibroblast conversion, proliferation, and inflammation.* Circ Res, 2004. **94**(4): p. 453-61.
212. Desmouliere, A., et al., *Transforming growth factor-beta 1 induces alpha-smooth muscle actin expression in granulation tissue myofibroblasts and in quiescent and growing cultured fibroblasts.* J Cell Biol, 1993. **122**(1): p. 103-11.
213. Peng, H., et al., *Ac-SDKP inhibits transforming growth factor-beta1-induced differentiation of human cardiac fibroblasts into myofibroblasts.* Am J Physiol Heart Circ Physiol, 2010. **298**(5): p. H1357-64.
214. Bujak, M. and N.G. Frangogiannis, *The role of TGF-beta signaling in myocardial infarction and cardiac remodeling.* Cardiovasc Res, 2007. **74**(2): p. 184-95.
215. Dean, R.G., et al., *Connective tissue growth factor and cardiac fibrosis after myocardial infarction.* J Histochem Cytochem, 2005. **53**(10): p. 1245-56.
216. Ikeuchi, M., et al., *Inhibition of TGF-beta signaling exacerbates early cardiac dysfunction but prevents late remodeling after infarction.* Cardiovasc Res, 2004. **64**(3): p. 526-35.
217. Segura, A.M., O.H. Frazier, and L.M. Buja, *Fibrosis and heart failure.* Heart Fail Rev, 2014. **19**(2): p. 173-85.

218. Verrecchia, F., M.L. Chu, and A. Mauviel, *Identification of novel TGF-beta /Smad gene targets in dermal fibroblasts using a combined cDNA microarray/promoter transactivation approach.* J Biol Chem, 2001. **276**(20): p. 17058-62.
219. Dobaczewski, M., et al., *Smad3 signaling critically regulates fibroblast phenotype and function in healing myocardial infarction.* Circ Res, 2010. **107**(3): p. 418-28.
220. Leask, A. and D.J. Abraham, *TGF-beta signaling and the fibrotic response.* FASEB J, 2004. **18**(7): p. 816-27.
221. Akhmetshina, A., et al., *Rho-associated kinases are crucial for myofibroblast differentiation and production of extracellular matrix in scleroderma fibroblasts.* Arthritis Rheum, 2008. **58**(8): p. 2553-64.
222. Dobaczewski, M., W. Chen, and N.G. Frangogiannis, *Transforming growth factor (TGF)-beta signaling in cardiac remodeling.* J Mol Cell Cardiol, 2011. **51**(4): p. 600-6.
223. Wipff, P.J., et al., *Myofibroblast contraction activates latent TGF-beta1 from the extracellular matrix.* J Cell Biol, 2007. **179**(6): p. 1311-23.
224. Sanghi, S., et al., *Activation of protein kinase A by atrial natriuretic peptide in neonatal rat cardiac fibroblasts: role in regulation of the local renin-angiotensin system.* Regul Pept, 2005. **132**(1-3): p. 1-8.
225. Sadoshima, J. and S. Izumo, *Molecular characterization of angiotensin II--induced hypertrophy of cardiac myocytes and hyperplasia of cardiac fibroblasts. Critical role of the AT1 receptor subtype.* Circ Res, 1993. **73**(3): p. 413-23.
226. Vatner, D.E., et al., *Determinants of the cardiomyopathic phenotype in chimeric mice overexpressing cardiac Gsalpha.* Circ Res, 2000. **86**(7): p. 802-6.
227. Rosenkranz, S., *TGF-beta1 and angiotensin networking in cardiac remodeling.* Cardiovasc Res, 2004. **63**(3): p. 423-32.
228. Bouzegrhane, F. and G. Thibault, *Is angiotensin II a proliferative factor of cardiac fibroblasts?* Cardiovasc Res, 2002. **53**(2): p. 304-12.
229. Leask, A., *TGFbeta, cardiac fibroblasts, and the fibrotic response.* Cardiovasc Res, 2007. **74**(2): p. 207-12.
230. Lijnen, P., et al., *Stimulation of collagen gel contraction by angiotensin II and III in cardiac fibroblasts.* J Renin Angiotensin Aldosterone Syst, 2002. **3**(3): p. 160-6.
231. Autelitano, D.J., et al., *Adrenomedullin inhibits angiotensin AT1A receptor expression and function in cardiac fibroblasts.* Regul Pept, 2003. **112**(1-3): p. 131-7.
232. Davis, J., et al., *A TRPC6-dependent pathway for myofibroblast transdifferentiation and wound healing in vivo.* Dev Cell, 2012. **23**(4): p. 705-15.
233. Emig, R., et al., *Human Atrial Fibroblast Adaptation to Heterogeneities in Substrate Stiffness.* Front Physiol, 2019. **10**: p. 1526.
234. Ugolini, G.S., et al., *Human cardiac fibroblasts adaptive responses to controlled combined mechanical strain and oxygen changes in vitro.* Elife, 2017. **6**.
235. Baxter, S.C., M.O. Morales, and E.C. Goldsmith, *Adaptive changes in cardiac fibroblast morphology and collagen organization as a result of mechanical environment.* Cell Biochem Biophys, 2008. **51**(1): p. 33-44.

236. Huang, X., et al., *Matrix stiffness-induced myofibroblast differentiation is mediated by intrinsic mechanotransduction.* Am J Respir Cell Mol Biol, 2012. **47**(3): p. 340-8.
237. Wang, H., et al., *Redirecting valvular myofibroblasts into dormant fibroblasts through light-mediated reduction in substrate modulus.* PLoS One, 2012. **7**(7): p. e39969.
238. Wang, H., et al., *Hydrogels preserve native phenotypes of valvular fibroblasts through an elasticity-regulated PI3K/AKT pathway.* Proc Natl Acad Sci U S A, 2013. **110**(48): p. 19336-41.
239. Atance, J., M.J. Yost, and W. Carver, *Influence of the extracellular matrix on the regulation of cardiac fibroblast behavior by mechanical stretch.* J Cell Physiol, 2004. **200**(3): p. 377-86.
240. Yu, J., et al., *Topological Arrangement of Cardiac Fibroblasts Regulates Cellular Plasticity.* Circ Res, 2018. **123**(1): p. 73-85.
241. Tondon, A. and R. Kaunas, *The direction of stretch-induced cell and stress fiber orientation depends on collagen matrix stress.* PLoS One, 2014. **9**(2): p. e89592.
242. Driesen, R.B., et al., *Reversible and irreversible differentiation of cardiac fibroblasts.* Cardiovasc Res, 2014. **101**(3): p. 411-22.
243. Arora, P.D., N. Narani, and C.A. McCulloch, *The compliance of collagen gels regulates transforming growth factor-beta induction of alpha-smooth muscle actin in fibroblasts.* Am J Pathol, 1999. **154**(3): p. 871-82.
244. Goffin, J.M., et al., *Focal adhesion size controls tension-dependent recruitment of alpha-smooth muscle actin to stress fibers.* J Cell Biol, 2006. **172**(2): p. 259-68.
245. Li, Z., et al., *Transforming growth factor-beta and substrate stiffness regulate portal fibroblast activation in culture.* Hepatology, 2007. **46**(4): p. 1246-56.
246. Olsen, A.L., et al., *Hepatic stellate cells require a stiff environment for myofibroblastic differentiation.* Am J Physiol Gastrointest Liver Physiol, 2011. **301**(1): p. G110-8.
247. Caliari, S.R., et al., *Stiffening hydrogels for investigating the dynamics of hepatic stellate cell mechanotransduction during myofibroblast activation.* Sci Rep, 2016. **6**: p. 21387.
248. Caiazzo, M., et al., *Defined three-dimensional microenvironments boost induction of pluripotency.* Nat Mater, 2016. **15**(3): p. 344-52.
249. Posern, G. and R. Treisman, *Actin' together: serum response factor, its cofactors and the link to signal transduction.* Trends Cell Biol, 2006. **16**(11): p. 588-96.
250. Miralles, F., et al., *Actin dynamics control SRF activity by regulation of its coactivator MAL.* Cell, 2003. **113**(3): p. 329-42.
251. Maekawa, M., et al., *Signaling from Rho to the actin cytoskeleton through protein kinases ROCK and LIM-kinase.* Science, 1999. **285**(5429): p. 895-8.
252. Bravo-Cordero, J.J., et al., *Functions of cofilin in cell locomotion and invasion.* Nat Rev Mol Cell Biol, 2013. **14**(7): p. 405-15.
253. Amano, M., M. Nakayama, and K. Kaibuchi, *Rho-kinase/ROCK: A key regulator of the cytoskeleton and cell polarity.* Cytoskeleton (Hoboken), 2010. **67**(9): p. 545-54.
254. Amano, M., et al., *Phosphorylation and activation of myosin by Rho-associated kinase (Rho-kinase).* J Biol Chem, 1996. **271**(34): p. 20246-9.

255. Kureishi, Y., et al., *Rho-associated kinase directly induces smooth muscle contraction through myosin light chain phosphorylation.* J Biol Chem, 1997. **272**(19): p. 12257-60.
256. Yue, X., et al., *Rnd3 haploinsufficient mice are predisposed to hemodynamic stress and develop apoptotic cardiomyopathy with heart failure.* Cell Death Dis, 2014. **5**: p. e1284.
257. Okamoto, R., et al., *FHL2 prevents cardiac hypertrophy in mice with cardiac-specific deletion of ROCK2.* FASEB J, 2013. **27**(4): p. 1439-49.
258. Hartmann, S., A.J. Ridley, and S. Lutz, *The Function of Rho-Associated Kinases ROCK1 and ROCK2 in the Pathogenesis of Cardiovascular Disease.* Front Pharmacol, 2015. **6**: p. 276.
259. Truebestein, L., et al., *A molecular ruler regulates cytoskeletal remodelling by the Rho kinases.* Nat Commun, 2015. **6**: p. 10029.
260. Shinde, A.V., C. Humeres, and N.G. Frangogiannis, *The role of alpha-smooth muscle actin in fibroblast-mediated matrix contraction and remodeling.* Biochim Biophys Acta Mol Basis Dis, 2017. **1863**(1): p. 298-309.
261. Lopez, B., et al., *Collagen cross-linking but not collagen amount associates with elevated filling pressures in hypertensive patients with stage C heart failure: potential role of lysyl oxidase.* Hypertension, 2012. **60**(3): p. 677-83.
262. Lopez, B., et al., *Role of lysyl oxidase in myocardial fibrosis: from basic science to clinical aspects.* Am J Physiol Heart Circ Physiol, 2010. **299**(1): p. H1-9.
263. Small, E.M., et al., *Myocardin-related transcription factor-a controls myofibroblast activation and fibrosis in response to myocardial infarction.* Circ Res, 2010. **107**(2): p. 294-304.
264. Miano, J.M., *Serum response factor: toggling between disparate programs of gene expression.* J Mol Cell Cardiol, 2003. **35**(6): p. 577-93.
265. Zhang, S.X., et al., *Identification of direct serum-response factor gene targets during Me2SO-induced P19 cardiac cell differentiation.* J Biol Chem, 2005. **280**(19): p. 19115-26.
266. Zhao, X.H., et al., *Force activates smooth muscle alpha-actin promoter activity through the Rho signaling pathway.* J Cell Sci, 2007. **120**(Pt 10): p. 1801-9.
267. Wang, R., et al., *Fibronectin's central cell-binding domain supports focal adhesion formation and Rho signal transduction.* J Biol Chem, 2005. **280**(31): p. 28803-10.
268. Zhou, Y., et al., *Inhibition of mechanosensitive signaling in myofibroblasts ameliorates experimental pulmonary fibrosis.* J Clin Invest, 2013. **123**(3): p. 1096-108.
269. Sandbo, N., et al., *Delayed stress fiber formation mediates pulmonary myofibroblast differentiation in response to TGF-beta.* Am J Physiol Lung Cell Mol Physiol, 2011. **301**(5): p. L656-66.
270. Chen, Y., et al., *MiR-1908 improves cardiac fibrosis after myocardial infarction by targeting TGF-beta1.* Eur Rev Med Pharmacol Sci, 2018. **22**(7): p. 2061-2069.
271. Gao, L., et al., *TNAP inhibition attenuates cardiac fibrosis induced by myocardial infarction through deactivating TGF-beta1/Smads and activating P53 signaling pathways.* Cell Death Dis, 2020. **11**(1): p. 44.

272. Chen, Y.H., et al., *Haplodeficiency of activin receptor-like kinase 4 alleviates myocardial infarction-induced cardiac fibrosis and preserves cardiac function.* J Mol Cell Cardiol, 2017. **105**: p. 1-11.
273. Hiesinger, W., et al., *Myocardial tissue elastic properties determined by atomic force microscopy after stromal cell-derived factor 1alpha angiogenic therapy for acute myocardial infarction in a murine model.* J Thorac Cardiovasc Surg, 2012. **143**(4): p. 962-6.
274. Wang, J., et al., *Mechanical force regulation of myofibroblast differentiation in cardiac fibroblasts.* Am J Physiol Heart Circ Physiol, 2003. **285**(5): p. H1871-81.
275. Chang, J., et al., *Activation of Rho-associated coiled-coil protein kinase 1 (ROCK-1) by caspase-3 cleavage plays an essential role in cardiac myocyte apoptosis.* Proc Natl Acad Sci U S A, 2006. **103**(39): p. 14495-500.
276. Shi, J., et al., *ROCK1 plays an essential role in the transition from cardiac hypertrophy to failure in mice.* J Mol Cell Cardiol, 2010. **49**(5): p. 819-28.
277. Shimizu, T., et al., *Fibroblast deletion of ROCK2 attenuates cardiac hypertrophy, fibrosis, and diastolic dysfunction.* JCI Insight, 2017. **2**(13).
278. Sunamura, S., et al., *Different roles of myocardial ROCK1 and ROCK2 in cardiac dysfunction and postcapillary pulmonary hypertension in mice.* Proc Natl Acad Sci U S A, 2018. **115**(30): p. E7129-E7138.
279. Rikitake, Y., et al., *Decreased perivascular fibrosis but not cardiac hypertrophy in ROCK1+/- haploinsufficient mice.* Circulation, 2005. **112**(19): p. 2959-65.
280. Zhang, Y.M., et al., *Targeted deletion of ROCK1 protects the heart against pressure overload by inhibiting reactive fibrosis.* FASEB J, 2006. **20**(7): p. 916-25.
281. Jatho, A., et al., *RhoA Ambivalently Controls Prominent Myofibroblast Characteritics by Involving Distinct Signaling Routes.* PLoS One, 2015. **10**(10): p. e0137519.
282. Turner, N.A., et al., *Simvastatin inhibits TNFalpha-induced invasion of human cardiac myofibroblasts via both MMP-9-dependent and -independent mechanisms.* J Mol Cell Cardiol, 2007. **43**(2): p. 168-76.
283. Porter, K.E., et al., *Simvastatin reduces human atrial myofibroblast proliferation independently of cholesterol lowering via inhibition of RhoA.* Cardiovasc Res, 2004. **61**(4): p. 745-55.
284. Schram, K., et al., *Regulation of MT1-MMP and MMP-2 by leptin in cardiac fibroblasts involves Rho/ROCK-dependent actin cytoskeletal reorganization and leads to enhanced cell migration.* Endocrinology, 2011. **152**(5): p. 2037-47.
285. Zhou, H., et al., *Fasudil hydrochloride hydrate, a Rho-kinase inhibitor, suppresses high glucose-induced proliferation and collagen synthesis in rat cardiac fibroblasts.* Clin Exp Pharmacol Physiol, 2011. **38**(6): p. 387-94.
286. Ongherth, A., et al., *p63RhoGEF regulates auto- and paracrine signaling in cardiac fibroblasts.* J Mol Cell Cardiol, 2015. **88**: p. 39-54.
287. Yang, R., et al., *High glucose induces Rho/ROCK-dependent visfatin and type I procollagen expression in rat primary cardiac fibroblasts.* Mol Med Rep, 2014. **10**(4): p. 1992-8.
288. Luo, S., et al., *ZYZ-168 alleviates cardiac fibrosis after myocardial infarction through inhibition of ERK1/2-dependent ROCK1 activation.* Sci Rep, 2017. **7**: p. 43242.

289. Ding, W.Y., et al., *Prostaglandin F2alpha facilitates collagen synthesis in cardiac fibroblasts via an F-prostanoid receptor/protein kinase C/Rho kinase pathway independent of transforming growth factor beta1.* Int J Biochem Cell Biol, 2012. **44**(6): p. 1031-9.
290. Seasholtz, T.M., et al., *Rho kinase polymorphism influences blood pressure and systemic vascular resistance in human twins: role of heredity.* Hypertension, 2006. **47**(5): p. 937-47.
291. Rankinen, T., et al., *A major haplotype block at the rho-associated kinase 2 locus is associated with a lower risk of hypertension in a recessive manner: the HYPGENE study.* Hypertens Res, 2008. **31**(8): p. 1651-7.
292. Masumoto, A., et al., *Possible involvement of Rho-kinase in the pathogenesis of hypertension in humans.* Hypertension, 2001. **38**(6): p. 1307-10.
293. Guilluy, C., et al., *RhoA and Rho kinase activation in human pulmonary hypertension: role of 5-HT signaling.* Am J Respir Crit Care Med, 2009. **179**(12): p. 1151-8.
294. Do e, Z., et al., *Evidence for Rho-kinase activation in patients with pulmonary arterial hypertension.* Circ J, 2009. **73**(9): p. 1731-9.
295. Kajikawa, M., et al., *Rho-associated kinase activity is an independent predictor of cardiovascular events in acute coronary syndrome.* Hypertension, 2015. **66**(4): p. 892-9.
296. Dong, M., et al., *Increased Rho kinase activity in congestive heart failure.* Eur J Heart Fail, 2012. **14**(9): p. 965-73.
297. Do e, Z., et al., *Rho-kinase activation in patients with heart failure.* Circ J, 2013. **77**(10): p. 2542-50.
298. Ocaranza, M.P., et al., *Markedly increased Rho-kinase activity in circulating leukocytes in patients with chronic heart failure.* Am Heart J, 2011. **161**(5): p. 931-7.
299. de Boer, R.A., et al., *Towards better definition, quantification and treatment of fibrosis in heart failure. A scientific roadmap by the Committee of Translational Research of the Heart Failure Association (HFA) of the European Society of Cardiology.* Eur J Heart Fail, 2019. **21**(3): p. 272-285.
300. Heymans, S., et al., *Searching for new mechanisms of myocardial fibrosis with diagnostic and/or therapeutic potential.* Eur J Heart Fail, 2015. **17**(8): p. 764-71.
301. Fang, L., A.J. Murphy, and A.M. Dart, *A Clinical Perspective of Anti-Fibrotic Therapies for Cardiovascular Disease.* Front Pharmacol, 2017. **8**: p. 186.
302. Ponikowski, P., et al., *2016 ESC Guidelines for the diagnosis and treatment of acute and chronic heart failure: The Task Force for the diagnosis and treatment of acute and chronic heart failure of the European Society of Cardiology (ESC)Developed with the special contribution of the Heart Failure Association (HFA) of the ESC.* Eur Heart J, 2016. **37**(27): p. 2129-2200.
303. Brilla, C.G., R.C. Funck, and H. Rupp, *Lisinopril-mediated regression of myocardial fibrosis in patients with hypertensive heart disease.* Circulation, 2000. **102**(12): p. 1388-93.
304. Ambari, A.M., et al., *Angiotensin Converting Enzyme Inhibitors (ACEIs) Decrease the Progression of Cardiac Fibrosis in Rheumatic Heart Disease Through the Inhibition of IL-33/sST2.* Frontiers in Cardiovascular Medicine, 2020. **7**(115).

305. Dagenais, G.R., et al., *Angiotensin-converting-enzyme inhibitors in stable vascular disease without left ventricular systolic dysfunction or heart failure: a combined analysis of three trials.* Lancet, 2006. **368**(9535): p. 581-8.
306. Mangiafico, S., et al., *Neutral endopeptidase inhibition and the natriuretic peptide system: an evolving strategy in cardiovascular therapeutics.* Eur Heart J, 2013. **34**(12): p. 886-893c.
307. King, J.B., et al., *Neprilysin Inhibition in Heart Failure with Reduced Ejection Fraction: A Clinical Review.* Pharmacotherapy, 2015. **35**(9): p. 823-37.
308. Steckelings, U.M., et al., *AT2 receptor agonists: hypertension and beyond.* Curr Opin Nephrol Hypertens, 2012. **21**(2): p. 142-6.
309. Kario, K., et al., *Efficacy and safety of LCZ696, a first-in-class angiotensin receptor neprilysin inhibitor, in Asian patients with hypertension: a randomized, double-blind, placebo-controlled study.* Hypertension, 2014. **63**(4): p. 698-705.
310. McMurray, J.J., et al., *Angiotensin-neprilysin inhibition versus enalapril in heart failure.* N Engl J Med, 2014. **371**(11): p. 993-1004.
311. Ferrari, L., S. Sada, and GrAm, *Efficacy of angiotensin-neprilysin inhibition versus enalapril in patient with heart failure with a reduced ejection fraction.* Intern Emerg Med, 2015. **10**(3): p. 369-71.
312. Richeldi, L. and R.M. du Bois, *Pirfenidone in idiopathic pulmonary fibrosis: the CAPACITY program.* Expert Rev Respir Med, 2011. **5**(4): p. 473-81.
313. Lopez-de la Mora, D.A., et al., *Role and New Insights of Pirfenidone in Fibrotic Diseases.* Int J Med Sci, 2015. **12**(11): p. 840-7.
314. King, T.E., Jr., et al., *A phase 3 trial of pirfenidone in patients with idiopathic pulmonary fibrosis.* N Engl J Med, 2014. **370**(22): p. 2083-92.
315. Iyer, S.N., G. Gurujeyalakshmi, and S.N. Giri, *Effects of pirfenidone on transforming growth factor-beta gene expression at the transcriptional level in bleomycin hamster model of lung fibrosis.* J Pharmacol Exp Ther, 1999. **291**(1): p. 367-73.
316. Yamagami, K., et al., *Pirfenidone exhibits cardioprotective effects by regulating myocardial fibrosis and vascular permeability in pressure-overloaded hearts.* Am J Physiol Heart Circ Physiol, 2015. **309**(3): p. H512-22.
317. Yamazaki, T., et al., *The antifibrotic agent pirfenidone inhibits angiotensin II-induced cardiac hypertrophy in mice.* Hypertens Res, 2012. **35**(1): p. 34-40.
318. Mirkovic, S., et al., *Attenuation of cardiac fibrosis by pirfenidone and amiloride in DOCA-salt hypertensive rats.* Br J Pharmacol, 2002. **135**(4): p. 961-8.
319. Nguyen, D.T., et al., *Pirfenidone mitigates left ventricular fibrosis and dysfunction after myocardial infarction and reduces arrhythmias.* Heart Rhythm, 2010. **7**(10): p. 1438-45.
320. Lewis, G.A., et al., *Pirfenidone in Heart Failure with Preserved Ejection Fraction-Rationale and Design of the PIROUETTE Trial.* Cardiovasc Drugs Ther, 2019. **33**(4): p. 461-470.
321. Duscher, D., et al., *Mechanotransduction and fibrosis.* J Biomech, 2014. **47**(9): p. 1997-2005.
322. Surma, M., L. Wei, and J. Shi, *Rho kinase as a therapeutic target in cardiovascular disease.* Future Cardiol, 2011. **7**(5): p. 657-71.
323. Loirand, G., P. Guerin, and P. Pacaud, *Rho kinases in cardiovascular physiology and pathophysiology.* Circ Res, 2006. **98**(3): p. 322-34.

324. Dong, M., et al., *A combination of increased Rho kinase activity and N-terminal pro-B-type natriuretic peptide predicts worse cardiovascular outcome in patients with acute coronary syndrome.* Int J Cardiol, 2013. **167**(6): p. 2813-9.
325. Tanna, A.P. and M. Johnson, *Rho Kinase Inhibitors as a Novel Treatment for Glaucoma and Ocular Hypertension.* Ophthalmology, 2018. **125**(11): p. 1741-1756.
326. Shibuya, M., et al., *Effect of AT877 on cerebral vasospasm after aneurysmal subarachnoid hemorrhage. Results of a prospective placebo-controlled double-blind trial.* J Neurosurg, 1992. **76**(4): p. 571-7.
327. Kishi, T., et al., *Rho-kinase inhibitor improves increased vascular resistance and impaired vasodilation of the forearm in patients with heart failure.* Circulation, 2005. **111**(21): p. 2741-7.
328. Zhang, X., et al., *Effects of Fasudil on Patients with Pulmonary Hypertension Associated with Left Ventricular Heart Failure with Preserved Ejection Fraction: A Prospective Intervention Study.* Can Respir J, 2018. **2018**: p. 3148259.
329. Jiang, R., et al., *Intravenous fasudil improves in-hospital mortality of patients with right heart failure in severe pulmonary hypertension.* Hypertens Res, 2015. **38**(8): p. 539-44.
330. Li, F., et al., *Acute inhibition of Rho-kinase attenuates pulmonary hypertension in patients with congenital heart disease.* Pediatr Cardiol, 2009. **30**(3): p. 363-6.
331. Nohria, A., et al., *Rho kinase inhibition improves endothelial function in human subjects with coronary artery disease.* Circ Res, 2006. **99**(12): p. 1426-32.
332. Ishikura, K., et al., *Beneficial acute effects of rho-kinase inhibitor in patients with pulmonary arterial hypertension.* Circ J, 2006. **70**(2): p. 174-8.
333. Fujita, H., et al., *Acute vasodilator effects of inhaled fasudil, a specific Rho-kinase inhibitor, in patients with pulmonary arterial hypertension.* Heart Vessels, 2010. **25**(2): p. 144-9.
334. Fukumoto, Y., et al., *Acute vasodilator effects of a Rho-kinase inhibitor, fasudil, in patients with severe pulmonary hypertension.* Heart, 2005. **91**(3): p. 391-2.
335. Mohri, M., et al., *Rho-kinase inhibition with intracoronary fasudil prevents myocardial ischemia in patients with coronary microvascular spasm.* J Am Coll Cardiol, 2003. **41**(1): p. 15-9.
336. Noma, K., et al., *Roles of rho-associated kinase and oxidative stress in the pathogenesis of aortic stiffness.* J Am Coll Cardiol, 2007. **49**(6): p. 698-705.
337. Vicari, R.M., et al., *Efficacy and safety of fasudil in patients with stable angina: a double-blind, placebo-controlled, phase 2 trial.* J Am Coll Cardiol, 2005. **46**(10): p. 1803-11.
338. Shimokawa, H., et al., *Anti-anginal effect of fasudil, a Rho-kinase inhibitor, in patients with stable effort angina: a multicenter study.* J Cardiovasc Pharmacol, 2002. **40**(5): p. 751-61.
339. Otsuka, T., et al., *Vasodilatory effect of subsequent administration of fasudil, a rho-kinase inhibitor, surpasses that of nitroglycerin at the concentric coronary stenosis in patients with stable angina pectoris.* Circ J, 2006. **70**(4): p. 402-8.

340. Fukumoto, Y., et al., *Anti-ischemic effects of fasudil, a specific Rho-kinase inhibitor, in patients with stable effort angina.* J Cardiovasc Pharmacol, 2007. **49**(3): p. 117-21.
341. Masumoto, A., et al., *Suppression of coronary artery spasm by the Rho-kinase inhibitor fasudil in patients with vasospastic angina.* Circulation, 2002. **105**(13): p. 1545-7.
342. Shibuya, M., et al., *Effects of fasudil in acute ischemic stroke: results of a prospective placebo-controlled double-blind trial.* J Neurol Sci, 2005. **238**(1-2): p. 31-9.
343. Shi, J. and L. Wei, *Rho kinases in cardiovascular physiology and pathophysiology: the effect of fasudil.* J Cardiovasc Pharmacol, 2013. **62**(4): p. 341-54.
344. Hattori, T., et al., *Long-term inhibition of Rho-kinase suppresses left ventricular remodeling after myocardial infarction in mice.* Circulation, 2004. **109**(18): p. 2234-9.
345. Phrommintikul, A., et al., *Effects of a Rho kinase inhibitor on pressure overload induced cardiac hypertrophy and associated diastolic dysfunction.* Am J Physiol Heart Circ Physiol, 2008. **294**(4): p. H1804-14.
346. Satoh, S., et al., *Chronic inhibition of Rho kinase blunts the process of left ventricular hypertrophy leading to cardiac contractile dysfunction in hypertension-induced heart failure.* J Mol Cell Cardiol, 2003. **35**(1): p. 59-70.
347. Kobayashi, N., et al., *Critical role of Rho-kinase pathway for cardiac performance and remodeling in failing rat hearts.* Cardiovasc Res, 2002. **55**(4): p. 757-67.
348. Breitenlechner, C., et al., *Protein kinase A in complex with Rho-kinase inhibitors Y-27632, Fasudil, and H-1152P: structural basis of selectivity.* Structure, 2003. **11**(12): p. 1595-607.
349. Davies, S.P., et al., *Specificity and mechanism of action of some commonly used protein kinase inhibitors.* Biochem J, 2000. **351**(Pt 1): p. 95-105.
350. Olson, M.F., *Applications for ROCK kinase inhibition.* Curr Opin Cell Biol, 2008. **20**(2): p. 242-8.
351. Sasaki, Y., M. Suzuki, and H. Hidaka, *The novel and specific Rho-kinase inhibitor (S)-(+)-2-methyl-1-[(4-methyl-5-isoquinoline)sulfonyl]-homopiperazine as a probing molecule for Rho-kinase-involved pathway.* Pharmacol Ther, 2002. **93**(2-3): p. 225-32.
352. Shi, X., et al., *Elasticity of cardiac cells on the polymer substrates with different stiffness: an atomic force microscopy study.* Phys Chem Chem Phys, 2011. **13**(16): p. 7540-5.
353. Elson, E.L. and G.M. Genin, *Tissue constructs: platforms for basic research and drug discovery.* Interface Focus, 2016. **6**(1): p. 20150095.
354. Berry, M.F., et al., *Mesenchymal stem cell injection after myocardial infarction improves myocardial compliance.* Am J Physiol Heart Circ Physiol, 2006. **290**(6): p. H2196-203.
355. Pislaru, C., et al., *Viscoelastic properties of normal and infarcted myocardium measured by a multifrequency shear wave method: comparison with pressure-segment length method.* Ultrasound Med Biol, 2014. **40**(8): p. 1785-95.
356. Ghista, D.N., H. Sandler, and W.H. Vayo, *Elastic modulus of the human intact left ventricle--determination and physiological interpretation.* Med Biol Eng, 1975. **13**(2): p. 151-61.

357. Mirsky, I. and W.W. Parmley, *Assessment of passive elastic stiffness for isolated heart muscle and the intact heart.* Circ Res, 1973. **33**(2): p. 233-43.
358. Xie, J., et al., *Substrate stiffness-regulated matrix metalloproteinase output in myocardial cells and cardiac fibroblasts: implications for myocardial fibrosis.* Acta Biomater, 2014. **10**(6): p. 2463-72.
359. Yeh, Y.C., et al., *Mechanically dynamic PDMS substrates to investigate changing cell environments.* Biomaterials, 2017. **145**: p. 23-32.
360. Cox, T.R. and J.T. Erler, *Remodeling and homeostasis of the extracellular matrix: implications for fibrotic diseases and cancer.* Dis Model Mech, 2011. **4**(2): p. 165-78.
361. Pedersen, J.A. and M.A. Swartz, *Mechanobiology in the third dimension.* Ann Biomed Eng, 2005. **33**(11): p. 1469-90.
362. Rhee, S., *Fibroblasts in three dimensional matrices: cell migration and matrix remodeling.* Exp Mol Med, 2009. **41**(12): p. 858-65.
363. Hinz, B., et al., *Alpha-smooth muscle actin expression upregulates fibroblast contractile activity.* Mol Biol Cell, 2001. **12**(9): p. 2730-41.
364. Hinz, B., *The myofibroblast: paradigm for a mechanically active cell.* J Biomech, 2010. **43**(1): p. 146-55.
365. Weinberger, F., I. Mannhardt, and T. Eschenhagen, *Engineering Cardiac Muscle Tissue: A Maturating Field of Research.* Circ Res, 2017. **120**(9): p. 1487-1500.
366. Tiburcy, M. and W.H. Zimmermann, *Modeling myocardial growth and hypertrophy in engineered heart muscle.* Trends Cardiovasc Med, 2014. **24**(1): p. 7-13.
367. Eschenhagen, T., et al., *Three-dimensional reconstitution of embryonic cardiomyocytes in a collagen matrix: a new heart muscle model system.* FASEB J, 1997. **11**(8): p. 683-94.
368. Lijnen, P., V. Petrov, and R. Fagard, *In vitro assay of collagen gel contraction by cardiac fibroblasts in serum-free conditions.* Methods Find Exp Clin Pharmacol, 2001. **23**(7): p. 377-82.
369. Burgess, M.L., et al., *Integrin-mediated collagen gel contraction by cardiac fibroblasts. Effects of angiotensin II.* Circ Res, 1994. **74**(2): p. 291-8.
370. Dworatzek, E., et al., *Sex-specific regulation of collagen I and III expression by 17beta-Estradiol in cardiac fibroblasts: role of estrogen receptors.* Cardiovasc Res, 2019. **115**(2): p. 315-327.
371. Nunohiro, T., et al., *Angiotensin II promotes integrin-mediated collagen gel contraction by adult rat cardiac fibroblasts.* Jpn Heart J, 1999. **40**(4): p. 461-9.
372. Knezevic, V., et al., *Isotonic biaxial loading of fibroblast-populated collagen gels: a versatile, low-cost system for the study of mechanobiology.* Biomech Model Mechanobiol, 2002. **1**(1): p. 59-67.
373. Occhetta, P., et al., *A three-dimensional in vitro dynamic micro-tissue model of cardiac scar formation.* Integr Biol (Camb), 2018. **10**(3): p. 174-183.
374. Wakatsuki, T. and E.L. Elson, *Reciprocal interactions between cells and extracellular matrix during remodeling of tissue constructs.* Biophys Chem, 2003. **100**(1-3): p. 593-605.
375. Wakatsuki, T., et al., *Cell mechanics studied by a reconstituted model tissue.* Biophys J, 2000. **79**(5): p. 2353-68.
376. Wagenseil, J.E., et al., *One-dimensional viscoelastic behavior of fibroblast populated collagen matrices.* J Biomech Eng, 2003. **125**(5): p. 719-25.

377. Kong, M., et al., *Cardiac Fibrotic Remodeling on a Chip with Dynamic Mechanical Stimulation.* Adv Healthc Mater, 2019. **8**(3): p. e1801146.
378. Marquez, J.P., et al., *High-throughput measurements of hydrogel tissue construct mechanics.* Tissue Eng Part C Methods, 2009. **15**(2): p. 181-90.
379. Wille, J.J., E.L. Elson, and R.J. Okamoto, *Cellular and matrix mechanics of bioartificial tissues during continuous cyclic stretch.* Ann Biomed Eng, 2006. **34**(11): p. 1678-90.
380. Tranquillo, R.T., M.A. Durrani, and A.G. Moon, *Tissue engineering science: consequences of cell traction force.* Cytotechnology, 1992. **10**(3): p. 225-50.
381. Barocas, V.H., A.G. Moon, and R.T. Tranquillo, *The fibroblast-populated collagen microsphere assay of cell traction force--Part 2: Measurement of the cell traction parameter.* J Biomech Eng, 1995. **117**(2): p. 161-70.
382. Ngu, J.M., et al., *Human cardiac fibroblast extracellular matrix remodeling: dual effects of tissue inhibitor of metalloproteinase-2.* Cardiovasc Pathol, 2014. **23**(6): p. 335-43.
383. Ibrahim, D.G., et al., *An in vitro study of scarring formation mediated by human Tenon fibroblasts: Effect of Y-27632, a Rho kinase inhibitor.* Cell Biochem Funct, 2019. **37**(2): p. 113-124.
384. Delvoye, P., et al., *Measurement of mechanical forces generated by skin fibroblasts embedded in a three-dimensional collagen gel.* J Invest Dermatol, 1991. **97**(5): p. 898-902.
385. Kolodney, M.S. and E.L. Elson, *Correlation of myosin light chain phosphorylation with isometric contraction of fibroblasts.* J Biol Chem, 1993. **268**(32): p. 23850-5.
386. Isenberg, B.C. and R.T. Tranquillo, *Long-term cyclic distention enhances the mechanical properties of collagen-based media-equivalents.* Ann Biomed Eng, 2003. **31**(8): p. 937-49.
387. Vettel, C., et al., *PDE2-mediated cAMP hydrolysis accelerates cardiac fibroblast to myofibroblast conversion and is antagonized by exogenous activation of cGMP signaling pathways.* Am J Physiol Heart Circ Physiol, 2014. **306**(8): p. H1246-52.
388. Asmani, M., et al., *Fibrotic microtissue array to predict anti-fibrosis drug efficacy.* Nat Commun, 2018. **9**(1): p. 2066.
389. Tiburcy, M., et al., *Defined Engineered Human Myocardium With Advanced Maturation for Applications in Heart Failure Modeling and Repair.* Circulation, 2017. **135**(19): p. 1832-1847.
390. Santos, G.L., et al., *Inhibition of Rho-associated kinases suppresses cardiac myofibroblast function in engineered connective and heart muscle tissues.* J Mol Cell Cardiol, 2019. **134**: p. 13-28.
391. Azeloglu, E.U. and K.D. Costa, *Cross-bridge cycling gives rise to spatiotemporal heterogeneity of dynamic subcellular mechanics in cardiac myocytes probed with atomic force microscopy.* Am J Physiol Heart Circ Physiol, 2010. **298**(3): p. H853-60.
392. Villemain, O., et al., *Myocardial Stiffness Evaluation Using Noninvasive Shear Wave Imaging in Healthy and Hypertrophic Cardiomyopathic Adults.* JACC Cardiovasc Imaging, 2019. **12**(7 Pt 1): p. 1135-1145.
393. Cunningham, F., et al., *Ensembl 2019.* Nucleic Acids Res, 2019. **47**(D1): p. D745-D751.
394. Ye, J., et al., *Primer-BLAST: a tool to design target-specific primers for polymerase chain reaction.* BMC Bioinformatics, 2012. **13**: p. 134.

395. Golden, H.B., et al., *Isolation of Cardiac Myocytes and Fibroblasts from Neonatal Rat Pups.*, in *Cardiovascular Development: Methods and Protocols*, X.P.a.M. Antonyac, Editor. *2012*, Springer Science+Business Media: Germany. p. 205-214.
396. Zimmermann, W.H., et al., *Tissue engineering of a differentiated cardiac muscle construct.* Circ Res, 2002. **90**(2): p. 223-30.
397. Meyer, T., W.H. Zimmermann, and M. Tiburcy, *Well Plate*. 2019, 20190106663: United States Georg-August-Universitaet Goettingen Stiftung Oeffentlichen Rechts, Universitaetsmedizin (Goettingen, DE).
398. Antoine, E.E., P.P. Vlachos, and M.N. Rylander, *Review of collagen I hydrogels for bioengineered tissue microenvironments: characterization of mechanics, structure, and transport.* Tissue Eng Part B Rev, 2014. **20**(6): p. 683-96.
399. Roeder, B.A., et al., *Tensile mechanical properties of three-dimensional type I collagen extracellular matrices with varied microstructure.* J Biomech Eng, 2002. **124**(2): p. 214-22.
400. Holder, A.J., et al., *Control of collagen gel mechanical properties through manipulation of gelation conditions near the sol-gel transition.* Soft Matter, 2018. **14**(4): p. 574-580.
401. Meyer, T., M. Tiburcy, and W.H. Zimmermann, *Cardiac macrotissues-on-a-plate models for phenotypic drug screens.* Adv Drug Deliv Rev, 2019. **140**: p. 93-100.
402. Ormerod, M.G., *Analysis of DNA - general methods, in Flow cytometry: a practical approach*. 3rd ed. The practical approach series, ed. M.G. Ormerod. 2000, Oxford England; New York: Oxford University Press. 83-97.
403. Bradford, M.M., *A rapid and sensitive method for the quantitation of microgram quantities of protein utilizing the principle of protein-dye binding.* Anal Biochem, 1976. **72**: p. 248-54.
404. Kruger, N.J., *The Bradford method for protein quantitation.* Methods Mol Biol, 1994. **32**: p. 9-15.
405. Hammond, J.B. and N.J. Kruger, *The bradford method for protein quantitation.* Methods Mol Biol, 1988. **3**: p. 25-32.
406. Shapiro, A.L., E. Vinuela, and J.V. Maizel, Jr., *Molecular weight estimation of polypeptide chains by electrophoresis in SDS-polyacrylamide gels.* Biochem Biophys Res Commun, 1967. **28**(5): p. 815-20.
407. Laemmli, U.K., *Cleavage of structural proteins during the assembly of the head of bacteriophage T4.* Nature, 1970. **227**(5259): p. 680-5.
408. Hjerten, S., *"Molecular-sieve" electrophoresis in cross-linked polyacrylamide gels.* J Chromatogr, 1963. **11**: p. 66-70.
409. Shi, Q.J., G., *One-dimensional polyacrylamide gel electrophoresis, in Gel electrophoresis of proteins: a practical approach*. 3rd ed. Practical approach series, ed. B.D. Hames. 1998, Oxford; New York: Oxford University Press. xx, 352 p.
410. Chen, B. and A. Chrambach, *Estimation of polymerization efficiency in the formation of polyacrylamide gel, using continuous optical scanning during polymerization.* J Biochem Biophys Methods, 1979. **1**(2): p. 105-16.
411. Towbin, H., T. Staehelin, and J. Gordon, *Electrophoretic transfer of proteins from polyacrylamide gels to nitrocellulose sheets: procedure and some applications.* Proc Natl Acad Sci U S A, 1979. **76**(9): p. 4350-4.

412. Burnette, W.N., *"Western blotting": electrophoretic transfer of proteins from sodium dodecyl sulfate--polyacrylamide gels to unmodified nitrocellulose and radiographic detection with antibody and radioiodinated protein A.* Anal Biochem, 1981. **112**(2): p. 195-203.
413. Mommaerts, K., et al., *Replacing beta-mercaptoethanol in RNA extractions.* Anal Biochem, 2015. **479**: p. 51-3.
414. van der Poel-van de Luytgaarde, S.C., et al., *Addition of beta-mercaptoethanol is a prerequisite for high-quality RNA isolation using QIAsymphony technology as demonstrated by detection of molecular aberrations in hematologic malignancies.* Genet Test Mol Biomarkers, 2013. **17**(6): p. 475-80.
415. Andrews, S., *FastQC A Quality Control tool for High Throughput Sequence Data.* 2014: Available online at http://www.bioinformatics.babraham.ac.uk/projects/fastqc/.
416. *Homo sapiens (hg38 version 89).* Available online at https://www.ensembl.org/Homo_sapiens/Info/Index)
417. Dobin, A., et al., *STAR: ultrafast universal RNA-seq aligner*. Bioinformatics, 2013. **29**(1): p. 15-21.
418. Liao, Y., G.K. Smyth, and W. Shi, *featureCounts: an efficient general purpose program for assigning sequence reads to genomic features.* Bioinformatics, 2014. **30**(7): p. 923-30.
419. *R/Bioconductor environment (version 3.4.2)*. Available online at www.bioconductor.org.
420. Love, M.I., W. Huber, and S. Anders, *Moderated estimation of fold change and dispersion for RNA-seq data with DESeq2.* Genome Biol, 2014. **15**(12): p. 550.
421. Durinck, S., et al., *Mapping identifiers for the integration of genomic datasets with the R/Bioconductor package biomaRt.* Nat Protoc, 2009. **4**(8): p. 1184-91.
422. Metsalu, T. and J. Vilo, *ClustVis: a web tool for visualizing clustering of multivariate data using Principal Component Analysis and heatmap.* Nucleic Acids Res, 2015. **43**(W1): p. W566-70.
423. Perez-Silva, J.G., M. Araujo-Voces, and V. Quesada, *nVenn: generalized, quasi-proportional Venn and Euler diagrams.* Bioinformatics, 2018. **34**(13): p. 2322-2324.
424. Huang da, W., B.T. Sherman, and R.A. Lempicki, *Bioinformatics enrichment tools: paths toward the comprehensive functional analysis of large gene lists.* Nucleic Acids Res, 2009. **37**(1): p. 1-13.
425. Eden, E., et al., *GOrilla: a tool for discovery and visualization of enriched GO terms in ranked gene lists.* BMC Bioinformatics, 2009. **10**: p. 48.
426. Mi, H., et al., *PANTHER version 14: more genomes, a new PANTHER GO-slim and improvements in enrichment analysis tools.* Nucleic Acids Res, 2019. **47**(D1): p. D419-D426.
427. Mi, H., et al., *Protocol Update for large-scale genome and gene function analysis with the PANTHER classification system (v.14.0).* Nat Protoc, 2019. **14**(3): p. 703-721.
428. Szklarczyk, D., et al., *STRING v11: protein-protein association networks with increased coverage, supporting functional discovery in genome-wide experimental datasets.* Nucleic Acids Res, 2019. **47**(D1): p. D607-D613.
429. Fabregat, A., et al., *The Reactome Pathway Knowledgebase.* Nucleic Acids Res, 2018. **46**(D1): p. D649-D655.

430. Fan, L., et al., *Cell contact-dependent regulation of epithelial-myofibroblast transition via the rho-rho kinase-phospho-myosin pathway.* Mol Biol Cell, 2007. **18**(3): p. 1083-97.
431. Tarbit, E., et al., *Biomarkers for the identification of cardiac fibroblast and myofibroblast cells.* Heart Fail Rev, 2019. **24**(1): p. 1-15.
432. Sweet, M.E., et al., *Transcriptome analysis of human heart failure reveals dysregulated cell adhesion in dilated cardiomyopathy and activated immune pathways in ischemic heart failure.* BMC Genomics, 2018. **19**(1): p. 812.
433. Strutz, F., et al., *Identification and characterization of a fibroblast marker: FSP1.* J Cell Biol, 1995. **130**(2): p. 393-405.
434. Rai, V., et al., *Relevance of mouse models of cardiac fibrosis and hypertrophy in cardiac research.* Mol Cell Biochem, 2017. **424**(1-2): p. 123-145.
435. Gyongyosi, M., et al., *Myocardial fibrosis: biomedical research from bench to bedside.* Eur J Heart Fail, 2017. **19**(2): p. 177-191.
436. Pampaloni, F., E.G. Reynaud, and E.H. Stelzer, *The third dimension bridges the gap between cell culture and live tissue.* Nat Rev Mol Cell Biol, 2007. **8**(10): p. 839-45.
437. Sadeghi, A.H., et al., *Engineered 3D Cardiac Fibrotic Tissue to Study Fibrotic Remodeling.* Adv Healthc Mater, 2017. **6**(11).
438. Westerhof, N., *Snapshots of Hemodynamics An Aid for Clinical Research and Graduate Education.* 2010.
439. Ahmad, S.A., et al., *Myocardial fibrosis and arrhythmogenesis in elite athletes.* Clin Cardiol, 2019.
440. Clark, J.A., J.C. Cheng, and K.S. Leung, *Mechanical properties of normal skin and hypertrophic scars.* Burns, 1996. **22**(6): p. 443-6.
441. Corr, D.T. and D.A. Hart, *Biomechanics of Scar Tissue and Uninjured Skin.* Adv Wound Care (New Rochelle), 2013. **2**(2): p. 37-43.
442. Buhimschi, C.S., et al., *Myometrial wound healing post-Cesarean delivery in the MRL/MpJ mouse model of uterine scarring.* Am J Pathol, 2010. **177**(1): p. 197-207.
443. Nakamura, Y., et al., *Permissive effect of fibronectin on collagen gel contraction mediated by bovine trabecular meshwork cells.* Invest Ophthalmol Vis Sci, 2003. **44**(10): p. 4331-6.
444. Taliana, L., et al., *Vitronectin or fibronectin is required for corneal fibroblast-seeded collagen gel contraction.* Invest Ophthalmol Vis Sci, 2000. **41**(1): p. 103-9.
445. Camasao, D.B., et al., *Elastin-like recombinamers in collagen-based tubular gels improve cell-mediated remodeling and viscoelastic properties.* Biomater Sci, 2020. **8**(12): p. 3536-3548.
446. Naydenov, N.G., et al., *N-ethylmaleimide-sensitive factor attachment protein alpha (alphaSNAP) regulates matrix adhesion and integrin processing in human epithelial cells.* J Biol Chem, 2014. **289**(4): p. 2424-39.
447. Yu, Z.Y., et al., *RhoA/ROCK signaling and pleiotropic alpha1A-adrenergic receptor regulation of cardiac contractility.* PLoS One, 2014. **9**(6): p. e99024.
448. Meyer-ter-Vehn, T., et al., *Contractility as a prerequisite for TGF-beta-induced myofibroblast transdifferentiation in human tenon fibroblasts.* Invest Ophthalmol Vis Sci, 2006. **47**(11): p. 4895-904.
449. Oku, Y., et al., *Multimodal effects of small molecule ROCK and LIMK inhibitors on mitosis, and their implication as anti-leukemia agents.* PLoS One, 2014. **9**(3): p. e92402.

450. Chevrier, V., et al., *The Rho-associated protein kinase p160ROCK is required for centrosome positioning.* J Cell Biol, 2002. **157**(5): p. 807-17.
451. Chircop, M., *Rho GTPases as regulators of mitosis and cytokinesis in mammalian cells.* Small GTPases, 2014. **5**.
452. Kosako, H., et al., *Rho-kinase/ROCK is involved in cytokinesis through the phosphorylation of myosin light chain and not ezrin/radixin/moesin proteins at the cleavage furrow.* Oncogene, 2000. **19**(52): p. 6059-64.
453. Melica, M.E., et al., *Substrate Stiffness Modulates Renal Progenitor Cell Properties via a ROCK-Mediated Mechanotransduction Mechanism.* Cells, 2019. **8**(12).
454. Mih, J.D., et al., *Matrix stiffness reverses the effect of actomyosin tension on cell proliferation.* J Cell Sci, 2012. **125**(Pt 24): p. 5974-83.
455. Shimizu, T. and J.K. Liao, *Rho Kinases and Cardiac Remodeling.* Circ J, 2016. **80**(7): p. 1491-8.
456. Berenjeno, I.M. and X.R. Bustelo, *Identification of the Rock-dependent transcriptome in rodent fibroblasts.* Clin Transl Oncol, 2008. **10**(11): p. 726-38.
457. Lau, C.L., et al., *Transcriptomic profiling of astrocytes treated with the Rho kinase inhibitor fasudil reveals cytoskeletal and pro-survival responses.* J Cell Physiol, 2012. **227**(3): p. 1199-211.
458. Boerma, M., et al., *Comparative gene expression profiling in three primary human cell lines after treatment with a novel inhibitor of Rho kinase or atorvastatin.* Blood Coagul Fibrinolysis, 2008. **19**(7): p. 709-18.
459. Wang, V., D.A. Davis, and R. Yarchoan, *Identification of functional hypoxia inducible factor response elements in the human lysyl oxidase gene promoter.* Biochem Biophys Res Commun, 2017. **490**(2): p. 480-485.
460. Gao, S., et al., *Hypoxia-response element (HRE)-directed transcriptional regulation of the rat lysyl oxidase gene in response to cobalt and cadmium.* Toxicol Sci, 2013. **132**(2): p. 379-89.
461. Segond, N., et al., *Transcriptome analysis of PPARgamma target genes reveals the involvement of lysyl oxidase in human placental cytotrophoblast invasion.* PLoS One, 2013. **8**(11): p. e79413.
462. Sethi, A., et al., *Transforming growth factor-beta induces extracellular matrix protein cross-linking lysyl oxidase (LOX) genes in human trabecular meshwork cells.* Invest Ophthalmol Vis Sci, 2011. **52**(8): p. 5240-50.
463. Gao, S., et al., *Cloning and characterization of the rat lysyl oxidase gene promoter: identification of core promoter elements and functional nuclear factor I-binding sites.* J Biol Chem, 2007. **282**(35): p. 25322-37.
464. Yokota, S., et al., *ROCK/actin/MRTF signaling promotes the fibrogenic phenotype of fibroblast-like synoviocytes derived from the temporomandibular joint.* Int J Mol Med, 2017. **39**(4): p. 799-808.
465. Esnault, C., et al., *Rho-actin signaling to the MRTF coactivators dominates the immediate transcriptional response to serum in fibroblasts.* Genes Dev, 2014. **28**(9): p. 943-58.
466. Narayanan, A.S., R.C. Siegel, and G.R. Martin, *On the inhibition of lysyl oxidase by -aminopropionitrile.* Biochem Biophys Res Commun, 1972. **46**(2): p. 745-51.
467. Jung, S.T., et al., *Purification of enzymatically active human lysyl oxidase and lysyl oxidase-like protein from Escherichia coli inclusion bodies.* Protein Expr Purif, 2003. **31**(2): p. 240-6.

468. El Hajj, E.C., et al., *Detrimental role of lysyl oxidase in cardiac remodeling.* J Mol Cell Cardiol, 2017. **109**: p. 17-26.
469. El Hajj, E.C., et al., *Cardioprotective effects of lysyl oxidase inhibition against volume overload-induced extracellular matrix remodeling.* Exp Biol Med (Maywood), 2016. **241**(5): p. 539-49.
470. Martinez-Martinez, E., et al., *The lysyl oxidase inhibitor (beta-aminopropionitrile) reduces leptin profibrotic effects and ameliorates cardiovascular remodeling in diet-induced obesity in rats.* J Mol Cell Cardiol, 2016. **92**: p. 96-104.
471. Balestrini, J.L., et al., *The mechanical memory of lung myofibroblasts.* Integr Biol (Camb), 2012. **4**(4): p. 410-21.
472. Nagaraju, C.K., et al., *Myofibroblast Phenotype and Reversibility of Fibrosis in Patients With End-Stage Heart Failure.* J Am Coll Cardiol, 2019. **73**(18): p. 2267-2282.
473. Gladka, M.M., et al., *Single-Cell Sequencing of the Healthy and Diseased Heart Reveals Cytoskeleton-Associated Protein 4 as a New Modulator of Fibroblasts Activation.* Circulation, 2018. **138**(2): p. 166-180.
474. Farbehi, N., et al., *Single-cell expression profiling reveals dynamic flux of cardiac stromal, vascular and immune cells in health and injury.* Elife, 2019. **8**.
475. Petrov, V.V., R.H. Fagard, and P.J. Lijnen, *Transforming growth factor-beta(1) induces angiotensin-converting enzyme synthesis in rat cardiac fibroblasts during their differentiation to myofibroblasts.* J Renin Angiotensin Aldosterone Syst, 2000. **1**(4): p. 342-52.
476. Imaizumi, T., et al., *Effect of human basic fibroblast growth factor on fibroblast proliferation, cell volume, collagen lattice contraction: in comparison with acidic type.* J Dermatol Sci, 1996. **11**(2): p. 134-41.
477. Tsuchiya, M., et al., *XBP1 may determine the size of the ameloblast endoplasmic reticulum.* J Dent Res, 2008. **87**(11): p. 1058-62.
478. Shaffer, A.L., et al., *XBP1, downstream of Blimp-1, expands the secretory apparatus and other organelles, and increases protein synthesis in plasma cell differentiation.* Immunity, 2004. **21**(1): p. 81-93.
479. Goldsmith, E.C., et al., *Organization of fibroblasts in the heart.* Dev Dyn, 2004. **230**(4): p. 787-94.
480. Stauffer, W.T., et al., *The ER Unfolded Protein Response Effector, ATF6, Reduces Cardiac Fibrosis and Decreases Activation of Cardiac Fibroblasts.* Int J Mol Sci, 2020. **21**(4).
481. Xiao, Y., et al., *Hippo pathway deletion in adult resting cardiac fibroblasts initiates a cell state transition with spontaneous and self-sustaining fibrosis.* Genes Dev, 2019. **33**(21-22): p. 1491-1505.
482. Walter, P. and D. Ron, *The unfolded protein response: from stress pathway to homeostatic regulation.* Science, 2011. **334**(6059): p. 1081-6.
483. Zhang, H., M. Shen, and J.C. Wu, *Generation of Quiescent Cardiac Fibroblasts Derived from Human Induced Pluripotent Stem Cells.* Methods Mol Biol, 2020.